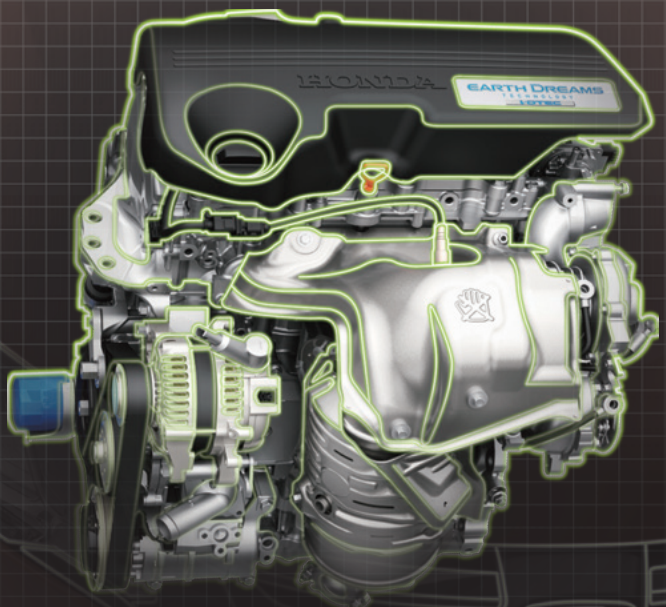
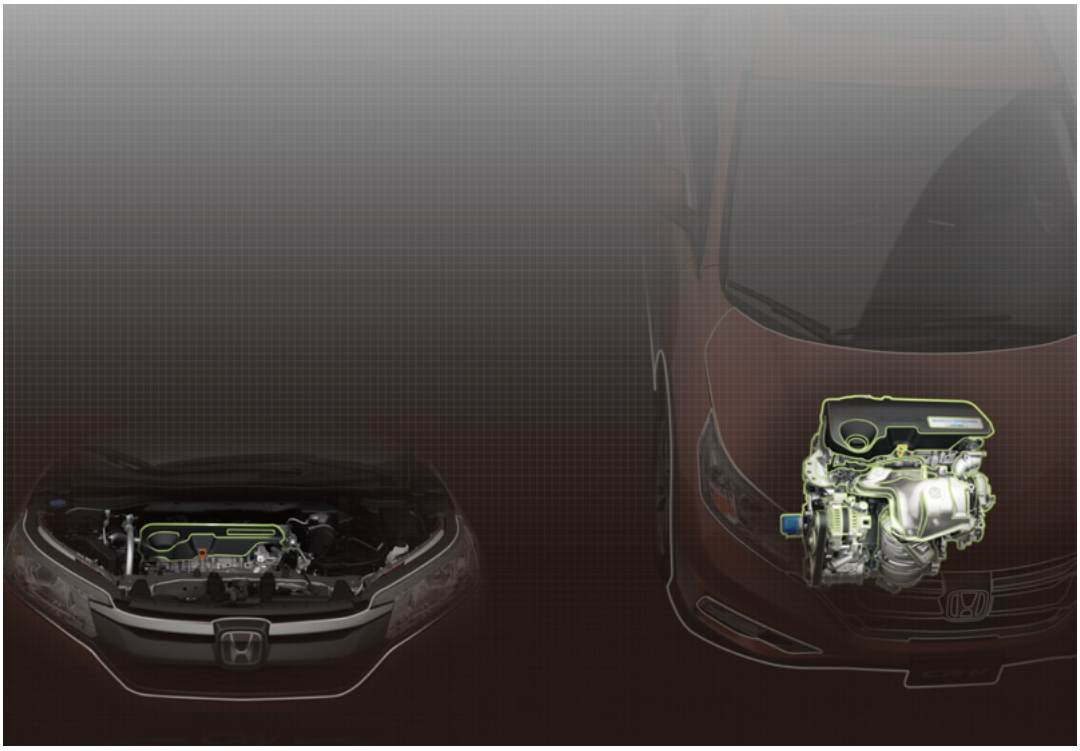
Honda R&D

Technical Review



October 2015
Vol.27 No.2



Comment on the Cover

The unending evolution of the engine never ceases to amaze me. It's thrilling to imagine the engines of the future — how they'll look, what they'll be capable of…

The motif that I chose for the design of this cover is engines, with all the excitement and future possibilities they entail.



Motorcycle R&D Center
Shota NAKAHIRA



Motorcycle R&D Center
Ryo ITO

Technical Review

October

2015

Honda R&D

CONTENTS

Introduction of new technologies

Technology for Realization of Gasoline Engine Brake Thermal Efficiency of 45%
. . . . . Ryutaro TAGISHI, Kenichiro IKEYA
Masanobu TAKAZAWA, Taketo YAMADA 1

Downsizing as Evolution of High Thermal Efficiency Gasoline Engine . . . . . Nobu TAKAHASHI 12

Development of New 1.6 L 2-stage Turbocharged Diesel Engine for Honda CR-V
. . . . . Junichi HATANO, Ken NISHIMORI, Hiroyuki FUKUSHIMA
Taro TABUCHI, Naoto KITAYAMA, Yoshinori ISHIHARA 21

Emission Reduction Technology Using Secondary Air for Generator Engine
. . . . . Ryo SAITO, Takanori SATO
Sayaka YASOSHINA, Yusuke NINOMIYA 30

Development of Transmission-mounted Transmission Control Unit
. . . . . Kazuki YAHATA, Koichi KONISHI
Genta INOUE, Takeharu MOTEKI 37

Development of New H_2 Refueling Method for FCV to Reduce Refueling Time
. . . . . Kiyoshi HANDA, Steve MATHISON 43

Establishment of Metal Die Fabrication Method with Short Production Work Hours
by Implementing Technology of Liquid Metal Forging for Cast Iron
. . . . . Takunori KITAMURA, Hiroki NAGURA 50

Technical papers

Optimization of Combustion Chamber Shape in High-efficiency Stoichiometric Combustion Gasoline Engine
. . . . . Masanobu TAKAZAWA, Tomoaki SASAGAWA, Atsushi OHTA
Noriyuki TAKEGATA, Taketo YAMADA 61

Intake Design for Reduction of Duration of Combustion
. . . . . Taketo YAMADA, Masayoshi TAKAHASHI
Kenichiro IKEYA, Noriyuki TAKEGATA 71

Study of Spray and Combustion Using Fast Response Common Rail Injector with Micro Orifice Nozzle
. . . . . Akira KATO, Katsuya MATSUURA, Yasuhiro YOSHIMI 80

Estimation Technology Establishment for Temperature Distributions of Engine
Based on Thermal Balance under Vehicle Running Conditions
. . . . . Tomokazu NOMURA, Koichiro MATSUSHITA
Yoshihiko FUJII, Hirofumi FIJIWARA 89

Technology for Prediction of Housing Wear due to Outer Ring Creep under Bearing Load
. . . . . Yayoi NAGASOE, Shigeharu WAKUI, Yuta MAEYOSHI 103

Simulation of Adhesively Bonded Parts for Multi-Material Bonding Structure
. . . . . Tomohiro SHIMAMIYA, Chiaki SATO, Eiichiro YOKOI
Toru FURUSAWA, Keiichi SATO 111

Development of Paint and Painting Method for Magnetically Formed Decorative Painting
with Enhanced Three Dimensionality
. . . . . .Akiko TANAKA, Ikue SATO 119

Technology for Realization of Gasoline Engine Brake Thermal Efficiency of 45%

Ryutaro TAGISHI* Kenichiro IKEYA*
Masanobu TAKAZAWA* Taketo YAMADA*

ABSTRACT

Seeking to achieve a brake thermal efficiency of 45% in gasoline engines, the development project discussed in this paper conducted research to increase the compression ratio in order to boost theoretical thermal efficiency and to realize an EGR technology making it possible to control knocking and reduce cooling loss.

At the same time, the basic framework of the engine was optimized in order to help realize these combustion targets. Based on the use of a long stroke to realize a stroke/bore ratio of 1.5, which is higher than that of mass-production engines, thermal efficiency was increased by reducing time loss and cooling loss through the selection of an optimal combustion chamber shape. With this engine framework as the basis, a variety of measures were applied, including the selection of an intake port shape that would enhance in-cylinder flow, the adjustment of the effective compression ratio by means of intake valve timing, control of in-cylinder fuel distribution, and high-energy sparking. These measures made it possible to realize Minimum advance for Best Torque operation at a compression ratio of 17 and stable operation at an external EGR rate of 35%, helping to enable the achievement of a maximum brake thermal efficiency of 45% in an actual single-cylinder engine.

1. Introduction

Today, the realization of increased automotive fuel efficiency and the reduction of exhaust emissions are demanded in order to reduce CO_2 emissions that contribute to global warming and protect the earth's environment, and as a result regulation values are becoming increasingly stringent year by year. Automotive electrification, including the use of electric vehicles (EV), is increasing in response to these demands; at present, the use of conventional vehicles operating exclusively by means of internal combustion engines, or hybrid vehicles which combine electric motors with internal combustion engines, can be considered the main trends in this area. Increasing the thermal efficiency of internal combustion engines will therefore be an important technological issue into the future. The maximum thermal efficiency of current gasoline internal combustion engines is 39%, but extrapolating from changes in fuel efficiency regulation values, a level of brake thermal efficiency of 45% will be necessary in several years. The realization of an increase in the level of brake thermal efficiency to 45% or higher can therefore be considered a significant issue to be addressed in gasoline internal combustion engines in the near future. The development discussed in this paper elucidated the technological elements necessary for the realization of a 45% level of brake thermal efficiency in gasoline engines, and verified its findings in an actual vehicle. Lean-burn operation[(1)] can be considered as a means of realizing a maximum brake thermal efficiency of 45%, but the project under discussion assumed stoichiometric operation from considerations of the level of complexity of exhaust gas treatment technologies. This paper provides an overview of the research.

2. Development Goals

2.1. Setting of Development Targets

The following targets were set at the commencement of the development process:

(1) Realization of a maximum brake thermal efficiency of 45%; and

* Automobile R&D Center

(2) Realization of the above target via stoichiometric operation using 91-octane regular gasoline.

2.2. Development Orientation

The necessary elements for the realization of increased thermal efficiency were identified, and the details of the main measures to be applied were determined. Figure 1 shows factors affecting the realization of increased thermal efficiency. The following orientations for the development were set based on a factor analysis:

(1) High compression ratio for increased stoichiometric thermal efficiency;
(2) High-EGR operation in order to reduce cooling loss and control knocking and realize Minimum advance for Best Torque (MBT) operation at a high compression ratio; and
(3) Realization of increased thermal efficiency by means of optimization of basic engine framework.

2.3. Setting of Conditions for Achievement of Development Targets

First, the tendencies of cooling loss, time loss, and change in friction in relation to engine load and EGR rate were determined from mass-production engine data. Brake thermal efficiency under MBT conditions was predicted by extrapolation from these results with boost pressure, EGR rate, and compression ratio as parameters. The operating condition for these calculations was an engine speed of 2000 rpm. The results of the calculations are shown in Fig. 2. These results indicate that MBT operation at a compression ratio of 15 or higher and a high boost pressure of 2.5 bar or higher is necessary for the realization of a brake thermal efficiency of 45%. Because the increased demand on the supercharger as the boost pressure rises also increases the level of technological challenge involved, it was decided to realize the target level of thermal efficiency at the minimum boost pressure, as shown by the circle in Fig. 2 (c). Based on these calculation results, the following development guidelines were set in order to realize a 45% level of brake thermal efficiency:

(1) MBT operation at a compression ratio of 17.0 and a boost pressure of 2.5 bar or higher; and
(2) Stable operation at an external EGR rate of 30% or higher.

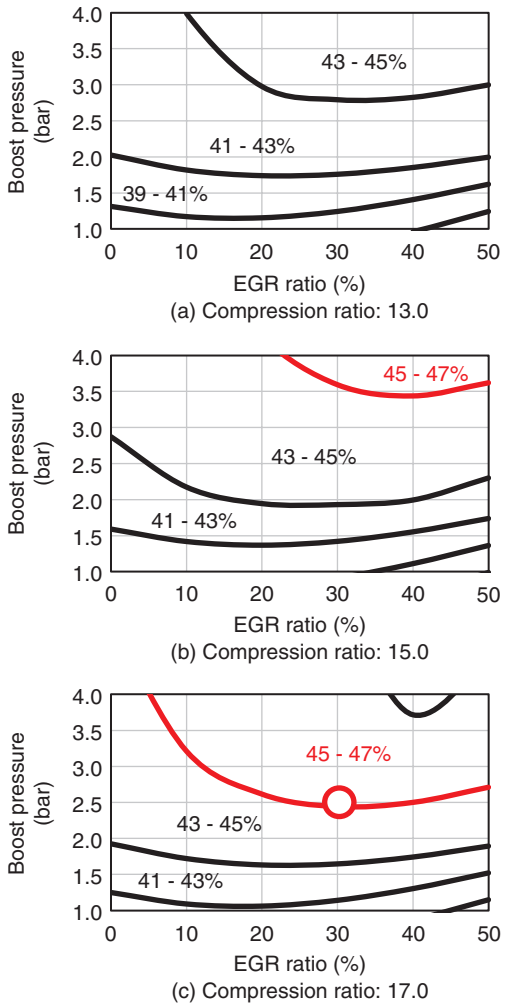


Fig. 2 Calculation of maximum brake thermal efficiency

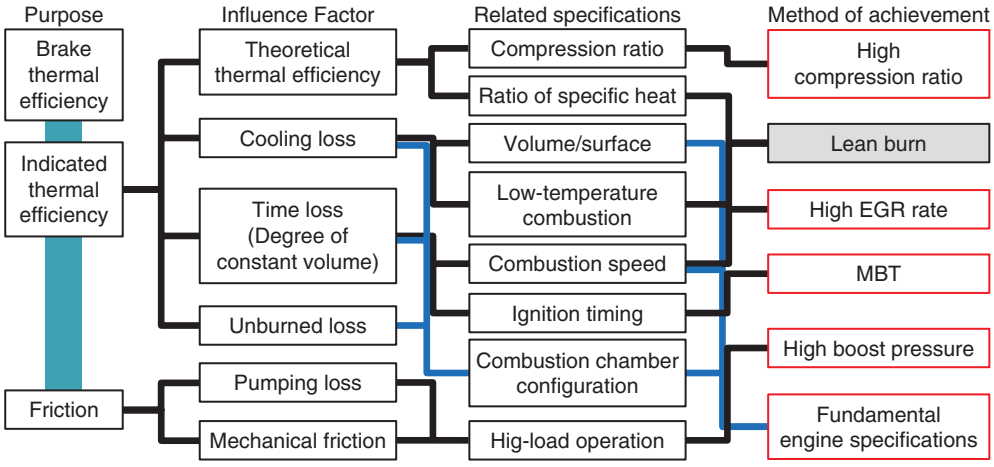


Fig. 1 Analysis of factors influencing brake thermal efficiency

3. Realization of Increased Compression Ratio

The reduction of combustion speed due to the flattening of the combustion chamber shape and the retardation of ignition timing due to knocking are the main factors that represent a challenge in increasing thermal efficiency through the use of a high compression ratio. In addition to the high EGR rate that will be discussed in Chapter 4, the present research responded to these factors by means of the following methods:

(1) Limitation of flattening of combustion chamber shape through use of a long stroke; and
(2) Adjustment of the effective compression ratio through delayed closure of the intake valve.

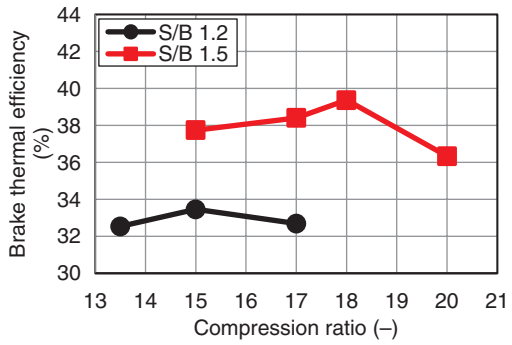
3.1. Use of Long Stroke

3.1.1. Effect in controlling reduction of combustion speed at high compression ratio

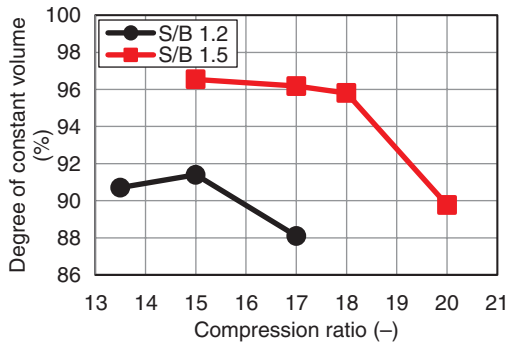
The use of a high compression ratio is an effective method of increasing theoretical thermal efficiency, but presents the tradeoff of reducing combustion speed due to the flattening of the combustion chamber shape. This issue is thought to result from the fact that the flattening of the combustion chamber increases the area of contact between the flame and the walls of the chamber, impeding flame propagation. The positioning of a cavity close to the spark plugs to help prevent any interference with initial flame formation has been proposed as a method of responding to this issue[(2)]. However, while this method is effective at the initial stage of combustion, it does not offer sufficient response to the reduction of combustion speed in the second half of the combustion process. In addition, the method necessarily involves the engineering of large concavities and convexities in the piston heads, creating a shape that is disadvantageous from the perspective of cooling loss. It was therefore determined that the use of a long stroke would be employed as a response in the research under discussion. The use of a long stroke makes it possible to increase the height of the combustion chamber without changing the compression ratio, making it possible to control the flattening of the combustion chamber and form piston head shapes with minimal concavities and convexities. In order to verify the effectiveness of the use of a long stroke at a high compression ratio, single-cylinder engines with stroke/bore ratios (S/B) of 1.2, corresponding to mass-production engines, and 1.5 were manufactured, and changes in thermal efficiency against the compression ratio were compared. Table 1 shows the test engine specifications, and Fig. 3 shows results for thermal efficiency at an engine speed of 2000 rpm, an Indicated Mean Effective Pressure (IMEP) of 520 kPa, and an EGR rate of 20% in MBT operation. Combustion speed was calculated using 3D models for each compression ratio and S/B, and the shape that produced the highest combustion speed was employed for the piston heads. Figures for brake thermal efficiency in the single-cylinder engines were calculated using mechanical friction corresponding to friction in an L4 engine and the calculated value of pumping loss for the supercharger. At an S/B of 1.2, thermal efficiency increases until a compression ratio of 15, but declines at a compression ratio of 17. By contrast, at an S/B of 1.5, thermal efficiency increases until a compression ratio of 18. The main factor producing the decline in thermal efficiency at high compression ratios is the decline in the

Table 1 Test engine specifications

Engine type	DOHC 4-valve single cylinder	
Bore (mm)	ϕ 81	
Stroke (mm)	96.9	121.5
S/B	1.2	1.5
Compression ratio	13.5, 15.0, 17.0, 18.0, 20.0	
Displacement (cm^3)	499	626
Intake port	Filling port	
Air supply	Supercharged	
EGR system	Low-pressure loop-cooled EGR	
Fuel supply	Port injection	



(a) Brake thermal efficiency



(b) Degree of constant volume

Fig. 3 Comparison of influence of compression ratio on brake thermal efficiency and degree of constant volume for different S/B

degree of constant volume. Figure 4 shows measurement results for the Mass Burn Fraction (MBF) at compression ratios from 15 to 20 for an S/B of 1.5, an engine speed of 2000 rpm, an IMEP of 520 kPa, MBT, and an EGR rate of 20%. At a compression ratio of 20, there is a sudden decline in the speed of combustion. The effect is particularly marked in the second half of the combustion process. This is thought to be due to the fact that there is a local increase in the Surface/Volume ratio (S/V) close to the ends of the bore, as shown in the diagram in Fig. 5, and this impedes the propagation of the flame. The use of a higher S/B makes it possible to increase the height of the combustion chamber without changing the compression ratio, helping to enable the use of a high compression ratio while avoiding this issue.

Figure 6 shows the mean effective combustion chamber height, H, against S/B and compression ratio. H was determined by dividing the combustion chamber volume, V_1, at Top Dead Center (TDC) by the bore cross-sectional area, A. The empty circles in Fig. 6 show the engine specifications displaying the highest compression ratios at which there was no increase in unburned HC or decline in combustion speed. When the average combustion chamber height, H, falls below 7 mm, there is a sudden decline in combustion speed and increase in unburned HC. Based on these results, it was judged that an S/B of 1.4 or higher would be necessary to obtain good combustion at a compression ratio of 17 and an average combustion chamber height of 7 mm or higher.

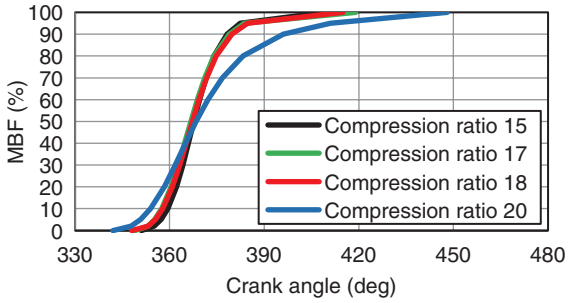


Fig. 4 Comparison of MBF for different compression ratios at S/B 1.5, engine speed 2000 rpm, IMEP 520 kPa, ignition timing MBT, and EGR ratio 20%

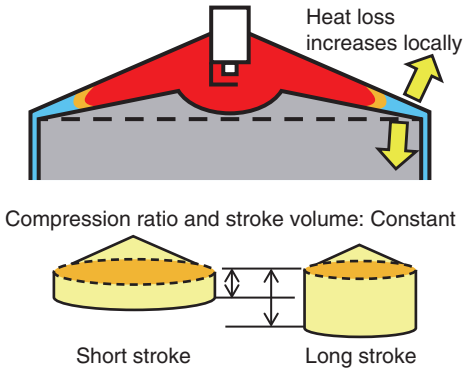


Fig. 5 Diagram of increase in local heat loss in flat combustion chamber and comparison of combustion chamber height for different S/B

3.1.2. Effect in reducing cooling loss

The use of a long stroke was not only important to the realization of a compression ratio of 17, but could also be expected to have the effect of reducing cooling loss as a result of a reduction in S/V[3]. Engines of the type shown in Table 1 were modified and thermal efficiency was measured at S/B of 1.2 to 2.0 at a bore diameter of ϕ81 and a compression ratio of 13.5 in order to determine the effect of S/B on thermal efficiency. Figure 7 shows results for an engine speed of 2000 rpm and an IMEP of 720 kPa. Brake thermal efficiency tends to increase from S/B of 1.2 to 1.5 and decline at S/B higher than 1.5. This is because the increase in Friction Mean Effective Pressure (FMEP) and Pumping Mean Effective Pressure (PMEP) due to the increased piston speed at S/B of above 1.5 exceeds the effect of reduction of cooling loss. The reduction in the effect of reduction of cooling loss is considered to be due to an increase in the heat transfer coefficient of the surfaces of the cylinder walls resulting from the enhanced in-cylinder flow produced by increased piston speed. The highest value of thermal efficiency occurs at an S/B of 1.5 with a balance between cooling loss and friction.

Up to this point, studies had been conducted for a fixed bore of ϕ81. A single-cylinder engine with a bore of ϕ73 was now manufactured, and tests were conducted under the same conditions as employed for the engine with a bore of ϕ81 in order to determine the optimum S/B when the bore was changed against a fixed displacement. Based on

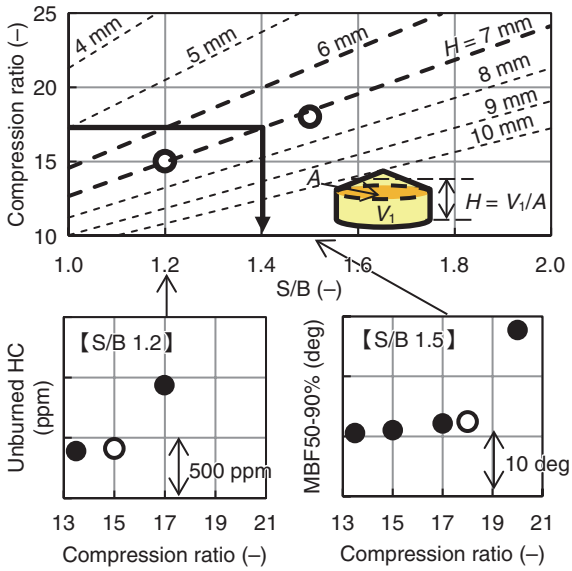


Fig. 6 Average combustion chamber height at TDC for different S/B and compression ratios

the test results for the ϕ81 and ϕ73 engines, the trend of change in combustion speed due to change in cooling loss in response to S/V and enhancement of in-cylinder flow in response to S/B was calculated, and FMEP was calculated with consideration of changes in bore and stroke, making it possible to estimate brake thermal efficiency in relation to stroke volume and S/B corresponding to conditions in an L4 engine. Figure 8 shows results for the estimation of maximum brake thermal efficiency at an engine speed of 2000 rpm and an EGR rate of 20%. The circled areas in Fig. 8 show the specifications that were actually tested. The estimation results show that even with changes in bore and displacement, the tendency for thermal efficiency to reach its highest level at around S/B of 1.5 remains unchanged.

Based on the above, 1.5 was selected as the optimum S/B that would both provide the necessary S/B for a compression ratio of 17, as discussed in the previous chapter, and increase thermal efficiency to its maximum level.

3.2. Atkinson Cycle with Delayed Closure of Intake Valve

Knocking is another significant issue associated with the use of a high compression ratio. This issue was responded to in the research under discussion by delaying the closure of the intake valve without changing the mechanical compression ratio (equivalent to the expansion ratio) in order to reduce the effective compression ratio. Using the S/B 1.5 engine shown in Table 1, a comparison was conducted of thermal efficiency when the timing of closure of the intake valve was changed at a mechanical compression ratio of 17 and thermal efficiency during Otto cycle operation at a compression ratio of 17. Figure 9 shows the results of measurements of brake thermal efficiency for each Brake Mean Effective Pressure (BMEP)

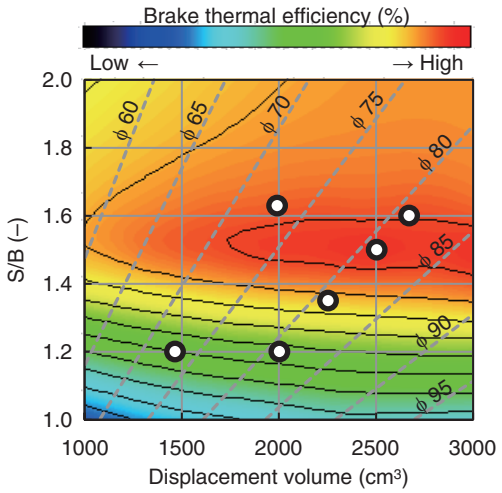


Fig. 8 Engine displacement and S/B in relation to maximum brake thermal efficiency

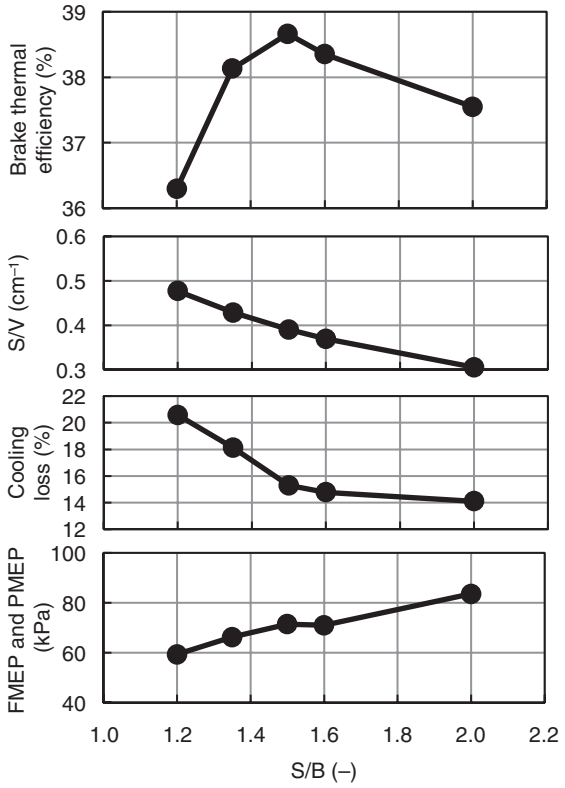


Fig. 7 Effect of S/B on thermal efficiency, cooling loss and friction

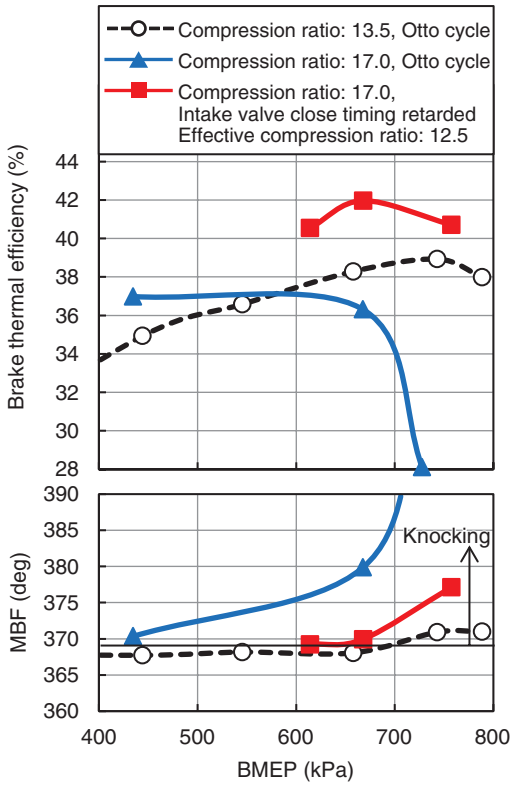


Fig. 9 Effect of effective compression ratio on brake thermal efficiency and knocking

figure at an engine speed of 2000 rpm and an EGR rate of 20%. The reduction of the effective compression ratio made it possible to increase the maximum thermal efficiency by helping to enable MBT operation up to a load close to that of an Otto cycle with a compression ratio of 13.5 and an expansion ratio of 17.

Figure 10 shows theoretical thermal efficiency when the effective compression ratio is changed at an expansion ratio of 17 and theoretical thermal efficiency for Otto cycle operation. The test results show that the theoretical thermal efficiency at an expansion ratio of 17 and an effective compression ratio of 12.5 is equivalent to the theoretical thermal efficiency at a compression ratio of 16.5 during Otto cycle operation, demonstrating that it was possible to realize a level of theoretical thermal efficiency equivalent to that for a compression ratio of 16.5 while achieving a level of knocking equivalent to that for a compression ratio of 13.5.

3.3. Direct Injection Technology

In realizing the use of a high compression ratio, the use of the latent heat of vaporization of the fuel in order to ameliorate knocking was taken into consideration, and direct injection was adopted for the final specifications, which will be discussed in Chapter 5. Figure 11 shows knocking, unburned loss, Indicated Specific Fuel Consumption (ISFC), and the amount of fuel adhering to the pistons and the cylinder sleeves (as calculated using a 3D model) in relation to injection timing at an engine speed of 2000 rpm and an IMEP of 810 kPa. The issue of using direct injection was the fact that injection of the fuel at a timing at which the intake flow speed was high would promote atomization of the fuel and advance knocking ignition timing, but the use of a fuel injection timing that would enable maximum control of knocking would increase unburned fuel loss and ultimately make it impossible to increase thermal efficiency. The main factor in unburned fuel loss is adhesion of fuel to the walls of the combustion chamber. At an injection timing that ameliorated knocking, fuel adhered to the cylinder sleeves. In order to reduce the amount of fuel adhering to the cylinder sleeves, the fuel spray was optimized to travel downwards, and the fuel injection timing was set close to the timing that would maximize the effect of amelioration of knocking and minimize the amount of fuel adhering to the walls of the combustion chamber, in order to realize the effect of direct injection to the greatest possible extent.

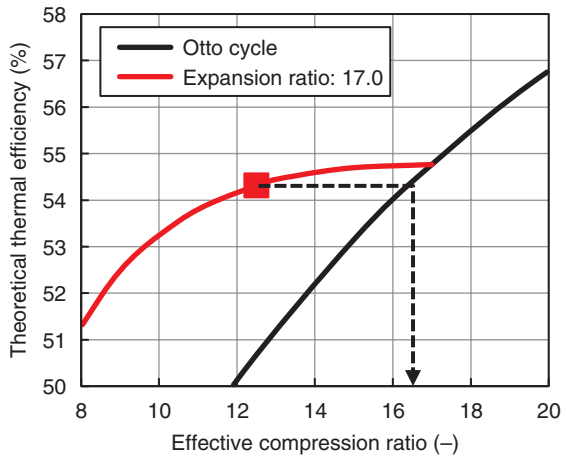


Fig. 10 Comparison of theoretical thermal efficiency

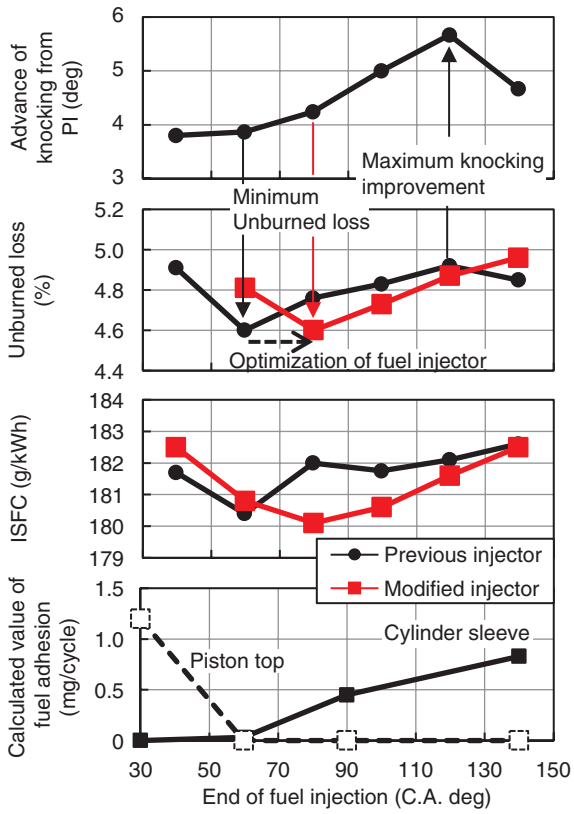


Fig. 11 Effect of fuel injection timing on knocking, unburned loss and ISFC, and calculated value of fuel adhesion

4. High-EGR Operation

Stable operation at an external EGR rate of 30% or higher was set as a target to help enable the reduction of cooling loss and the control of knocking, and the realization of MBT operation at a high compression ratio. The main issues presented by high-EGR operation are reduction of the speed of flame propagation and decline in ignition performance. The reduction in the speed of flame propagation was responded to by enhancement of in-cylinder flow through selection of the intake port shape. The decline in ignition performance

was responded to by selecting a combustion chamber shape that would help to eliminate factors impeding initial flame growth and adjust the vortical center of the in-cylinder flow, in addition to the use of high-energy sparking. If either of the respective measures to respond to the speed of flame propagation and sparking performance was lacking, it would not be possible to realize stable operation while increasing the EGR rate. The application of both measures was important.

4.1. Enhancement of In-cylinder Flow

Methods of increasing the tumble ratio are widely used in order to increase in-cylinder turbulence energy to the level necessary to help ensure the desired flame propagation speed in a high-EGR environment. Restriction of the size of the intake port is the most widely used method of increasing the tumble ratio, but this method basically results in a trade-off with the flow coefficient. Reduction of the flow coefficient increases the load on the supercharger, increasing pumping loss and resulting in a decline in thermal efficiency. In addition, even if the tumble ratio is increased, in-cylinder turbulence energy will not necessarily increase. Figure 12 shows calculated values for tumble ratio and turbulence energy for different intake port shapes. The results indicate that turbulence energy varies significantly even at the same tumble ratio. It is therefore important to control the increase in the tumble ratio to the minimum while efficiently producing turbulence energy.

The in-cylinder non-steady-state flow speed distribution was calculated for Specifications A and B in Fig. 12. Figure 13 shows 5 m/s isosurfaces during the intake stroke. If the isosurfaces are considered the axes of the vortical centers, while the axis of the vortical center for Specification A, for which turbulence energy is high, is comparatively stable, the axis of the vortical center for Specification B undulates significantly during the intake stroke. This undulation of the axis of the vortical center is considered to be energy loss, producing a decline in turbulence energy. The direction of the main intake flow from the intake valve was focused on as a factor in this undulation. For Specification A, the main intake flow moves towards the outside of the bore, while for Specification B, the main intake flow moves towards the inside of the bore. The flow balance was defined as shown in Fig. 14[4] in order to quantitatively express the directions of the main flows. When the flow balance is positive, the main flow moves in the direction of the outside of the bore, and when it is negative, the main flow moves in the direction of the inside of the bore.

Figure 15 shows values calculated for turbulence energy when the flow balance was changed while the tumble ratio remained the same. Turbulence energy was highest for flow balances from 0 to 2. Intake port shapes that would generate flow balances within this range were calculated using 3D models. An intake port shape that generated a tumble ratio 1.7 times higher than the mass-production engine and a flow balance between 0 and 2 was reflected in the final specifications.

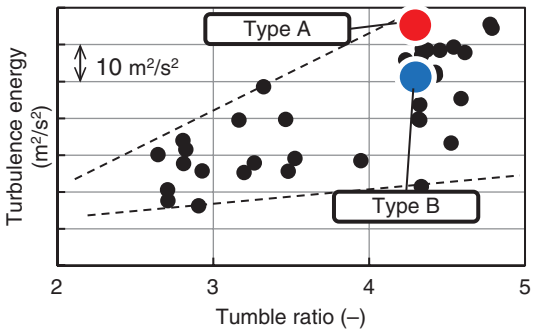


Fig. 12 Calculation results for tumble ratio and turbulence energy for different intake port shapes

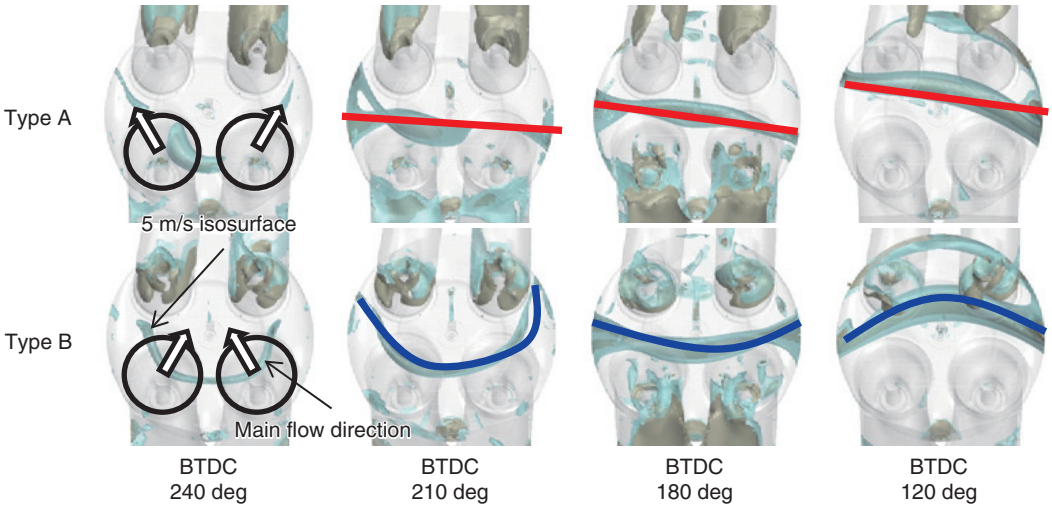


Fig. 13 Comparison of vortical center axes resulting from direction of intake flow

4.2. Measures to Respond to Reduced Ignitability

In a high-EGR environment, the initial flame tends not to grow due to the decline in the laminar burning velocity, and the enhancement of the in-cylinder flow in order to reduce the combustion period extinguishes the spark-plug spark and reduces ignitability. This section will discuss the use of a combustion chamber shape to promote the growth of the initial flame and the enhancement of spark energy in order to help prevent extinguishing the flame by in-cylinder flow.

4.2.1. Realizing ignitability in relation to combustion chamber shape

The initial flame that is produced in a high-EGR environment makes contact with the pistons, cylinder heads or other walls, and this can result in heat loss and the extinguishing of the flame or reduction of the speed of flame propagation. In order to help prevent this, it is important to attempt to ensure sufficient volume in the vicinity of the plugs. Figure 16 shows test results for the EGR rate that represents the limit for combustion stability at an engine speed of 2000 rpm and an IMEP of 810 kPa when the volume in the vicinity of the plugs is changed by means of the shape of the piston heads. The ratio between the volume V_1, when a virtual sphere with the plug electrodes at TDC as its center first makes contact with a piston or a cylinder head; and V, the volume of the entire combustion chamber, (V_1/V), was used to express the distance between the spark plugs and the pistons.

The EGR rate that represents the limit for combustion stability increases as V_1/V increases, becoming relatively constant at ratios of 2% and above. When V_1/V is low, the initial flame makes contact with the piston heads or the walls of the combustion chamber at an early stage, and heat loss results in a decline in the speed of combustion. Alternatively, the flame is extinguished and the limit EGR rate for combustion stability declines. When the initial flame grows to a certain extent, the stability of main combustion rather than ignitability is the dominant factor, and this domain determines the limit EGR rate for stable combustion. Attempting to ensure ignitability and not hindering the growth of the initial flame by realizing a V_1/V of 2% or above is important in realizing high-EGR operation. In order to realize a high compression ratio like 17 and a V_1/V of 2% or above at an S/B of 1.2, as in a mass-production engine, it is necessary to use a convex shape for the piston heads, which is an undesirable shape from the perspectives of heat loss and flame propagation. By contrast, realizing an S/B of 1.5 offers a margin in the direction of the height of the combustion chamber, making it possible to use a shallow-dish shape for the pistons while realizing a V_1/V of 2%. This makes it possible to balance ignitability with good combustion. The use of a long stroke is also effective from this perspective. Figure 17 shows the combustion chamber shapes for S/B of 1.2 and 1.5 at a compression ratio of 17 and a V_1/V of 2%.

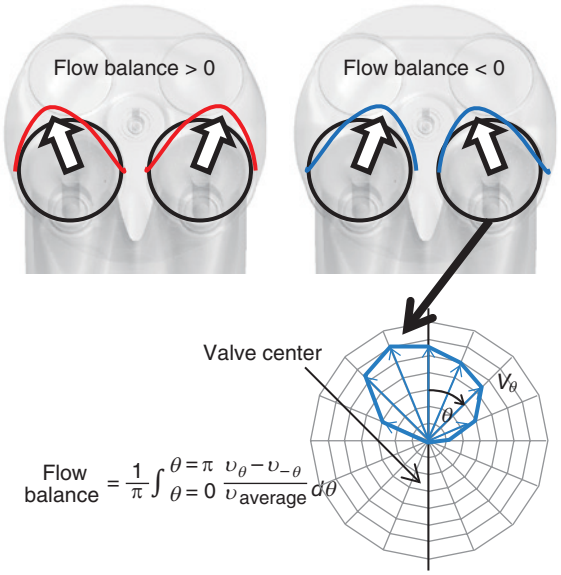


Fig. 14 Definition of flow balance

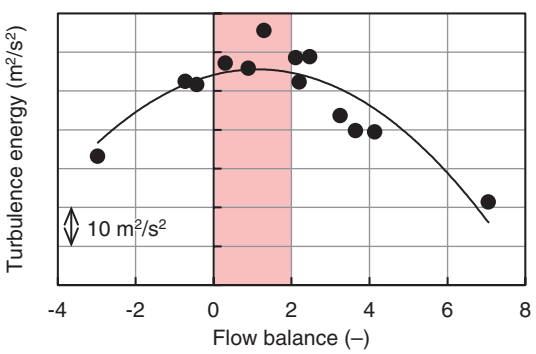
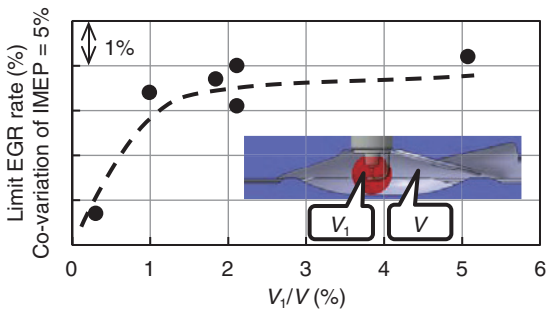


Fig. 15 Turbulence energy for different flow balances



V: Combustion chamber volume at TDC
V_1: Volume when virtual sphere centering on ignition-plug electrode touches piston or cylinder head

Fig. 16 Effect of V_1/V on EGR rate (Co-variation of IMEP: 5%)

4.2.2. Adjustment of position of vortical center of in-cylinder flow

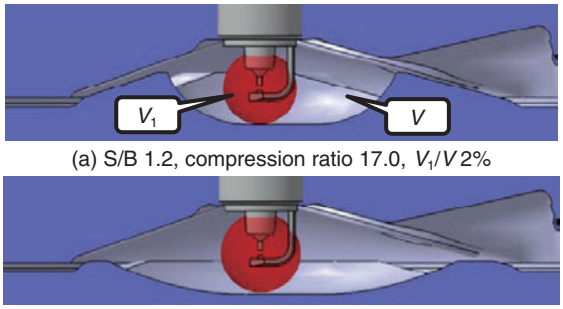
The position of the vortical center of the in-cylinder flow is an important factor in realizing good ignition performance and forming the initial flame. If there is significant deviation between the positions of the spark plug electrodes and the vortical center of the in-cylinder flow, the in-cylinder flow tends to extinguish the spark-plug spark, resulting in a decline in ignition performance. In addition, even if the initial flame formation is successful, the flame will be carried by the flow and diverted to one side of the combustion chamber, extending the combustion period. It is necessary to align the positions of the spark plugs and the vortical center in order to help avoid these issues. A shallow-dish shape was employed for the piston heads in order to adjust the position of the vortical center. Figure 18 shows calculation results for in-cylinder flow for the flat piston shape and the shallow-dish piston shape. At close to spark timing, the vortical center is forced towards the bore center by the shallow-dish shape, aligning the positions of the spark plugs and the vortical center.

In addition to these modifications, further changes including the reduction of the piston-top land height and the squish height were made to the combustion chamber shape in order to reduce unburned HC and increase combustion speed, and these were reflected in the final specifications[5], to be discussed in Chapter 5.

4.2.3. High-energy sparking

Even when sufficient volume had been realized in the vicinity of the spark plugs and the position of the vortical center had been optimized, the enhancement of spark energy was an important factor in igniting the air-fuel mixture and forming the initial flame in the high-EGR environment. In the research under discussion, the spark was enhanced by means of multiple discharge in order to realize high-energy sparking. Up to this point, the single-cylinder engine had been modified in order to produce a high flow rate generating a tumble ratio 1.7 times higher than that of a mass-production engine and fitted with a combustion chamber shape that did not hinder flame propagation. Tests were now conducted in order to determine how the limit EGR rate for stable combustion would change with change in the spark energy employed. Energy per unit time was held constant, and the period of supply of energy was changed in order to adjust the amount of energy supplied to the spark plugs. Figure 19 shows the results. The limit EGR rate for stable combustion increases with the amount of energy supplied, becoming relatively constant at 1500 mJ and above. It is considered that in the domain at 1500 mJ and above, rather than an issue of ignitability, the in-cylinder flow is insufficient and the main combustion period varies, increasing co-variation of IMEP and determining the limit EGR rate. In order to further increase the limit EGR rate, it was necessary to further enhance the in-cylinder flow. Because power consumption increases with increase in the amount of energy supplied, becoming a factor in reducing efficiency, a setting of 450 mJ was ultimately adopted in order to help enable ignition at the target EGR rate of 30% and above and minimize any effect on fuel consumption.

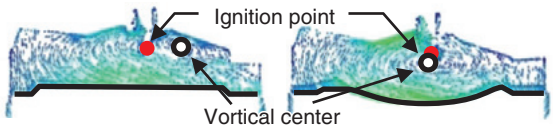
The measures discussed above to increase the flow rate, modify the shape of the combustion chamber, and realize high-energy sparking in order to help enable high-EGR operation were applied in a single-cylinder engine, and tests were conducted in order to verify their effect. Figure 20 shows test results for an engine speed of 2000 rpm and an IMEP of 810 kPa. The results demonstrate that even at an external EGR rate of 30% and above, operation is stable, and the effect of the high EGR rate in reducing cooling loss and controlling knocking has increased brake thermal efficiency.



(a) S/B 1.2, compression ratio 17.0, V_1/V 2%

(b) S/B 1.5, compression ratio 17.0, V_1/V 2%

Fig. 17 Comparison of combustion chamber configuration for S/B 1.2 and 1.5



(a) Flat piston (b) Shallow dish piston

Fig. 18 Influence of piston shape on vortical center

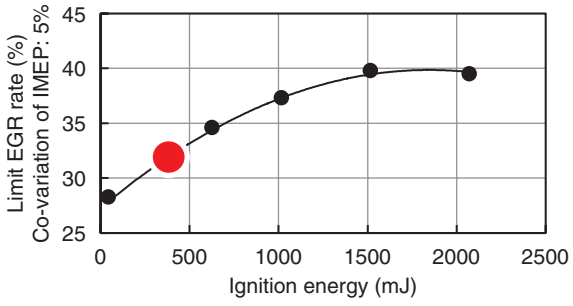


Fig. 19 Influence of ignition energy on EGR rate (Co-variation of IMEP: 5%)

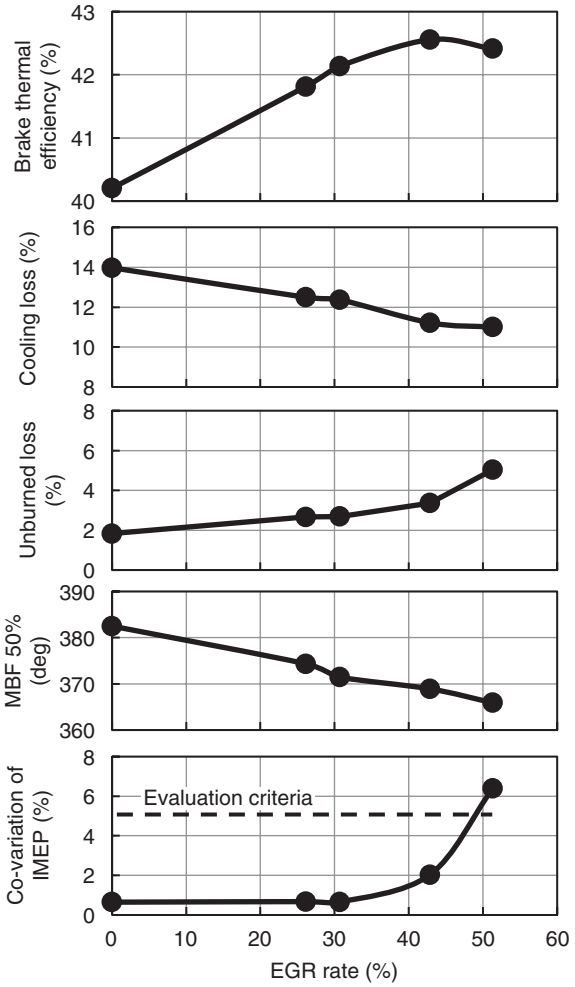


Fig. 20 Change in thermal efficiency due to increased EGR rate

Table 2 Final test engine specifications

Engine type	DOHC 4-valve single cylinder
Bore (mm) × Stroke (mm)	ϕ81 × 121.6 S/B 1.5
Compression ratio (–)	12.5
Expansion ratio (–)	17.0
Displacement (cm^3)	627
Intake port	Tumble port
Air supply	Supercharged
EGR system	Low-pressure loop-cooled EGR
Fuel supply	DI
Piston shape	Shallow dish
Ignition energy (mJ)	450

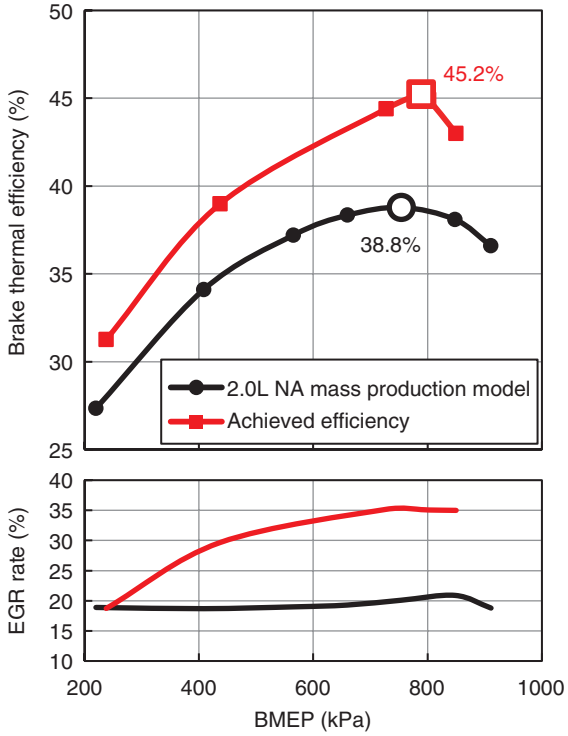


Fig. 21 Achieved brake thermal efficiency at engine speed of 2000 rpm

5. Achieved Thermal Efficiency

A single-cylinder engine incorporating the basic framework, technologies for the control of knocking, technologies to increase in-cylinder flow, and technologies to increase ignitability discussed above was manufactured, and the achieved values were tested. Table 2 shows the final specifications of the engine, and Fig. 21 shows results for thermal efficiency. The increase in the potential of the basic framework realized through the use of a long stroke, the increased theoretical thermal efficiency realized through the use of a high compression ratio, the enhanced in-cylinder flow realized through the modification of the shapes of the intake port and the combustion chamber, and the application of high-energy sparking and direct injection have resulted in the achievement of a brake thermal efficiency of 45.2%.

6. Conclusion

The research discussed in this paper realized MBT operation using 91-octane regular gasoline at a stoichiometric air-fuel ratio with a mechanical compression ratio of 17 and an EGR rate of 35%, increasing brake thermal efficiency to 45.2%.

A combustion chamber shape exploiting the freedom in shape design offered by a long stroke (S/B 1.5) was selected and the timing of the closure of the intake valve was delayed, making it possible to advance knocking spark timing through the use of an Atkinson cycle. This

helped to enable the realization of MBT operation up to a load equivalent to that of an Otto cycle engine with a compression ratio of 13.5 while controlling reduction in the speed of combustion even at a high compression ratio (a mechanical compression ratio of 17).

The selection of an intake port shape that balanced intake resistance with the enhancement of turbulence energy during high-EGR operation, the use of a combustion shape that helped to ensure sufficient volume in the vicinity of the spark plugs and optimized the flow, and the application of 450 mJ high-energy sparking have made it possible to realize stable operation even at an EGR rate of 30% and above.

7. Afterword

The achieved thermal efficiency indicated in Chapter 6 was realized in a single-cylinder engine. Numerous issues remain to be resolved in order to help enable the technologies discussed in this paper to be applied in multi-cylinder automotive engines.

The main issues are the increase in engine height due to the use of a long stroke and measures to respond to condensed water and increase EGR responsiveness in order to realize a Low-Pressure Loop-cooled EGR (LPL-EGR) system for high-EGR operation. In addition, in order to respond to the reduction in exhaust energy due to the use of a high expansion ratio and high-EGR operation, it will be necessary to develop a boost system that balances the supercharger efficiency necessary for increased thermal efficiency with the flow-rate range necessary for increased maximum power.

It will be important to address these issues at an early stage in order to apply the technologies discussed in this paper to automotive gasoline engines. The authors believe that this will be an important focus for future development initiatives.

References

(1) Nogawa, S., Nakata, K., Kanda, M., Improvement of Thermal Efficiency by Lean Boosted Engine, The proceedings of the 21st Internal Combustion Engine Symposium, A7-4, p.533-538 (2010) (in Japanese)
(2) Hirose, I., Kudo, H., Kihara, T., Yamakawa, M., Hitomi, M.: Introduction of SKYACTIV-G 2.0L Gasoline Engine, The proceedings of the 22nd Internal Combustion Engine Symposium, p.37-42 (2011) (in Japanese)
(3)Ogawa, H., Kimura, K., Sasaki, K., Sato, Y., Sako, T.: Performance Improvements in a Spark Ignition Gas Engine with Longer Strokes, The proceedings of the 20th Internal Combustion Engine Symposium, p.325-330 (2009) (in Japanese)
(4) Yamada, T., Takahashi, M., Ikeya, K., Takegata, N.: Intake Design for Reduction of Duration of Combustion, Honda R&D Technical Review, Vol. 27, No. 2, p. 71-79
(5) Takazawa, M., Sasagawa, T., Ohta, A., Takegata, N.: Optimization of Combustion Chamber Shape in High-efficiency Stoichiometric Combustion Gasoline Engine, Honda R&D Technical Review, Vol. 27, No. 2, p. 61-70

■ Author ■


Ryutaro TAGISHI


Kenichiro IKEYA


Masanobu TAKAZAWA


Taketo YAMADA

Downsizing as Evolution of High Thermal Efficiency Gasoline Engine

Nobu TAKAHASHI*

ABSTRACT

In order to achieve downsizing as an evolution in the high thermal efficiency engine, the possibilities of increasing specific power were examined.

In order to achieve a balance between the specific power that is required for downsizing the engine and the high compression ratio (high expansion ratio) that is the basis for thermal efficiency, high knock resistance in the high engine speed range is necessary. The issue in realizing high power was that sufficient reduction in effective compression ratio through valve timing could not be obtained in the high engine speed range. It became possible to reduce the effective compression ratio by enhancing the intake system, and an increase in specific power was obtained by knock enhancement, but the increase was limited to the equivalent of a naturally aspirated engine. Raising thermal efficiency and downsizing are mutually contradictory techniques, and it became clear that any further increase in specific power would necessitate lowering the mechanical compression ratio itself.

At the same time that downsizing is a technique for improving fuel economy by reducing the displacement, it can also be expected to heighten dynamic performance by achieving lighter weight and greater compactness. In that sense, the approach of downsizing by increasing specific power is crucial for achieving evolution of the high thermal efficiency gasoline engine. In order to achieve this, it will be necessary to build and apply variable compression ratio mechanisms and other such radical technology.

1. Introduction

It has been predicted[(1)] that the number of vehicles with internal combustion engines will continue increasing up to the year 2040. Even as the electrification of vehicles progresses in the future, it will be important for the internal combustion engine to evolve (Fig. 1).

The societal significance of the electrification of vehicles is in the reduction of CO_2 emissions. Consequently, the issue faced for internal combustion engines that support that advance is the reduction of CO_2 emissions, or in other words the comprehensive enhancement of thermal efficiency.

An engine is a machine that converts the energy in fuel into motive power. The higher the efficiency of that conversion, or in other words the thermal efficiency, the more superior the machine can be said to be. On the other hand, if the engine is considered as one of the devices that make up a vehicle, then there is a demand for lighter weight and compactness in the interest of installability and weight balance. In other words, no matter how high the thermal efficiency of an engine may be, it cannot be expected to contribute very much to limiting the impact on

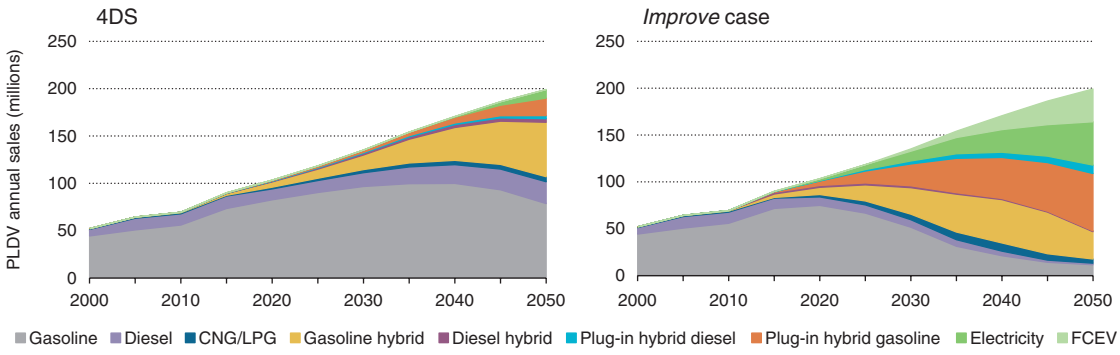


Fig. 1 Global portfolio of technologies for passenger LDVs, (4DS: 4°C scenario, Improve case: Technology improvements that lowers GHG emissions)

* Automobile R&D Center

the environment if there are such issues with installing the engine that the vehicles in which it can be used are limited.

Automobiles are not just a means of mobility, since they also embody an element of fun experienced in driving them. This is where they differ from public means of transportation, and it is also important to manufacture automobiles that are able to provide customers with fun while also curbing the environmental impact. Making the engine lighter in weight and more compact is an important element that ultimately contributes to reducing the vehicle weight and enhancing its dynamic performance.

This paper focuses on achieving a balance between high thermal efficiency and downsizing (Fig. 2) as an engine technology for seeking a balance between limiting environmental impact and providing fun. It will describe the issues faced in this effort and the techniques for addressing them.

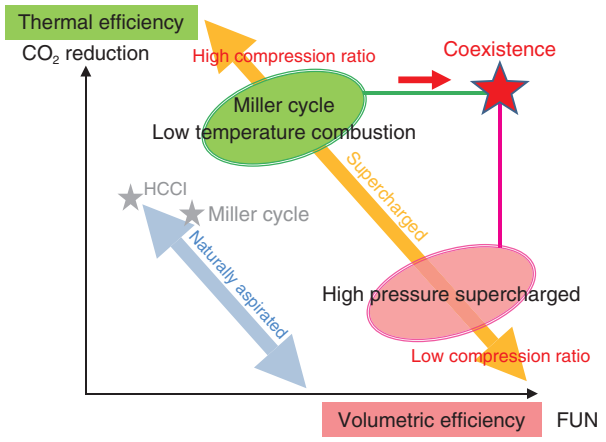


Fig. 2 Coexistence of thermal efficiency and volumetric efficiency

2. Value of Downsizing

The downsizing and boosting[2] technique for fuel economy improvement came into widespread use mainly in Europe, and now has become standard technology. It was introduced into the United States nearly a decade late, and in Japan, too, its introduction began to accelerate as more of these vehicles were imported.

Downsizing and boosting is not a technique for raising thermal efficiency. Rather, thermal efficiency is diminished as downsizing progresses. The main factor in that is the reduction in compression ratio made to match with supercharging. The tendency for a rise in maximum brake mean effective pressure (BMEP) to be accompanied by a decrease in the compression ratio (Fig. 3) can also be observed in the configuration of commercially available engines. Care needs to be taken, therefore, to note that fuel economy and thermal efficiency are not synonymous.

The mechanism by which fuel economy improves with downsizing is the shift of the engine operating point into a high thermal efficiency region. This effect is obtained by optimizing the displacement (reducing the displacement) with respect to the driving load, and the usual practice is to combine this with boosting in order to recover power (Fig. 4). A displacement matched to fuel economy can generally be envisioned as downsizing of approximately 65% (equivalent to a change from 2.4 L to 1.5 L), in which case obtaining dynamic performance on a par with a conventional naturally aspirated (NA) engine would necessitate boosting to a level of 2200 kPa at maximum load.

Downsizing is not simply a matter of bringing down the displacement. As the term indicates, it is also important to make the engine lightweight and compact. Making the engine more lightweight contributes to reducing the weight

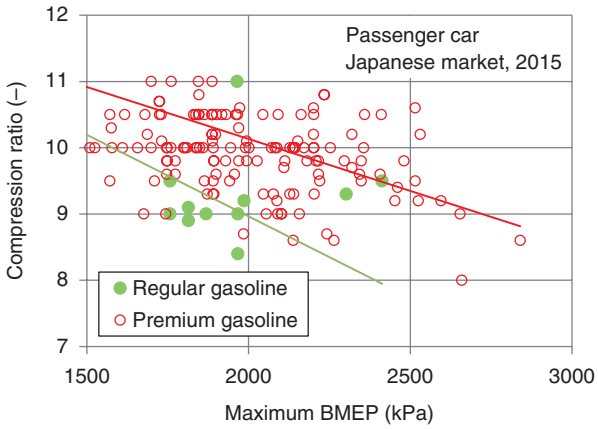


Fig. 3 Tendency of compression ratio to move inversely to BMEP of gasoline engine

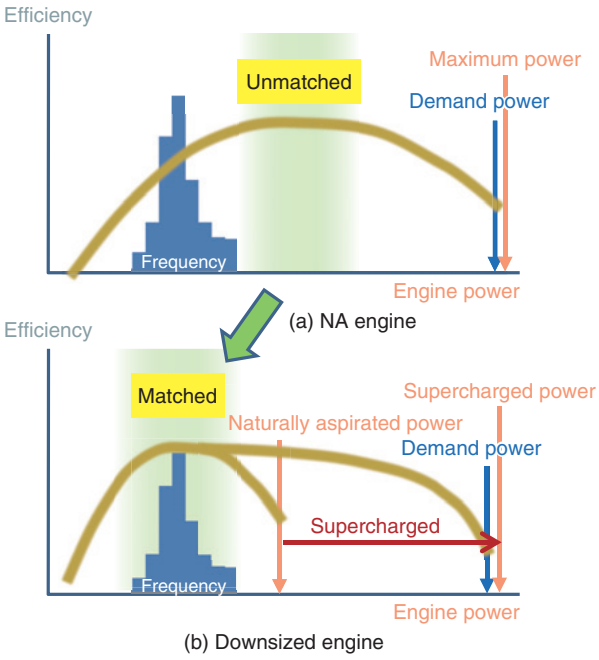


Fig. 4 Fuel economy improvement by downsizing

of the chassis, which supports the engine, and the reduction in driving energy improves the fuel economy. The dynamic performance obtained by making the chassis lighter can also be used to advantage by further reducing the engine displacement and weight, giving rise to a virtuous cycle. A lightweight, compact engine enlarges the freedom to distribute weight in the vehicle, and enhancement of maneuverability can also be expected. These are important elements of fun, the pleasure of driving the vehicle.

On the other hand, the technology to achieve the thermal efficiency of 45% that is assumed for the present project involves reducing the effective compression ratio, which means a real reduction in the displacement. In other words, the increase in specific power due to boosting does not go beyond the level of making up for the displacement reduction. This means that in order to assure dynamic performance, the displacement will remain as it was. However, thermal efficiency enhancement is obtained in all regions, so even when a region with greater frequency of use does not coincide with the region of high thermal efficiency, the amount of enhancement in thermal efficiency will still contribute directly to improved fuel economy (Fig. 5).

If the operating point and the region of high thermal efficiency could be made to coincide, further fuel economy improvement could be expected. The main methods used include reducing the displacement, concentration of operating points in application to a hybrid electric vehicle (HEV), expansion of the high thermal efficiency region to lower loads by lean burn or other such means, but the only one of these approaches that contributes to weight reduction and greater compactness is reducing the displacement.

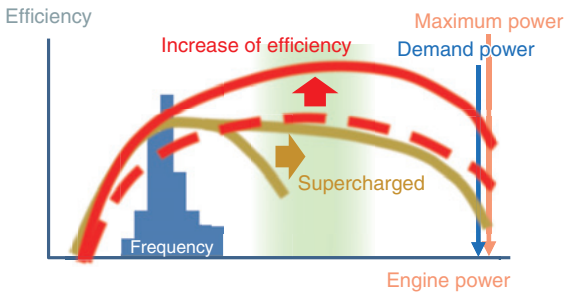


Fig. 5 Fuel economy improvement by increase of thermal efficiency

3. Characteristics of a High Thermal Efficiency Engine

A variety of different measures have been used to increase the thermal efficiency of gasoline engines. According to the research of Tagishi et al.[3], the main specifications that have achieved brake thermal efficiency of 45.2% with regular gasoline and a stoichiometric air-fuel ratio are as follows:

(1) Mechanical compression ratio of 17, exhaust gas recirculation (EGR) rate of 35%;
(2) Stroke bore ratio (S/B ratio) of 1.5; and
(3) Intensification of in-cylinder turbulence kinetic energy and high-energy ignition.

The thermal efficiency achieved was the result of having a displacement of 626 cm^3 per cylinder. The lean-burn approach, which has a higher specific heat ratio than EGR, has greater theoretical efficiency, but given the aftertreatment and knocking issues, efficiency is being pursued instead with a stoichiometric air-fuel ratio.

The following will discuss the issues in achieving a balance between high thermal efficiency and downsizing with these specifications.

3.1. Requirements of Enhanced Thermal Efficiency

In order to seek thermal efficiency, it is necessary to combine enhancement of theoretical efficiency with reduction of relevant types of loss, and a high compression ratio is the precondition that is a basis for enhancing theoretical efficiency. Figure 6 shows a correlation diagram of the technical items necessary in enhancing thermal efficiency. The respective specifications are not simply added together to make a contribution to enhanced efficiency, but instead function interdependently. One example of this follows.

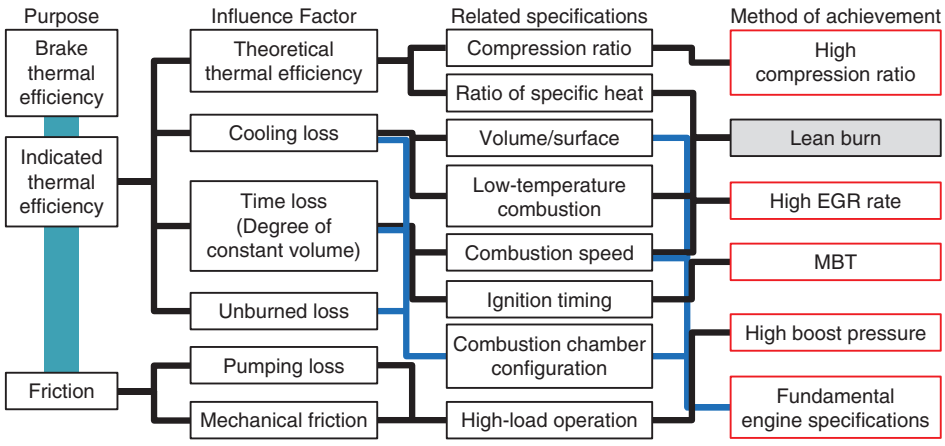


Fig. 6 Analysis of factors influencing brake thermal efficiency

Setting the displacement and S/B ratio properly brings a reduction in combustion chamber surface/volume ratio (S/V ratio) that yields amelioration of cooling loss, but it also helps enable the combustion of diluted mixture at a high compression ratio. In order to realize high-efficiency combustion, it is necessary to have a combustion chamber with a height that does not inhibit flame propagation, and at high compression ratios that result in a flat combustion chamber, the demanded S/B ratio will be correspondingly larger. With a compression ratio of 17, an S/B ratio of 1.4 or greater is necessary (Fig. 7). If an S/B ratio of 1.2 were to be chosen, then not only would there be a simple decrease in efficiency due to the increased cooling loss, but there would also be a failure to achieve combustion itself with a compression ratio of 17. Thermal efficiency so high that it reaches 45% can only be obtained when all the specifications are configured without compromise.

In the mass-production automobile gasoline engines made by Honda over the past 10 years, the specifications have included compression ratios ranging from 8.8 to 13.0, single-cylinder displacement from 220 to 610 cm^3, and S/B ratios from 1.0 to 1.2. A compression ratio of 17, single-cylinder displacement of 626 cm^3, and S/B ratio of 1.5 achieving brake thermal efficiency of 45% greatly exceeds that range. Figure 8 shows the influence of S/B ratio and displacement on thermal efficiency. The maximum thermal efficiency point is located in the vicinity of a single-cylinder displacement from 600 to 650 cm^3 and S/B ratio of around 1.5. This configuration of specifications is a necessary condition for achieving 45% thermal efficiency.

3.2. Output Power Characteristics of the High Thermal Efficiency Engine

With the high compression ratio that is a basis for enhancement of thermal efficiency, the reduction of burning velocity, increase in unburned loss, and knocking become significant issues. Combustion issues are addressed, as described above, by setting a high S/B ratio. Knocking is addressed mainly by introducing EGR and retarding the intake valve close (IVC) timing in order to lower the effective compression ratio (Miller cycle) and reduce the temperature at compression top dead center (TDC).

Introducing EGR and retarding the IVC timing results in a decrease in actual engine displacement. When EGR of 35% is introduced in combination with a mechanical compression ratio of 17 as the basis for retarding the IVC timing to yield an effective compression ratio of 12.5, then the actual displacement decreases to about 50% of the mechanical displacement (0.65 for EGR × 0.72 for IVC = 0.47) (Fig. 9).

A brake thermal efficiency of 45% is achieved with BMEP of 800 kPa at 2000 rpm, and the charging efficiency

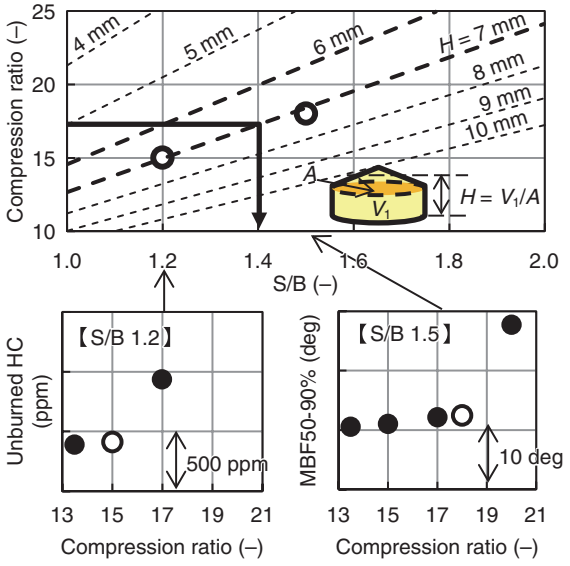


Fig. 7 Average combustion chamber height at TDC for different S/B and compression ratios

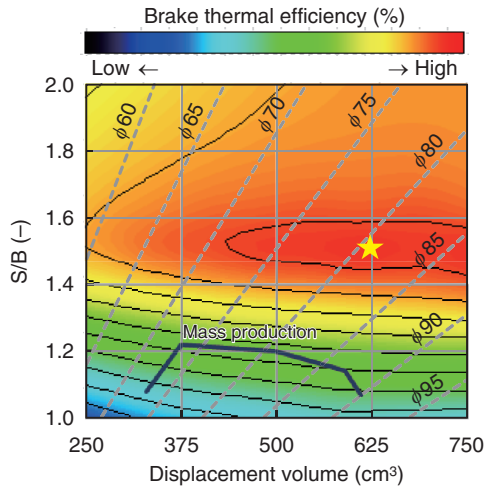


Fig. 8 Engine displacement and S/B in relation to maximum brake thermal efficiency

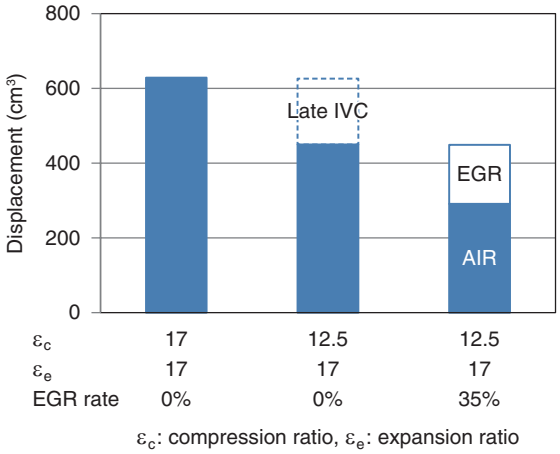


Fig. 9 Reduction of actual displacement by late intake valve close (IVC) timing and exhaust gas recirculation (EGR)

(η_c) then is approximately 60%. If it is an NA engine, η_c 60% can be achieved in the throttling range; however, for the reasons noted above, boosting to 20 kPa (gauge pressure) is necessary in order to assure the air quantity obtained.

Raising the BMEP to a high level in a high thermal efficiency engine has the following issues:

(1) Obtaining the boosting pressure to force in the necessary quantity of air; and

(2) Limitations due to the trade-off between increasing the air quantity and retarding the ignition timing at which knocking occurs.

Since a high thermal efficiency engine has a large S/B ratio, there are limitations on how high the engine speed can go. When transposition from an NA engine with the same displacement is envisioned, the maximum load demand value to achieve equal dynamic performance is about BMEP 1400 kPa, and the maximum power output speed is about 5000 rpm.

In order to provide for η_c at the maximum load point, EGR is not introduced and only IVC timing is used for knocking avoidance. Even then, however, there is only about 70% of actual displacement. In order to obtain 1400 kPa at 2000 rpm, an η_c of 100% is necessary, and the boosting pressure to achieve that is estimated at 70 kPa (gauge pressure). General downsizing of boost engines can achieve BMEP 2000 kPa at this boost pressure level.

Boosting systems use turbochargers for the efficiency. The turbocharger size was configured on the maximum power flow side, but the high expansion ratio (mechanical compression ratio of 17) by comparison with ordinary boost engines means that the exhaust enthalpy is low. This became an issue in providing boost pressure of 2000 rpm. Having exhaust enthalpy remains an issue for realizing a boost system in a high thermal efficiency engine.

If the actual displacement is increased, the boost pressure for obtaining the same air quantity could be lower and the maximum boost pressure could be made even higher (Fig. 10) so that the demand air quantity was obtained by advancing the IVC timing. While advancing the IVC timing causes the effective compression ratio to increase together with the actual displacement, it also retards the ignition timing at which knocking occurs. Consequently, thermal efficiency decreases, but even so, assuring the air quantity (heating value) makes the target of 1400 kPa achievable (Fig. 11). In the low-speed range, the actual boost pressure limit becomes the BMEP limit.

On the other hand, even if the IVC timing is retarded in the high-engine-speed range, the resistance that returns fresh mixture to the intake port side is large and the effective compression ratio is higher than at low speeds. In both cases shown in Fig. 12 of cylinder pressure at engine speeds of 2000 and 5000 rpm, although the IVC is set to the same delayed closure timing, no rise in pressure was observed after bottom dead center at 2000 rpm. It is

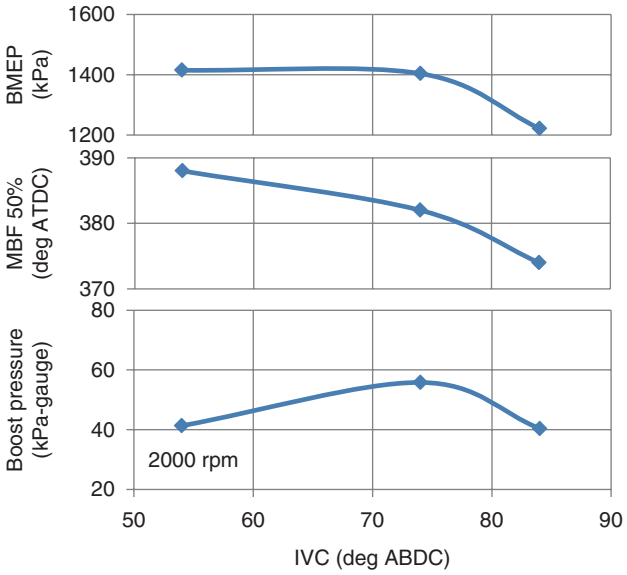


Fig. 11 Influence of effective compression ratio

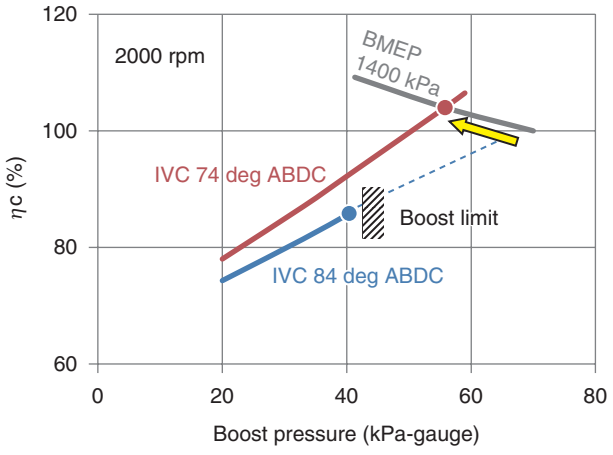


Fig. 10 BMEP limit by air quantity

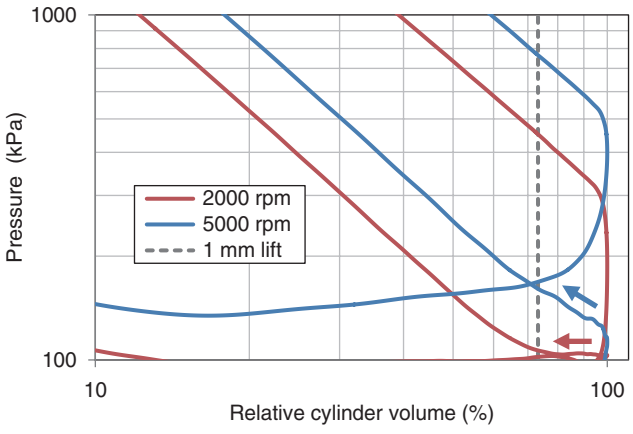


Fig. 12 Effective compression comparison

apparent that during that time, fresh mixture returns to the intake port side so that the effective compression ratio can be lowered. At 5000 rpm, on the other hand, compression begins from bottom dead center even though the intake valve is open. The effective compression ratio is not lowered, so that the temperature at compression TDC rises to about 900 K. The temperature rises to the region where homogeneous charge compression ignition (HCCI) can occur, but since the reaction time is short at high speeds, HCCI combustion does not occur. The ignition timing is retarded for knocking avoidance, so that even if the air quantity (heating value) is increased, it is canceled out by the reduced thermal efficiency, and the BMEP upper limit was reached (Fig. 13).

Knocking is a phenomenon that occurs when the pressure and temperature of unburned mixture in the vicinity of the combustion chamber wall (end-gas) rise due to compression and the influence of that rise results in auto-ignition. The ignition delay time becomes shorter because of the rise in temperature and pressure, so that higher temperatures and higher pressures make knocking more likely to occur. Ordinary regular gasoline is known to have a region with a negative temperature coefficient, called the NTC region. In this region, the ignition delay time is not shortened even when the temperature rises (Fig. 14). Ordinarily, long ignition delay times at low temperatures make knocking less likely to occur, but in this region, it appears likely that even lowering the air-fuel mixture temperature will not mitigate knocking.

The fact is that at 5000 rpm, where the temperature at compression TDC reaches 900 K, no knocking mitigation at all was obtained, even when intake air cooling with direct fuel injection and intercoolor is used to realize a temperature reduction of about 30 K. The difference of 30 K is, empirically, the level of change that is obtained by advancing the ignition timing at which knocking occurs by about five degrees. Figure 15 shows the temperature at compression TDC (calculated values) for each compression ratio together with the temperature sensitivity of the knocking phenomenon.

The reaction process that leads to auto-ignition goes through the cycle of air-fuel mixture compression by the piston and the process of end-gas compression by the combustion gases. When the conditions of this reaction process largely overlap the temperature and pressure of the NTC region, then the temperature sensitivity with respect to ignition delay time will be lower than when the process passes through other regions. In this case, it can be surmised that the reduction of temperature from direct fuel injection and other such factors did not yield an anti-knock effect because of the NTC influence.

A high compression ratio is an essential condition of high thermal efficiency. However, obtaining high power with a high compression ratio involves issues that can be summarized as follows.

(1) Lowering the effective compression ratio by retarded IVC timing is a means of knocking avoidance that does not operate effectively at high engine speeds.

(2) As a result, air-fuel mixture temperature in the cylinder

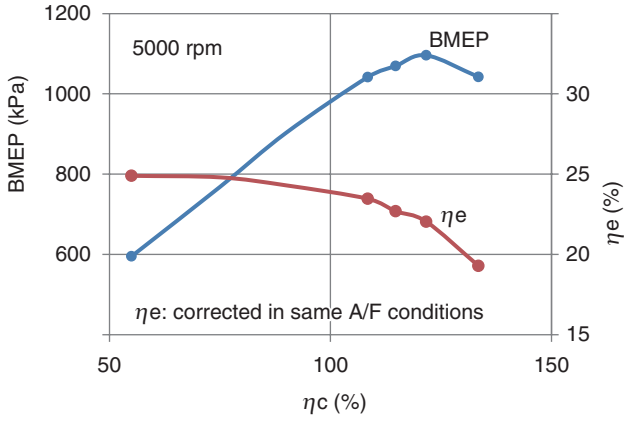


Fig. 13 BMEP limit by reduction of thermal efficiency (ηc: charging efficiency; ηe: brake thermal efficiency)

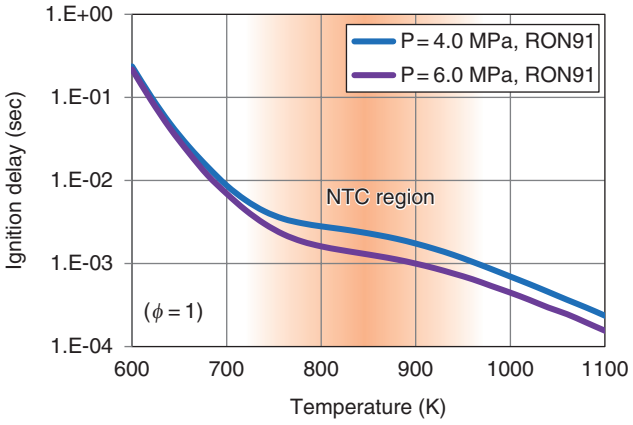


Fig. 14 Negative temperature coefficient (NTC) region of ignition delay

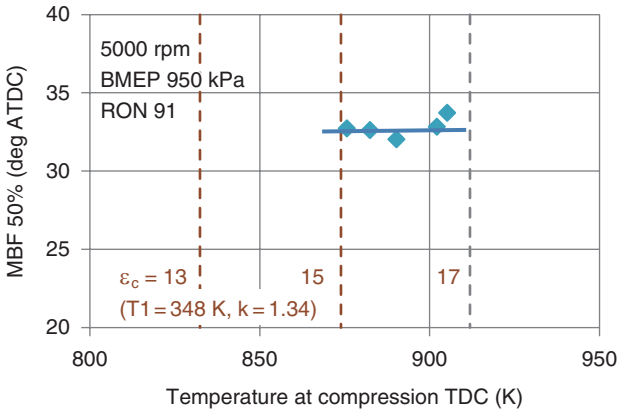


Fig. 15 Temperature sensitivity in knocking

is high so that direct fuel injection and other such measures do not produce a sufficient cooling effect.

With specifications that obtained a brake thermal efficiency of 45%, the BMEP did not rise beyond about 1100 kPa at 5000 rpm. This did not reach the level of 1400 kPa that is necessary for transposition from an NA engine.

4. Examining Possibilities for Realizing High Power

In order to achieve a transition from the already existing NA engine to the high thermal efficiency engine, and to further realize a balance with downsizing, measures are taken to mitigate knocking, which impedes the realization of high power. Those measures and their effects are discussed here. Table 1 shows the specifications of the engine used in this examination.

4.1. Seeking Power Output with a Boost Miller Cycle

Under conditions in which no temperature sensitivity is observed in knocking, it may mistakenly appear as though these various techniques have no effect on knocking. However, it is reasonable to expect knocking to be mitigated if the combination of further measures made it possible to lower the temperature of the air-fuel mixture to a region where temperature sensitivity can be observed.

Figure 16 shows the envisioned knock enhancement logic. First, in order to obtain a reduction of the effective compression ratio by retarding the IVC timing, it is necessary to smooth out the flow returning from the cylinder to the port. As a result of reduction in the resistance of the intake port and the area surrounding the intake valve, IVC timing becomes an effective method for reducing the effective compression ratio. This then enables steps to lower the temperature at compression TDC (Fig. 17). Reducing the intake resistance reduces the work of boosting so that pumping mean effective pressure (PMEP) is decreased. When the exhaust pressure becomes relatively low and the internal EGR is diminished, the effect of reducing the air-fuel mixture temperature can take place. Reducing the intake resistance lowers the velocity of flow into the cylinder so that there is also thought to have been an effect of reduced heat transfer from high-temperature areas. The magnitude of the respective effects attributable to the various factors cannot be separated out at present, but they are all consistent in being measures oriented toward temperature reduction. In port selection, consideration of a flow volume sufficient to help ensure power output and reduction of the air-fuel mixture temperature are necessary, in addition to the high-intensity turbulence demanded for high-efficiency combustion in the low-speed range.

The result of lowering the air-fuel mixture temperature in the cylinder and taking knock enhancement measures was that the target of power output equal to that of an NA engine was met with a BMEP of 1400 kPa at 5000 rpm (Table 2).

Table 1 Specifications of test engine

Bore (mm) × Stroke (mm)	ϕ73 × 109.5, S/B 1.5
Compression ratio (-)	Variable by IVC timing
Expansion ratio (-)	17.0
Engine type	DOHC 4-valve
Number of cylinders	4
Displacement (cm^3)	1833
Intake port	Tumble port
Air supply	Turbo charger
Fuel supply	Direct injection
Gasoline	RON91

Table 2 Port flow comparison and test result

	Base port	High flow port
Mean effective opening area (cm^2)	3.55	5.04
Intake valve diameter (mm)	ϕ28	ϕ29
Temperature at TDC (K), ηc 100%	826	772
Exhaust pressure (kPa), ηc 100%	128	143
MBF 50% (deg), ηc 100%	36.4	33.1
Maximum BMEP (kPa)	1100	1400

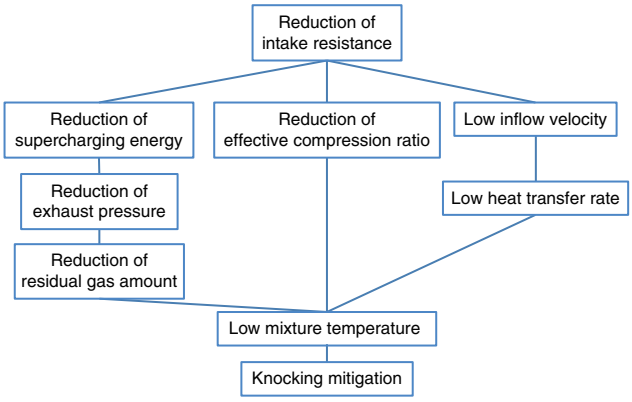


Fig. 16 Knocking mitigation by reduction of intake resistance

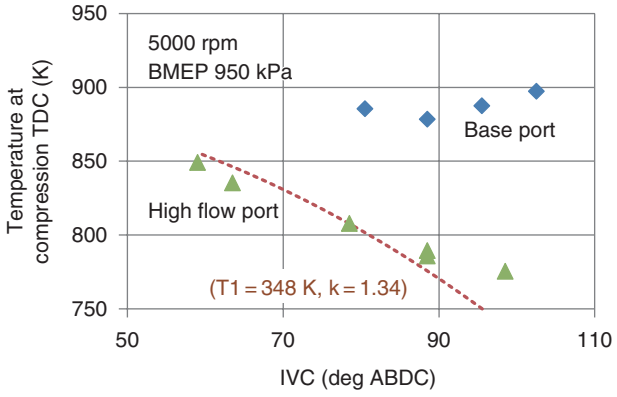


Fig. 17 Relationship between IVC and effective compression ratio

4.2. Variable Compression Ratio

The result of increasing power output by enhancing the specifications was confirmed up to equality with an NA engine. However, a level that would enable downsizing the engine was not achieved. In order to obtain further increased power output, drastic countermeasures against knocking will be necessary.

Figure 18 shows the relationship between the maximum BMEP and compression ratio of engines in commercially available vehicles. They reach a BMEP on the level of 2000 kPa at a compression ratio of 11. This means that if the compression ratio can be lowered to this degree, then a BMEP at a level enabling engine downsizing can be obtained.

With a high thermal efficiency engine, the effective compression ratio reduction effect obtained 5000 rpm and 1400 kPa even with a compression ratio of 17. Using a similar delayed closure of the intake valve, it is possible that a BMEP on a par with a commercially available vehicle could be obtained with a compression ratio higher than that of a commercially available vehicle. An increase in the BMEP attributable to the thermal efficiency resulting from a high S/B ratio can also be expected. The high thermal efficiency engine specification allows for the possibility of a compression ratio set higher than 11 at a BMEP of 2200 kPa, and it also has greater potential for high-load efficiency than commercially available boost-downsizing engines.

If the specific power can be increased from a BMEP of 1400 kPa to 2200 kPa, then the engine displacement can be reduced to about 65%. In order to obtain the fuel economy improvement from downsizing, the driving load and thermal efficiency need to be matched. This matching was considered in terms of a FIT-class vehicle with inertia weight 1090 kg envisioned driving in Worldwide harmonized Light vehicle Test Procedures (WLTP) mode. When the frequency distribution of the power output is calculated on the basis of fuel consumption, the power of 14 kW at 50% cumulative frequency is the equivalent of 15% of the maximum output of 96 kW of a currently available NA engine (Fig. 19). Figure 20 shows the relationship between the iso-power contour line and thermal efficiency that obtains when this engine is envisioned in terms of a boost engine with a maximum thermal efficiency point at 2000 rpm and 800 kPa and a maximum power output point at 5000 rpm and 2200 kPa. Power output at the maximum thermal efficiency point is 15% of maximum power output, and can be made to coincide with power output at 50% cumulative frequency. Power output at 80% cumulative frequency is 23% of maximum power output, and the efficiency is within -2 points of maximum thermal efficiency. This suggests that in an engine with a maximum power output point at 5000 rpm and 2200 kPa, the driving load in WLTP mode would generally fall within the high thermal efficiency range.

For each operating range of the engine, there is an optimal compression ratio in terms of thermal efficiency or maximum load. However, a complex mechanism would be necessary in order to implement continuously variable compression that can be optimized to all ranges. In the

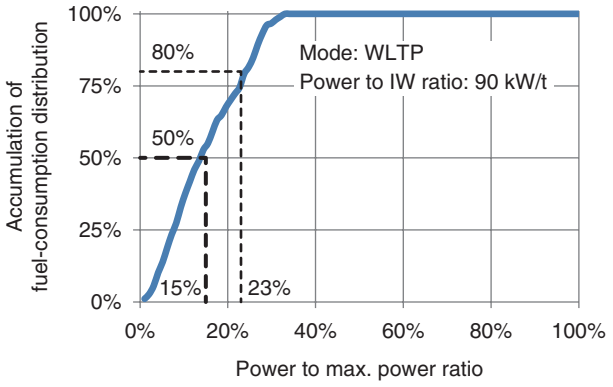


Fig. 19 Fuel consumption distribution

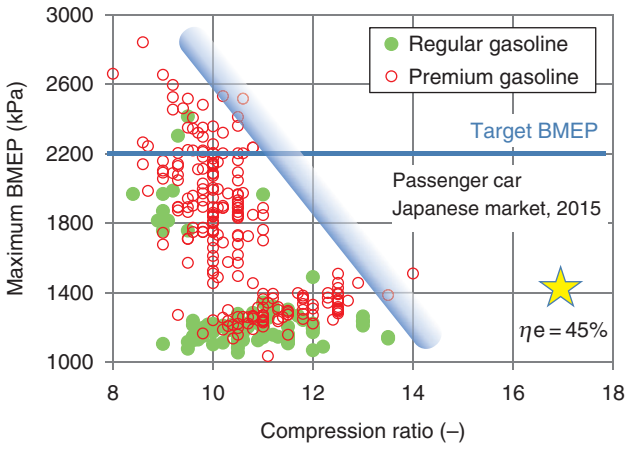


Fig. 18 BMEP limit by mechanical compression ratio

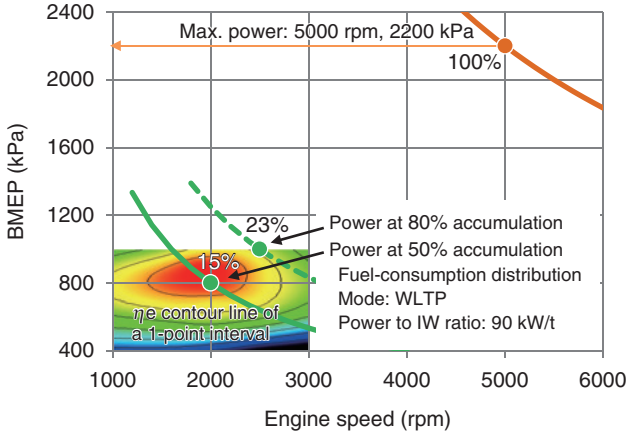


Fig. 20 Relationship of power ratio to max. power and thermal efficiency

event that the variable compression ratio is selected, it would be preferable to have a simple and easy switching mechanism in line with the compactness that is the original aim. As described above, an examination was made of one example of an engine with the specific power of 2200 kPa at 5000 rpm in which mode driving using relatively high loads fits within the high thermal efficiency region. The high compression ratio that achieved high thermal efficiency (17: η_e 45%)was therefore made a basic specification, and a two-stage shift that realizes a lower compression ratio in order to yield power output (11: BMEP 2200 kPa) was used for specifications that simultaneously produce high thermal efficiency, downsizing, and compactness.

5. Conclusion

The possibilities of increasing specific power were examined as a way of achieving downsizing as an evolution in the high thermal efficiency engine.

(1) By reducing the air-flow resistance at the intake valve and intake port, it became possible to return fresh mixture from the cylinder to the port by delayed closure of the intake valve even at 5000 rpm. As a result, it became possible to lower the effective compression ratio, and advancing the ignition timing at which knocking occurs obtained a higher BMEP. The maximum BMEP at 5000 rpm became 1400 kPa, making it clear that specific power up to a level equivalent to an NA engine could be achieved with a mechanical compression ratio of 17.

(2) In order to obtain further increased specific power output, drastic countermeasures against knocking become necessary, and enabling a variable mechanical compression ratio is an effective approach. If the compression ratio demand value of 17 in the high thermal efficiency region and the compression ratio of 11 in the power output region could be made variable, it would become possible to achieve a balance of 45% brake thermal efficiency and 2200 kPa. Using this engine, WLTP mode driving in a vehicle with a 90 kW/t power-weight ratio could generally fit within the high thermal efficiency range.

6. Afterword

The automobile society will come sooner or later to the developing countries and to the base of the pyramid (BoP), and it is one of the duties of the automobile manufacturers to guide this society into a healthy environment. In that sense, limiting the environmental impact is a fundamental element of performance demanded of a low-cost basic engine.

When pursuing thermal efficiency, expensive and complex devices such as boosting systems and EGR systems become necessary. In order for a basic engine to obtain high thermal efficiency with the minimum device, it is especially important for it to have outstanding basic performance.

The foundation for thermal efficiency enhancement techniques is appropriate selection of the basic structure and specifications of the engine. By means of configuration, even a non-boost engine can obtain brake thermal efficiency of around 42%. Depending on the power output required, upsizing may become necessary, but such an engine may become an option in a market that places value on high thermal efficiency, high reliability, and low cost.

The development of a high thermal efficiency engine should be pursued in a form that, in addition to outstanding basic performance, allows the selection of appropriate devices suited to market demands.

References

(1) International Energy Agency: Part4 Scenarios and Technology Roadmaps, Chapter13 Transport, Energy Technology Perspective 2012, p. 443 (2012)

(2) Ota, T., Kono, R., Ito, N., Matsumura, Y., Takahashi, N.: Development of Gasoline Turbo Engine Conforming to U.S. ULEV2 Regulations, Honda R&D Technical Review, Vol. 18, No. 2, p. 36-43

(3) Tagishi, R., Ikeya, K., Takazawa, M., Yamada, T.: Technology for Realization of Gasoline Engine Brake Thermal Efficiency of 45%, Honda R&D Technical Review, Vol. 27, No. 2, p. 1-11

■ Author ■



Nobu TAKAHASHI

Development of New 1.6 L 2-stage Turbocharged Diesel Engine for Honda CR-V

Junichi HATANO* Ken NISHIMORI* Hiroyuki FUKUSHIMA*
Taro TABUCHI* Naoto KITAYAMA* Yoshinori ISHIHARA*

ABSTRACT

This newly developed engine is based on a downsized 1.6 L 88 kW (55 kW/L) engine, with dynamic performance aimed to replace the previous 2.2 L 110 kW (50 kW/L) diesel engine. The new engine uses a 2-stage turbocharger to achieve high power while maintaining the maximum commonality with the structure of the 1.6 L 88 kW diesel engine. The bearing cap, head gasket and other parts have been specially designed to reinforce the engine structure, realizing high-specific power of 118 kW (74 kW/L). In addition, a newly developed NOx storage catalyst is used, complying with the European EURO 6 emission standards. Technologies for enhancing fuel economy include further reduction of mechanical friction and enhancement of combustion efficiency by combustion calibration. These technologies were applied to develop a EURO 6-compliant power unit that provides high power with low fuel consumption, and this power plant was mounted in the 2015 CR-V for Europe.

1. Introduction

Recently, concern for environmental issues such as global warming and energy resources is growing, and there are strong social demands for reduction of CO_2 emissions from passenger vehicles. Demands are also increasing for dynamic performance, and the further evolution of diesel engines that have both good drivability and low-fuel-consumption performance is anticipated from these viewpoints. In this background, Honda developed a 2.2 L inline 4-cylinder i-CTDi turbocharged diesel engine[1] in 2003, and mounted it in the Accord for the European market. Since then, the same diesel engine has been used in multiple models such as the CR-V and Civic. Honda developed an i-DTEC diesel engine[2, 3] in 2008 as a second-generation 2.2 L engine. This engine had completely new combustion system specifications, such as the compression ratio and injector, which enabled compliance with the European EURO 5 emission standards (EURO 5) and also enhanced fuel economy performance. The CR-V released in 2009 was equipped with this i-DTEC diesel engine and achieved CO_2 emissions of 149 g/km in the New European Driving Cycle (NEDC) mode.

Honda announced the "EARTH DREAMS TECHNOLOGY" engine series in November 2011, which offers next-generation powertrain efficiency to provide a superior combination of fuel economy and dynamic performance. As the first step, a 1.6 L 88 kW i-DTEC diesel engine was released as a third-generation diesel engine and mounted in the Civic for Europe at the start of 2013[4]. This engine was realized by completely reforming and downsizing the conventional 2.2 L diesel engine[5, 6], which made it the lightest-weight engine in its class known to date and increased the power train efficiency by measures such as reducing friction to a level comparable to that of a gasoline engine. This resulted in a EURO 5-compliant vehicle with top-class fuel economy.

In addition to the low fuel consumption concept, this development aimed to further enhance driving performance, and increased the power based on a 1.6 L diesel engine. The basic parts of the main engine structural components, such as the aluminum cylinder block with an open deck structure[7], are shared with those of the existing 1.6 L engine. A CR-V equipped with the new engine complied with the European EURO 6 emission standards (EURO 6), and achieved the fuel economy performance of CO_2 emissions of 129 g/km in NEDC mode even while possessing driving performance enabling replacement of the 2.2 L diesel engine. This paper describes the technologies applied to the new engine to increase power, comply with EURO 6, and enhance fuel economy.

* Automobile R&D Center

Table 1 Engine specifications

	2.2 L 110 kW (150 PS)	1.6 L 88 kW (120 PS)	1.6 L 118 kW (160 PS)
Engine	Inline 4-cylinder DOHC 4 valves		
Bore x Stroke	ϕ85 x 96.9 mm	ϕ76 x 88 mm	
Displacement	2199 cm^3	1597 cm^3	
Compression ratio	16.3	16.0	
Cylinder block	Advanced semi-solid casting technology (ASCT) closed deck	High pressure die-casting (HPDC) open deck	
Max. torque	350 Nm /2000-2750 rpm	300 Nm /2000 rpm	350 Nm /2000 rpm
Max. power	110 kW(150 PS) /4000 rpm	88 kW(120 PS) /4000 rpm	118 kW(160 PS) /4000 rpm
Crankshaft main bearing diameter (mm)	ϕ62	ϕ55	ϕ55
Conrod bearing diameter (mm)	ϕ51	ϕ39	ϕ42
Balancer	Applied	N/A	Applied
Turbocharger	Variable geometry turbocharger, Honeywell GT14	Variable geometry turbocharger, Honeywell GT12	Serial-sequential 2-stage turbocharger, Honeywell GT10/GT15
Common-rail fuel injector	Piezo (Max. 180 MPa) ϕ0.123 mm x 7 holes	Solenoid (Max. 180 MPa) ϕ0.114 mm x 8 holes	
EGR system	HP hot EGR of HP cooled EGR	HP hot EGR and/or LP cooled EGR	
Aftertreatment	DOC and DPF	NSC and DPF	NSC and DPF
Emissions	EURO5		EURO6
Vehicle	CR-V 4WD	CR-V 2WD	New CR-V 4WD
Fuel consumption (NEDC)	149 g/km	119 g/km	129 g/km

2. Overview of Newly Developed Engine

Table 1 lists the main specifications of the new engine and Fig. 1 shows the engine system layout. The new engine takes into account commonality with the engine frame of the previously released 1.6 L 88 kW i-DTEC diesel engine[7]. The main parts share common combustion system specifications, such as the piston combustion chamber design and the injector[8], and the engine is equipped with a low-pressure exhaust gas recirculation (LP-EGR) system[8, 9] as an emission control device. The three technical items noted below as features of the new engine were set as development concepts.

(1) A serial-sequential 2-stage turbocharger is used to increase power. In addition, the head gasket, bearing cap and reciprocating parts use special high-power designs allowing it to withstand the in-cylinder pressure boosted by supercharging.
(2) A newly developed NOx storage catalyst is used to achieve compliance with EURO 6.
(3) Turbocharging specifications that take into account reduced pumping loss are used, mechanical friction has been further reduced[10] and combustion calibration has been optimized in order to enhance fuel economy.

The following chapters describe the details of these technologies.

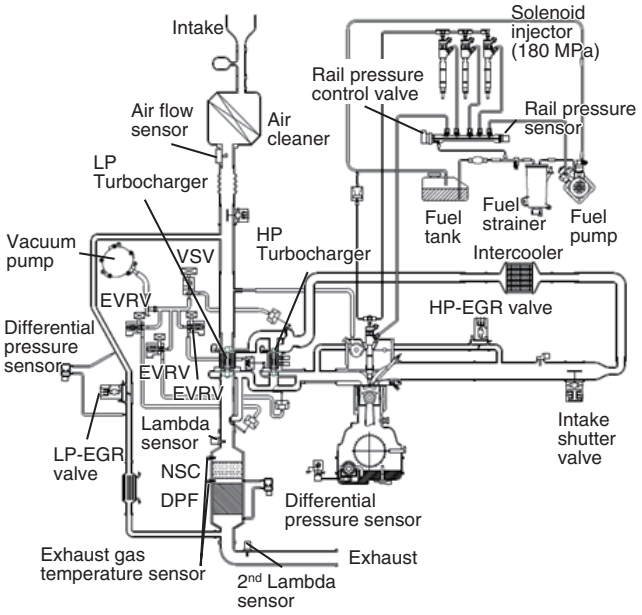


Fig. 1 Engine system layout

3. Technologies Applied to the Newly Developed Engine

3.1. High Power Using a 2-stage Turbocharger

When increasing the power it is necessary to secure an intake air flow corresponding to the target power, so the turbocharger size should be appropriate. Figure 2 shows a concept diagram related to turbocharger size selection. Figure 2 also shows an image of a compressor map obtained from the corrected air flow and pressure ratio of the turbocharger. To increase the specific power, the required air flow necessarily becomes larger than that of the single turbocharger utilized in the previous 1.6 L 88 kW model, so the turbocharger size increases. However, there was the issue that the boost performance, fuel economy performance and transient response performance under low-engine-speed, low-load operating conditions are lower than those of a compact turbocharger[10), (11)].

To address these issues, the new engine uses a 2-stage turbocharger made by Honeywell, which is the first 2-stage turbocharger used by Honda. Figure 3 shows the appearance. The low-pressure-stage turbocharger (LP turbocharger) needs to satisfy power performance of 118 kW, so a size that secures sufficient air flow should be selected as shown in the image in Fig. 2. Therefore, a GT15 with a maximum supercharging pressure of 2.98 bar and a maximum turbine speed of 226000 rpm was used. In addition, a GT10 with a maximum turbine speed of 290000 rpm was selected for the high-pressure-stage turbocharger (HP turbocharger) as a compact turbocharger with the surge limit shifted to the high-power-ratio side compared to the 88 kW single turbocharger in order to secure acceleration performance from the low-engine-speed range. Here, the GT10 turbocharger is not a wastegate valve (WGV) type, and instead uses a variable geometry turbine (VGT)-type turbocharger with a structure that enables the turbine operating gas flow to be varied as shown in Fig. 4.

Figure 5 shows the approach toward selecting the HP turbocharger. This figure shows the effect of the turbocharger specifications on NEDC mode fuel

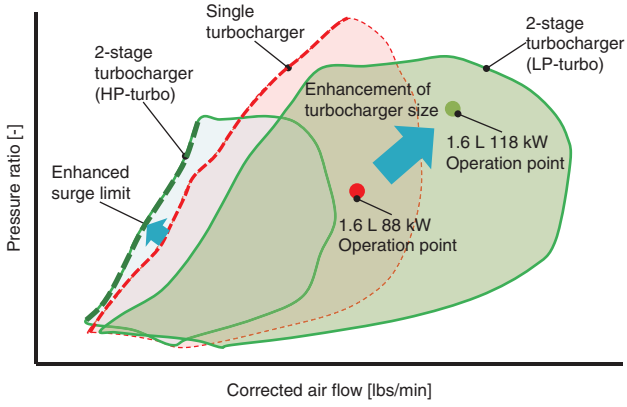


Fig. 2 Concept for determining turbocharger size

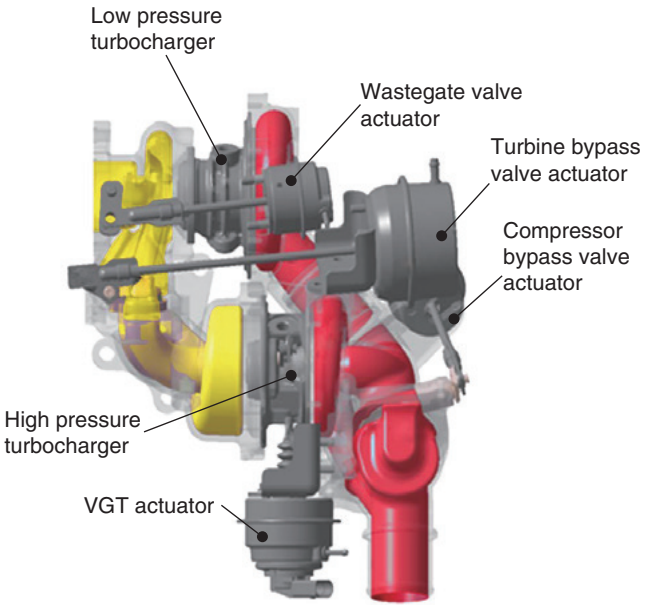


Fig. 3 Overview of 2-stage turbocharger

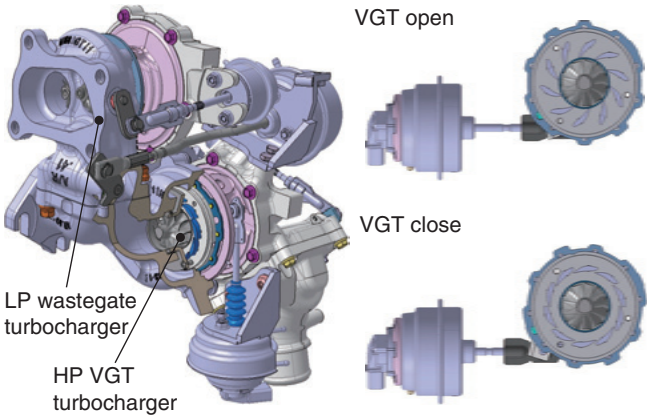


Fig. 4 Structure of VGT

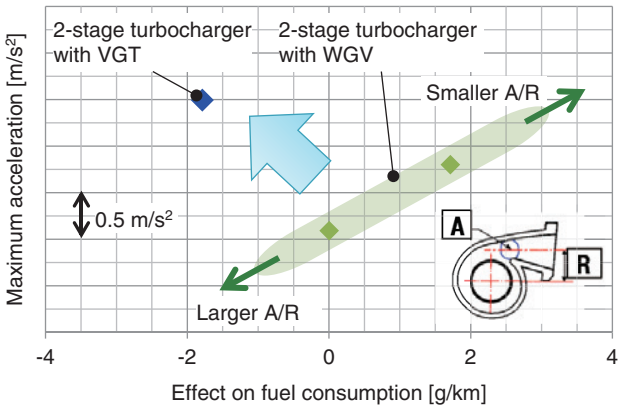


Fig. 5 Effect on dynamic performance and fuel consumption between WGV and VGT for HP turbocharger system

consumption on the horizontal axis, and the peak acceleration when accelerating with the throttle fully open in 3rd gear on the vertical axis. The typical 1.6 L-class 2-stage turbocharger structure performs boost control using a WGV on both the low-pressure and high-pressure sides. However, when a fixed turbine is used in the HP turbocharger, acceleration performance and the effect on fuel economy due to pressure loss have a trade-off relationship according to the selected ratio (A/R) of the sectional area (A) at the turbine inlet and the turbine wheel radius (R), which is a size index, and it is a challenge to realize both performances.

Therefore, the newly developed engine used a VGT-type turbocharger as the HP turbocharger of a mass-produced 2-stage turbocharger for a 1.6 L-class passenger vehicle, which is the first such case known to date. This simultaneously secured smooth acceleration performance by increasing supercharging performance at low engine speeds, and enhanced fuel economy performance by reducing pumping loss in the HP turbocharger operation range. The use of a VGT type enables obtaining the target supercharging pressure by setting an arbitrary vane angle in accordance with the operating conditions. This makes it possible to approach the exhaust backpressure of a single turbocharger in NEDC mode, and contributes to pumping loss reduction. Figure 6 compares the backpressure and shows the fuel consumption reduction effects of each turbocharger control system. The VGT type enabled reduction of the back-pressure at the same required boost pressure compared to the WGV system, and effectively reduced CO_2 emissions in NEDC mode by 3.5 g/km.

Figure 7 shows a schematic diagram of the 2-stage turbocharger used. The valve configuration used to switch the HP turbocharger and LP turbocharger locates a compressor bypass valve (CBV) for bypassing the HP turbocharger compressor on the intake side, and a turbine bypass valve (TBV) for bypassing the HP turbocharger turbine on the exhaust side. The boost pressure is controlled by operating the four CBV, TBV, VGT and WGV devices in accordance with the engine operating range.

Here, Fig. 8 shows how each valve operates in accordance with the operating conditions. At low engine speeds, the boost pressure is controlled using only the VGT, and the other valves are all closed [Fig. 8 (a)]. In the medium engine speed range, once the VGT is fully opened, the supercharging pressure is controlled by the TBV, and the CBV and WGV are closed [Fig. 8 (b)]. Then, after the TBV has also opened fully, the boost pressure is controlled by the LP turbocharger WGV, and the CBV also opens so

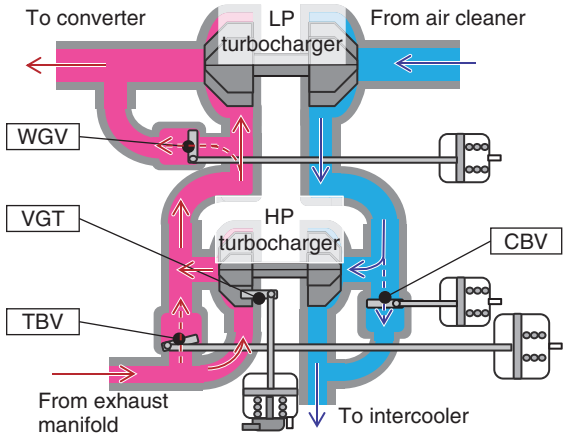


Fig. 7 Diagram of 2-stage turbocharger

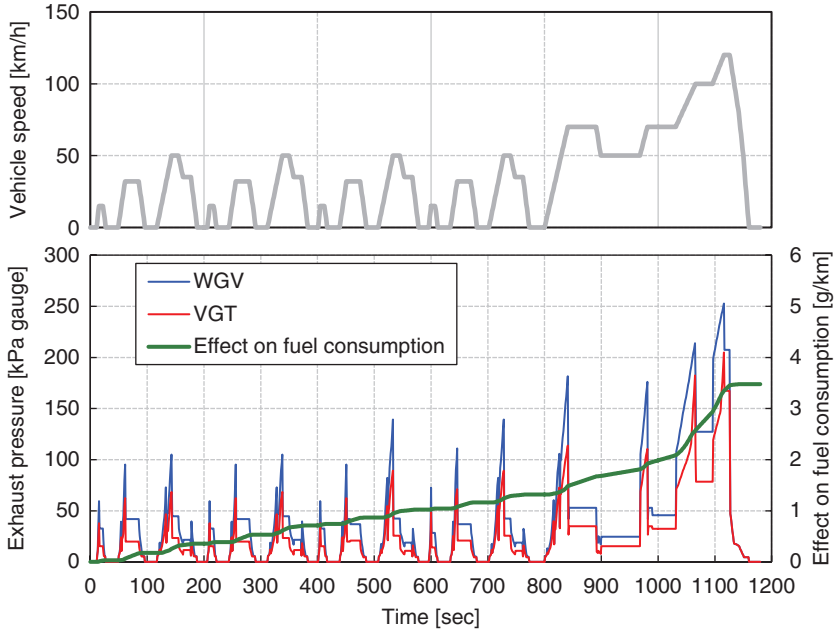


Fig. 6 Effect of pumping loss reduction between VGT and WGV

that the boost pressure is controlled by the LP turbocharger alone [Fig. 8 (c)]. The transition between each range is realized by model-based valve collaborative control.

3.2. Engine Structure that Supports High Power

Two performances are required of the hardware when increasing the power. The first requirement is an engine frame strength capable of withstanding the increase in in-cylinder pressure due to higher boost. For this reason, the connecting rod bearing diameter was increased from ϕ39 for the 1.6 L 88 kW model to ϕ42 to support the increased combustion load. An increase to 118 kW was anticipated when designing the 88 kW specifications, so a common engine block was used with a main journal diameter of ϕ55. Other changes to reinforce the engine frame include increased bearing cap stiffness and changes to the seal structure and head gasket materials.

The second performance required of a high-power engine frame is countermeasures for the increased thermal load. The layout of the engine oil cooling channels that cool the pistons was optimized, and the cooling jet flow was increased from the standard 1.5 L/min to 3.8 L/min to cool interbore temperature. The cooling jet flow rate increase was kept at the minimum required with fuel consumption in mind. In addition, the valve timing of the previous model was designed to reduce the pumping loss on the low-engine-speed side and enhance fuel economy during low- to medium-load driving. In contrast, the new engine design increases the intake valve-opening angle to support high output, as well as the intake and exhaust valve lift amounts to increase the volumetric efficiency at the power point. This enabled enhancement of fuel economy performance at all loads, reduced the excessive thermal load to the cylinder block and cylinder head, and helped to withstand high specific power.

Adoption of an engine frame that supports higher boost and increased power output as described above enabled the newly developed engine to achieve a maximum torque of 350 Nm at 2000 rpm and maximum output of 118 kW at 4000 rpm as shown by the power and torque curve in Fig. 9.

3.3. Technology for EURO 6 Compliance

The new engine has the maximum commonality with the 1.6 L 88kW engine specifications, enabling simultaneous achievement of high power and low cost. For this reason, the fuel injection system specifications (number of nozzle holes, nozzle hole diameter, nozzle cone angle, maximum injection pressure), the piston combustion chamber shape, and the compression ratio are the same as the 1.6 L 88 kW specifications[8]. Therefore, like the previous EURO 5-compliant model, high-efficiency combustion was

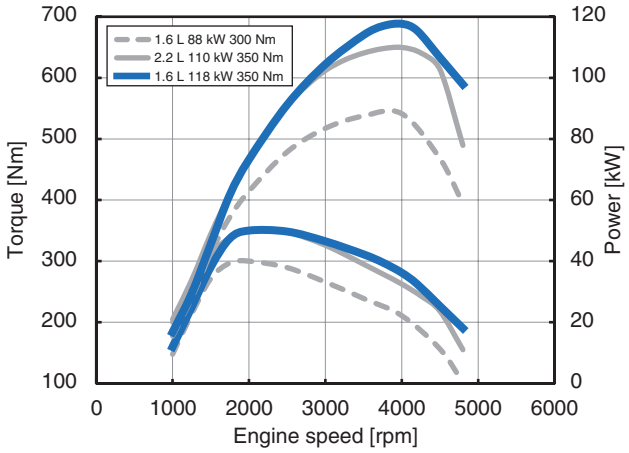


Fig. 9 Power and torque curve

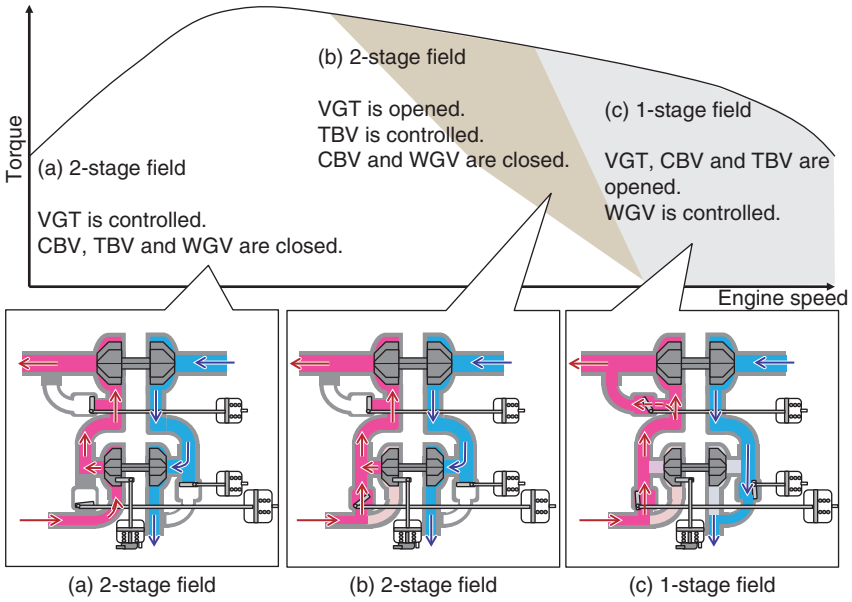


Fig. 8 Turbocharger operating strategy in engine map

obtained by LP-EGR, and the combustion settings secure a high degree of constant volume mainly for diffusive combustion that uses full-range 2-step pilot injection (PI) as the basic injection pattern[8), 9)]. The concept for complying with EURO 6 was to avoid an increase in pumping loss and drop in combustion efficiency due to high boost and high EGR, achieve low-fuel-consumption performance while maintaining the feed gas level at the EURO 5 standard[8)], and add an aftertreatment system.

However, there is the issue that a drop in exhaust temperature cannot be avoided as shown in Fig. 10, due to lower fuel consumption and an increased heat mass as a result of using a 2-stage turbocharger. Development of a new catalyst capable of adsorbing and storing NOx even at low temperatures is demanded to support a lower NOx storage catalyst (NSC) bed temperature due to this drop in exhaust temperature. In addition, conventional NSC do not have conversion performance capable of satisfying the EURO 6 NOx regulations, so the NOx conversion rate needs to be increased by 40 points or more compared to EURO 5, and the NOx conversion performance is necessary over a wide temperature range including high temperatures.

To address this issue, the catalyst adsorbent was changed from the zeolite used in the previous model to barium, and the optimum platinum group metal (PGM) carrier density was selected. By optimizing the catalyst surface structure and increasing the PGM amount compared to the previous catalyst, a lower conversion start temperature could be realized and the NOx was oxidized by the PGM, which increased the adsorptivity to the barium surface in the lean atmosphere from the cold condition. As a result, the NOx conversion rate could be further increased over a wide catalyst temperature range from low to high temperatures, and CO and HC conversion performance also increased as shown in Fig. 11.

3.4. Technology for Enhancing Fuel Economy

Technologies used to enhance the fuel economy of the newly developed engine can be broken down into reduction of mechanical friction, reduction of pumping loss using a 2-stage turbocharger with a VGT-type HP turbocharger, and enhancement of combustion by applying after-injection.

The main goal of reducing mechanical friction is to reduce the sliding friction of reciprocating parts. This was accomplished by reducing the piston skirt area as shown in Fig. 12, applying a low-friction coating to the chain guide, and machining the cam journal to reduce the surface roughness and lower the sliding resistance. In addition, the shape of the balancer weight that was set as a part for increasing power was optimized as shown in Fig. 13 to reduce the resistance when the balancer agitates the surface of the oil accumulated in the oil pan. These technologies reduced the mechanical friction at 1500 rpm by 50% compared to the previous 2.2 L 110 kW engine[11)-13)].

The collision noise produced when the balancer drive chain and sprocket mesh is an issue when using specifications that achieve a driving speed-increasing ratio of 2x using only the chain. Therefore, the balancer shown in Fig. 14 that was applied to the new engine has specifications that reduce this collision noise and further enhance quietness by reducing the speed-increasing ratio of

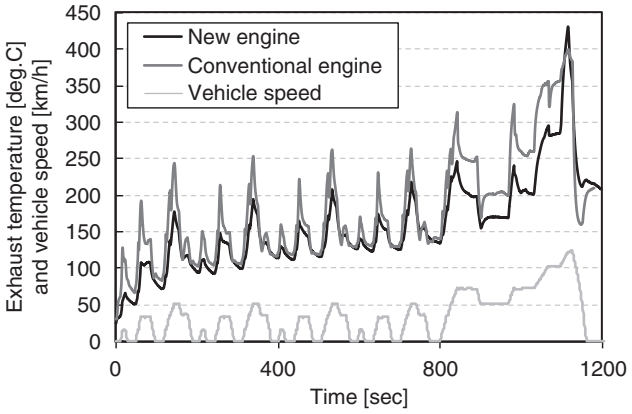


Fig. 10 Exhaust gas temperature in NEDC mode

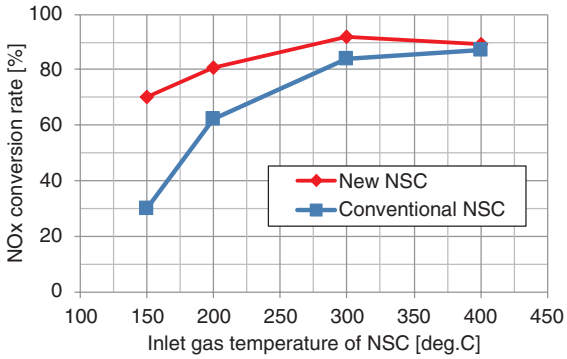


Fig. 11 NOx conversion rate of new NSC (test piece)

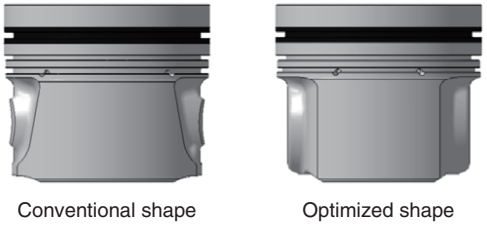


Fig. 12 Comparison of piston skirt area

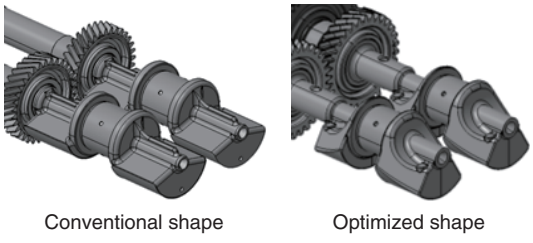


Fig. 13 Optimization of balancer weight shape

the chain to 1.3x and using a 1.5x speed-increasing gear to increase the speed to 2x.

Regarding combustion calibration, after-injection was used to reduce cooling loss and enhance the degree of constant volume in order to further increase the thermal efficiency compared to the 1.6 L 88 kW model. Figure 15 shows the rate of heat release at 1500 rpm, BMEP 645 kPa when after-injection is used. The main combustion fuel amount needed for the same required torque is reduced by the after-injection amount, so the rate of heat release during main combustion is suppressed, enabling reduction of the cooling loss from the combustion chamber and cylinder head wall surfaces. In addition, the ignition timing angle can be advanced without increasing the combustion noise produced by the main combustion, so the degree of constant volume increases, which contributes to reducing fuel consumption. As described above, the basic injection pattern is total 3-step injection that adds main injection (MI) to full-range 2-step PI. Combustion calibration used model-based calibration (MBC)[5] to obtain fuel economy enhancement effects from after-injection. In addition, after-injection was additionally set only in the low- to medium-load range. These measures obtained fuel economy enhancement effects of 0.5% in NEDC mode.

In the standalone engine format, the technologies for reducing fuel consumption described above provided brake-specific fuel consumption (BSFC) enhancement effects (1500 rpm) as shown in Fig. 16 compared to the previous 2.2 L model.

3.5. Vehicle Power, Emissions and Fuel Economy Performance

Each technology described thus far related to increasing power, EURO 6 compliance and low fuel consumption was applied to the power unit mounted in the new CR-V for Europe released from 2015. Tests to compare the dynamic performance when mounted in a vehicle were performed by mounting the new engine and previous engines in CR-V and accelerating with the throttle fully open in third gear. Figure 17 shows these results. The new engine increased the absolute value of the maximum attained acceleration (peak G), which is one index of acceleration performance, by 7.5% and also shortened the time required to reach peak G, which is another index of acceleration performance. This enabled attainment of product appeal equivalent to not only the previous 1.6 L 88 kW specification model, but also running performance that allowed replacement of the 2.2 L model, which was the target.

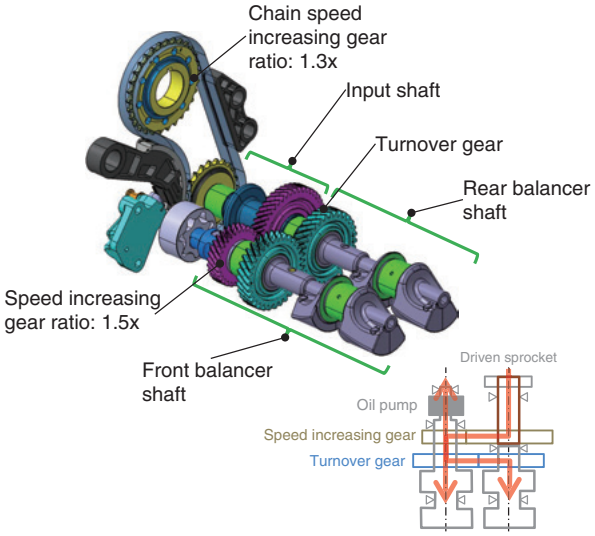


Fig. 14 Overview of balancer system

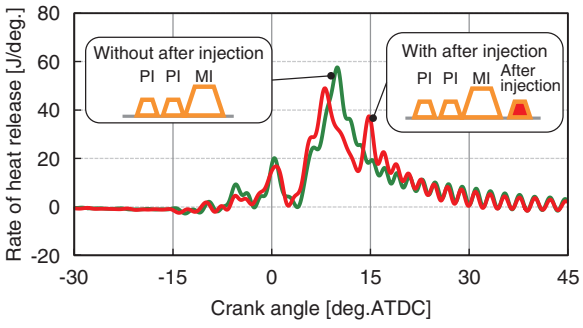


Fig. 15 Rate of heat release with after injection

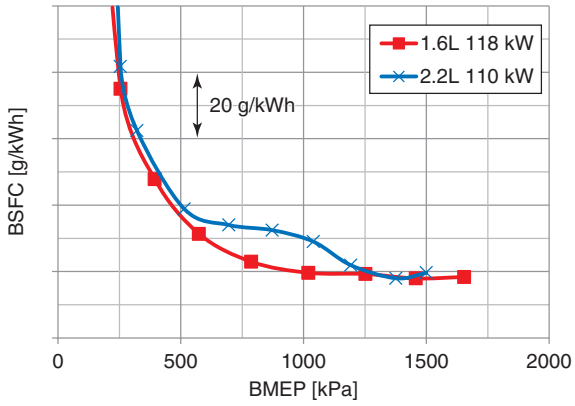


Fig. 16 Enhancement of BSFC from previous engine

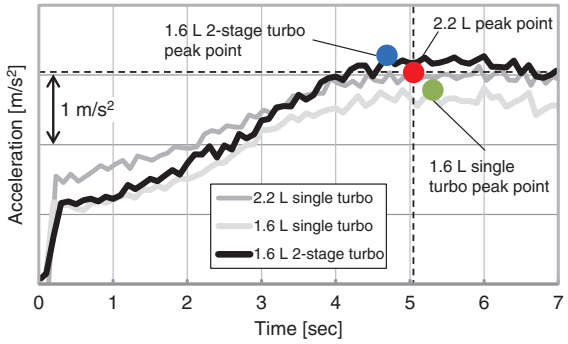


Fig. 17 Dynamic performance of 2-stage turbocharger

Figure 18 compares the engine output with that of competitors. The fuel consumption and engine power trend line for 4WD, MT specifications in the SUV segment shows that the new engine simultaneously achieved low fuel consumption and dynamic performance equivalent to the top class among competitors[11]-[13].

In addition, Fig. 19 (a) and (b) respectively show the achieved emissions and fuel economy values. The 2.2 L model complied with EURO 5 and had CO_2 emissions of 149 g/km, however the new engine complied with EURO 6, achieved CO_2 emissions of 129 g/km, and also increased fuel economy by 13.4%.

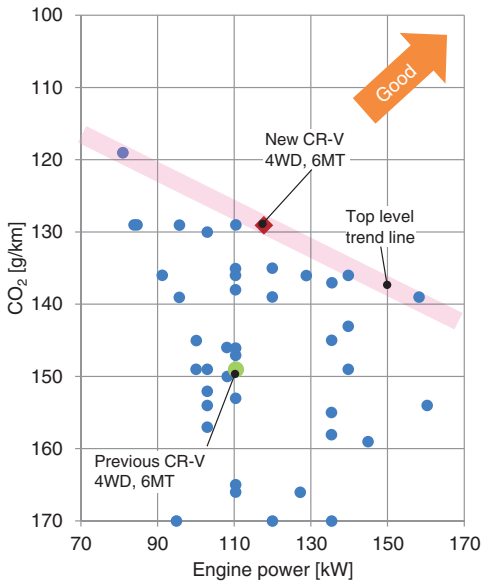
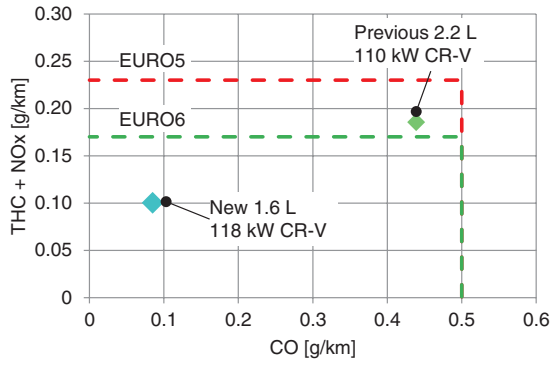
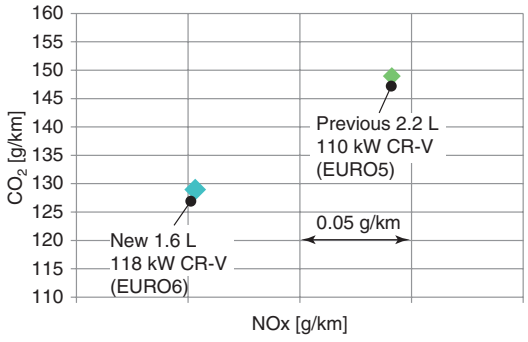


Fig. 18 Fuel consumption and engine power compared with competitors



(a) CO and THC + NOx



(b) NOx and CO_2

Fig. 19 Comparison of emissions with previous engine

4. Conclusion

A high power, EURO 6-compliant 1.6 L diesel engine with low fuel consumption was developed by using a 2-stage turbocharger, representing a first for Honda. As a result of this development, the following technical results were obtained.

(1) To achieve a high power output of 118 kW, a 2-stage turbocharger was used to gain the necessary high boost pressure. Only minimal changes were required to the engine architecture to support the increased in-cylinder pressure, keeping additional costs to a minimum.

(2) A new NSC was developed that exhibits a high conversion rate from low to high temperatures, enabling compliance with EURO 6 emissions regulations while maintaining high combustion efficiency.

(3) Boost pressure response and pumping loss were enhanced from the low-engine-speed range by applying the VGT system to the HP turbocharger of the 2-stage turbocharger. In addition, by reducing mechanical friction and enhancing combustion calibration, the new CR-V for Europe released in 2015 achieved fuel economy performance of CO_2 emissions of 129 g/km in NEDC mode, and simultaneously realized top-class fuel economy and dynamic performance.

References

(1) Abe, T., Matsui, R.: Development of New Turbocharged Common Rail Diesel Engine, JSAE Symposium Text, No. 10-04, p. 1-7, (2004)

(2) Matsui, R., Shimoyama, K., Chiba, I., Hidaka, S., Nonaka, S.: Development of High-performance Diesel Engine Compliant with Euro-V, Honda R&D Technical Review, Vol. 20, No. 1, p. 20-26

(3) Hidaka, S.: Development of a High-performance Diesel Engine Compliant with Euro 5, JSAE Forum Text, No.10 Forum-6, p. 31-41, (2010) (in Japanese)

(4) Ikegami, N., Yamano, J., Ikoma, K., Matsui, R., Mori, S., Yano, T., Murata, Y.: Development of New 1.6L Diesel Engine, JSAE Symposium Text, No. 10-12, p. 24-30 (2013) (in Japanese)

(5) Murata, Y., Tajiri, K., Sasaki, Y., Fukushima, H., Tsuda, M., Ueno, T., Koide, S.: Development of New 2.2L Fuel-Efficient Diesel Engine, JSAE Symposium Text, No. 15-11, p. 1-11 (2012) (in Japanese)

(6) Murata, Y., Tajiri, K., Sasaki, Y., Fukushima, H., Ueno, T., Koide, S.: Development of the New 2.2l Fuel-Efficient Diesel Engine for Honda CIVIC, 21st Aachen Colloquium Automobile and Engine

Technology, (2012)
(7) Shuto, Y., Tachikawa, T., Emori, H., Ogino, K., Mori, S.: Development of New Generation 1.6L Diesel Engine (First Report), JSAE Annual Congress Proceedings, No. 63-13, p. 1-4 (2013) (in Japanese)
(8) Kabashima, T., Takasawa, S., Yoshida, Y., Matsui, K.: Development of New generation 1.6L Diesel Engine (Second Report), JSAE Annual Congress Proceedings, No. 6-13, p. 5-8 (2013) (in Japanese)
(9) Nishio, Y., Hasegawa, M., Tsutsumi, K., Goto, J., Iizuka N.: Development of New generation 1.6L Diesel Engine (Third Report), JSAE Annual Congress Proceedings, No. 5-13, p. 7-12 (2013) (in Japanese)
(10) Hoshino, S., Katsumata, K., Fukushima, H., Noto, T., Yasuda, J.: Development of New Generation 1.6L Diesel Engine (Fourth Report), JSAE Annual Congress Proceedings, No. 64-13, p.5-8 (2013) (in Japanese)
(11) Ishihara, Y., Murakami, O., Tabuchi, T., Sasaki, Y., Hatano, J., Fukushima, H., Aoyagi, S., Matsuo, Y.: Development of High Power and Low Emission 1.6L Diesel Engine, JSAE Annual Congress Proceedings, No. 131-14, p. 7-10 (2014) (in Japanese)
(12) Nishimori, K., Hatano, J., Ueda, K., Murakami, O., Imai, T., Fukushima, H., Matsuo, Y.: Development of 1.6L diesel engine with two stage turbocharger achieving Euro6 emission regulation, JSAE Symposium Text, No. 15-14, p. 52-57 (2015) (in Japanese)
(13) Matsuura, H., Ishihara, Y., Murakami, O., Tabuchi, T., Sasaki, Y., Hatano, J., Fukushima, H., Aoyagi, S., Matsuo, Y.: New Generation 1.6l Diesel Engine for the Honda CR-V, 36th International Vienna Motor Symposium, (2015)

Author


Junichi HATANO


Ken NISHIMORI


Hiroyuki FUKUSHIMA


Taro TABUCHI


Naoto KITAYAMA


Yoshinori ISHIHARA

Emission Reduction Technology Using Secondary Air for Generator Engine

Ryo SAITO* Takanori SATO*
Sayaka YASOSHINA* Yusuke NINOMIYA*

ABSTRACT

An emission reduction system that uses secondary air injection and a catalyst was developed to meet emission standards for domestic gasoline engine generators enacted by India in 2014.

Gasoline engine generators require a compact size and high portability, so there are many restrictions on the exhaust system layout, and it has been a challenge to realize secondary air injection using the exhaust pulsation effect.

This development discovered the proper exhaust pipe and secondary air pipe lengths that increase the pulsation effect of the secondary air pipe, and realized a compact system that complies with both emission and generator noise standards and fits within the mass-production generator chassis.

In addition, regarding emission measurement methods, the raw gas measurement method and dilute gas measurement method were compared and verified, and a measurement method that does not influence the secondary air quantity was found.

1. Introduction

Environmental issues such as air pollution are increasing in severity around the world, and emission standards even for general-purpose engines are becoming stricter every year.

Gasoline engine generators are used for a wide range of applications such as leisure, commercial, household, and emergency use. Generators in India in particular are used as emergency power sources due to the country's power situation with frequent power outages.

Typical use cases often involve operation near houses and shops (Fig. 1), and when a power outage occurs in an urban area, households and shops start their generators all at once, so emissions and noise are becoming social issues. For this reason, both emissions and noise are strictly regulated for generators sold in India.



Fig. 1 Example of generator usage in India

This paper introduces the technology of an emission reduction system that uses secondary air injection and a catalyst, which was installed in generators to meet emission standards that were strengthened in 2014, and the method used to verify this system.

2. Development Goals and Target Values

2.1. Emission Standard Values

Emission standards for gasoline engine generators are being led by the Small Off-Road Engines (SORE) regulations established by the Air Resources Board (ARB) of the State of California, U.S.A. and by Indian emission standards for generator sets on petrol and kerosene[(1)] established by the Indian Ministry of Environment and Forests. The emission standards enforced by India in 2014 are currently the strictest known to date, and mandate a carbon monoxide (CO) level 1/2 or less than that of the ARB regulation, and an HC+NOx level 1/6 that of the ARB regulation for the displacement class of 99 cm^3 or less (Figs. 2 and 3).

Next, Figs. 4 and 5 show the CO and HC+NOx emission levels of conventional mass-production generators relative to Indian emission standard values.

* Power Products R&D Center

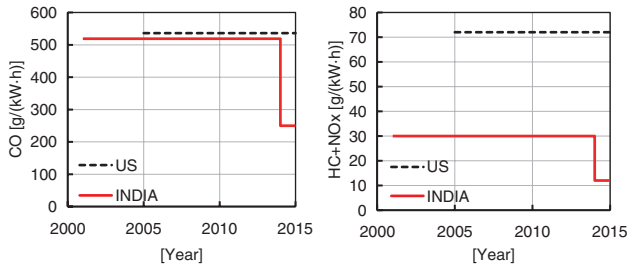


Fig. 2 Emission standard values for displacement of 50 to 80 cm^3 in CARB and up to 99 cm^3 in India

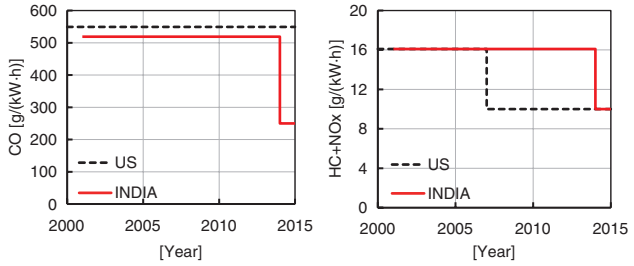


Fig. 3 Emission standard values for displacement of 80 to 225 cm^3 in CARB and 99 to 225 cm^3 in India

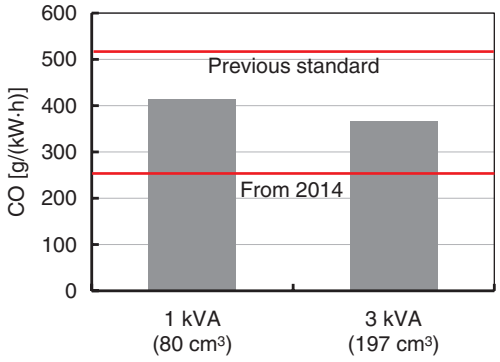


Fig. 4 CO values of conventional models

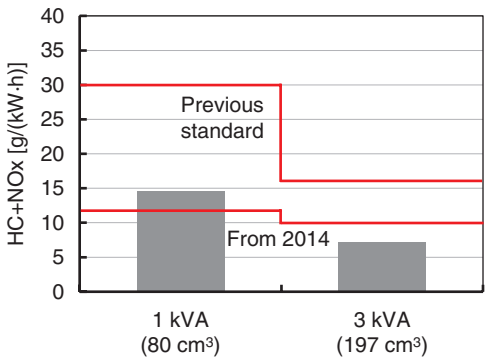


Fig. 5 HC+NOx values of conventional models

Table 1 Indian emission standards for generator sets on petrol and kerosene

Emission class	Displacement [cm^3]	CO [g/(kW·h)]	HC+NOx [g/(kW·h)]
1	≤ 99	≤ 250	≤ 12
2	> 99 ≤ 225	≤ 250	≤ 10
3	> 225	≤ 250	≤ 8

Table 2 Test cycle for emission testing

Mode no.	1	2	3
Load percent	100	75	50
Weighting factor	0.3	0.5	0.2

Table 3 Indian noise standard for generators

Output	3/4 of rated power
Sound power level (L_{WA}) [dB]	86

Table 4 Specifications of each model

Generator output class		1 kVA	2 kVA	3 kVA
Model name		EP1000	EX2400	EU30i
Engine displacement	cm^3	80	163	197
Fuel system		Carburetor	Carburetor	Carburetor
Air fuel ratio (Average)		12.5	12.6	12.4
Max AC output	VA	850	2100	3000
Dimensions (L × W × H)	mm	404 × 352 × 431	965 × 470 × 327	710 × 422 × 570
Emission class		1	2	2
Sound power level 3/4 load (L_{WA})	dB	85	85	85

2.2. Development Goals

The goals of this development were to achieve the following three items for the 1-, 2- and 3-kVA class gasoline engine generators sold for use in India.

(1) Compliance with emission standards (Tables 1 and 2)
(2) Compliance with the noise standard for generators (Table 3)
(3) A layout that fits within the current mass-production chassis

Table 4 lists the specifications of the applicable gasoline engine generators.

3. Investigation of Methods for Meeting Standards

Fuel is supplied to gasoline engine generators using an inexpensive carburetor with a simple structure. The ratio of the air-fuel mixture supplied to the engine during operation is around 12.5, and while this met the old emission standards, it is unable to comply with the new standards. The two methods considered here for reducing the CO emission level are as follows.

(1) Adjustment of the air-fuel mixture to the stoichiometric air-fuel ratio
(2) CO reduction by adding secondary air injection to the exhaust pipe and a catalyst

When the carburetor in a gasoline engine generator is used to adjust to the stoichiometric air-fuel ratio, combustion becomes unstable and engine speed stability and load fluctuation tracking performance drop, resulting in issues such as increased frequency fluctuation range. For this reason, it is a challenge to apply adjustment of the air-fuel mixture to the stoichiometric air-fuel ratio as a CO reduction technology for gasoline engine generators. A secondary air injection system was therefore adopted that uses the pulsation effect of the exhaust pipe, and a catalyst was built into the muffler to increase the oxidation effect.

4. Achieved Technology

4.1. Secondary Air Injection System

4.1.1. Secondary air quantity requirement values

The secondary air quantity requirement values were set based on the air quantity that satisfies the emission standard values, noise standard values and catalyst temperature. Figure 6 shows the CO emission level, HC+NOx emission level, catalyst temperature, and noise value characteristics relative to the 1-kVA and 3-kVA class secondary air quantities as an example of the settings.

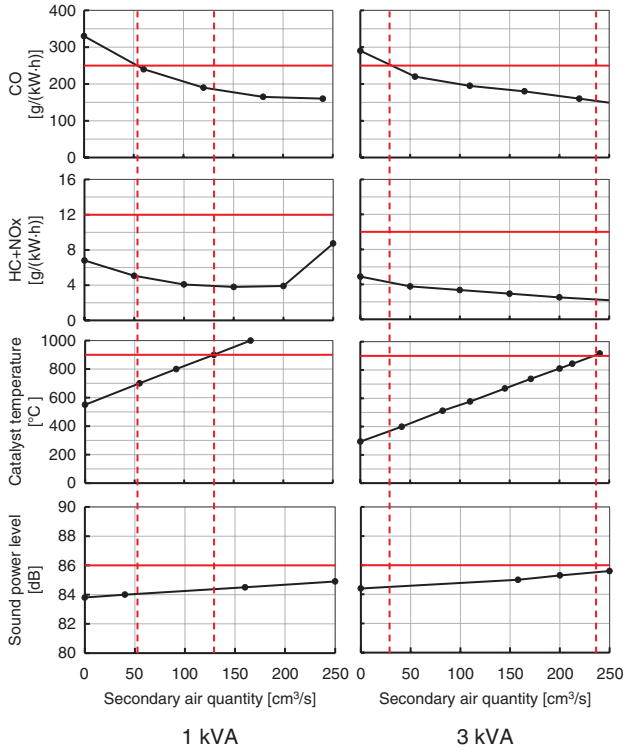


Fig. 6 Relationship between secondary air quantity and performances

The secondary air quantity requirement values were set as follows based on the characteristics shown in Fig. 6.

1 kVA: 55 to 130 cm^3/s

3 kVA: 30 to 230 cm^3/s

Examples of development for the 1 kVA and 3 kVA models are described below.

4.1.2. Optimization of the exhaust pipe and secondary air pipe

Secondary air injection used a system that makes use of the negative pressure component of the exhaust pipe to take in outside air using a reed valve in the same manner as a motorcycle engine. Motorcycle engines have a long pipe length from the exhaust valve to the exhaust pipe outlet (exhaust pipe length), which makes it easy to obtain the negative pressure component of the exhaust pipe pressure. In contrast, gasoline engine generators require compactness, so the exhaust pipe length is as short as possible. This makes it a challenge to obtain a negative pressure component inside the exhaust pipe, which is a structural issue for secondary air injection. Figure 7 compares the exhaust system layouts of a motorcycle and a generator. The exhaust pressure pulsation of a gasoline engine generator with a lengthened exhaust pipe was measured, and the results confirmed an increase in the amplitude of the negative pressure component (Fig. 8).

However, this development had the constraint of a layout that fits within the current mass-production chassis, so the issue was to secure the required secondary air quantity by some element other than the exhaust pipe length.

Therefore, design calculations were performed for the exhaust pipe and secondary air pipe that determine the secondary air quantity, and the pulsation effect of the

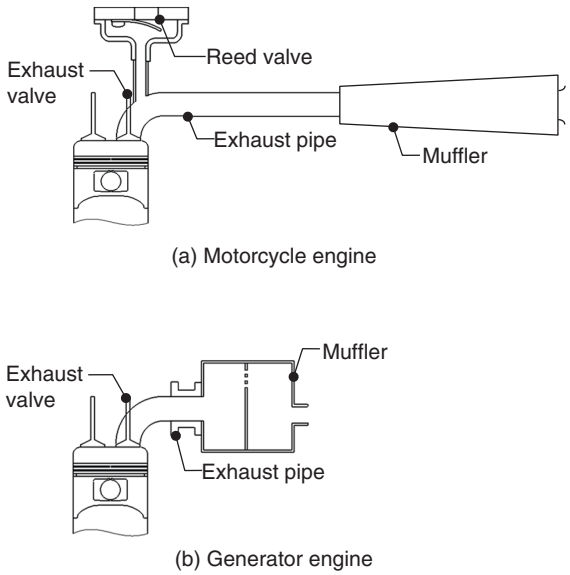


Fig. 7 Comparison of exhaust layouts

secondary air pipe was used to amplify the negative pressure component of the exhaust pipe inside the secondary air pipe[2].

Figure 9 shows a schematic of an emission reduction system using secondary air injection and a catalyst.

Figures 10 and 11 show the air quantity characteristics relative to the secondary air pipe length for the 3 kVA and 1 kVA models, respectively.

Table 5 Exhaust system length

Length [mm]	1 kVA		3 kVA
	Current	Developed	Developed
Exhaust passage	550	750	1050
Secondary air pipe	900 or more	400	850

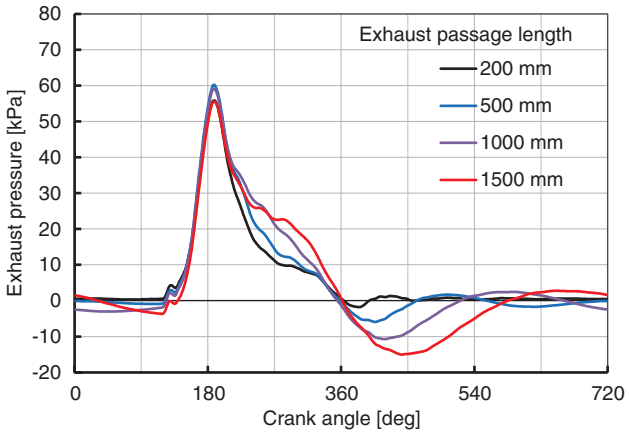


Fig. 8 Relationship between length of exhaust passage and pressure at rated load

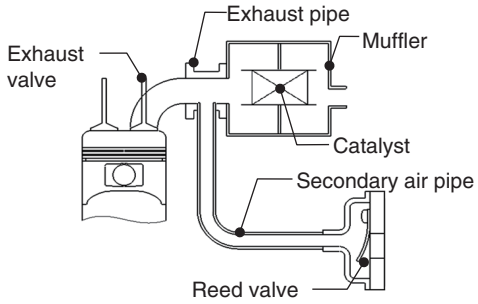


Fig. 9 Secondary air system

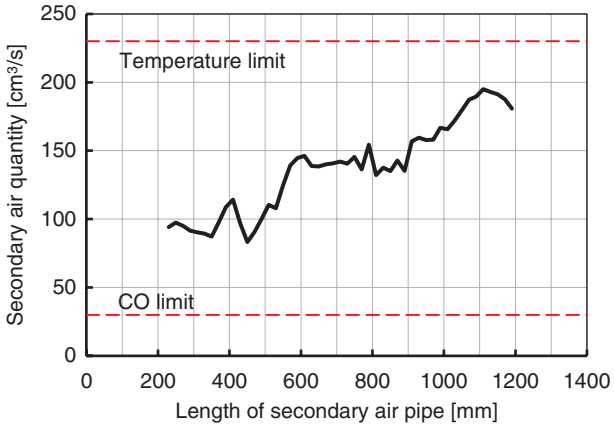


Fig. 10 Relationship between length of secondary air pipe and secondary air quantity at rated load (3 kVA)

As shown in Fig. 10, the 3 kVA model has a secondary air pipe length range that satisfies the required air quantity, so a length of 850 mm was selected based on the constraint of fitting within the chassis. In contrast, given the exhaust pipe length of the current mass-production muffler, the 1 kVA model requires a secondary air pipe length of 900 mm or more to satisfy the required air quantity (Fig. 11), so a layout that fits within the chassis is not feasible. The exhaust pipe was therefore lengthened by 200 mm and a secondary air pipe length was set to 400 mm in order to satisfy the required air quantity and fit the exhaust pipe and secondary air pipe within the chassis (Table 5).

4.2. Catalyst

The catalyst used to convert the HC and CO in exhaust gas is the same catalyst with a metal honeycomb carrier widely used in motorcycles. Therefore, in consideration of the following points, the catalyst was positioned inside the muffler.

(1) The catalyst temperature is the catalyst activation temperature or more, but lower than the temperature leading to degradation.

(2) The structure passes all of the engine exhaust gas and secondary air through the catalyst to prevent a drop in the reduction rate.

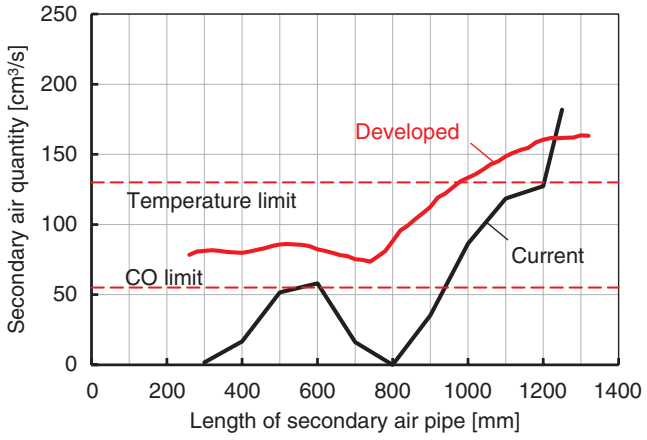


Fig. 11 Relationship between length of secondary air pipe and secondary air quantity at rated load (1 kVA)

Figure 12 shows a schematic of the muffler based on the above considerations.

4.3. Packaging

Figures 13 and 14 show the 1-kVA class and 3-kVA class systems that achieved the required secondary air quantity target values with layouts that allowed fitting within the exterior dimensions. Compared to the mass-production model, the 1 kVA model has a longer exhaust pipe and adds a secondary air pipe. This is achieved by bending the exhaust pipe and secondary air pipe into "U" shapes that cross over and under each other, and realized a compact layout that fits within the current mass-production chassis.

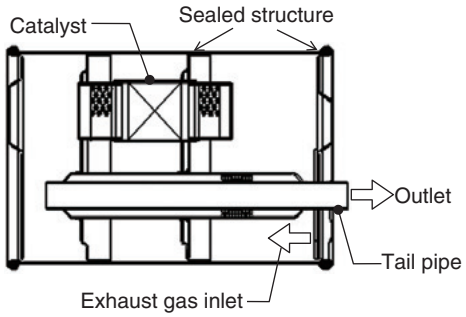
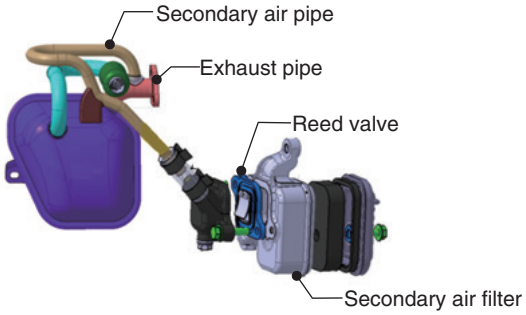


Fig. 12 Schematic of muffler



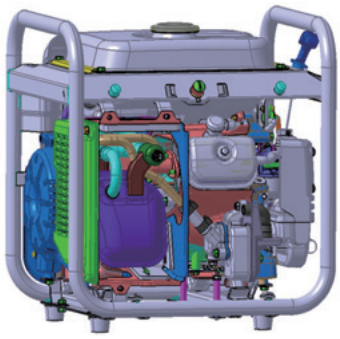
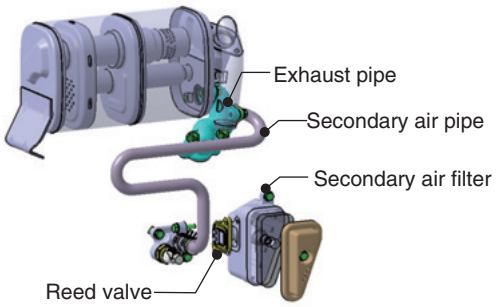


Fig. 13 1 kVA (EP1000)



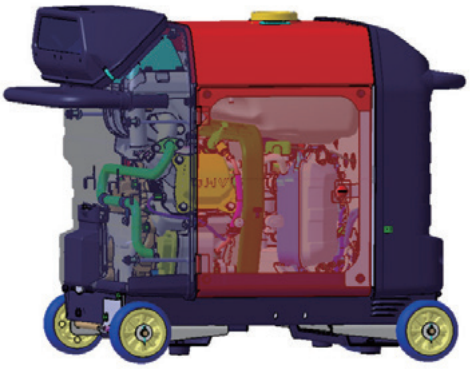


Fig. 14 3 kVA (EU30i)

5. Verification Method

5.1. Emission Quantity Measurement Methods

There are two major exhaust emission measurements[3].

(1) Raw gas measurement method

(2) Dilute gas measurement method

Both measurement methods were verified during the course of this development, and the results showed that in a secondary air injection system that uses exhaust pulsation, the raw gas measurement method and dilute gas measurement method give different secondary air quantity values. Figure 15 shows the difference in the air quantity measurement values for both methods.

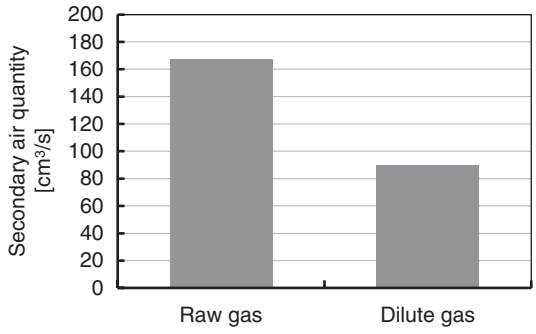


Fig. 15 Comparison of raw gas sampling and dilute gas sampling (1 kVA)

Figures 16 and 17 show schematics of the measurement environment for both methods, and Fig. 18 shows the difference in the exhaust emission measurement values. The raw gas measurement method requires that the exhaust pipe be lengthened, which has the effect of increasing the secondary air quantity as described above, making it unsuitable for measuring the true value. Therefore, the dilute gas measurement method was used.

The regulatory authorities were lobbied based on these verification results, and the dilute gas measurement method, which was previously not accepted, was formally added to the applicable laws and regulations.

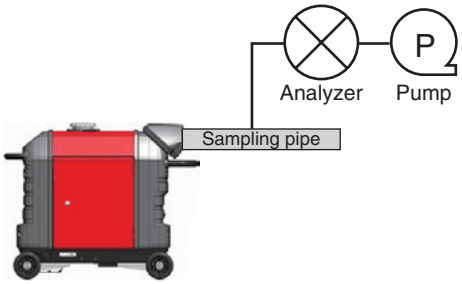


Fig. 16 Raw gas emission analysis method

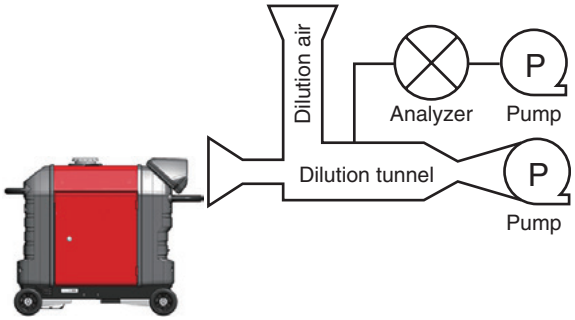


Fig. 17 Dilute gas emission analysis method

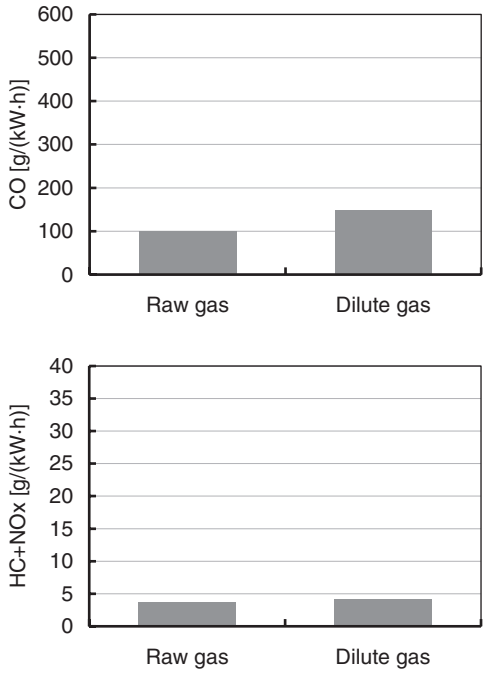


Fig. 18 Comparison of raw gas sampling and dilute gas sampling (1 kVA)

6. Achieved Values

6.1. Achieved Emission and Noise Values

The 1 kVA, 2 kVA and 3 kVA models all cleared both the emission and noise standards for gasoline engine generators used in India. Figure 19 shows the achieved emission values.

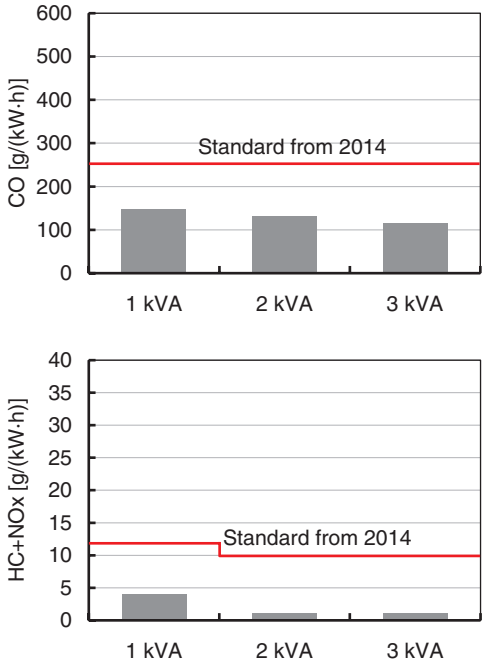


Fig. 19 Emission results of new models

7. Conclusion

An emission reduction system for generator engines was created using secondary air injection and a muffler with built-in catalyst, which is a first for Honda Power Products. This system achieved the following results.

(1) The developed system complied with Indian emission standards and generator noise standards, even for generator engines with different displacements.

(2) Honda Power Products' original optimization of the secondary air pipe and exhaust pipe enabled creation of a compact layout that fits within the mass-production chassis.

(3) The influence of the exhaust pipe length on the secondary air quantity in this system was clarified, permitting establishment of an accurate exhaust emission measurement method.

References

(1) Indian emission standards for generator sets on petrol and kerosene
(2) Yasoshina, S., Saito, R.: Pulsed Secondary Air Injection System for Emission Reduction in Small Generator Sets, SAE Technical Paper, 2014-32-0035, (2014)
(3) ISO 8178-1:2006 2nd edition: Exhaust emission measurement

Author


Ryo SAITO


Takanori SATO


Sayaka YASOSHINA


Yusuke NINOMIYA

Development of Transmission-mounted Transmission Control Unit

Kazuki YAHATA* Koichi KONISHI*
Genta INOUE* Takeharu MOTEKI*

ABSTRACT

A transmission control unit able to be directly mounted on the transmission has been developed for applications ranging from small to medium-sized vehicles.

Direct mounting of the unit has reduced the distance between the transmission and the control device, making it possible to reduce the length of the harnesses. In addition, hierarchical design of the control software and sharing of the solenoid driver have made it possible to apply the unit to the control of a variety of transmissions.

Vehicle tests and simulations were conducted in order to obtain a detailed understanding of the temperature of the electronic components inside the unit under the conditions it would be exposed to when direct-mounted and implement appropriate responses. As a result, the maximum operating temperature of the unit was increased against conventional body-mounting conditions. The rigidity of the mounting bracket and the connector terminals was also increased, increasing the maximum allowable vibration frequency to 2000 Hz. These measures made it possible to apply the unit to a wide variety of vehicle types, from small to medium-sized.

1. Introduction

The realization of increased fuel efficiency is an important issue from the perspective of reducing the burden automobiles place on the global environment. In the engine, the use of direct injection technologies and electronic devices, and in the transmission, the use of multi-stage and DCT technologies, are widely used methods of achieving this goal. As a result, the combinations of engines and transmissions are diversifying. Conventionally, the range of these combinations has been limited. Because of this, it was possible to reduce shared casing parts and electronic components by controlling the engine and the transmission using a single control unit (Fig. 1). However, today's diversification of the combinations of engines and transmissions means that the same number of integrated control units as the number of combinations is necessary (Fig. 2).

It was therefore considered that it would be possible to reduce the number of necessary types of control units by separating the control units for the engine and the transmission[(1)] (Fig. 3).

In addition, it would also be possible to share control units between different transmissions by examining transmission control specifications and clarifying which sections general-purpose specifications could be employed

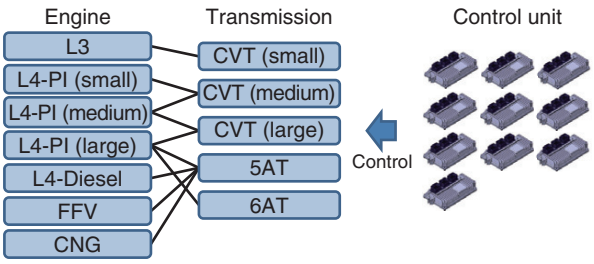


Fig. 1 Former integrated engine and transmission control unit

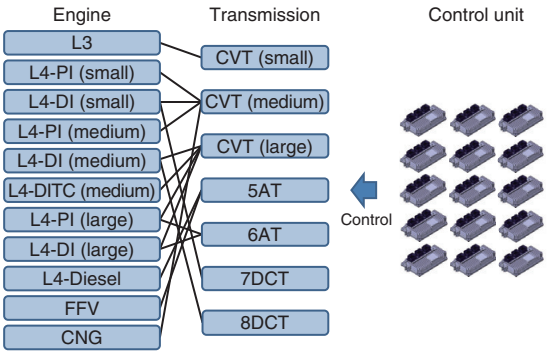


Fig. 2 Current integrated engine and transmission control units

* Automobile R&D Center

in and which sections necessitated specialized design.

Up to the present, Honda has fitted powertrain transmission control units (TCU) to the body of the vehicle, in the cabin or the engine compartment (Fig. 4). The TCU developed in the research discussed in this paper is directly mounted on the transmission. Direct mounting offers the merit of reducing the distance between the control device and the object of control, making it possible to reduce the length of the harnesses (Fig. 5).

In addition, when the TCU is fitted to the vehicle body, it is necessary to use a bracket to fix it in place on the body framework. When the same combination of engine and transmission is used but the vehicle is changed, the effect of the positioning of the battery, lights, and other surrounding parts makes it necessary to use a special TCU bracket for each vehicle. Direct mounting on the transmission would make it possible to fix the mounting position. It was predicted that this would reduce the number of types of bracket in comparison to mounting in the engine compartment.

At the same time, direct mounting of the control unit on the transmission would necessitate the use of measures to protect the electronic components and the casing and other structural parts from environmental conditions, including heat and vibration from the engine and transmission.

This paper will discuss the development of a direct-mounted TCU able to control a variety of transmissions via a single unit.

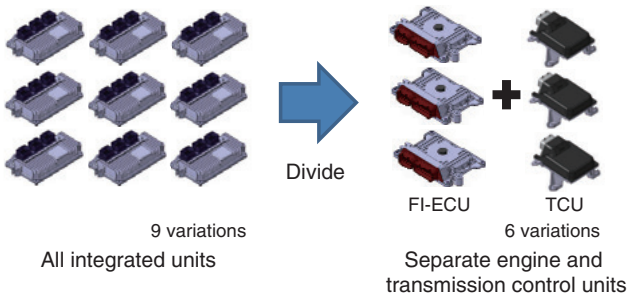


Fig. 3 Change in number of control units

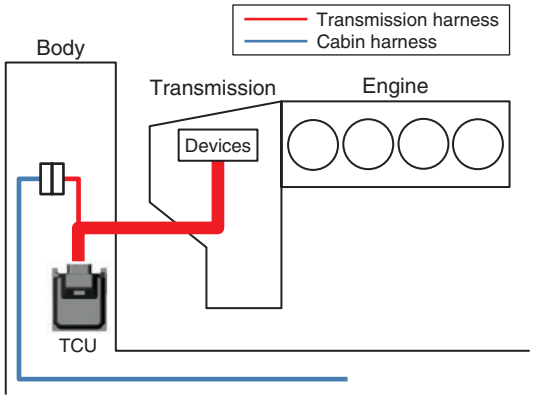


Fig. 4 Body-mounted TCU

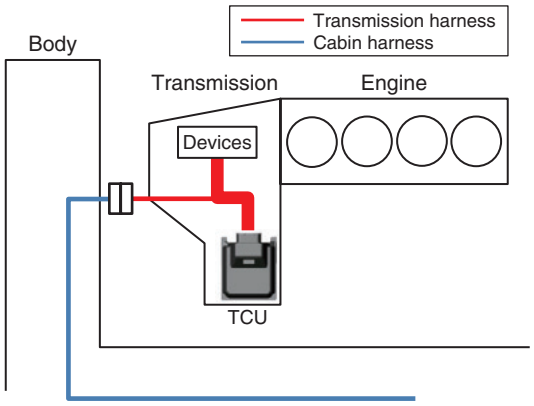


Fig. 5 Transmission-mounted TCU

2. Development Goals

Figure 6 shows the layout of the transmission-mounted TCU developed for application to a CVT for a 1.5L turbo-charged engine.

The following development goals were set for the design of the transmission-mounted TCU:

(1) General applicability, making it possible to control multiple transmission types with minimal change to parts; and

(2) Reliability of parts in relation to vibration and heat in vehicles ranging from small to medium-sized.

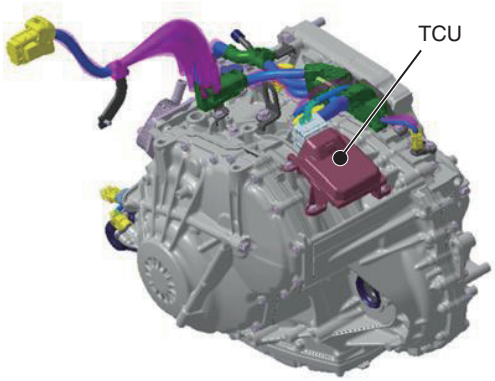


Fig. 6 Layout of transmission-mounted TCU

3. Design for General Applicability

Three types of functions are demanded of a TCU: Basic functions, including input and output and reprogramming; transmission control functions, to control the operation of the target transmission; and vehicle control functions, including meter display and cooperative operation with the engine. Conventional transmission control does not

clearly demarcate these functions, and when one function is changed, it is necessary to change the others. This means that TCU have possessed limited general applicability.

The present research, by contrast, clearly specified the domains of the TCU functions. Using a systems modeling language[2], the functions were divided into three domains based on the AUTOSAR standard: A platform (PF) domain, an application (APL) domain, and an interface (I/F) domain (Fig. 7). This increased the independence of the functions, and made it possible to use the TCU for different transmissions simply by modifying the APL domain.

Conventional TCU also use current feedback control in the driver IC to control the current of the solenoid that controls the hydraulic channels in the transmission (Fig. 8). Applying feedback control in the driver IC has the merit of reducing the number of electronic components and doing away with the need for adjustment during the manufacturing process[3]. However, because current feedback control has an effect on shift responsiveness and durability and reliability, it is necessary to modify the control settings depending on the transmission type. At the same time, the range of modification of feedback gain and other settings for a driver IC without software is limited. Because of this, up to the present it has been challenging to apply the same driver IC to different types of transmission. In the method developed in the research discussed here, the driver IC only measures current; current feedback control is conducted by a software program in a microprocessor (Fig. 9). As a result, it is possible to apply the TCU to different transmissions by modifying the program in the microprocessor.

As described above, it has been possible to develop a TCU able to control different transmissions without any change to the basic configuration of the hardware via hierarchical design of the domains of functions and the sharing of a solenoid driver.

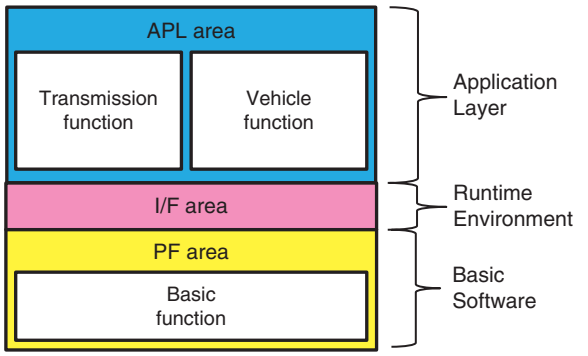


Fig. 7 Diagram of enhanced software system

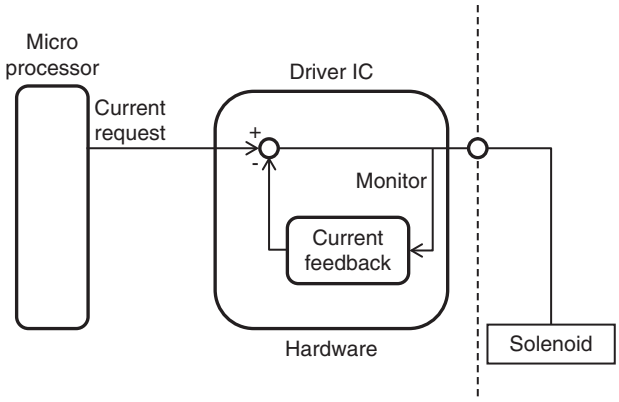


Fig. 8 Design of conventional solenoid current feedback control

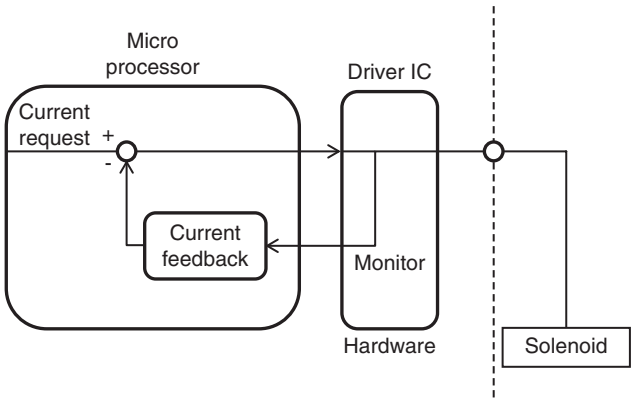


Fig. 9 Current design for solenoid current feedback control

4. Reliability of Parts in Vibration Environment

4.1. Vibration Environment

Powertrain vibration is damped by the engine mounts and transmitted to the body frame. Because of this, conventional body-mounted TCU were designed to resist the frequency domain up to 400 Hz, the frequency of second-order engine speed-related vibration.

When direct mounting of the TCU was under consideration, the vibration environment was first studied. The vibration acceleration at the mounting position of the unit against the vibration frequency of the engine was measured for 4-cylinder engines of various displacements fitted in a range of vehicle types (Fig. 10).

At close to 200 Hz and below, vibration acceleration is high, proportional to second-order engine speed-related vibration.

In the higher frequency domain, vibration acceleration peaks appear irregularly due to powertrain resonance, but in each case the vibration acceleration is less than half of second-order engine speed-related vibration. In addition, because the displacement that produces stress on the parts declines in inverse proportion to the square of frequency, input conditions for acceleration at the mounting position of the direct-mounted TCU were set based on second-order engine speed-related vibration, and the frequency band was set at 2000 Hz and below.

4.2. Vibration-resistance Measures

To help prevent damage to the electronic components fitted on the base plate, it was necessary to reduce the stress generated in each section to the allowable loading force for the component materials or below. A 3D model of the TCU assembly was therefore formulated, and a frequency response analysis was performed.

Vibration acceleration with second-order engine speed-related vibration as the base vibration was input to the TCU mounting points, and resonance frequency and response acceleration were measured in the 2000 Hz and below frequency band.

Rib shapes were added to the bracket between the transmission mounting bosses in order to increase the rigidity of the unit in response to resonance. A parameter study of the rib shapes was conducted using eigenvalue analysis in order to determine specifications realizing an optimal balance between mass and rigidity (Fig. 11).

Tapping screws were employed for the connection between the base plate and the connector casing in order to increase coupling rigidity.

In addition, the rigidity of the connector terminals themselves was increased, and their resonance frequency was set at 2000 Hz or above, outside the powertrain resonance domain.

A simulation study conducted in order to verify the effectiveness of these measures showed that the resonance frequency close to 690 Hz had increased to 740 Hz, and the overall vibration acceleration level had been reduced (Fig. 12).

4.3. Verification of Vibration-resistance Performance

Measurements of vibration acceleration in the connector section in an actual vehicle were conducted in order to compare the rate of change of acceleration in the connector section in relation to the unit mounting points before and after the application of the vibration-resistance measures (Fig. 13).

The increase in the coupling rigidity of the bracket and the connectors reduced the level of resonance at close to 700 Hz, verifying the effectiveness of the specification employed.

In addition, the results of vibration durability tests using direct-mounting input conditions showed that no issues such as dropouts of the electronic components or breakage of the connector terminals occurred, and the electrical

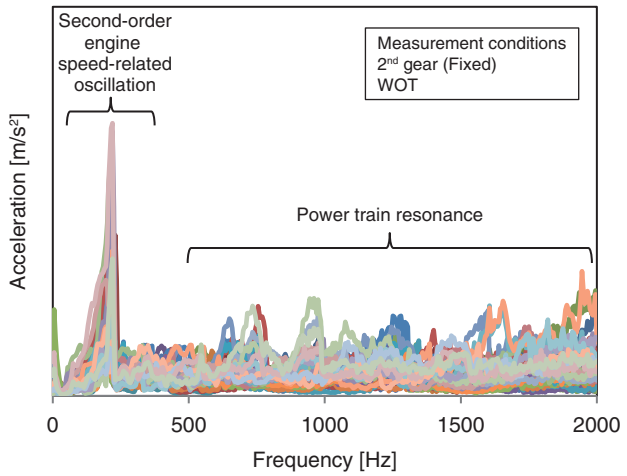


Fig. 10 Vibration acceleration at unit mounting point

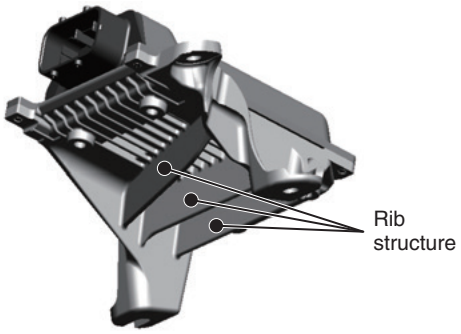


Fig. 11 Realization of enhanced unit rigidity

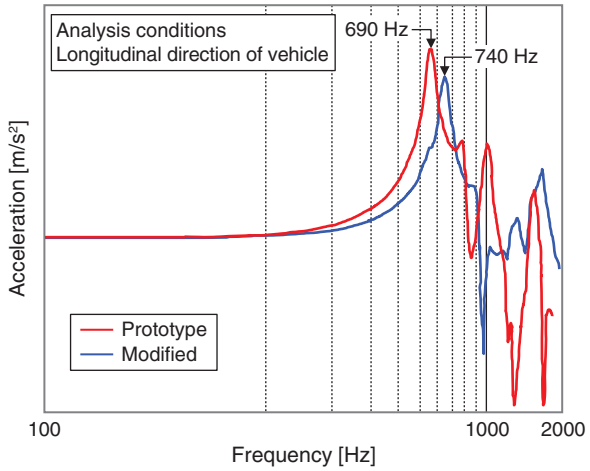


Fig. 12 Frequency response characteristic

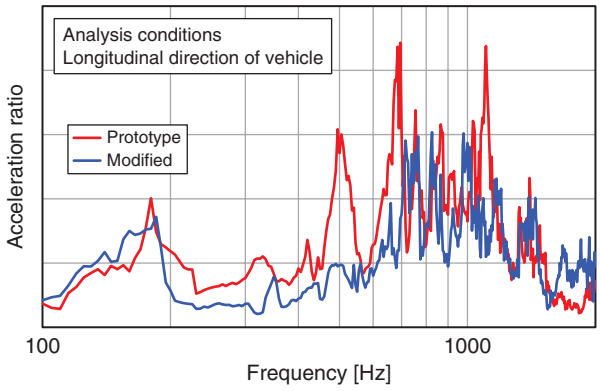


Fig. 13 Comparison of rate of change in vibration acceleration of connector in vehicle

characteristics following the test satisfied the performance demands from the unit.

5. Component Reliability in Heat Environment

5.1. Temperature Environment

The temperature of the engine compartment reaches its maximum point following the elapse of a fixed period of time after the vehicle has been stopped. The transmission case, on which the TCU is mounted, receives heat from the transmission fluid during high-load operation, and its temperature is at its maximum immediately after the vehicle is stopped. Self-heating due to power loss resulting from the driving of the actuator by the solenoid and other parts is also a factor in increasing the temperature of the TCU.

In the case of conventional positioning of the TCU in the engine compartment, the unit's design only took into consideration the temperature within the engine compartment. With the direct mounting of the unit, however, it was necessary to consider multiple factors in temperature increase, including the effect of heat received from the transmission case and the increase in temperature due to the self-heating of the TCU.

Factors involved in increasing the unit's temperature were divided into external factors including the temperature of the external environment and the wind produced during vehicle operation, and internal factors due to power loss in the TCU. The conditions to which the unit would be exposed were designed as follows. The most severe conditions were applied, based on the assumption of the fitting of the unit in vehicle sizes ranging from small to medium.

(1) Driving mode in which internal temperature of engine compartment reaches its maximum
(2) Driving mode in which temperature of transmission case reaches its maximum
(3) No wind during vehicle operation
(4) Driving mode in which solenoid current consumption reaches its maximum

A heat simulation of the temperature distribution in the engine compartment during soak following hill-climbing mode was conducted (Fig. 14). The area of the engine compartment in which the temperature was highest was close to the exhaust system, an area that is affected by radiant heat.

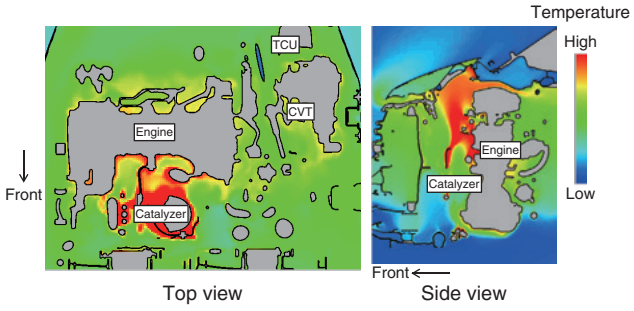


Fig. 14 Results of heat simulation

Based on these results, the highest allowable temperature for the transmission-mounted TCU was set 10% higher than had previously been the case for mounting in the engine compartment (Fig. 15).

5.2. Temperature-resistance Measures

Heat simulations were conducted in order to determine the heat produced by each of the electronic components in the different driving modes. Taking the effect of heat received from the transmission case into consideration, the simulations incorporated a transmission case model rather than using a TCU model in isolation. In addition, to help prevent the concentration of power in specific electronic components, a dispersed design was adopted in which functions were divided across multiple electronic components, and the power to each component was reduced. For example, the number of FET, a heat-producing component, was increased from four to six, and the power per element was reduced. The heat-producing components were also clustered on the heat dispersion side of the base plate, producing a configuration that promoted heat dispersion. As a result, the temperature of all the components remained below the maximum allowable temperature (Fig. 16).

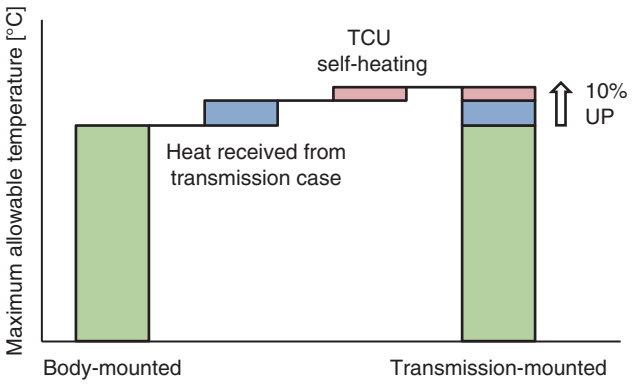


Fig. 15 Maximum allowable temperature

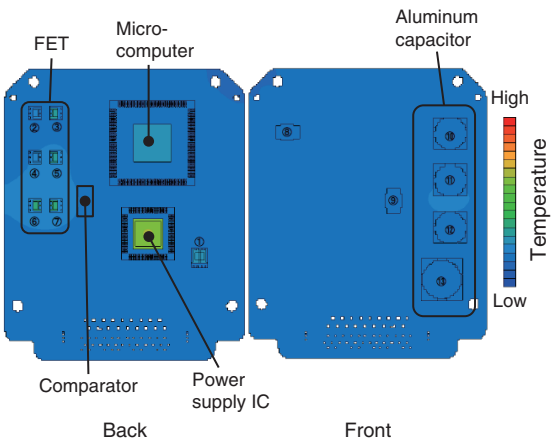


Fig. 16 Temperature distribution

5.3. Verification of Heat-resistance Performance

Tests were conducted in order to measure temperatures in an actual vehicle in different driving modes, including the driving modes in which the temperatures of the engine compartment and the transmission case reach their maximum. The results showed that the maximum temperatures of the electronic components remained below the maximum allowable temperature in all the driving modes (Fig. 17).

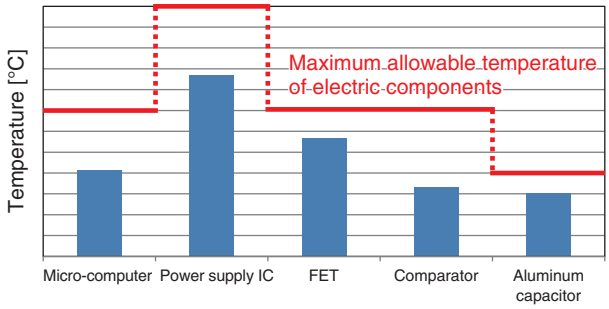


Fig. 17 Heat generation

6. Conclusion

During the process of development of a transmission-mounted transmission control unit, the couplings were reinforced in order to respond to issues due to the vibration environment, and the control software was hierarchically designed to help ensure a generally applicable design. The following results were obtained.

(1) Hierarchical design of the domains of functions and optimization of the role of the solenoid driver IC has made it possible for the unit to control a range of transmissions.

(2) The realization of increased rigidity in the mounting bracket and connector terminals and dispersed design of the electronic components has helped to ensure the reliability of the electronic components in use environments (heat and vibration) of vehicles ranging from small to medium-sized.

References

(1) Murakami, M., Yamanaka, T., Kaitani, Y.: Development of Highly Functional ECU for Next Generation of Inline-four Engines, Honda R&D Technical Review, Vol. 26, No. 1, p. 18-22

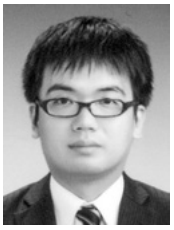
(2) Araki, H., Saito, K., Ohguchi, R., Funakoshi, M., Yamamoto, K.: Model-Based Development Technologies to Support Increasingly Complex Power Train Systems, Honda R&D Technical Review, Vol. 26, No. 2, p. 107-116

(3) Sakai, T., Okahara, A., Yamakawa, Y., Fujimoto, M.: Development of Linear Solenoid Driver IC, FUJITSU TEN TECH. J., No. 12, p. 21-29 (1999)

■ Author ■


Kazuki YAHATA


Koichi KONISHI


Genta INOUE


Takeharu MOTEKI

Development of New H_2 Refueling Method for FCV to Reduce Refueling Time

Kiyoshi HANDA* Steve MATHISON **

ABSTRACT

A new refueling method was developed to shorten the hydrogen refueling time of FCV. The conventional method determined the pressure ramp rate according to the ambient temperature, and the temperature to which the supplied hydrogen is precooled to prevent overheating when refueling did not influence the pressure ramp rate. The new method added real-time control of the pressure ramp rate according to the precooled hydrogen temperature. Consideration was also given to compatibility, so the only changes to the hydrogen refueling station side were the addition of a temperature sensor and software changes, and no changes to the control and hardware on the vehicle side are needed. Under the conditions above, vehicle tests were performed with the cooperation of General Motors and Mercedes-Benz, with the result that the new refueling method enabled shortening of the refueling time in the summer by 30% or more compared to the conventional method and without lowering the precooled hydrogen temperature. This enables refueling in less than four minutes in most cases year-round in the Los Angeles district, United States. In addition, a State of Charge equivalent to that of the conventional method was also secured.

1. Introduction

The fuel used as the power source for automobiles began with coal and has gone through changes to petroleum, natural gas and hydrogen. This is the history of carbon reduction, and at the same time is also the history toward smaller molecules. Having reached the smallest molecule, hydrogen, automobiles have now achieved carbon-free driving.

On the other hand, a higher storage pressure is required compared to conventional fuel. As a result of seeking a driving range equivalent to that of a gasoline vehicle, the vessel pressure of fuel cell vehicles (FCV) has reached 70 MPa. SAE has taken a leading role in establishing standards to help achieve the safe refueling of this high-pressure hydrogen. An issue unique to hydrogen refueling is heat generation inside the vessel of the vehicle. The refueling system basically consists of four heat transfer systems connected in series (Fig. 1). The hydrogen is cooled (precooled) to approximately -40°C (I) to prevent it from overheating inside the vessel of the vehicle. The temperature of the cooled hydrogen is increased by the heat mass of the breakaway, hose, nozzle and other station parts (II) and the heat mass of the vehicle tube (III). When the hydrogen enters the vessel, it is compressed, which generates heat (IV). That final temperature needs to be 85°C or less in accordance with requirements such as the ANSI standard[1].

When the ambient temperature (T_{amb}) is high, the refueling time is lengthened to promote the diffusion of heat to the vessel body. The pressure ramp rates at which overheating does not occur are obtained from hundreds of simulation times, and these results are compiled into a data table and stored in the hydrogen refueling station control unit. Refueling is performed while referencing this table, so this is called the look-up table (L/T) refueling method.

The actual control first measures the ambient temperature, and then reads the pressure ramp rate from the table and controls the flow control valve to maintain a fixed pressure ramp rate during refueling. Assuming the SAE standard conditions (ambient temperature T_{amb} 20°C, initial pressure P_0 10 MPa), refueling completes in approximately 3 1/2 minutes (the black circle in Fig. 2).

High ambient temperatures are an issue for the L/T refueling method. The maximum temperatures were analyzed for the Los Angeles (LA) district, U.S. which is one of the main markets, and the results showed that the temperature with a cumulative frequency of 98% was 35°C. The refueling time at 35°C requires up to five minutes or more, which is thought to be an issue for customer

* Automobile R&D Center

** HONDA R&D AMERICAS, INC.

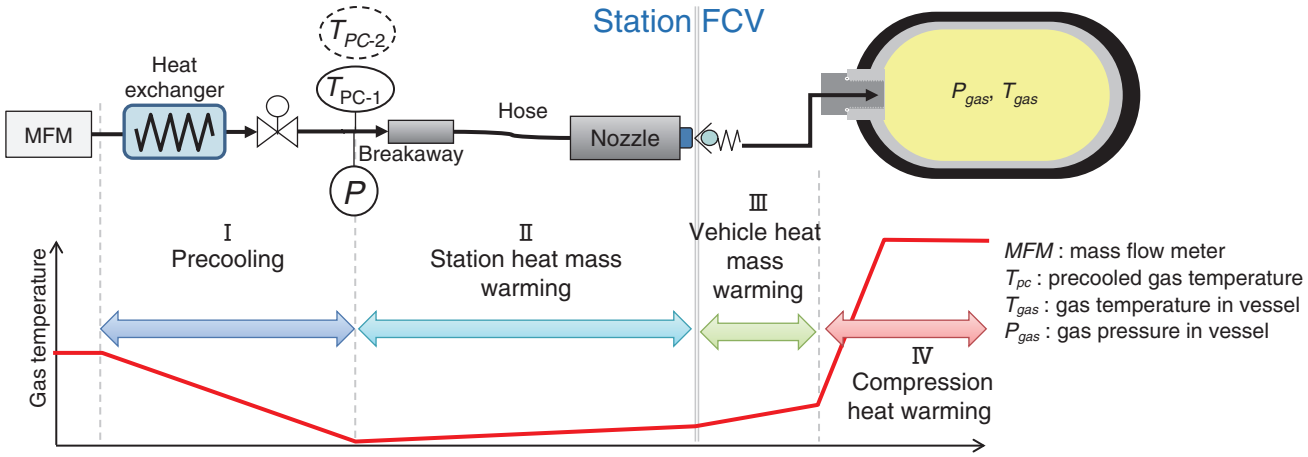


Fig. 1 Overall refueling system

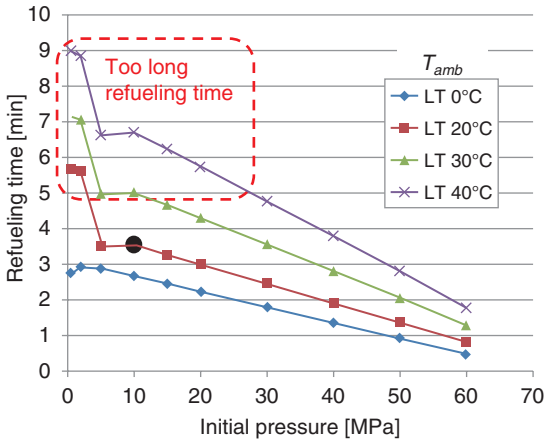


Fig. 2 Effect of ambient temperature

satisfaction. Therefore, Honda has conducted original research on hydrogen refueling technology[2), 3)]. The newly developed refueling method was named the MC-Formula refueling method. Here, M comes from the Mass inside the vessel, C comes from the heat Capacity of the vessel, and Formula comes from the fact that the pressure ramp rate is calculated in real time using a numerical formula. This paper introduces this MC-Formula refueling method.

2. Development Goals

The new refueling method was developed with the following goals.

(1) Refueling is completed in less than 4 minutes even during the summer in the LA district.
(2) The approach toward safety is carried over unchanged from the L/T refueling method.
(3) The FCV system is not changed.
(4) The hydrogen refueling station hardware is changed as little as possible. Changes to the software are limited to version upgrades with downward compatibility.

The L/T refueling method constantly maintains a fixed pressure ramp rate. This pressure ramp rate is set for the case when the precooled hydrogen temperature is -33°C, which is the upper limit of the specified tolerance, but the actual temperature is lower than this tolerance upper limit (Fig. 3). This means that the refueling time is the same even when the actual temperature is lower than -33°C.

However, when the precooled hydrogen temperature is lower, it should be possible to perform refueling faster in accordance with the lower temperature inside the vessel (Fig. 4).

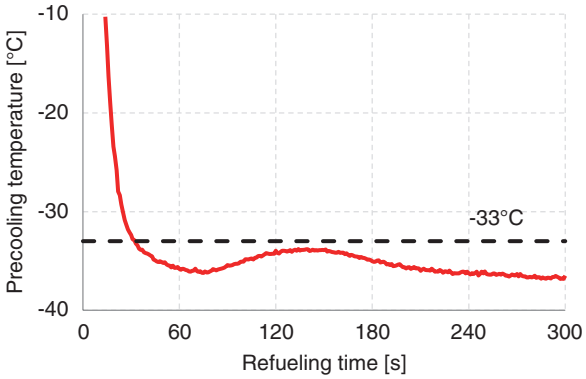


Fig. 3 Example of precooling temperature

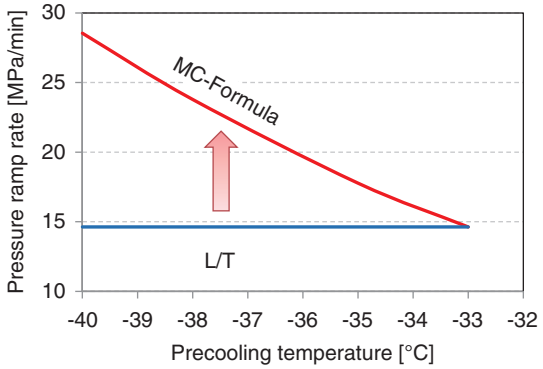


Fig. 4 Effect of precooling temperature

It is thought that if the pressure ramp rate could be determined in real time in accordance with the actual precooled hydrogen temperature, refueling could be performed more quickly even at the same precooled hydrogen temperature.

3. System Configuration

A method that calculates the pressure ramp rate in real time from the measured precooled hydrogen temperature was created for the control software.

3.1. Mass Average Processing of the Precooled Hydrogen Temperature

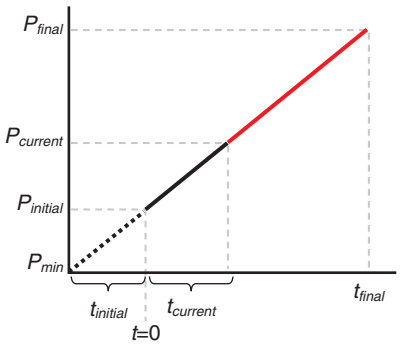
The pressure ramp rate is determined based on the precooled hydrogen temperature sensor value (T_{PC}) in Fig. 1. Equation (1) was used to perform mass average processing on the precooled hydrogen temperature using the mass flow rate sensor value m. Here, i is the control time step.

$$MATC_{(i)} = \frac{\sum_1^i [(m_{(i)} - m_{(i-1)}) \times 0.5(T_{PC(i)} + T_{PC(i-1)})]}{\sum_1^i (m_{(i)} - m_{(i-1)})} \quad (1)$$

3.2. Introduction of a Refueling Time Parameter

The refueling time t_{final} was made into a parameter in order to add precooled hydrogen temperature feedback control (Fig. 5).

t_{final} is the refueling time after refueling starts from the specified initial pressure (P_{min} 0.5 or 5 MPa) until refueling ends at the specified end pressure (83.5 MPa). For example, when refueling is started from the initial pressure $P_{initial}$ of the vehicle's vessel, this is viewed as starting from partway through refueling that started from P_{min}. When the initial pressure $P_{initial}$ of the vehicle is higher than P_{min}, the amount of heat generated inside the vessel decreases. Therefore, only the P_{min} case, which has the greatest amount of heat generation, needs to be considered.



t_{final} : time required to refuel from P_{min} to P_{final}
$t_{current}$: time measured since refueling began
$t_{initial}$: imaginal time before refueling began
P_{final} : maximum allowed dispenser pressure
$P_{current}$: current dispenser pressure
$P_{initial}$: initial pressure when refueling began
P_{min} : minimum allowed starting pressure

Fig. 5 Pressure ramp rate control methodology

Two different P_{min} were prepared to shorten the practical refueling time. The case when $P_{initial}$ is 5 MPa or less is the rare case immediately before running out of fuel. In this case, the compression ratio and the amount of heat generation increase, so the refueling time becomes quite long. If this case is used as the premise for control, the refueling time would become longer even for other, more typical cases in order to support a few rare cases. For this reason, the case with 5 MPa or less is handled separately in the control.

3.3. Calculation of the Pressure Ramp Rate in Accordance with the Precooled Hydrogen Temperature

The MC-Formula refueling method performs refueling by varying the pressure ramp rate that was a fixed value according to the ambient temperature with the L/T refueling method.

In Fig. 5, actual refueling starts from $P_{initial}$, so this point is $t = 0$ in actual time. Here, the time $t_{initial}$ from P_{min} to $P_{initial}$ is a hypothetical refueling time that does not actually exist. $t_{initial}$ is obtained by Eq. (2) from the proportional distribution of the pressure.

$$t_{initial} = \left(\frac{P_{initial} - P_{min}}{P_{final} - P_{min}} \right) \times t_{final} \quad (2)$$

t_{final} is the value including the hypothetical time $t_{initial}$. This is calculated for each ambient temperature and each precooled hydrogen temperature. The condition is that the hydrogen temperature inside the vessel reaches the upper limit of 85°C at t_{final}. Overheating occurs when filling is performed faster than this t_{final}, so t_{final} is the shortest refueling time. This t_{final} calculation simulates the complex heat transfer phenomena inside the tube and vessel, and six precooled hydrogen temperature patterns × 15 ambient temperature patterns = 90 patterns are calculated beforehand via simulations. In this development, the boundary conditions, vessel and other parameters in the simulations used the same values as those of the conventional L/T refueling method.

The relationship between the precooled hydrogen temperature and t_{final} at any given ambient temperature was approximated using a cubic equation to provide continuity.

$$t_{initial(Tamb)} = a_{(Tamb)} \times MATC^3 + b_{(Tamb)} \times MATC^2 + c_{(Tamb)} \times MATC + d_{(Tamb)} \quad (3)$$

Fifteen different combinations of the coefficients a, b, c and d can be set for each ambient temperature. These combinations expressed in table format are called maps in the MC-Formula refueling method. These maps have two

initial pressure patterns × four vessel capacity patterns for a total of eight maps that are stored in the hydrogen refueling station control unit.

Concretely, the map is selected according to the vessel capacity and the initial pressure, and the coefficients a, b, c and d are determined by the ambient temperature. Linear interpolation is performed at the intermediate temperatures. t_{final} can then be calculated by substituting the measured mass average precooled hydrogen temperature $MATC$ into the equation.

Next, the pressure Ramp Rate (RR) is calculated from t_{final}.

According to Fig. 5, at the actual current time $t_{current}$, the required pressure difference until the end of refueling is P_{final} - $P_{current}$. The time required for this is expressed by Eq. (4) using Eq. (2).

$$t_{final} - t_{initial} - t_{current} = t_{final} - \left(\frac{P_{initial} - P_{min}}{P_{final} - P_{min}}\right) \times t_{final} - t_{current}$$
$$= \left(\frac{P_{final} - P_{initial}}{P_{final} - P_{min}}\right) \times t_{final} - t_{current} \quad (4)$$

Therefore, at $t_{current}$, the pressure ramp rate until the end of refueling is the ratio of the pressure difference to the time, and can be expressed by Eq. (5).

$$RR = \frac{P_{final} - P_{current}}{t_{final}\left(\frac{P_{final} - P_{initial}}{P_{final} - P_{min}}\right) - t_{current}} \quad (5)$$

When RR has been determined, the target pressure to be achieved at the next control step (i) is given by Eq. (6).

$$P_{(i+1)} = P_{(i)} + RR_{(i)} \times (t_{(i+1)} - t_{(i)}) \quad (6)$$

The control method that performs flow control for the hydrogen refueling station to reach the target pressure is exactly the same as that used by the L/T refueling method. This enabled a feedback of the actual precooled hydrogen temperature to the refueling time without overheating.

3.4. End Pressure Setting

The gasoline full state can be detected by the height of the fuel surface. The hydrogen pressure changes according to the temperature, so it cannot be used as a full state index. For this reason, the full state is defined by the density. SAE J2601[4] defines a hydrogen density of 40.2 kg/m^3 at a temperature of 15°C and pressure of 70 MPa as a State Of Charge (SOC) of 100%.

However, the hydrogen density cannot be measured directly, so it needs to be calculated from the pressure and temperature. Therefore, SAE J2799[5] established a communication refueling system (IR communication system) that sends the information of the temperature inside the vessel of the vehicle to the station via IR communication. This enabled real-time calculation of the hydrogen density for accurate full vessel judgment.

The method of ending refueling is basically the same as that of the L/T refueling method. The temperature inside the vessel is received from the vehicle via IR communication, the hydrogen density is calculated, and refueling is stopped.

Figure 6 shows an overall image of this control.

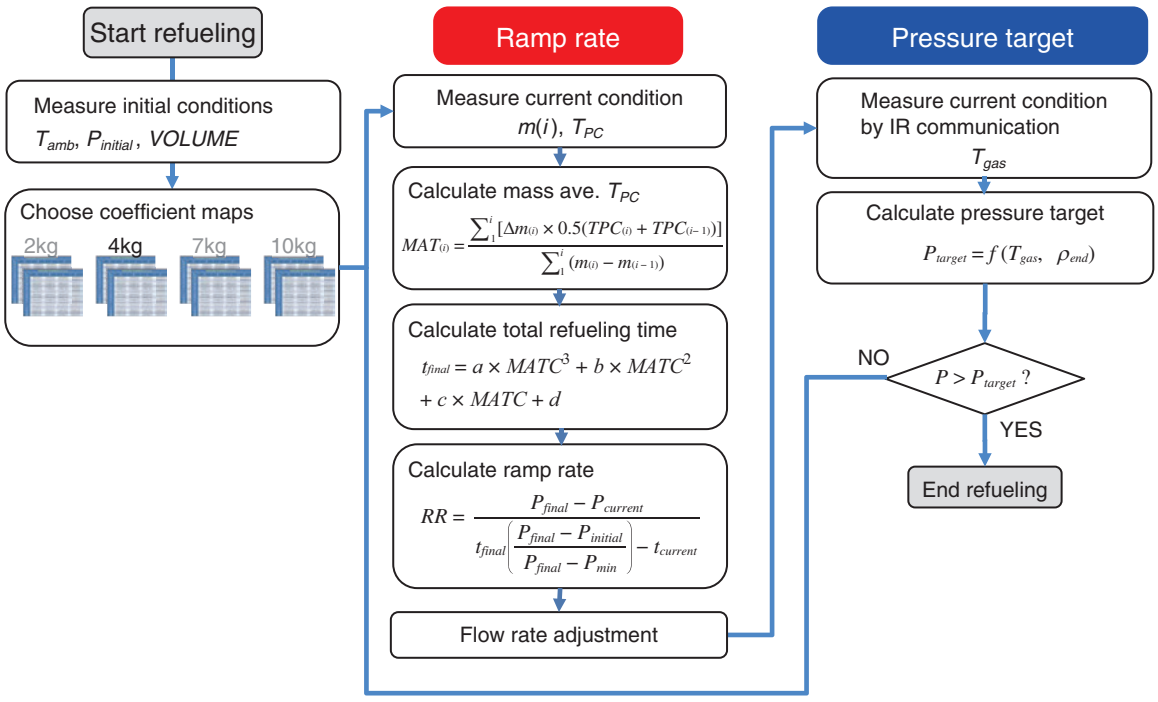


Fig. 6 MC-Formula refueling control structure

3.5. Hardware Configuration

3.5.1. Addition of a precooled hydrogen temperature sensor

The only change from the L/T refueling method is the addition of the precooled hydrogen temperature sensor $T_{PC\text{-}2}$ shown in Fig. 1. $T_{PC\text{-}1}$ and $T_{PC\text{-}2}$ measure the temperature in the same location, and compare the measured values with each other. When an issue occurs in either sensor, the values diverge, enabling failure detection. Note that there is no change in the maximum hydrogen flow rate, so there is no need for changes to the hydrogen tube or other parts.

3.5.2. Control unit

The MC-Formula refueling method uses a larger amount of calculations than the L/T refueling method. That said, the MC-Formula refueling method requires only one cycle of 1360 floating decimal point calculations every few seconds, which can be supported by a programmable logic controller (PLC), which is a type of compact computer commonly used to control typical facilities. Actual operation showed that the MC-Formula refueling method software operates without issues on a previous-generation PLC that requires 125 μsec per floating decimal point operation.

4. Proving Tests

The MC-Formula refueling method was introduced to a commercial hydrogen refueling station made by Airproducts Inc., which is the most common type in the U.S., and refueling tests were performed under various conditions using actual FCV and a test vessel.

4.1. Hydrogen Refueling Station

The tests were performed using a hydrogen refueling station at the Honda R&D Los Angeles Center in the City of Torrance, CA, U.S.A. This hydrogen refueling station is able to use both the L/T and MC-Formula refueling methods (Fig. 7).



Fig. 7 Hydrogen refueling station at which MC-Formula was applied

4.2. Test Vessels and Vehicles

Three different types of vessel system were used, two of which were actual FCVs. Cooperation was obtained from General Motors (GM) and Mercedes-Benz for the tests.

The GM Equinox FCV has three vessels with a total capacity of 114 liters (Fig. 8).

The Mercedes-Benz B-Class F-CELL FCV has three vessels with a total capacity of 95 liters (Fig. 9).

The vessel system used to measure the temperature used an aluminum liner vessel with an internal capacity of 105 liters (Fig. 10). Two thermocouples were inserted to



Fig. 8 Photo of General Motors Equinox FCV



Fig. 9 Photo of Mercedes-Benz F-CELL FCV

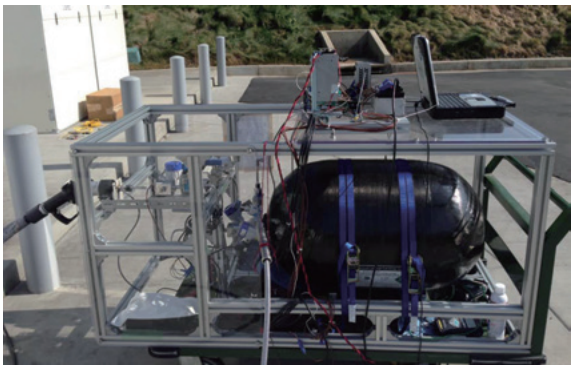


Fig. 10 Photo of single vessel test rig

measure the hydrogen temperature inside the vessel. The heat capacity of the tube parts (tubes, valves, other) was set to the maximum heat capacity noted in SAE J2601. The pressure drop in the tube was also adjusted to the maximum SAE J2601 value using a needle valve.

4.3. Test Results

The results showed that the refueling time could be shortened while observing the upper limit of the hydrogen temperature inside the vessel, and that an SOC equivalent to that of the conventional L/T refueling method could be obtained.

4.3.1. Refueling time

The tests were performed on days with a high ambient temperature, and test data was obtained at temperatures up to around 35°C. Data at higher temperatures was not obtained, so some temperatures that differ from the actual temperatures were tested by manual input. Vehicle tests were performed at the actual temperatures without manual input. Figure 11 shows the refueling time results. The variance in the data is due to factors such as different initial pressures and the need for leak checks during refueling as prescribed by laws and regulations unique to the U.S.

When the ambient temperature is low, there is negligible concern for overheating, and the pressure ramp rate is limited by the rate upper limit value, so there is no difference between the two methods. The difference between the methods widens as the ambient temperature increases. In contrast to the L/T refueling method that assumes a precooled hydrogen temperature that is the upper limit value of the temperature tolerance, the MC-Formula refueling method uses the actual hydrogen temperature, so the refueling time was approximately 30% shorter. This enabled refueling in less than four minutes in most cases in the LA district.

4.3.2. Hydrogen temperature inside the vessel

Figure 12 shows the hydrogen temperatures inside the vessels of the GM Equinox FCV at the end of refueling. These results show that although the hydrogen temperature rose by an average of approximately 8°C due to the increased pressure ramp rate, the temperature was still 70°C or less, which is sufficiently below the upper limit value of 85°C.

The reason for this is thought to be that the three-vessel system has a large vessel wall surface area relative to the hydrogen quantity, so the hydrogen is cooled by the heat mass of the vessel body and the hydrogen temperature does not rise easily.

4.3.3. SOC

Figure 13 shows the SOC during communication refueling.

This station has an end target of an SOC between 98% and 100%. Both refueling methods calculate the density and perform end of refueling control using the temperature obtained by communication refueling. The control method is the same, so no difference was apparent in the actual SOC.

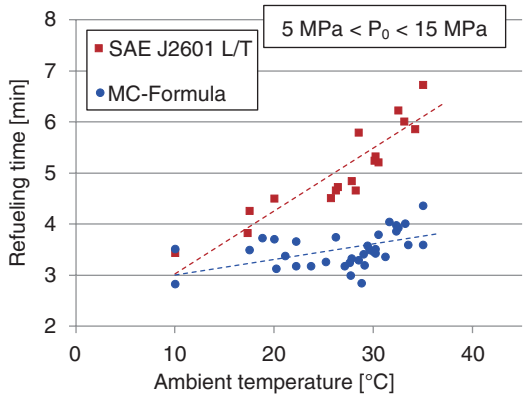


Fig. 11 Refueling time on ambient temperature

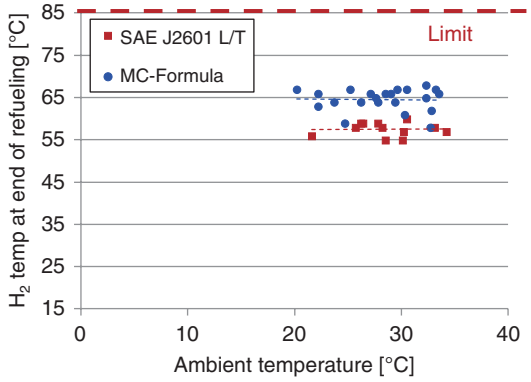


Fig. 12 Ending H_2 temperature in vessel

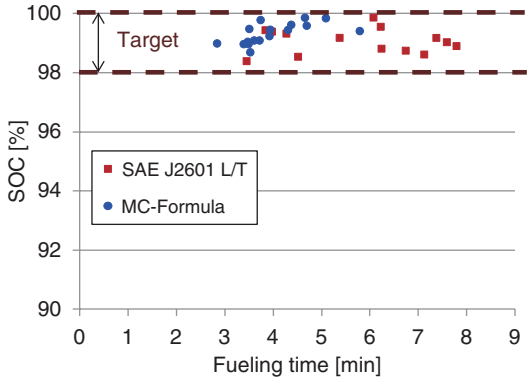


Fig. 13 Ending SOC of communication refueling on test vessel

5. Conclusion

The MC-Formula refueling method was developed to shorten the hydrogen refueling time of FCV.

(1) Real-time control of the pressure ramp rate in accordance with the precooled hydrogen temperature was added. This made it possible to shorten the refueling time by 30% or more in the summer without lowering the precooled hydrogen temperature, which enables refueling in less than four minutes in most cases year round in the LA district.
(2) The boundary conditions, vessel and other parameters in the simulation of t_{final} that determines the pressure ramp rate used the same values as those of the L/T refueling method, and the approach toward safety was also carried over. The refueling end method is also the same, which helped to achieve an SOC equal to that of the conventional L/T refueling method.
(3) No changes were made to either the hardware or the software on the vehicle side.
(4) The only change to the hydrogen refueling station hardware was the addition of a temperature sensor. The amount of calculations performed by the hydrogen refueling station software increased, but the software was able to operate on the previous-generation PLC. Therefore, the developed system can also be installed in existing stations.

6. Afterword

The MC-Formula refueling method is currently under deliberation as a proposed revision to the SAE J2601 standard (as of July 2015).

References

(1) ANSI HGV 2-2014: Compressed hydrogen gas vehicle fuel containers (2014)
(2) Harty, R., Mathison, S.: Improving Hydrogen Tank Refueling Performance Through The Use Of An Advanced Fueling Algorithm - The MC Method, Proceedings of the National Hydrogen Association Conference (2010)
(3) Mathison, S., Handa, K., Mcguir, T., Brown, T., Goldstein, T., Johnston, M.: Field Validation of the MC Default Fill Hydrogen Fueling Protocol, SAE Technical Paper, 2015-01-1177 (2015)
(4) SAE J2601: Fueling Protocols for Light Duty Gaseous Hydrogen Surface Vehicles (2014)
(5) SAE J2799: Hydrogen Surface Vehicle to Station Communications Hardware and Software (2014)

■ Author ■



Kiyoshi HANDA



Steve MATHISON

Establishment of Metal Die Fabrication Method with Short Production Work Hours by Implementing Technology of Liquid Metal Forging for Cast Iron

Takunori KITAMURA* Hiroki NAGURA*

ABSTRACT

A technology has been sought for the metal mold fabrication that could be used for a trial manufacturing in the stage of a product development and/or the actual production stage for a small production volume to make the vehicle development flexible and conducted in timely manner. For the dies used for high pressure casting, surpassing mechanical properties are needed because of the severe requirements for durability in their operations. Therefore, hot forming die steel is usually used for the die steel material. However, this material is disadvantageous to machinability and takes longer period for its fabrication. With this background, the study on a technology of liquid metal forging for cast iron was conducted, in which ductile cast iron is cast in a mold and solidified under high pressure. By implementing the adjustments of the base material structure together with enhancements in surface properties, the production method was established to fulfill the requirements in dimensional accuracies, qualities of inner material and the life of mold.

1. Introduction

A large number of cast aluminum parts are used in a motorcycle. The prototype of such parts is usually produced by sand casting in the development stage of a new model to maintain flexibility for design changes while taking into account the production cost. The aluminum material such as JIS AC2B is used in the sand casting. Meanwhile in the mass production, the parts are produced by the high pressure die casting (HPDC) using the material like JIS ADC 12. It should be noted that there are differences in the mechanical properties between the two materials mentioned above. The product made by sand casting is less precise than the one made by HPDC. It is therefore necessary to verify durability of the part produced by HPDC in the final stage of product development. If a lack of strength or durability is found in that stage, a design change is required. A design change affects development schedule and development cost. Due to recent diversification of demands from the market, the needs for small-volume, multiple-model production are increasing. Under such circumstances, there is a requirement for a die manufacturing method applicable to the prototype manufacturing in the development stage as well as to the small-volume production in the mass-production stage.

The die for high pressure die casting is generally subjected to strong impacts from the molten metal charged into the die at a high speed under high-temperature and high pressure conditions. Accordingly, the cavity section is generally made of a high strength material such as the hot die steel. Machining of such a high strength material, however, is difficult, requiring electro discharge machining (EDM) and hand polishing in the latter processes. Consequently, the total die manufacturing period becomes lengthy, which is an issue in the die manufacturing from the perspectives of cost and schedule.

To deal with this issue, studies have been conducted to produce dies by casting using the ductile cast iron (FCD)[(1)]. In those studies, the die is produced by two manufacturing methods. For one, it is the semi-full-mold method using the ceramic shell mold requiring no machining of the cavity. In that die manufacturing method, the warpage of cast material, the rough surface and the metal structures on the surface were the concerns. The second one is the full mold method using foamed styrol and sand mold. The cavity section is machined. Though there is no quality-related problem in this method, there are issues in the production cost and the schedule.

With the aforementioned in the backgrounds, this project is targeted at realization of die manufacturing by the liquid metal forging using FCD as the die material. To allow use of FCD as a die material, it is necessary to take into account the inaccuracy of cavity shape due to the solidification contraction at the time of casting and the reduction of strength due to porosity. To deal with the said issues, the authors and others sought feasibility of liquid metal forging

* Motorcycle R&D Center

for cast iron. In this manufacturing method, retention of precise cavity shape and control of porosity are prospective by letting the molten FCD to solidify while being pressurized, thereby allowing reduction of total production time period by elimination of cavity machining, EDM and hand polishing from the die manufacturing processes. It is also considered that the control of porosity prevents lowering of strength, and allows application of the method to the die casting. Mentioned in this paper are the development process of HPDC dies by the liquid metal forging and the results of validation for practical applications.

2. Quick Die Production Method

2.1. Die Production Processes and Total Production Time Period

In the die manufacturing, the part that takes a long production time is the cavity because it is a reverse copy of the cast product having a complex 3D shape. The cavity production processes are shown in Fig. 1. Firstly, the cavity machining data is created from the 3D data of die using CAM. Then, the cavity is machined by the NC machine. At that time, the small section and/or the deep part shown red in the picture are left without being machined. Accordingly, the EDM is conducted after the machining. Although the EDM is an effective method to remove un-machined objects, it takes a long processing time because the metal is removed by electric erosion. As the metal property changes on the work surface in the EDM, the hand polishing is required in the final process. Consequently, the cavity production takes a long period of time.

Keeping in mind the aforementioned, the authors and others simulated the total production time for each part expended at the time of HPDC die production. The subject part is the crankcase of motorcycle engine. The size is; X: 300 mm Y: 195 mm Z: 60 mm. The high-pressure die cast machine having a die clamp force of 500 ton is applied. The material of the die bases is presumed as FCD 550, and the cavity material as SKD 61. It has been clarified upon the computer simulation that the total cavity production time shares approximately 58% of the entire die production period. We accordingly decided to work out a way that allows minimization of machining, EDM and hand polishing at the time of cavity production.

2.2. Quick Die Manufacturing Method

Roughly classified, there are two ways that can shorten cavity machining processes. One is such a method that applies finishing after producing a cast material having a shape that corresponds to the roughly-machined cavity. The other one is the liquid metal forging that fills molten metal in a mold and let it solidify while pressurizing. The liquid metal forging is a production method that ensures precise cavity shape while having less porosity inside. In the feasibility study, the preciseness of cavity shape was targeted at ±0.1 mm, which was set taking into account the cavity dimensions being X: 350 mm Y: 400 mm Z: 180 mm with the general tolerance of product at ±0.4 mm. The die production time in those two methods were simulated. In the first method, the time saving is approximately 20% for the cavity made of SKD 61. Meanwhile in the second method, a saving as high as 50% is prospective. That's an end result of time saving from the machining, EDM and hand polishing. In view of the above, it was decided to start development of die production method based on the liquid metal forging.

The die manufacturing processes by the liquid metal forging are shown in Fig. 2. Firstly the forging die is designed by reversing the cavity from the 3D data of the die. After preparing the machining pass by CAM, the forging die is fabricated by the machining center. Then, the forging die is set on the fixture and heated with the heater. After the forging die is heated to the prescribed temperature, the molten FCD is charged in the forging die, and pressurized. Then, the die is cooled down until completion of solidification while maintaining the pressure. The die is separated from the mold upon completion of solidification, thus completing the cavity manufacturing. In the liquid metal forging, a material having the following characteristics is required.

- Shall be able to maintain strength and shape preciseness under high temperature conditions
- Shall be inexpensive and easily available
- Shall have good machinability

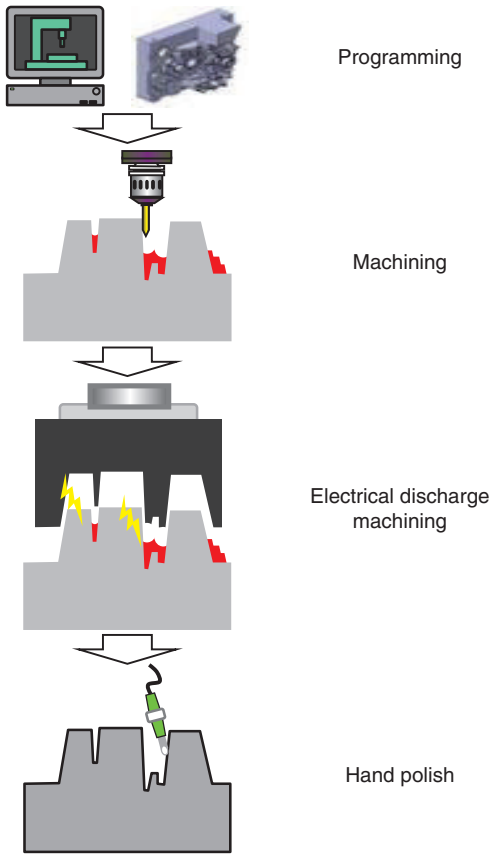


Fig. 1 Mold fabrication process

The authors and others therefore considered use of graphite for the die material. The graphite is commercially available and inexpensive. In addition to that, it resists heat as high as 3000°C in an inert gas while exceling in the shape preciseness. Moreover, its machinability is better than the hot forming die steel, thereby allowing forging die production in a short period of time. The graphite, however, has a thermal conductivity approximately three times higher than that of steel. Accordingly, as the molten metal is quickly cooled, faulty duplication of shape such as misrun tends to occur. To deal with this issue, die temperatures that ensure correct running of molten metal were analyzed.

2.3. Graphite Die Temperature Analysis

The charged FCD is cooled from the part that contacts the graphite, reducing flowability. As a result of reduced flowability, the material is missing in some areas, causing faults from misrun on the surface as shown in Fig. 3 in some cases. Accordingly, the relationship between the misrun and the die temperature was analyzed using the test piece created by the liquid metal forging. The shape of test piece was chosen from a part of the crankcase of motorcycle engine as shown by Fig. 4. Moreover, the part having a complex shape including ribs having a tip width of 2 mm and a depth of more than 80 mm was selected taking into account the difficulty of high-pressure die-casting of parts having a large number of ribs. In the test piece preparations, the molten metal temperature was set at 1400°C. The graphite die temperature was increased from 400°C up to 1000°C with an increment of 50°C, having a total of 13 dies prepared. The die temperature was measured in the center of die and at a depth of 20 mm from surface of the deepest part of cavity. The test pieces were prepared under the abovementioned conditions and the number of misrun occurring on the surface was counted. At that time, a misrun was determined when the fault was as extensive as to require correction by welding.

The test results are shown in Fig. 5. When the die temperature is under 600°C, the number of the surface defects decreases rapidly along with an increase of temperature of the graphite die. As the die temperature is further increases, the number of the surface defects saturates and becomes close to zero. From the abovementioned findings, we concluded that it was necessary to set the die temperature at above 700°C in order to obtain acceptable surface quality.

2.4. Feasibility of Die Manufacturing by Liquid Metal Forging

The manner the FCD solidifies is a mushy solidification. In the mushy solidification, the molten metal becomes like mush as the cooling advances. It is such a manner of

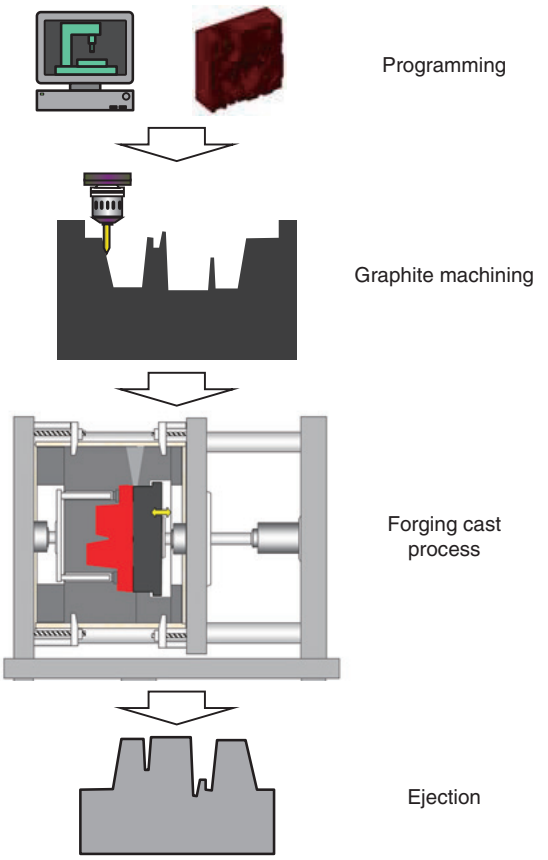


Fig. 2 Mold fabrication by forging cast process



Fig. 3 Appearance of surface defects



Fig. 4 Appearance of test piece

solidification in that the solidification completes all at once as soon as the cooling advances further and the temperature becomes lower than the solidus temperature. Due to the said characteristics, the pressurized molten metal stays closely in contact on the graphite die until completion of solidification. Additionally in the liquid metal forging, the molten metal is supplemented by the pressure at the time of contraction. Accordingly, an improvement of shape preciseness and internal quality is prospective from the liquid metal forging. The results of analysis on the shape preciseness and the internal quality are described hereafter.

2.4.1. Liquid metal forging process

How to inject molten metal into the liquid metal forging die is shown in Fig. 6. The "bottom gate" design in which the molten metal enters from the lower part of the cavity is selected to control occurrence of molten-metal balls and lowering of temperature due to spread of molten metal in its end. An overflow well is provided in the upper part to allow escape of excess molten metal and gas at the time of injection.

Next, the processes from the injection up to the ejection are shown in Fig. 7. The graphite die is composed of three parts. One is the fixed die having a reversed shape of the die cavity. The second one is the fore-and-aft sliding die for pressurizing of molten metal after completion of injection. In addition to that, the drawing system is incorporated for ejection. The third one is the retainer die which supports the sliding die. After securing the three dies in the fixture, the die is heated, and as soon as the graphite die reaches the prescribed temperature, injection of molten metal starts from the gate. After confirming that the molten metal is discharged from the overflow well, the slide die is moved

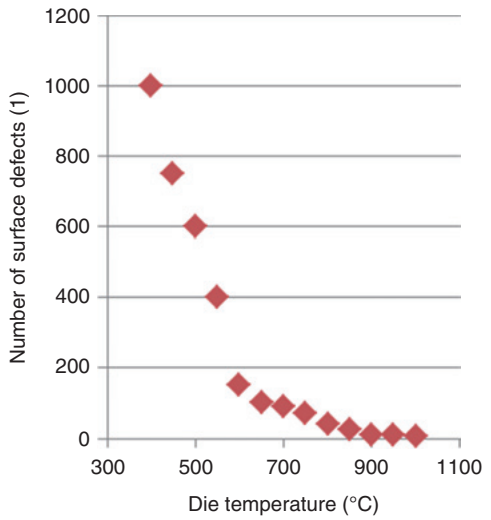


Fig. 5 Surface defects and die temperature

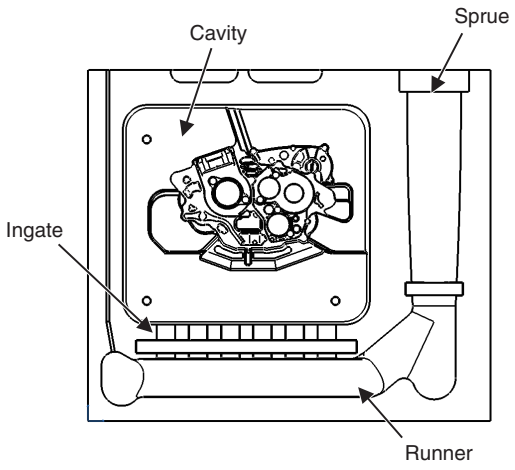


Fig. 6 Casting plan

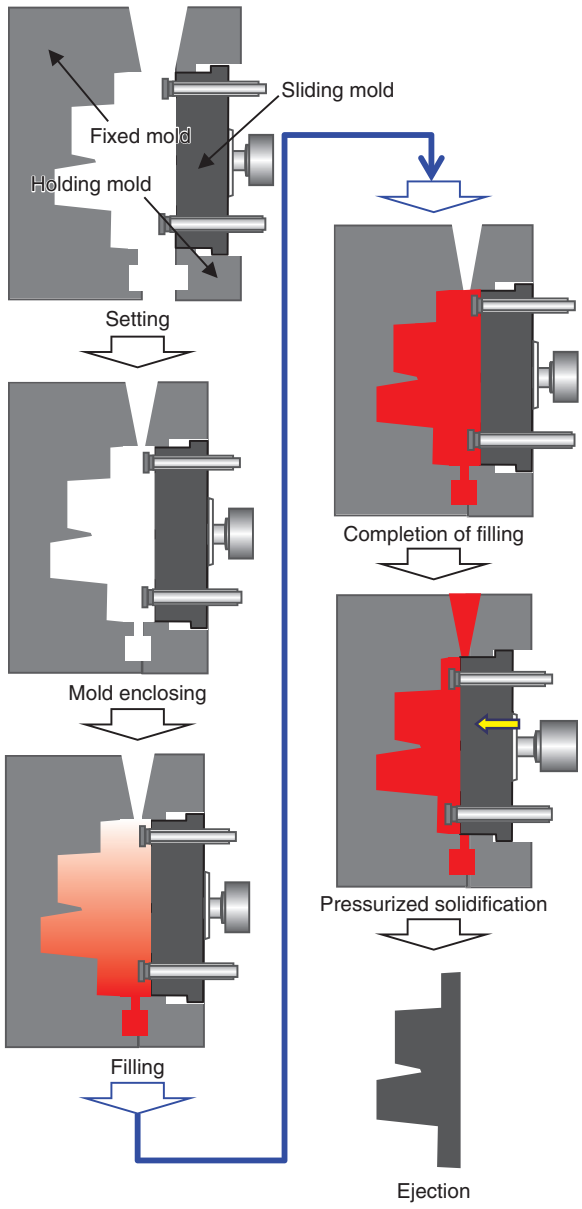


Fig. 7 Forging cast process

forward. The pressurizing starts as soon as the sliding die passes the gate and the overflow well, and continues until the pressure reaches the prescribed level. When the pressure reaches the prescribed level, cooling of the graphite die starts. As soon as the graphite die temperature has lowered to the prescribed level, the slide die is reversed. Thus, the die is separated from the graphite die.

2.4.2. Preciseness of shape transfer

How the solidification under the pressure affected the shape transfer preciseness was analyzed using the test piece shown in Fig. 4. The shapes of two kinds of test pieces prepared by the gravity casting and the liquid metal forging were measured, and the preciseness was compared. The non-contact laser contour measurement system was used for the measurement. The 3D shape data and the errors were calculated. The results of measurement are shown in Fig. 8. The negative side of color scale indicates the direction the shape shrinks and the positive side means the direction the shape expands. The left picture refers to the test piece prepared by the gravity casting. There is a maximum shape error of approximately 0.5 mm. Meanwhile, the right picture concerns the test piece prepared by the liquid metal forging. It is evident that the shape error is within ±0.1 mm in all measurement points. Note that the blue-dotted part appearing on the upper left part of test piece is a deformation from the ejector pin, rather than an incorrect transfer of shape.

From the aforementioned findings, it has been confirmed that the solidification under the high pressure allows control of solidification contraction and strain as well as ensuring highly precise shape transfer.

2.4.3. Internal quality analysis

How the solidification under pressure affected the internal quality was analyzed using the test piece shown in Fig. 4. The test piece was sliced at an interval of 10 mm, and the dye penetrant inspection (JIS-Z2343) was conducted on all cross sections. Typical example of inspection data is shown in Fig. 9. The left picture refers to the test piece prepared by the gravity casting. Presence of porosity is seen. Meanwhile, the right picture concerns the test piece prepared by the liquid metal forging. No porosity is seen. It has been confirmed from these findings that the solidification under pressure prevents porosity.

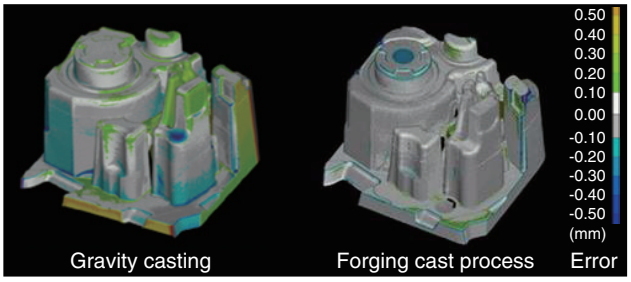


Fig. 8 Comparison of duplication accuracies

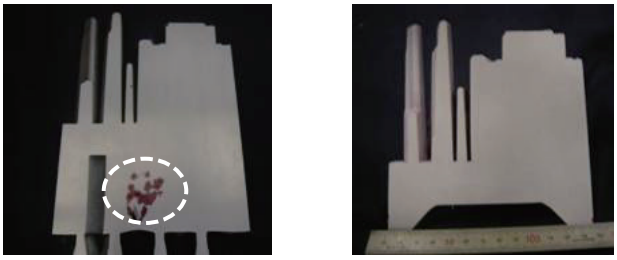


Fig. 9 Comparison of internal defects test results

3. Improvement of Durability of FCD Die

As this project is aimed at dies suitable for small-volume production, the following goals have been set for the durability.

- No damage after 10000 shots
- Heat checks within tolerance of appearance

Compared to other casting methods, the injection pressure is high in the HPDC, and the molten aluminum contacts on the die surface at a high speed. In addition to that, the water-soluble de-molding agent is sprayed on the die after ejection of the casting. Accordingly, thermal stresses from heating and cooling occur in the die. The tensile strength of FCD is lower than that of a hot forming die steel. Accordingly, heat checks occur earlier in the die made of FCD than the die made of SKD 61. The heat checks are transferred to the casting, negatively affecting the product appearance. Growth of heat checks eventually causes breaking of the die. To deal with this issue, the basic metal structure of FCD was analyzed and the material composition was adjusted to make the material suitable for HPDC. The following two test methods were employed. One is the “heat check test” by approximately inducing cool/heat cycle. The second one is the “die cast test”, in which the durability is assessed by actual casting.

3.1. Basic Metal Structures of HPDC Die and Adjustment of Material Composition

3.1.1. Life estimation by heat check test

The heat check test shown in Fig. 10 is one of the methods to test durability of the basic metal structures of die material. The heat check test is generally conducted using an induction hardening equipment. After induction-heating the test piece to the prescribed temperature, water cooling and air cooling are conducted. It is a test to assess heat check resistance by approximately duplicating the cool/heat cycle occurring on the die surface at the time of casting.

The conditions under which the heat check test is conducted are described hereafter. The test piece diameter is 42 mm and its length is 80 mm. The outer circumference and the end surfaces are machined. The surface temperature is increased to 620°C by heating for 10 sec, and after that, the surface temperature is lowered to 50°C by the 15 sec

water cooling and 5 sec air cooling. The said procedures complete a cycle. Also in the tests at this occasion, SKD 61 was selected as the durability reference material. The number of cracks in SKD 61 occurring after conducting 1000 cycles of the aforementioned test was used as the reference. In this project, the durability of SKD 61 die was presumed at 50000 shots. As the durability of FCD die is targeted at 10000 shots, the target number of cycles at which the number of cracks and its length become equal to the reference corresponds to 200 cycles.

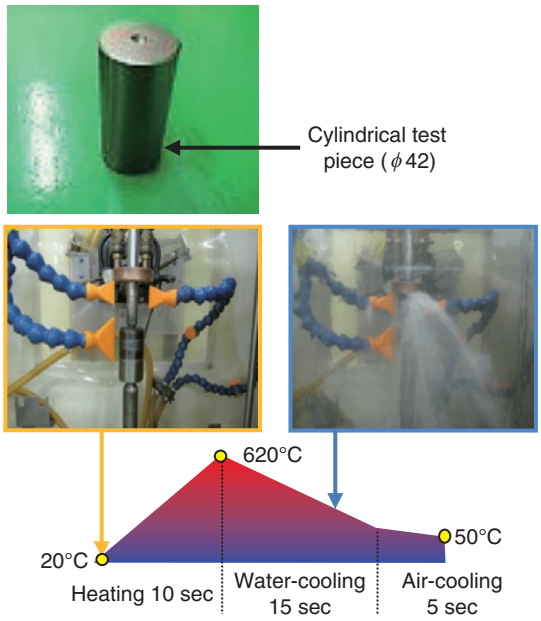


Fig. 10 Test conditions for heat check

Table 1 Specification of test piece

TP	Structure	Ferrite (%)	Pearlite (%)	Hardness (HRC)
(1)	Ferrite	100	0	<0
(2)	Ferrite-rich	95	5	10
(3)	Ferrite-Pearlite	40	60	22
(4)	Pearlite-rich	5	95	25
(5)	Martensite			37
(6)	Bainite			42
(7)	Cementite			51

3.1.2. Relationship between basic metal structure and occurrence of heat checks

The following seven types of metal structure were designated for the test piece to conduct heat check tests. Major specifications are shown in Table 1. The rate of ferrite and pearlite in the chart is by the rate of respective area with the graphite excluded. The hardness is shown in HRC scale converted from the Brinell hardness.

Test piece (1) All ferrite
Test piece (2) Ferrite-pearlite (ferrite-rich)
Test piece (3) Ferrite-pearlite
Test piece (4) Ferrite-pearlite (pearlite-rich)
Test piece (5) Martensite
Test piece (6) Bainite
Test piece (7) Cementite

The test results are shown in Fig. 11. The following characteristics are seen in the diagram. The trend is such that the higher the hardness, the number of cycles decreases until

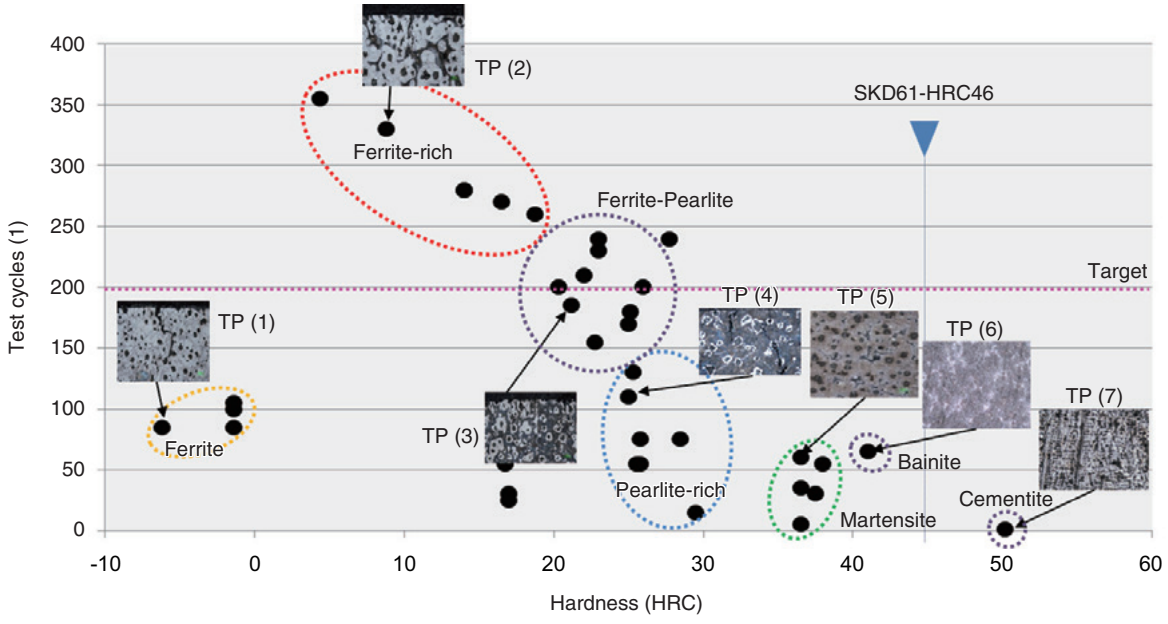


Fig. 11 Results of heat check classified by metallographic structure

reaching the aforementioned reference level. Also, in the test piece having two kinds of metal structures such as the ferrite-pearlite structure, the number of cycles is large until entirely reaching the reference level. Especially in the test piece rich with ferrite, the durability exceeds the target. Meanwhile, none having a single metal structure satisfies the target.

Next, the details of heat check were observed with the metallurgical microscope. Taken for the observation were four kinds of the test pieces, i.e., the test piece (1) and (4) in which the number of test cycles was small, and the test piece (2) and (3) in which the number of test cycles was large. The results of observation are shown in Fig. 12. In the test piece (1), the heat check grows along the graphite in the ferrite structure. The same applies to the test piece (4) featuring pearlite. On the other hand, in the test piece (2) and (3), while the heat check grows along the graphite, in some areas, the heat check occurring in the ferrite stops growing at the ferrite-pearlite interface. It is also known that the FCD having ferrite-pearlite two-phase mixed structure is highly ductile[2]. In view of the above, the authors and others have considered that the growth of heat check can be controlled by making the basic metal structure composed of two kinds, i.e., ferrite and pearlite.

3.1.3. Influence of material composition to heat check

With respect to the material composition, our attention was focused on manganese (hereafter Mn). The FCD contains Mn by approximately 0.2-1.0 wt%. The Mn is added to remove sulfur in the molten metal by forming its chemical compound (manganese sulfide). The residual Mn unrelated to the forming of manganese sulfide becomes carbide[3]. The carbide is brittle, hard and easy to crack.

Table 2 Enhanced toughness against heat check by decreased Mn content

TP	Structure	Mn (wt%)	Hardness (HRC)
A	Ferrite-rich	0.39	17
B	Ferrite-rich	0.13	15
C	Ferrite-Pearlite	0.36	22
D	Ferrite-Pearlite	0.11	20
E	Pearlite-rich	0.37	28
F	Pearlite-rich	0.12	24

Accordingly, in an attempt to clarify how the Mn content affects the growth of heat check, 6 kinds of test pieces with various Mn contents were prepared and heat check tests were conducted. The test piece A and B were prepared with a target hardness of HRC 15, C and D at HRC 20, E and F at HRC 25 (Table 2). The difference of hardness was created by changing the ferrite/pearlite ratio. The test results are shown in Fig. 13. The test piece with the Mn content reduced to 0.1 wt% achieved the targeted 200 cycles.

On the basis of the above findings, the sample B, which is the best from the strength standpoint, has been employed.

3.1.4. Die cast test

To verify durability of the FCD die in actual casting operations, 3000-shot die cast test was conducted using the HPDC machine having a clamp force of 350 ton. The overview of the die and the test piece are shown in Fig. 14. Three criteria were defined for the judgment to meet the requirements for die durability. Those are the dimensional

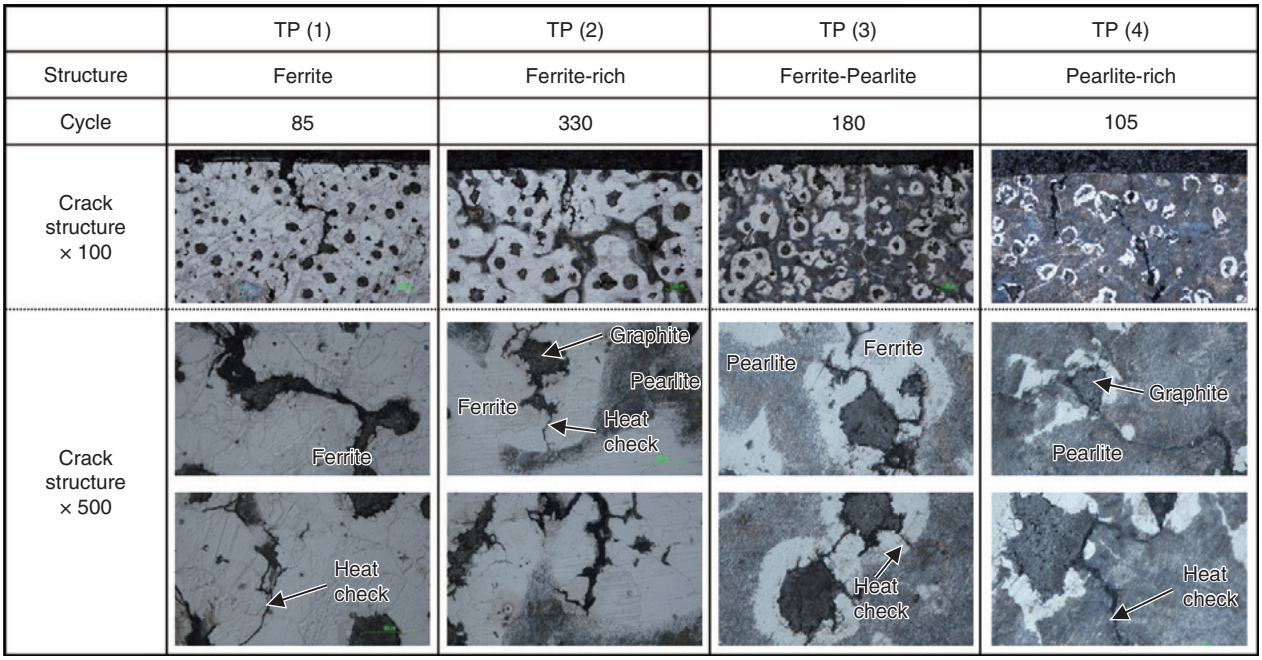


Fig. 12 Cross sections showing heat checks in micro structures

accuracies and the quality of appearance of the casted products together with the existence of breakages on the dies.

The shape preciseness test method is described hereafter. The shape of product produced by HPDC at the 10th shot and 3000th shot was measured with the industrial CT scanner. The dimension variance between the measured data of 10th shot and the 3D data is shown in the left picture of Fig. 15. The dimension variance is within ±0.1 mm. The right picture shows the dimension variance between the measured data of 3000th shot and that of 10th shot. The dimension variance is within ±0.1 mm with an exception in a part. The cause of the shape deviation more than -0.2 mm in that part is due to the seizure of aluminum on the die, rather than a die deformation. No part of the die was broken either.

The overview of the product at 3000th shot is shown in Fig. 16. It can be seen that the large number of heat checks occurring in net-like patterns on the die surface is transferred on the product. The fault was beyond the tolerance of cosmetic quality of the product. The enlarged picture of heat checks on the die surface is in Fig. 17, and its cross-section in Fig. 18. The whitish aluminum

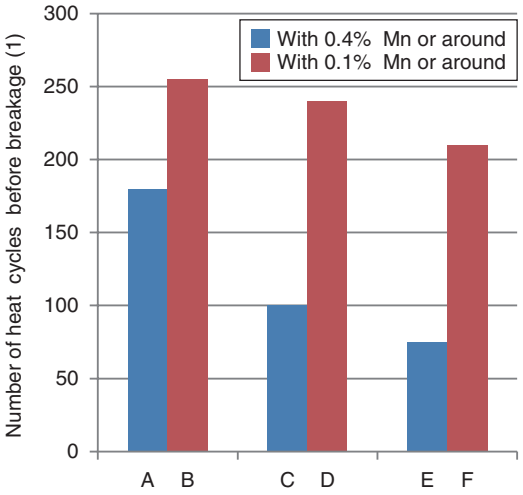


Fig. 13 Enhanced toughness against heat check by decreased Mn content

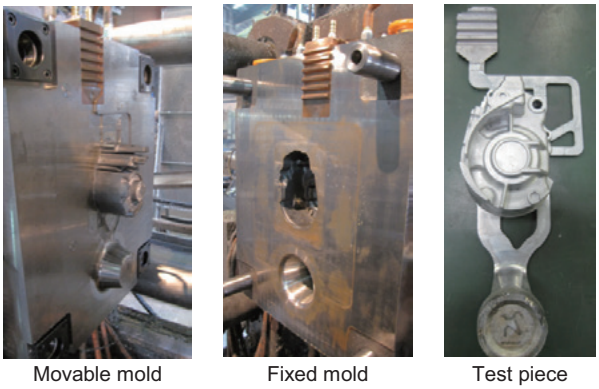


Fig. 14 Dies and test piece

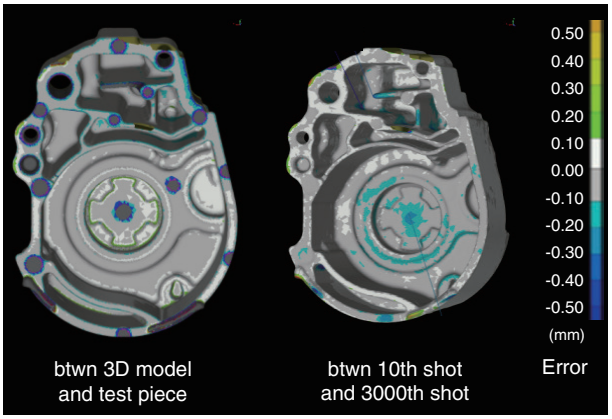


Fig. 15 Results of shape disparities checking

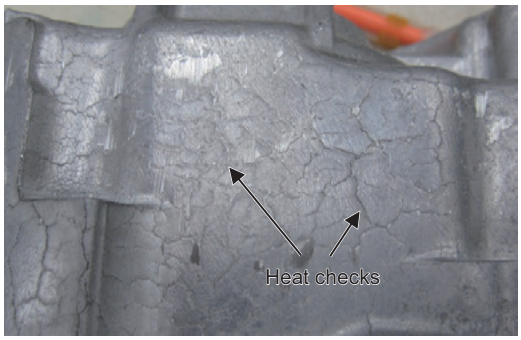


Fig. 16 Transferred heat checks

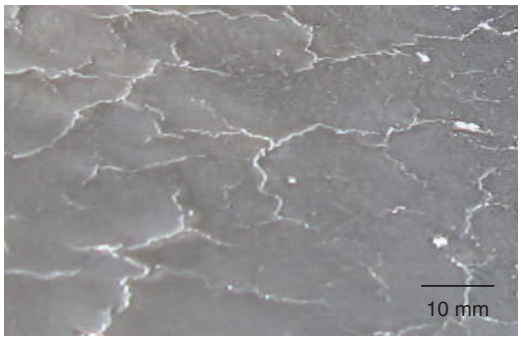


Fig. 17 Heat checks occurred on die surface

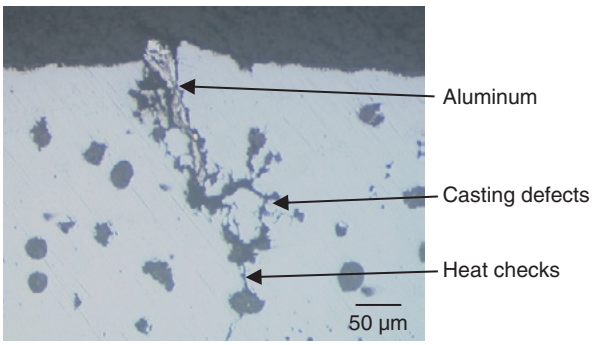


Fig. 18 Cross section at surface corrugation

penetrating in the heat check forms ridges on the die surface. With the ridges transferred, depressions occur on the product, causing lowering of cosmetic quality. The aforementioned findings mean that while the requirements on the retention of shape preciseness and the absence of die damage are satisfied, the cosmetic quality requirement is not satisfied due to the transfer of heat checks on the die to the product. Accordingly we decided to prevent formation of ridges in the opening of heat check.

3.2. Prevention of Ridges by Surface Modification

In the die cast tests, the cosmetic quality lowered to beyond the tolerable level due to the transfer of ridges on the product. It has therefore been decided to improve cosmetic quality by preventing formation of ridges on the die surface. As a means to prevent formation of ridges, the surface modification reformation was considered.

3.2.1. How heat checks that form ridges on the surface occur

How the ridges are formed in the opening of heat check is explained using the image picture shown in Fig. 19. Firstly in the early stage of the casting cycle, small heat checks occur from the surface toward the graphite. However, as the gap is small, no aluminum penetrates. After that, along with repetition of casting cycles, the heat checks in the stress-concentrated area grow deep along the graphite. When the depth of heat checks becomes larger than a certain level, the oxide matter falls from the surface, causing an opening. The molten aluminum is charged in the opening at a high pressure at the time of injection. It can be presumed that a plastic deformation occurs around the opening in the process the die surface shrinks after solidification of the charged aluminum, causing formation of ridges. To deal with this issue, it was considered that the plastic deformation could be prevented by providing a hard layer on the die surface.

3.2.2. Validation of surface modification

Nitriding is generally applied to a die made of a hot forming die steel, etc. to improve heat check resistance[4]. It is mainly aimed at prevention of heat checks. In this project, the authors and others considered that the nitriding would be effective for prevention of ridges on the opening of heat checks occurring in the dies made of FCD. Then, the salt bath soft nitriding was selected, and die cast tests were conducted. The cosmetic appearance was compared by the product made at the 3000th shot for validation of effectiveness of the soft nitriding treatment. The overview is shown in Fig. 20. Compared to the earlier-mentioned product, the ridge is controlled and the transferred depression on the product is less. The measurement points of depression transferred on the product are shown in Fig. 21, and the

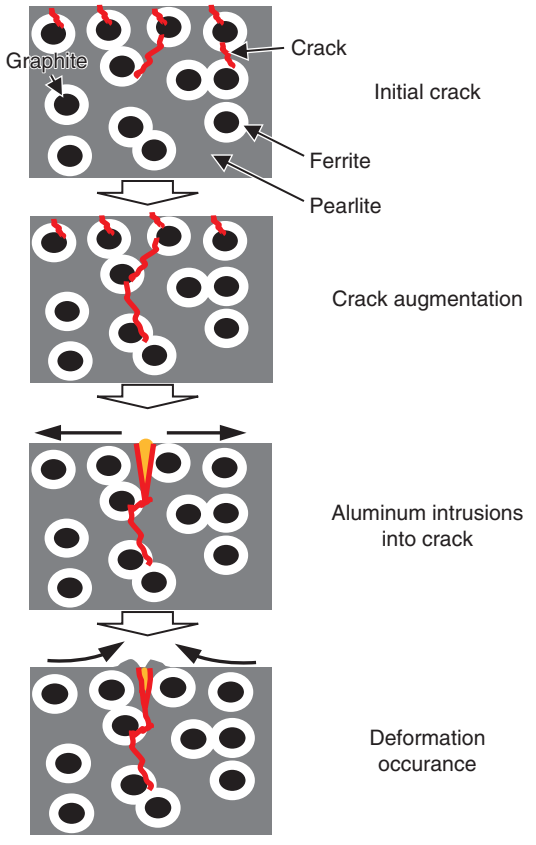


Fig. 19 Heat check generating mechanism in material structure



Fig. 20 Crack control effect by surface modification

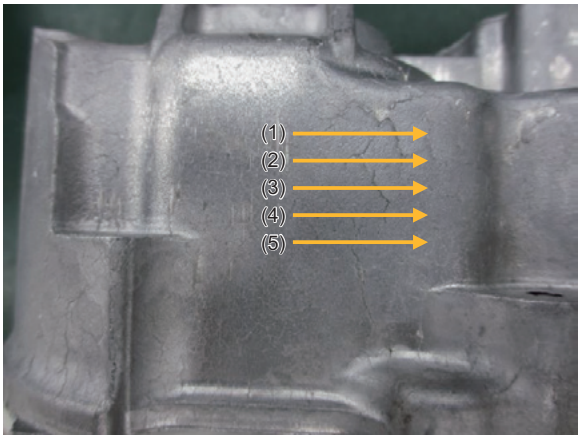


Fig. 21 Trace lines of depths measurement of transferred diches on molded parts at corresponding locations of heat checks

measured data in Fig. 22. The depth of depression was measured using the surface roughness tester. The maximum depth of depression transferred on the product made with the die without the soft nitriding is 0.13 mm. Compared to that, the maximum depth is 0.07 mm in the product made with the die having the soft nitriding applied. From these findings, it can be presumed that the hard layer created on the die by the soft nitriding reduces formation of ridges. The first goal, i.e., improvement of cosmetic quality, has thus been achieved.

3.3. Durability after 10000 Shots

To verify the durability of FCD die at the targeted 10000 shots, durability tests were conducted by actually casting the product. The crankcase of a single-cylinder engine was selected for the tests. The shape of cavity is shown in Fig. 23. Using the HPDC machine having a clamp force of 500 ton, 10000 shots of actual casting was conducted. Three criteria were defined for the judgment to meet the requirements for die durability. Those are the dimensional accuracies and the quality of appearance of the casted products together with the existence of breakages on the dies.

The tests were conducted by the method mentioned in 3.1.4. Note that the measurement was taken from the products at 3000th shot, 5000th shot and 10000th shot. The shape preciseness data are shown in Fig. 24. The shape deviation up to the 5000th shot was within ±0.1 mm. The dimension variance at the 10000th shot was within ±0.1 mm with an exception of a part. The variance more than ±0.2 mm seen in a part results from a deformation of product due to an increase of ejection resistance attributable to heat checks rather than a deformation of the die. Also, the variance is larger than 0.2 mm in the parts colored orange or red in the picture because the shape to be removed by machining is indicated in the 3D data.

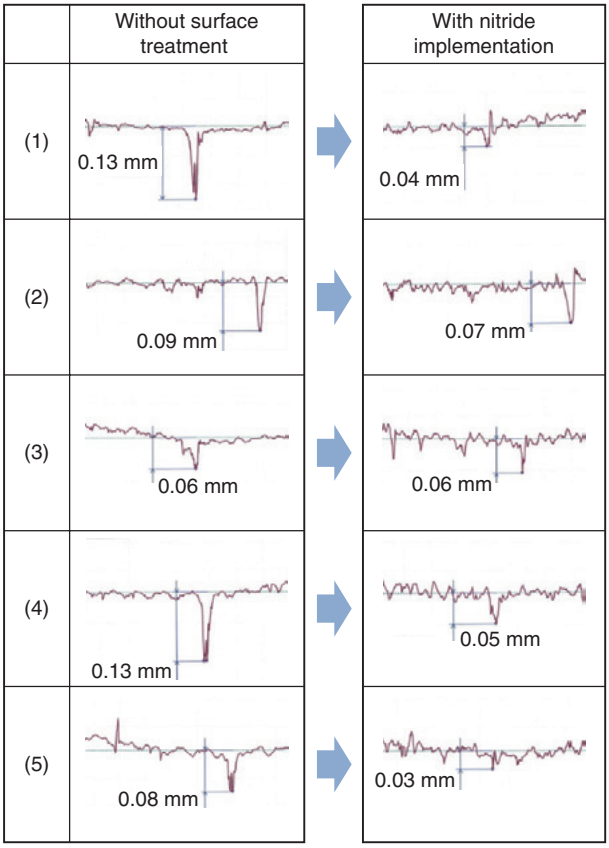


Fig. 22 Measurement results of transferred diches depths on molded parts at corresponding locations of heat checks



Fig. 23 Appearance of cavity

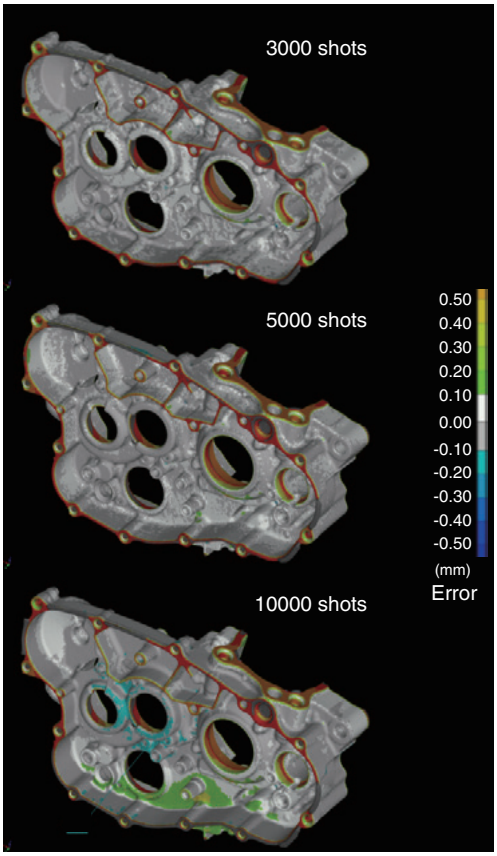


Fig. 24 Shape comparison results of whole shots

There was no damage in the protruding part (6 mm in diameter, 12 mm in length) shown in Fig. 25 and considered as the weakest part of the die. There was no chipping or large crack in other parts of the die.

The overview of the product at the 10000th shot is shown in Fig. 26. Though heat cracks with patched patterns are transferred in some areas, it was not as significant as to affect the marketability. It has been confirmed from the tests that the FCD die developed through this project has the targeted durability.



Fig. 25 Shape section after 10000 shots



Fig. 26 Raw material appearance after 10000 shots

4. Conclusion

Through the studies of manufacturing method of HPDC dies suitable for small-volume production, the new method that satisfies requirements on the shape preciseness, the internal quality and the die life has been developed, allowing reduction of die manufacturing period to a half. The knowledge acquired through the project is described below.

(1) When employing graphite for a forging die, liquid metal forging should be performed after heating the graphite die to a temperature above 700°C. In doing so, a good quality free of fault on the cavity surface is attainable.
(2) After filling the graphite die with the molten metal and applying pressure, the die should be cooled to allow solidification. In doing so, it is possible to fabricate FCD die cavity having shape preciseness with a deviation less than ±0.1 mm and free of internal porosity.
(3) The control of basic metal structures of FCD to a combination of ferrite and pearlite improves heat crack resistance. The higher the ferrite ratio, the less the heat checks occur.
(4) Reduction of Mn content in FCD improves heat checks resistance.
(5) The formation of ridges on the opening of heat check due to plastic deformation can be prevented by the soft nitriding treatment.

References

(1) Anzai, K., Aoyama, S., Niiyama, E., Ebisawa, M., Nagasawa, O., Kaneuchi, T., Hayano, I., Motohashi, T., Sawada, T., Ishikawa, T., Asada, J., Kinoshita, Y., Kuboki, I., Murakami, M., Mizuno, R., Itamura, M., Kanno, T., Kikuchi, T., Nishi, N.: Chuutetsu sei Daikasuto Kani Kanagata ni Kansuru Chousa Kenkyuu, Japan Die Casting Association, p. 96 (2009) (In Japanese)
(2) Rin, W., Kawabata, M.: Mechanism of Eutectoid Transformation of Ductile Iron with Ferrite-Pearlite Duplex Structure, Hitachi Kinzoku Technical Reviews, Vol. 28, p. 20-25 (2012) (In Japanese)
(3) http://www.nbk-okamoto.co.jp/DataBook/d220.htm
(4) Tsujii, N.: Kanagata no Hason Keitai to Jyumyou Koujyou Taisaku, Sanyo Technical Report Vol. 7, No. 1, p. 65-71, (2000) (In Japanese)

■ Author ■



Takunori KITAMURA



Hiroki NAGURA

Optimization of Combustion Chamber Shape in High-efficiency Stoichiometric Combustion Gasoline Engine

Masanobu TAKAZAWA* Tomoaki SASAGAWA* Atsushi OHTA*
Noriyuki TAKEGATA* Taketo YAMADA*

ABSTRACT

The combustion chamber shape of an engine with high compression ratio, long stroke, high-quantity cooled EGR, and retarded intake-valve-closing specifications was optimized to increase the EGR limit and minimize unburned loss and time loss with the aim of enhancing the brake thermal efficiency of a stoichiometric gasoline engine. A piston shallow-dish shape was adopted to optimize the tumble center and the piston top surface distance from the spark plug, and the combustion chamber peripheral shape was optimized to minimize unburned loss. The resulting enhancement of the external EGR rate limit and increase in combustion speed reduced both time loss and unburned loss, and achieved a brake thermal efficiency of 45.2%.

1. Introduction

Recently, interest is increasing in technology for achieving high-efficiency engines with good fuel economy and emissions characteristics from the viewpoint of global environmental issues and reduction of fuel costs.

In order to increase efficiency it is necessary to enhance theoretical thermal efficiency by increasing the compression ratio. Issues for increasing the compression ratio include a delayed ignition timing angle due to thermal loss and knocking, slower combustion speed due to a flatter combustion chamber shape, and reduced thermal efficiency due to increased unburned loss. Introduction of cooled EGR is an effective means of reducing this thermal loss and reducing knocking[(1)]. However, introduction of high-capacity EGR has the issue that the combustion limit and unburned loss increase. In addition, reduction of the effective compression ratio by retarding the intake valve-closing timing (Atkinson cycle) is an effective measure against knocking, but unburned loss due to reduced flow becomes an issue[(2)]. Use of the latent heat of vaporization due to direct injection is an effective measure against knocking produced by a higher compression ratio, but there is the issue that the knocking enhancement effect is reduced by the adherence of fuel to the combustion chamber wall surface[(3)].

An effective method of addressing these issues accompanying an increase in the compression ratio is to increase the length of the engine stroke. Use of a long stroke enables reduction of the flattening of the combustion chamber at the top dead center (TDC). In addition, the surface/volume ratio (S/V ratio) also decreases, enabling reduction of thermal loss. Furthermore, use of a long stroke increases the piston speed, which also enhances the combustion limit by strengthening the flow[(4), (5)].

As described above, the introduction of cooled EGR and use of a long-stroke direct injection engine are effective measures when increasing the compression ratio with the aim of enhancing the brake thermal efficiency of the engine. Potential methods for further increasing engine efficiency in this manner include increasing the EGR limit, reducing unburned loss, and reducing adherence of the direct injection spray to the combustion chamber wall surface.

A long-stroke engine has some degree of freedom in the combustion chamber shape at the same compression ratio. This study positioned enhancement of combustion by the combustion chamber shape as an important factor for pursuing brake thermal efficiency. Investigations were conducted with the aim of presenting a combustion chamber shape that enhances combustion by making use of the degree of freedom of the combustion chamber obtained

* Automobile R&D Center

by increasing the stroke length. The aim of this study was to enhance combustion in terms of the following items by optimizing the combustion chamber shape to enhance the brake thermal efficiency at the stoichiometric air-fuel ratio of a direct injection Atkinson engine with a high compression ratio and a long stroke.

(1) Enhancement of the EGR limit by increasing ignitability
(2) Reduction of time loss by shortening the combustion period
(3) Reduction of unburned loss by changing the combustion chamber wall surface

This paper describes enhancement of the combustion chamber shape, adaptation of the flow and the direct injection spray shape to this new combustion chamber shape, and the resulting achievement of a brake thermal efficiency of 45.2% at the stoichiometric air-fuel ratio in a direct injection Atkinson engine with a high compression ratio and a long stroke.

2. Study Method

2.1. Single-cylinder Engine

Table 1 shows the specifications of the base engine used to optimize the combustion chamber shape.

The brake thermal efficiency (ηe) was obtained from the following equation using the mechanical friction (*FMEP*) and pumping loss (*PMEP*) of a four-cylinder engine relative to the indicated thermal efficiency (ηi) and indicated mean effective pressure (*IMEP*) of a single-cylinder engine.

$$\eta e = \frac{IMEP - FMEP - PMEP}{IMEP} \times \eta i$$

BMEP in this paper refers to the brake mean effective pressure. In addition, the EGR limit in this paper is the value at which the *IMEP* cycle fluctuation exceeds 3%.

2.2. Visualization Engine

Table 2 shows the specifications of the visualization engine.

Visualization was performed by recording the naturally emitted light with a high-speed camera via a side window (Fig. 1). All visualization in this study was performed at an engine speed of 2000 rpm.

2.3. CFD

The flow inside the cylinder was evaluated by 3D-CFD of the engine described in Table 1. Turbulent kinetic energy (TKE) was used as an index of the flow inside the cylinder. Evaluation of TKE inside the engine combustion chamber mainly used 3D-CFD software (VECTIS) made by Ricardo Software. The standard k-ε was used as the turbulence model. Calculation of the boundary conditions used 1D-CFD software and the engine simulation code WAVE made by Ricardo Software.

All CFD in this study was performed at engine speed = 2000 rpm.

Table 1 Specifications of test engine

Bore (mm) × Stroke (mm)	ϕ81 × 121.6 S/B 1.5
Compression ratio (–)	12.5
Expansion ratio (–)	17.0
Engine type	DOHC 4-valve single cylinder
Number of cylinders	1
Displacement (cm^3)	627
Intake port	Tumble port
Air supply	Supercharged
Fuel supply	PI/DI
Piston shape	Shallow dish
Ignition energy (mJ)	450
Gasoline	RON91

Table 2 Specifications of visualization engine

Bore (mm) × Stroke (mm)	ϕ81 × 121.6 S/B 1.5
Compression ratio (–)	11.0
Expansion ratio (–)	15
Engine type	DOHC 4-valve single cylinder
Number of cylinders	1
Displacement (cm^3)	627
Intake port	Tumble port
Air supply	Supercharged
Fuel supply	PI
Ignition energy (mJ)	450
Gasoline	RON91

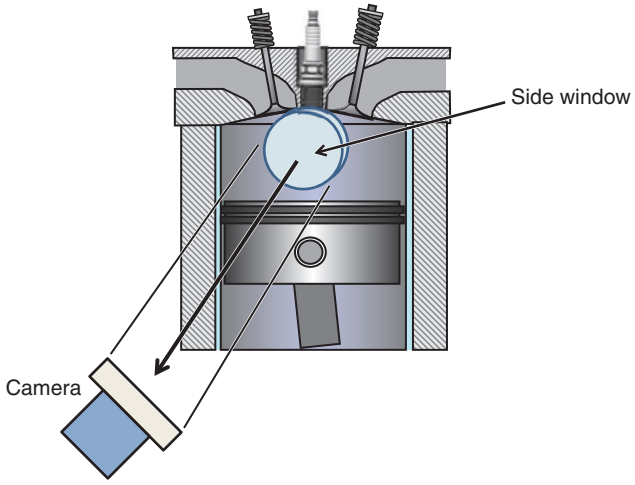


Fig. 1 Method of visualizing combustion

3. Results and Examination

This chapter describes the investigation of methods for achieving each goal and the confirmation results for the combustion chamber shape used to achieve the three goals described in Chapter 1.

3.1. Enhancement of EGR Limit by Increasing Ignitability

In order to enhance the combustion limit when introducing high-capacity EGR, it is necessary to enhance

ignitability. The initial flame behavior is an important factor for enhancing ignitability. Therefore, the factors influencing the initial flame behavior were identified, combustion chamber shapes that enhance this behavior were investigated, and the effects were confirmed in an actual engine.

3.1.1. Combustion chamber shapes that enhance initial flame behavior

Tests were performed using a visualization engine to understand the current initial flame behavior.

Figure 2 shows the results of visualizing the initial flame with a high-speed camera via the side window. The left side in the figure is the IN side (hereafter, the left side is the intake port in all combustion chamber figures), and the light-gray area shows the flame inside the cylinder at ATDC -12 deg. The center of gravity of this light-gray area is labeled "D." The flame in the figure approximates a circle of equal radius centering on D. The radius of this circle is labeled "R."

The dots in Fig. 3 plot the flame center of gravity positions at the timing when R = 10 mm for each cycle. In addition, the star indicates the average position of the flame center of gravity positions for 100 cycles. Assuming the flame is globe-shaped, the timing when R = 10 mm is defined as the heat generation start point, and is thought to reflect the initial combustion.

These results show that the initial flame center of gravity position varies within the combustion chamber. In particular, there is insufficient space in the combustion chamber height direction, so there are concerns that flame growth may be impeded by contact with the piston top surface and the head.

The visualization engine test results indicate that potential measures for avoiding contact between the initial flame and the combustion chamber wall surface include reduction of contact between the initial flame and the piston at the cycle average, and reduction of cycle variation in the flame center of gravity position. Specific methods for achieving each of these are described below.

The influence of piston shape on the mass-combustion rate at the timing when the flame has grown to contact the piston after ignition was investigated by calculations. Here, the flame was assumed to grow around the center of the ignition point, and the mass-combustion rate used the ratio of the flame volume to the combustion chamber volume at the radius when the flame contacts the piston top surface, at the piston TDC position.

The piston shape was investigated with the assumption that the mass-combustion rate at the time of contact increases together with the piston top surface distance from the bottom of the spark plug (plug). A flat piston shape was used as the base shape (A in Fig. 4), and investigations were performed for a shape joined by a large curve (B in Fig. 4) and a shape further carved out only below the plug (C in Fig. 4).

Figure 4 shows the calculation results of the mass-combustion rate at the time of contact between the initial flame and the piston according to the piston shape. All results in the figure are the results at the piston TDC position. The ignition point was set to the midpoint between the head and the piston top surface.

In order to enhance ignitability, it is thought that the flame surface should contact the piston after the flame has grown sufficiently. This investigation found that contact between the flame surface and the piston top surface can be delayed by securing a sufficient piston top surface distance from the bottom of the plug.

When using the base piston shape (A), the flame contacts the piston at the timing when the mass-combustion

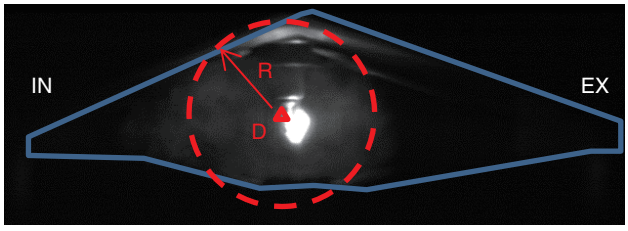


Fig. 2 Initial flame image by visualization

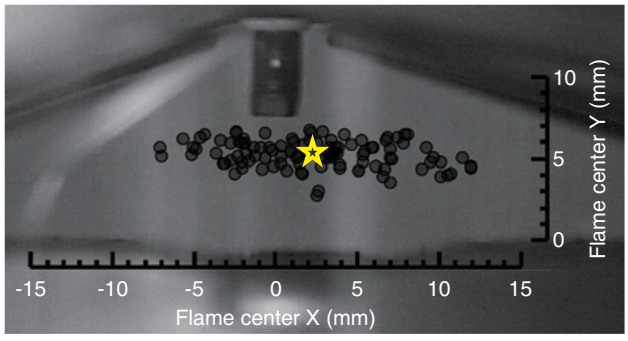


Fig. 3 Cycle variation of initial flame position

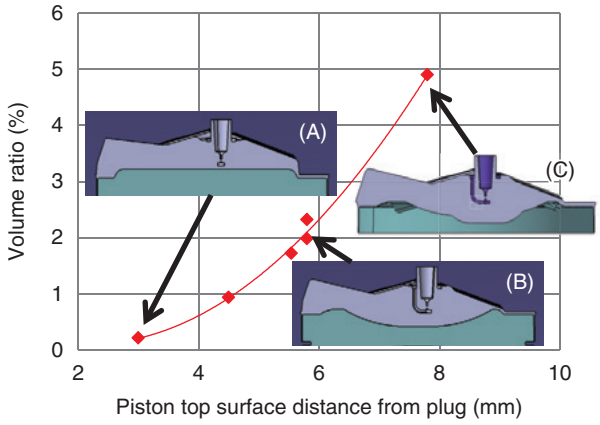


Fig. 4 Calculation results of contact timing between flame and piston top surface

rate is less than 1%. In contrast, the enhanced piston shape (C) provided prospects for delaying the mass-combustion rate at the time of contact by up to 5%.

The mass-combustion rate at the time of contact required during high EGR combustion was confirmed by tests.

Next, regarding a combustion chamber shape that stabilizes initial flame behavior, CFD and visualization tests were performed to organize the approach to stabilizing initial flame behavior.

This engine uses a flow port with strong tumble to support slower combustion speeds due to the introduction of high-capacity EGR. Therefore, bulk flow of approximately 30 m/s is present at the ignition point even during ignition (BTDC 40 deg) (Fig. 5).

Figure 6 shows the results of visualizing the discharge arc shape inside the cylinder during strong flow. The bulk flow indicated in the figure is thought to be present at the ignition point, and this figure shows that the discharge arc is shifted by this bulk flow.

This bulk flow is thought to shift the initial flame from the ignition point. The cycle variation of the initial flame center of gravity shown in Fig. 3 is thought to be a result of fluctuation in the bulk flow near the ignition point for each cycle. To reduce the cycle variation of the initial flame position and obtain stable ignition, it is considered necessary to reduce the bulk flow variation near the ignition point. The bulk flow near the ignition point needs to be reduced while maintaining sufficient flow, and it is thought that this can be effectively achieved by bringing the vortex center of the in-cylinder flow closer to the ignition point.

A combustion chamber shape that brings the vortex center closer to the ignition point was investigated.

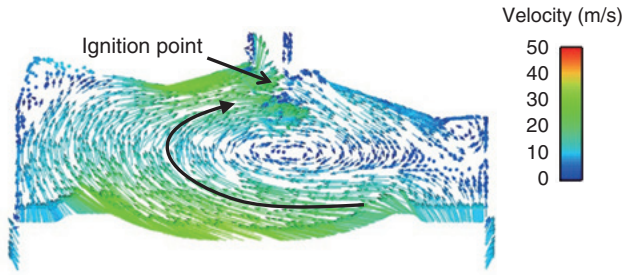


Fig. 5 Bulk flow from tumble

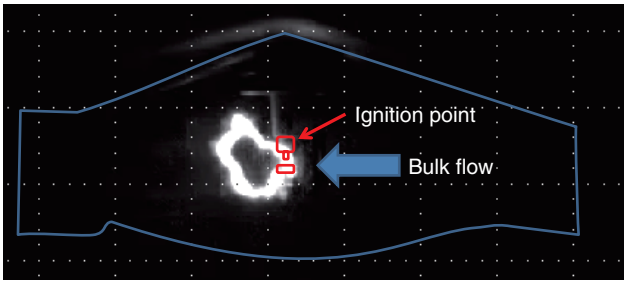


Fig. 6 Bending of discharge arc by bulk flow

Figure 7 shows the difference in the behavior of the tumble vortex center for different piston top surface shapes as calculated by CFD. The base piston shape has a flat piston top surface, so the vortex center is offset from the ignition point. In contrast, for the piston with a shallow-dish top surface shape, the vortex center tends to move towards the center of the shallow dish near the TDC.

It is thought that locating the shallow-dish center directly below the plug enables stabilization of the initial flame behavior even in the condition with high in-cylinder flow.

The effects of a shallow-dish piston shape to control the vortex center were confirmed by tests described hereafter.

In order to enhance the combustion limit when introducing high-capacity EGR, it is thought necessary to delay the timing at which the initial flame contacts the piston by increasing the piston top surface distance from the plug.

In addition, it is also thought necessary to reduce the flow speed near the plug and stabilize the initial flame behavior by giving the piston top surface a shallow-dish shape with the center directly below the plug to lead the tumble vortex center close to the plug.

The following section describes confirmation of the combustion enhancement effects of a piston shape based on the above concepts in an actual engine.

3.1.2. Confirmation of effects by engine tests

The effects of piston shape on enhancement of ignitibility were confirmed from the above-noted viewpoints. Figure 8 shows the tested piston specifications, including the distance from the top surface of each piston to the ignition point, and the mass-combustion rate at the calculated time of contact between the flame and the piston top surface shown in Fig. 4.

Piston (a) in Fig. 8 is the base piston. Pistons (b)

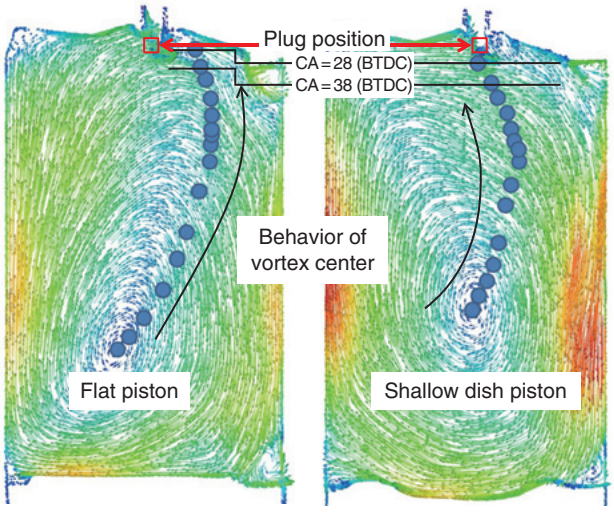


Fig. 7 Behavior of vortex center position by piston shape

through (e) varied the piston top surface distance from the plug with a shallow-dish shape, and piston (f) used a shape carved out below the plug to further increase the piston top surface distance from the plug.

Figure 9 shows the EGR limit relative to the piston top surface distance from the plug. The test was performed under conditions of engine speed = 2000 rpm and IMEP = 810 kPa.

The red line in the figure shows the results of confirming the EGR limit enhancement effect of the pistons shown in Fig. 8. In addition, the black line shows the effect when the plug height is changed with the base piston (flat top surface).

This shows that when the piston has a shallow-dish shape, the EGR limit depends on the piston top surface distance from the plug. However, when using the flat shape, the EGR limit is not enhanced even if the piston top surface distance from the plug is increased by the plug position. In addition, the EGR limit decreased for a piston shape with the part below the plug carved out to increase the piston top surface distance from the plug, such as piston shape (d) in Fig. 8.

	Piston top surface distance from plug (mm)	Mass combustion rate at time of contact (%)
(a)	3	0.21
(b)	5.8	2.32
(c)	4.5	0.93
(d)	5.8	1.98
(e)	5.54	1.72
(f)	9.8	4.90

Fig. 8 Test piston shape list

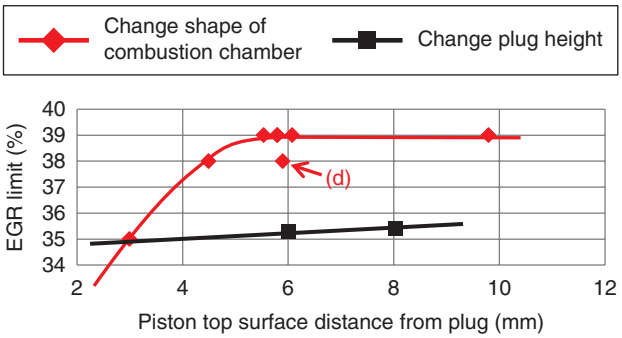


Fig. 9 Test results of EGR limit due to piston top surface distance from plug

In order to increase the EGR limit by enhancing ignitability, it is necessary to stabilize the initial combustion behavior by using a shallow-dish piston to lead the vortex center close to the plug, and also to secure sufficient distance between the piston top surface and the plug. It was found that a piston top surface distance from the plug of 6 mm is needed to enhance ignitability. The mass-combustion rate at the time of contact in this case is approximately 2%.

3.2. Reduction of Time Loss by Shortening the Combustion Period

The drop in thermal efficiency due to an expanded combustion period is an issue for engines with a high compression ratio and high-capacity EGR introduction.

Therefore, the factors comprising the combustion period were extracted, combustion chamber shapes that shorten the combustion period were investigated, and the effects were confirmed in an actual engine.

3.2.1. Investigation of combustion chamber shape to shorten the combustion period

Figure 10 shows the factors comprising the combustion period.

In order to shorten the combustion period, it is necessary to increase the flame propagation speed and reduce the flame propagation distance.

Of the factors shown in Fig. 10, assuming that the engine framework is not changed, the bore diameter cannot be changed, so the flame propagation distance cannot be reduced. Furthermore, if the intake air is the same, the laminar burning velocity will also be the same.

Therefore, combustion chamber shapes that increase the turbulence strength and combustion chamber shapes that realize flame propagation from the center of the combustion chamber while reducing the combustion chamber size were investigated by calculations and visualization tests.

As shown in Fig. 10, strengthening the flow is an important factor for shortening the combustion period. To obtain sufficient TKE at the compression end inside the combustion chamber, it is necessary to maintain the tumble

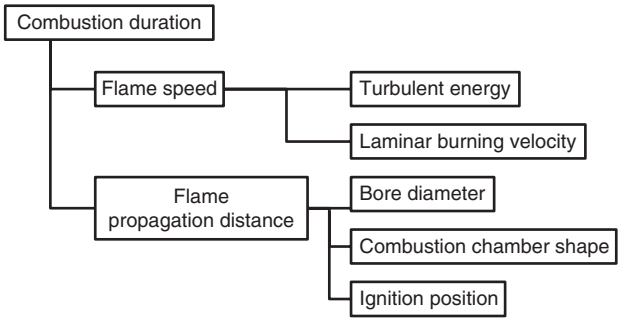


Fig. 10 Tree diagram for combustion period shortening

created by the intake stroke and to form a squish flow in the combustion chamber end-part.

Figure 11 shows the TKE calculation results for the shallow-dish shape. These results show that use of a shallow-dish shape as the piston top surface shape effectively maintains the turbulence strength.

Another approach to increasing the turbulence strength during the compression stroke is to use squish flow. Squish flow creates flow in the combustion chamber end-part during the second half of the compression stroke. This is thought to increase the combustion speed during the second half of combustion and reduce unburned loss.

Figure 12 shows the TKE calculation results by diagonal squish length. The shape with a squish clearance of 14 mm enabled achievement of strong TKE near TDC after a crank angle of -20 deg.

However, the combustion chamber requires a complex shape to realize a squish shape, so there are concerns over an increase in unburned loss and thermal loss.

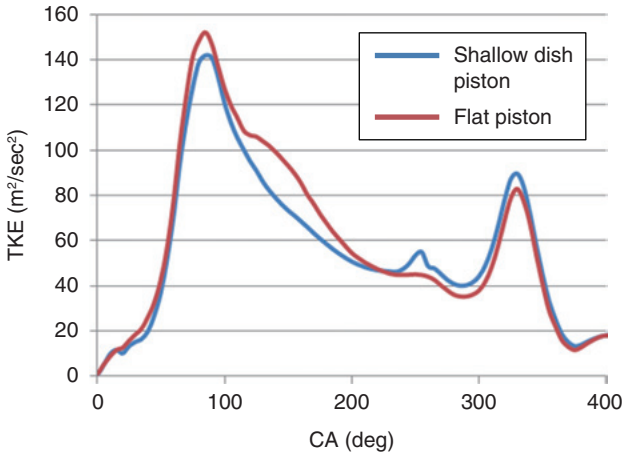


Fig. 11 TKE by piston shape

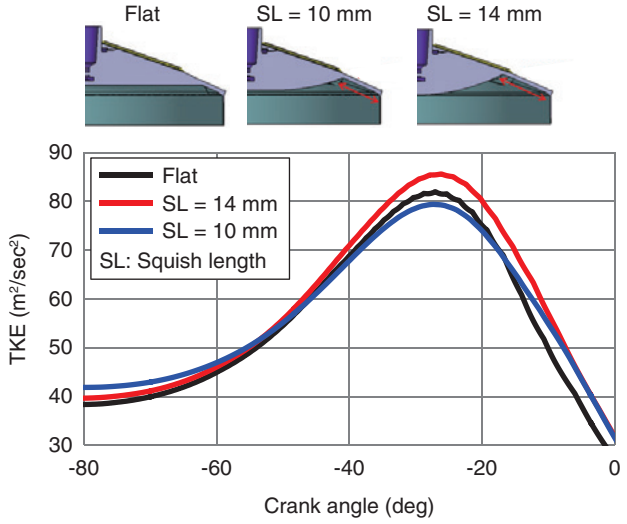


Fig. 12 TKE by squish length

Figure 13 shows the results of visualizing the initial flame with a high-speed camera via the side window. The circles in the figure indicate the flame center of gravity D, and the color of each circle indicates the period from a mass-combustion rate of 50% to 90%. As shown in the figure, the period of the second half of combustion is shorter for cycles in which the initial flame is near the center of the combustion chamber, but the second half of combustion tends to become longer in cycles where the initial flame is shifted toward the intake valve side. The reason for this is thought to be that when combustion starts from one end of the combustion chamber, the flame propagation distance to the opposite end increases. To minimize the flame propagation distance, combustion needs to propagate from the center of the combustion chamber.

The need for a shallow-dish piston shape with the center directly below the plug was described in section 3.1.1. It is thought that locating the vortex center near the plug enables stabilization of the initial flame behavior near the plug and at the same time reduces the flame propagation distance and shortens the combustion period. Therefore, a piston top surface shape that has a shallow-dish shape with the center directly below the piston is also better from the viewpoint of shortening the combustion period.

Figure 14 shows the flame radius and burned volume calculation results. These calculations assume a globe of radius R with the center near the plug to be the flame, and treat the volume V, which excludes the parts cut out from this globe by the combustion chamber wall surface, as the burned area. The burned area reaches the combustion chamber volume at the time when the flame radius is the bore radius of 40.5 mm. The piston shapes used the base shape and the shallow-dish shape shown in Table 3.

Assuming the flame propagation speed to be constant, the flame radius R has a proportional relationship with the period from the start of combustion. The shallow-dish shape piston tends to have a larger burned volume V at the same flame radius R compared to the flat piston, which indicates that the combustion chamber shape of the shallow-dish piston achieves the same mass-combustion rate at an earlier timing. This leads to a shorter combustion period by reduction of the flame propagation distance as shown in Fig. 10.

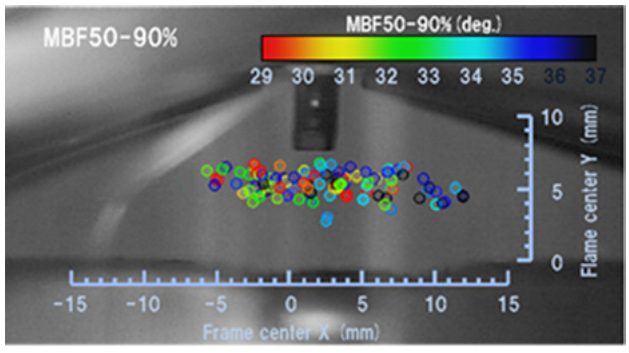


Fig. 13 Combustion period by initial flame position

Table 3 Final piston shape

Piston shape	Swallow dish (wide)
Piston top surface distance from plug (mm)	6
Top land height (mm)	3.5
Squish height (mm)	0.8
Squish	No squish

A compact combustion chamber shape with the volume collected near the plug is thought to be necessary to shorten the combustion period, as expressed by Fig. 14.

Summarizing the above, the following items are considered necessary.

- The piston top surface should use a shallow-dish shape to enhance the flow maintainability in order to shorten the combustion period.
- The piston top shape should use a shallow-dish shape with the center directly below the plug to promote flame growth from the center of the combustion chamber.
- The combustion chamber volume should be collected near the plug to reduce the combustion chamber size and minimize the combustion distance.

The following section describes the results of confirming the combustion enhancement effects of piston shapes based on the above concepts in an actual engine.

3.2.2. Confirmation of effects by engine tests

Figure 15 shows the effects of strengthening the flow by diagonal squish length on unburned loss and time loss. An engine test was performed using the three types of piston shapes shown in Fig. 12. The test was performed under conditions of engine speed = 2000 rpm and IMEP = 810 kPa.

This test used the high-load condition of IMEP = 810 kPa, so the ignition timing angle is delayed by knocking. The introduction of cooled EGR alleviates knocking and also reduces time loss. However, at the external EGR rate conditions, high EGR lengthens the combustion period, which increases time loss. This same tendency was seen for all piston shapes.

Expanding the squish area did not notably enhance the combustion period. On the other hand, unburned loss increased. The reason for this is thought to be that the flame could not propagate to the squish area, so the air-fuel mixture in the squish area could not combust and became dead volume. This indicated that diagonal squish provided no efficiency enhancement effect.

Next, the results of confirming the effects of using a shallow-dish piston to shorten the combustion period are described as follows. Figure 16 shows the results of confirming the reduction in time loss due to piston shape. This test was performed with the plug height changed in accordance with the piston shape to maintain a piston top surface distance from the plug of 6 mm. The test was performed under conditions of engine speed = 2000 rpm

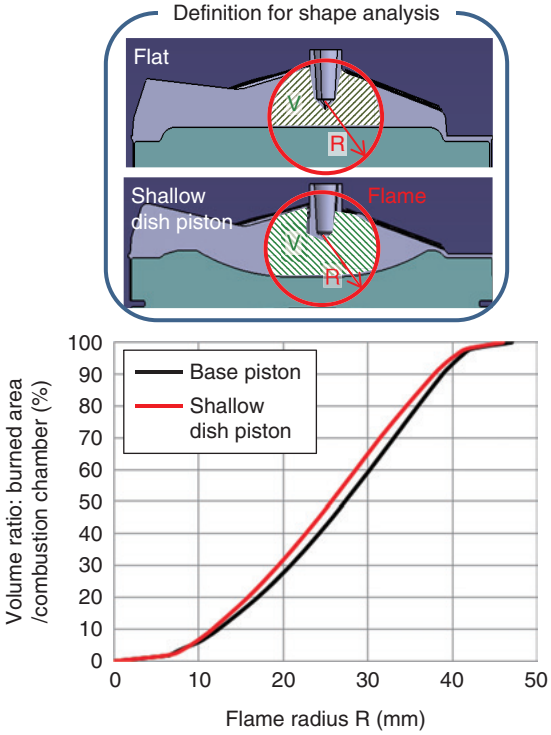


Fig. 14 Difference in burned volume at same flame radius by piston shape

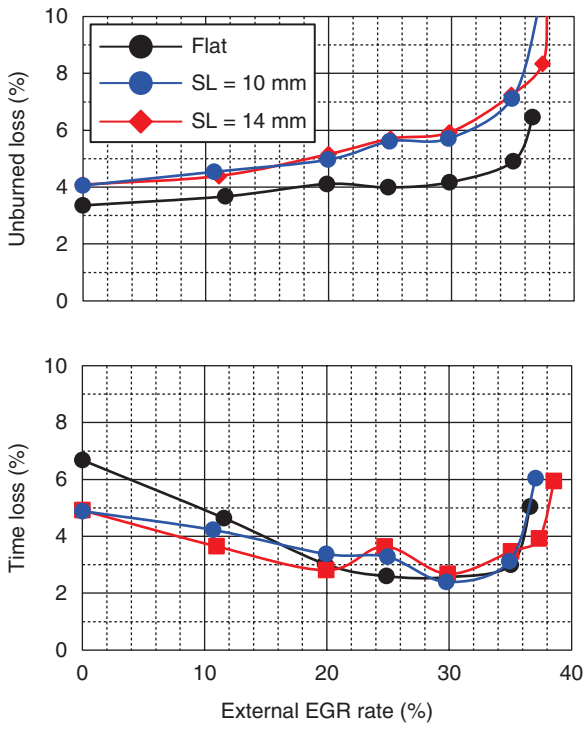


Fig. 15 Effects of squish on unburned loss and time loss

and IMEP = 810 kPa.

Compared to the flat piston, the shallow-dish shapes enabled shortening of the combustion period and reduction of time loss at the same external EGR rate. In addition, combustion was possible without lowering the combustion speed even at higher external EGR rates. This also enabled reduction of time loss by reducing knocking.

3.3. Reduction of Unburned Loss by Changing the Combustion Chamber Wall Surface

A flatter combustion chamber increases unburned loss in engines with a high compression ratio. The reason for this is thought to be that the combustion chamber end-part becomes narrow, so the flame does not reach the end.

3.3.1. Investigation of end-part shape to reduce unburned loss

The combustion chamber end-part shape was investigated focusing on the top land height and the squish height.

The top land is the clearance area between the piston above the top ring and the sleeve as shown in Fig. 17. This area has almost no thickness, so flame is unable to propagate.

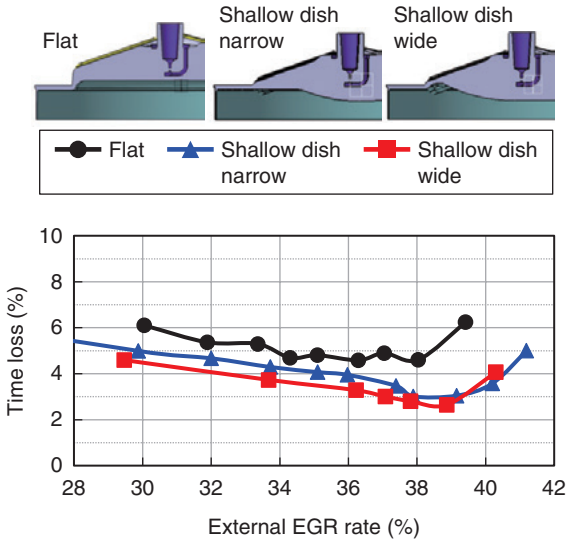


Fig. 16 Time loss reduction by piston shape

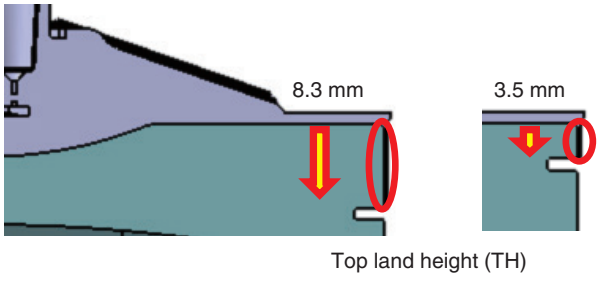


Fig. 17 Definition of top land height

Therefore, unburned loss corresponding to the volume of the top land part is always present. The volume of the top land part is proportional to the first order of the bore, and the combustion chamber volume is proportional to the second order of the bore, so unburned loss becomes more noticeable in engines with a smaller bore. Reduction of the top land part is considered necessary to reduce unburned loss.

This study used a top land height of 3.5 mm, which is the minimum value for which Honda has mass-production results.

The squish height is the part between the piston and the head at the combustion chamber periphery as shown in Fig. 18. This part has a thin height of around 1 mm, making it a challenge for flame to propagate.

For enhancement it was thought necessary to increase the squish height to promote flame propagation, and to minimize the top land height to reduce the unburned area.

This study used a squish height of 0.8 mm, which is the minimum value for which Honda has mass-production results.

3.3.2. Test results

Figure 19 shows the combustion test results for different top land heights. The test was performed under conditions of engine speed = 2000 rpm and IMEP = 810 kPa.

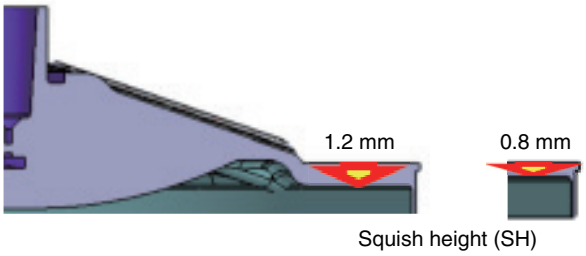


Fig. 18 Definition of squish height

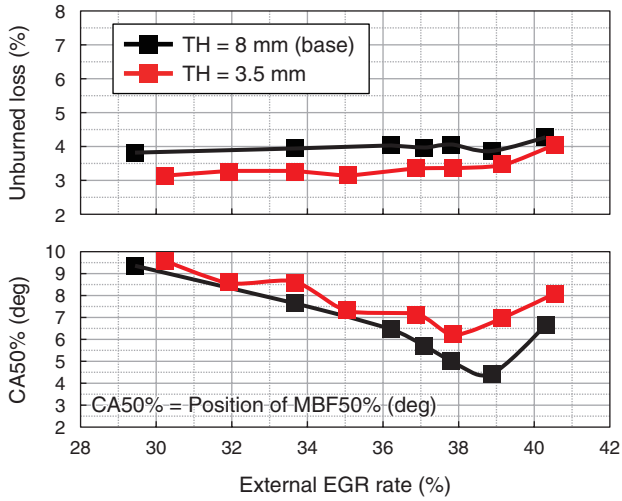


Fig. 19 Unburned loss reduction by piston shape

Unburned loss tended to increase together with the external EGR rate for both pistons. The piston shape with a lower top land height reduced unburned loss at any external EGR rate. However, pistons with a reduced top land height also exhibited a delayed ignition angle due to knocking. The reason for this is thought to be that more of the unburned HC was able to be combusted.

Figure 20 shows the combustion test results for different squish heights. The test was performed under conditions of engine speed = 2000 rpm and IMEP = 810 kPa.

These results show that flame propagation can be enhanced by setting the squish height to 2 mm or more, and that the unburned area can be reduced by setting the squish height to 1 mm or less, both of which enable unburned loss to be reduced. A delay in the ignition timing angle due to knocking was seen in the same manner as when reducing the top land height.

In order to increase the squish height, it is necessary to secure volume at the combustion chamber periphery. This poses a restriction on realizing the combustion chamber concept of securing volume near the plug as described in sections 3.1 and 3.2.

There is no difference in effect when expanding or shrinking the squish part, so it is necessary to reduce the squish height from the viewpoints of EGR limit and combustion period.

3.4. Brake Thermal Efficiency Enhancement Effects of Changing the Combustion Chamber Shape

The efficiency enhancement effects of changing the combustion chamber as described in sections 3.1 to 3.3 were confirmed. Table 3 shows the specifications of the final piston shape, and Fig. 21 shows the final combustion chamber shape. The top land height and squish clearance were set to the minimum values for which there are results in a mass-production engine.

Figure 22 shows the efficiency enhancement effects obtained by this combustion chamber shape. These test results show the effects of optimizing the direct injector spray in addition to the effects of the combustion chamber shape introduced in this paper. The test was performed under conditions of engine speed = 2000 rpm and IMEP = 810 kPa.

Use of a shallow-dish piston and modification of the direct injection spray enhanced the EGR limit and reduced the combustion period, which enhanced efficiency by 0.6 pt compared to the base piston. In addition, reduction of unburned loss by reducing both the top land height and the squish clearance enhanced brake thermal efficiency by 0.6 pt. These measures achieved enhancement of 1.2 pt compared to the base flat piston.

Lastly, to clarify the positioning of brake thermal efficiency in this study, Fig. 23 shows the load characteristics for a shallow-dish piston (TH = 3.5 mm/SH = 0.8 mm) and optimized injector. The external EGR rate was set to maximize the brake thermal efficiency at each load.

As a result, an external EGR rate of 38% was introduced and achieved a maximum brake thermal efficiency of 45.2%.

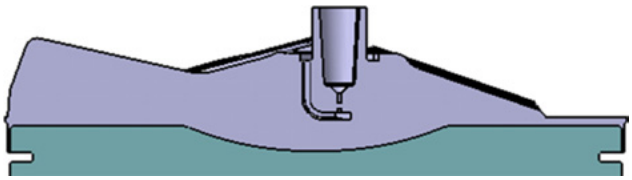


Fig. 21 Final shape of combustion chamber

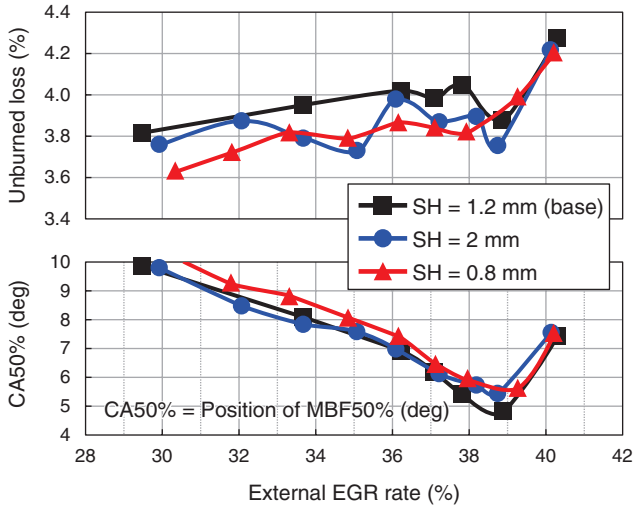


Fig. 20 Unburned loss and knock impact of squish height

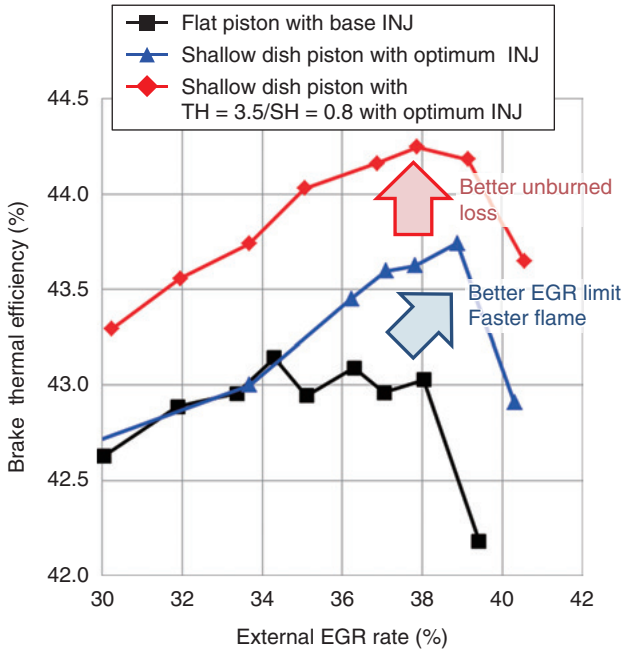


Fig. 22 Brake thermal efficiency due to combustion chamber optimization

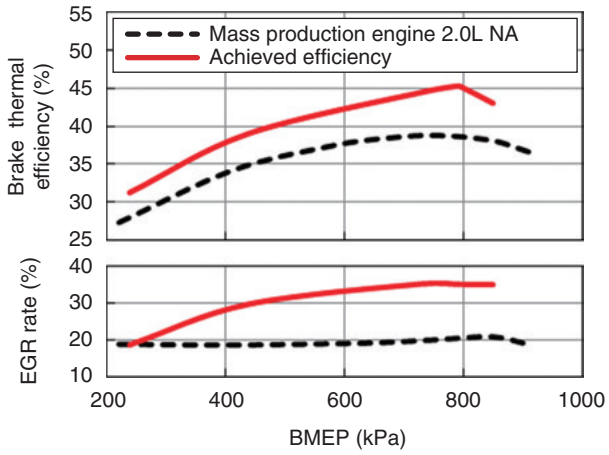


Fig. 23 Final achieved brake thermal efficiency

4. Conclusion

An effort was made to enhance combustion by optimizing the combustion chamber to enhance the brake thermal efficiency at the stoichiometric air-fuel ratio of a direct injection Atkinson engine with a high compression ratio and a long stroke. The following results were obtained.

(1) Delaying the timing angle at which the initial flame contacts the piston and stabilizing initial flame behavior were found to effectively enhance ignitability when the air-fuel mixture is highly diluted by EGR. Ignitability was enhanced and a higher EGR limit was obtained by setting the piston top surface distance from the plug to 6 mm or more and by changing the piston top shape to a shallow-dish shape with the center directly below the plug.

(2) Promotion of turbulence strength by maintaining the flow during the compression stroke, flame propagation from the center of the combustion chamber, and reducing the combustion chamber size to reduce the flame propagation distance were found to effectively shorten the combustion period.
A shallow-dish piston shape was used to maintain tumble during the compression stroke, dead volume such as squish was reduced around the combustion chamber periphery, and the combustion chamber volume was collected around the plug. In addition, the piston top shape used a shallow-dish shape with the center directly below the plug so that the flame grows from the center of the combustion chamber. This resulted in reduced time loss.

(3) Minimizing the volume of the combustion chamber end-part where the flame does not propagate was found to effectively reduce unburned loss.
In particular, minimizing both the top land height and squish height within the ranges that achieve the required durability enabled reduction of unburned loss.

The direct injector spray shape was optimized for the combustion chamber described above. As a result, a brake thermal efficiency of 45.2% was achieved in a direct injection Atkinson engine with a high compression ratio and a long stroke.

References

(1) Alger, T., Mangold, B., Roberts, C., Gingrich, J.: The Interaction of Fuel Anti-Knock Index and Cooled EGR on Engine Performance and Efficiency, SAE Int. J. Engines 5(3), p. 1229-1241 (2012)

(2) Kishi, K., Satou, T.: The new Nissan high efficient 1.2L 3cyl GDI Supercharged Engine enables 95g/km CO_2 Emissions and High Driving Performance, Forstschr Ber Vol Reihe12, 749 Bd2, p. 35-49 (2012)

(3) Sagawa, T., Fujimoto, H., Nakamura, K.: Study of Fuel Dilution in Direct-injection and Multipoint Injection Gasoline Engines, SAE Technical Paper, 2002-01-1647 (2002)

(4) Tagishi, R., Ikeya, K., Takazawa, M., Yamada, T.: Technology for Realization of Gasoline Engine Brake Thermal Efficiency of 45%, Honda R&D Technical Review, Vol. 27, No. 2, p. 1-11

(5) Ikeya, K., Takazawa, M., Yamada, T., Park, S., Tagishi, R.: Thermal Efficiency Enhancement of a Gasoline Engine, SAE Int. J. Engines 8(4), 2015-01-1263 (2015)

■ Author ■


Masanobu TAKAZAWA


Tomoaki SASAGAWA


Atsushi OHTA


Noriyuki TAKEGATA


Taketo YAMADA

Intake Design for Reduction of Duration of Combustion

Taketo YAMADA* Masayoshi TAKAHASHI**
Kenichiro IKEYA* Noriyuki TAKEGATA*

ABSTRACT

Intake design has been conducted as part of research seeking to realize a level of thermal efficiency of 45% in gasoline engines in order to reduce the duration of combustion, which had been extended by EGR dilute combustion. First, the relationship between burning velocity (m/sec) and the square root (m/sec) of turbulent kinetic energy (m^2/sec^2) was studied, and it was determined that these parameters were effective in reducing the duration of combustion. Next, the fact that differences in turbulent kinetic energy occurred due to the direction of the flow passing the intake valve even in the case of flow motion with the same tumble ratio was focused on, and specifications were selected in order to make it possible to obtain a higher level of turbulent kinetic energy from intake ports displaying the same tumble ratio.

A prototype engine head was manufactured using the selected intake port specifications, and test results showed that the target of a main combustion duration of no more than 20 deg was realized under conditions of dilute combustion at an external EGR rate of 30%.

1. Introduction

Today, the realization of increased fuel efficiency and the reduction of exhaust emissions are demanded of automotive manufacturers as part of efforts to reduce the burden on the environment, and associated regulation values are tending to increase in stringency year by year. It is considered that the internal combustion engine will continue to be employed as the source of drive power for motor vehicles for the foreseeable future[1], and the realization of increased thermal efficiency in automotive engines is an important research agenda. Honda has therefore been engaged in research seeking to increase the current maximum level of gasoline engine thermal efficiency of around 39% to 45% or higher[2].

In the course of this research, the results of tests using engines on the market were employed in order to study the necessary conditions for the realization of a level of brake thermal efficiency of 45%. Based on the results of these investigations, the conditions were set at Minimum advance for Best Torque (MBT) operation at a compression ratio of 15 or higher, an absolute boost pressure of 2.5 bar or higher, and an external exhaust gas recirculation (EGR) rate at the 30% level. At the same time, the issue in terms of combustion was to attempt to restrict the main combustion duration during which the mass burn fraction (*MBF*) increases from 10% to 90%, $MBF_{10\text{-}90\%}$, to a crank angle of no more than 20 deg.

2. Research Issues and Approaches

The purpose of the research discussed in this paper was to design an intake that would contribute to the reduction in the combustion period necessary for the realization of a level of brake thermal efficiency of 45%.

During high-EGR combustion, an increase in the quantity of inert gas results in a decline in the laminar burning velocity (S_L), presenting the issue of an increase in the combustion period. In addition, because parameters including the amount of intake air, the equivalent ratio, gas temperature, and pressure are already determined, and S_L is determined by these physical values, restoring S_L to its original value following its decline is considered challenging. The present development therefore focused on restoring the decline in burning velocity by reducing S_L to its original value through the realization of increased turbulent burning velocity (S_T). This was achieved by increasing the turbulent kinetic energy (*TKE*) of the air-fuel mixture.

Turbulence of the air-fuel mixture is obtained through a process of transition to small-scale operation with the collapse of the bulk flow during the compression stroke. The bulk flow focused on in the present research was a tumble flow, and in this case it is normal to strengthen the tumble flow formed by the intake port or increase the ability to maintain the tumble flow by modifying the shape of the tops of the pistons as measures to increase *TKE* during combustion.

However, this presents an issue. The use of an intake

* Automobile R&D Center
** HRD Sakura

port shape that forms a strong tumble flow results in an increase in intake pressure loss. In addition, despite the fact that the tumble ratio is increased in measurements conducted in steady-state flow tests, during actual engine operation, the air-fuel mixture taken into the cylinders flows back to the intake port, and it is not possible to increase the magnitude of the tumble formed in the combustion chamber above a fixed level. As a result, there is a limit to the increase in burning velocity that can be achieved by means of increasing the tumble ratio. Knocking becomes severe in engines employing a high compression ratio. In order to respond to this issue, the research under discussion incorporated the Atkinson cycle in its engine concept, reducing the effective compression ratio by retarding the timing of closure of the intake valve. However, under these conditions the tumble ratio able to be formed in the combustion chamber is lower than the tumble ratio for a standard valve timing.

Because of this, in addition to the generation of a more powerful tumble flow, the achievement of a higher *TKE* from a flow that maintained the same tumble ratio represented another issue for the research.

In general, research focuses on the shape of the combustion chamber, and studies are conducted in order to determine which shapes result in adequate retention of the tumble vortex following its formation[3), (4)]. Little study has been directed towards the retention of the tumble flow during the intake stroke or the degree of dissipation of kinetic energy during the process of formation of the tumble flow. During the present research it was observed that differences sometimes occurred in the *TKE* obtained for the same combustion chamber shape at the same tumble ratio, indicating that the process of formation of the intake air flow was an important factor. A study was therefore conducted that focused on the direction of the intake air flow.

Using the findings obtained, 3D-CFD was employed in order to determine the optimum intake port design, and a prototype engine head was manufactured. The results of tests conducted to verify that the target reduction in the duration of combustion had been achieved demonstrated the validity of the results of the study.

3. Engine Specifications and Indicator for Evaluation of Combustion

3.1. Main Specifications of Engines employed in Study

Table 1 shows the specifications of the engines employed in studies of tumble ratio, strength of turbulence, and duration of combustion.

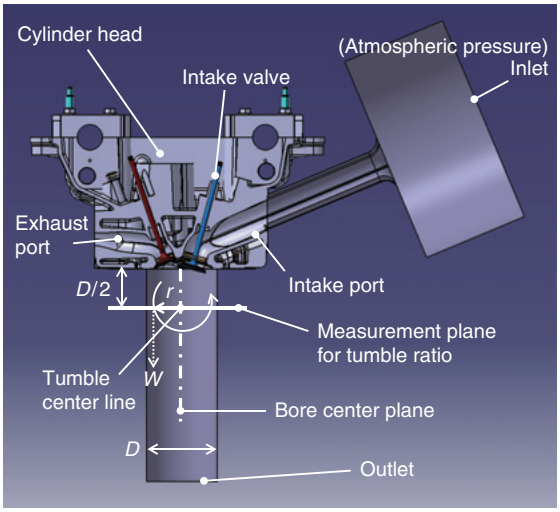
3.2. Method of Evaluation of Tumble Ratio

VECTIS, the 3D-CFD software manufactured by Ricardo Software, was the main tool used in the evaluation of the tumble ratio. Standard k-ε was employed as the turbulence model, and non-steady-state calculations were conducted until the inlet and outlet flow rates converged.

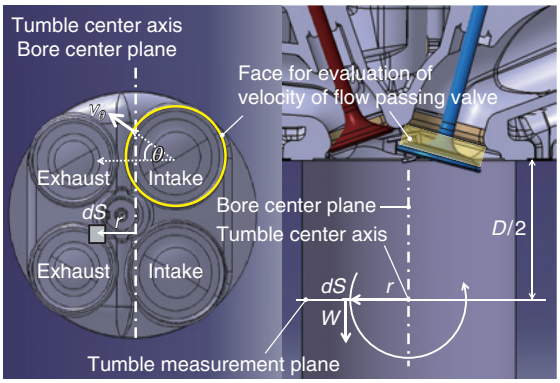
Figure 1 shows a schematic diagram of the relationships between important positions in the entrance region used in calculations. The pressure differential before and after the intake valve (the pressure differential between Inlet and Outlet in the figure) was set at 6 kPa, and the inlet pressure was set at atmospheric pressure. In relation to the bore diameter, D, the measurement plane was positioned $D/2$ mm below the cylinder head gasket plane. Taking the bore center plane including the crankshaft into consideration, the line that intersected the measurement plane was defined as the tumble center line. Angular velocity was calculated from the velocity components passing the measurement plane with the tumble center line as the central axis of rotation, and this angular velocity was used to calculate the tumble ratio[5].

Table 1 Engine specifications

Designation	A	B
Engine type	4-valve SI engine	
Number of cylinders	1	4
Bore × Stroke [mm]	81 × 121.6	73 × 109.6
Intake valve diameter [mm]	30	28
Fuel supply	PI	DI



(a) Evaluation point and position of axis



(b) Method of calculation of tumble ratio and direction of intake flow

Fig. 1 Set-up for steady-state 3D-CFD and evaluation point

The infinitesimal area dS mm^2, extending for r mm from the tumble center line in the direction running from the intake port to the exhaust port, was focused on, and the perpendicular downward velocity component was termed W mm/sec. The average velocity passing the measurement plane, S, was termed W_{ave} mm/sec. The angular velocity in the measurement plane, S, at this time, termed ω rad/sec, is expressed by Eq. (1).

$$\omega = \int (W - W_{ave})\, r^2 dS \Big/ \int r^2 dS \qquad (1)$$

Assuming that W_{ave} and the average piston speed are identical, then the rotational angular velocity of the crank, ω_{mot}, is expressed by Eq. (2).

$$\omega_{mot} = (\pi / L)\, W_{ave} \qquad (2)$$

The tumble ratio when the intake valve lifts x mm, $TR(x)$, is defined by Eq. (3) as the ratio between the angular velocity of the fluid, $\omega(x)$, and the angular velocity of the crank as determined by Eq. (2).

$$TR(x) = \omega(x) / \omega_{mot} \qquad (3)$$

The stroke values shown in Table 1 were employed in the calculation of the average piston speed.

Now, valve lift, $x(CA)$ mm, instantaneous piston speed, $pv(CA)$ mm/sec, and average piston speed, mpv mm/sec, at a crank angle of CA deg during engine operation are considered. With the crank angle when the intake valve is open and closed as CA_{IVO} and CA_{IVC} respectively, the average tumble ratio is defined based on these parameters by Eq. (4).

$$TR = \frac{1}{CA_{IVC} - CA_{IVO}} \int_{CA_{IVO}}^{CA_{IVC}} \frac{\omega[x(CA)]}{\omega_{mot}} \left[\frac{pv(CA)}{mpv} \right]^2 dCA \qquad (4)$$

3.3. Method of Evaluation of *TKE*

As in the case of the tumble ratio, VECTIS was used in the evaluation of *TKE* in the combustion chamber. Ricardo Software's 1D-CFD engine simulation code WAVE was employed to calculate boundary conditions. Boundary conditions at the upstream end of the intake manifold and the exhaust-facing cylinder head face were calculated using a model simulating an engine test environment.

Stoichiometric combustion at an engine speed, *NE*, of 2000 rpm was set as the operating condition. With regard to load, the point at which the indicated mean effective pressure (IMEP) reached 810 kPa was selected. When studying differences in combustion duration at the same laminar burning velocity, measurements were taken and calculations were conducted with the volumetric efficiency (η_V) set at the level at which the IMEP was 810 kPa during MBT operation.

3.4. Indicator for Evaluation of Combustion

The timing at which the *MBF* was 50%, known as the combustion center of gravity and notated as $MBF_{50\%}$, was employed as the indicator for evaluation of combustion. $MBF_{10\text{-}90\%}$ is often used in the evaluation of combustion duration, and is also used as a method of expressing target values. Because S_L and S_T are employed in studying the dimension of velocity (m/sec), $MBF_{10\text{-}90\%}$ was also studied by converting it into the dimension of velocity using the bore diameter, as shown in Eq. (5). Here, this parameter is defined as S_C, the in-cylinder virtual flame velocity.

$$S_C = [(D/2) \times (0.9 - 0.1)] / MBF_{10\text{-}90\%} \qquad (5)$$

A method of evaluation of the strength of turbulence is an important factor in increasing S_T. In the present research, the average flow velocity at a fixed point was determined, and the standard deviation of the magnitude of flow velocity (the rms value of change in velocity) was defined as the turbulence velocity (u'). The relationship between *TKE*, which is often used to evaluate the strength or weakness of turbulent flows in relation to combustion in engines is $TKE = 1.5u'^2$, and as in the case of the discussion of $MBF_{10\text{-}90\%}$, u' was employed for comparison with S_C.

3.5. Selection of Timing for Evaluation of Air-fuel Mixture

The *TKE* of the air-fuel mixture normally changes with time, and also differs depending on the area of the combustion chamber. In addition, research results show that the position of the flame front varies moment to moment, and that the scale of the eddies that can be used varies depending on the size of the flame front[6]. The modeling of all of this would entail a significant computation cost. In order to employ a simplified method and be selective with specifications to a certain extent, the present study used Engine A in Table 1 to determine whether it would be possible to use average values for the combustion chamber at specific timings to represent the situation overall.

Tests were conducted of the effect on $MBF_{10\text{-}90\%}$ of varying the flow as a result of differences in the shape of the intake port or the timing of closure of the intake valve. The conditions discussed in Section 3.3. were used for *NE* and the load conditions. Five representative measurement points were selected for comparison: TDC; ignition timing; BTDC 30 deg, which represents the greatest difference to *TKE*; the average value from BTDC 30 deg to ATDC 30 deg, which was assumed to represent the combustion duration; and the average value for the intake compression stroke. Figure 2 shows the relationship between the results and *TKE* in the combustion chamber as determined by CFD, and Table 2 shows the respective coefficients of correlation.

A variety of arguments exist regarding methods of evaluation of *TKE*. The present research found that *TKE* at BTDC 30 deg, which displayed the greatest difference with average *TKE* in the combustion chamber, had the strongest correlation with $MBF_{10\text{-}90\%}$. The coefficient of correlation between the two parameters was also sufficiently greater than 0.8. BTDC 30 deg was therefore adopted as the timing for evaluation of *TKE* in the present research. This value will be notated as $TKE_{\text{BTDC 30 deg}}$ below.

Table 2 Coefficient of correlation between *TKE* and $MBF_{10\text{-}90\%}$

Measurement point	Coefficient of correlation
TDC	−0.7341
Ignition timing	−0.7165
BTDC 30 deg	−0.9397
Average from BTDC 30 deg to ATDC 30 deg	−0.9214
Intake and compression stroke average	−0.8538

3.6. Definition of Flow Passing Valve

In order to consider the degree of turbulence and the direction of the intake flow, the flow passing between the intake valve and the valve seat was studied in the present research. This flow was termed the flow passing the valve, and its magnitude was defined as the flow velocity passing the valve. The positions for evaluation of this parameter are shown in Fig. 1. The intake port of the engine employed in the study was symmetrical with the center of the bore. The single side of the valve shown in Fig. 1(b) was studied. The flow velocity passing the valve in the area forming an angle of θ rad with the directional axis from the intake valve in the direction of the exhaust valve, in the opposite direction to the cylinder center, was termed v_θ.

The average flow balance (FB) was defined as a scale to express whether the flow was directed inwards or outwards. Equations (6) and (7) respectively show the average velocity, $v_{ave}(x)$ and the FB value, $FB(x)$, of the flow passing the valve at a valve lift of x mm, $v_\theta(x)$.

$$v_{ave}(x) = \int_{\theta=0}^{\theta=2\pi} v_\theta(x)\, d\theta / 2\pi \qquad (6)$$

$$FB(x) = \frac{1}{\pi}\int_{\theta=0}^{\theta=\pi} \frac{v_\theta(x) - v_{-\theta}(x)}{v_{ave}(x)}\, d\theta \qquad (7)$$

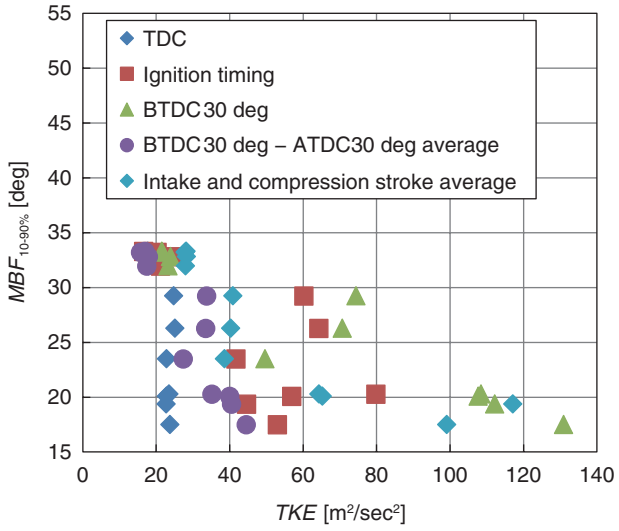


Fig. 2 Relationship between *TKE* and $MBF_{10\text{-}90\%}$

With the flow coefficient termed $Cf(x)$, the FB value is defined in the same way as the average tumble ratio by Eq. (8).

$$FB = \frac{1}{CA_{IVC} - CA_{IVO}} \int_{CA_{IVO}}^{CA_{IVC}} \frac{FB[x(CA)]}{Cf[x(CA)]} \left[\frac{pv(CA)}{mpv}\right]^2 dCA \qquad (8)$$

In the present case, 16 divisions were employed in the space around the intake valve, and 15-deg increments were used for the crank angle.

4. Correlation between $MBF_{10\text{-}90\%}$ and u' of Air-fuel Mixture

First, studies were conducted in order to determine whether the realization of increased *TKE* was effective in reducing the duration of $MBF_{10\text{-}90\%}$. Taking into consideration the expression of *TKE* as the dimension of velocity in studying the correlation, the evaluation was conducted for $u' = \sqrt{TKE/1.5}$. The relationship between this figure and S_C was studied.

4.1. Relationship between $MBF_{50\%}$ and S_C

S_C is also affected by $MBF_{50\%}$. It was necessary to correct S_C in order to render the conditions uniform. Tests were therefore conducted using the two engines shown in Table 1 to study the relationship between $MBF_{50\%}$ and S_C.

Figure 3 shows the results of the study of the relationship between the two parameters with different ignition timings at several EGR recirculation rates and η_V, at an engine speed of 2000 rpm. There is a first-order negative correlation between the position of the combustion

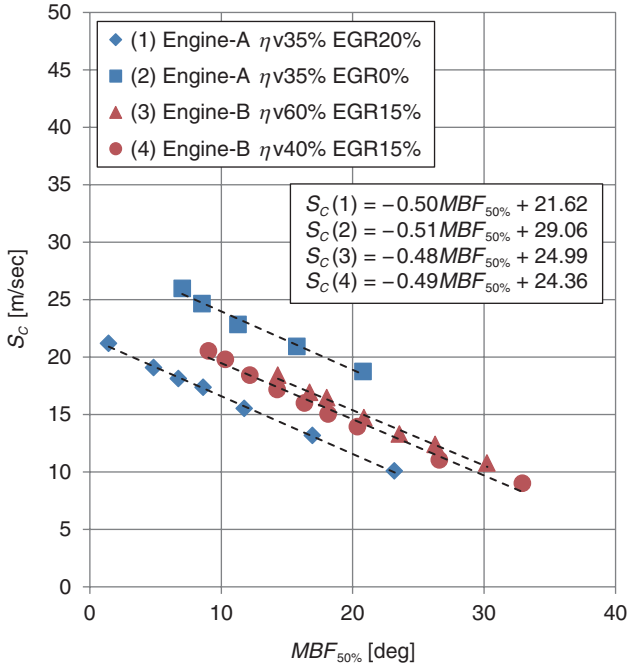


Fig. 3 Relationship between S_C and $MBF_{50\%}$ to determine amount of correction

center of gravity and S_C, and the gradient was judged to be the same in each case. Taking into consideration the fact that the effect of differences in the load points is expressed as changes in the intercepts in the graph, S_C was corrected based on the relationship shown in Eq. (9), and the relationship between S_C and u' was examined.

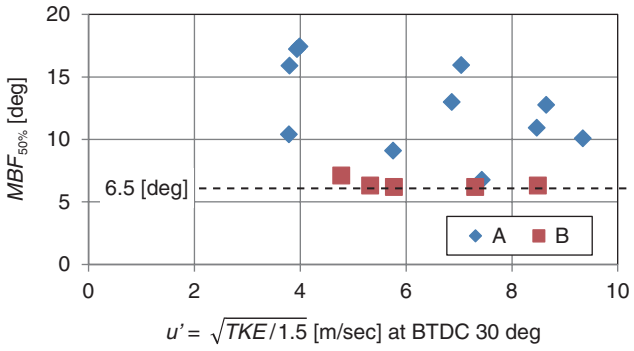
$$\partial SC / \partial MBF_{50\%} = -0.5 \qquad (9)$$

4.2. Correlation between Duration of Combustion and u' of Air-fuel Mixture

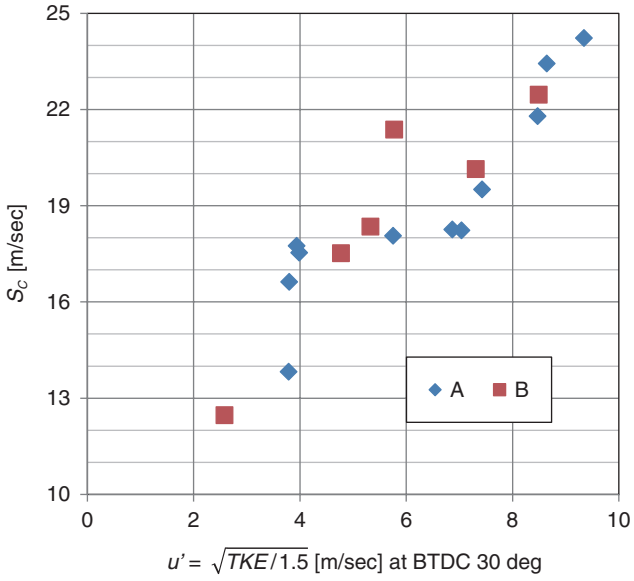
Tests were conducted in which a variety of spacers were employed in the intake ports of the different engines shown in Table 1 in order to determine how the duration of combustion would change with changes in *TKE*. Results for an S_C corresponding to an $MBF_{50\%}$ of 6.5 deg were isolated from $MBF_{10\text{-}90\%}$ and $MBF_{50\%}$ obtained from actual engine tests. Figure 4(b) shows the relationship between these results and $u' = \sqrt{TKE/1.5}$ obtained from 3D-CFD. Despite possessing different frameworks, the two engines can be approximated by the same lines, and a first-order correlation could be observed between in-cylinder S_C and $\sqrt{TKE}$. The results could be approximated as shown in Eq. (10).

$$S_C = 1.36u' + 10.7 = 1.11\sqrt{TKE} + 10.7 \qquad (10)$$

It was therefore considered that increasing *TKE* was effective in increasing burning velocity at least within the scope shown in Fig. 4(b).



(a) $MBF_{50\%}$ for each measurement point



(b) Relationship between $u'_{\text{BTDC 30 deg}}$ and S_C following correction of $MBF_{50\%}$

Fig. 4 First-order correlation between $u'_{\text{BTDC 30 deg}}$ and S_C following correction of $MBF_{50\%}$

5. Correlation between Tumble Ratio and *TKE*

Next, cases in which a different *TKE* was obtained at the same tumble ratio were focused on, and a study was conducted in order to determine the factors producing these differences.

5.1. Study of Correlation between *TKE* and Tumble Ratio

The correlation between the tumble ratio and *TKE* was studied using Engine B in Table 1. In order to greatly change the tumble ratio, a tumble plate of the type shown in Fig. 5 was fitted in the intake port. The study was conducted using a shape model with the angle between the horizontal direction and the direction of the plate (θ_1), the plate length (L_1), and position in the direction of plate height (x_1) as parameters.

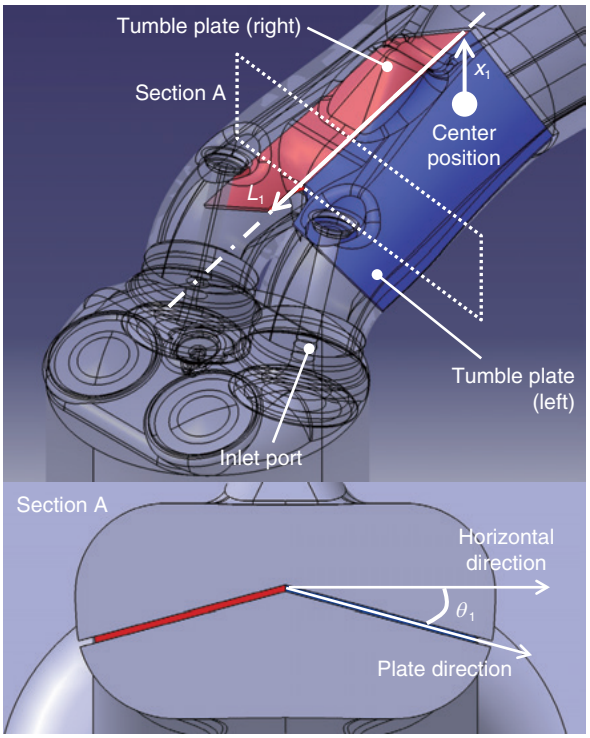


Fig. 5 Shape of tumble plate to change tumble ratio

Figure 6 shows the relationship between *TKE* and the tumble ratio determined by the study. There is a positive correlation between the tumble ratio and *TKE*, but a range of values for *TKE* can be obtained at the same tumble ratio. Within the range $4.25 < TR < 4.45$ (termed "Range 1" below), *TKE* values of 65.5 m^2/sec^2 and 21.4 m^2/sec^2 are obtained. This equates to S_C of 19.6 m/sec and 15.8 m/sec using Eq. (10). If the figures are substituted in Eq. (5), this results in a difference of 4.35 deg at $MBF_{10\text{-}90\%}$.

5.2. Quantification of Direction of Flow and Correlation with *TKE*

The study discussed in the previous section was conducted using the same engine framework specifications, including the combustion chamber shape, and the same intake conditions, including the quantity of intake gas. It was therefore judged that the differences in *TKE* were due to differences in the behavior of the intake air flow from the intake port into the cylinders. This will be considered in this section. First, a comparison will be conducted of results from Range 1 in Fig. 6, at the same tumble ratio. Characteristic values were taken from this range, and the distribution of the flow passing the valve and the tumble ratio were calculated. Figure 7 shows the distribution of the flow velocity passing the valve through horizontal cross-sections. The calculated distribution of flow velocity passing the valve differs depending on the direction of the flow passing the valve, despite the fact that the tumble ratio is the same. In the case of inward flows, there are high-flow-velocity areas close to the center of the sleeve on the exhaust side. As the flow is directed outwards, the high-velocity areas shift to the side.

Figure 8 shows the relationship between Range 1 *FB* values and *TKE*. *TKE* displays a tendency towards dependence on the value of *FB*. When *FB* exceeds 1, *TKE* reaches its peak. These results indicate the existence of an optimum direction for the intake air flow.

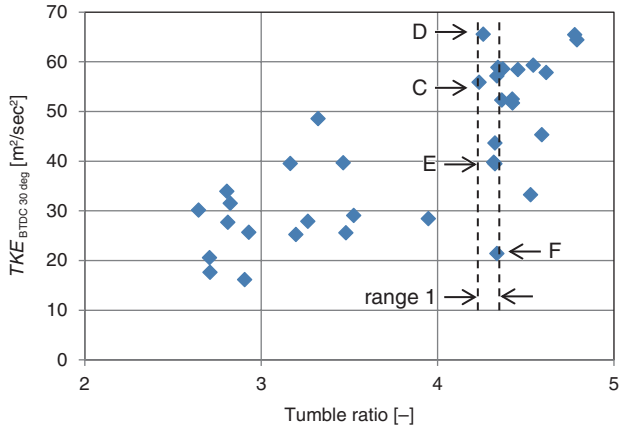


Fig. 6 Distribution of results for $TKE_{BTDC\ 30\ deg}$ for same tumble ratio

5.3. Consideration concerning Relationship between Direction of Flow and *TKE*

The results of steady-state flow calculations showed that *TKE* reached its peak at a point at which the flow passing the valve was directed outwards. In order to consider the meaning of this, a study was conducted to determine how tumble vortex are formed, and how they are related to differences in *TKE*. Based on the principle that the flow speed at the center of a vortex is 0 m/sec, the center of a vortex were observed via iso-velocity surfaces expressing low-flow-

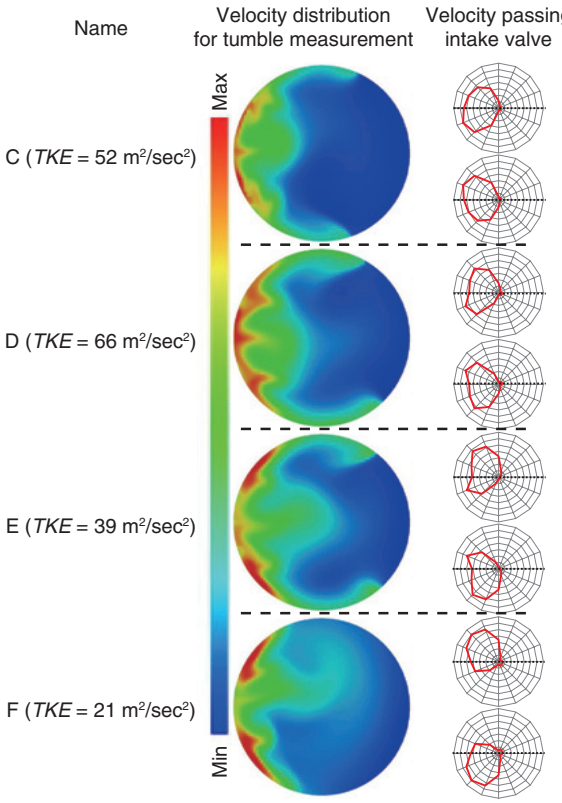


Fig. 7 Distribution of air flow velocity through horizontal cross-section

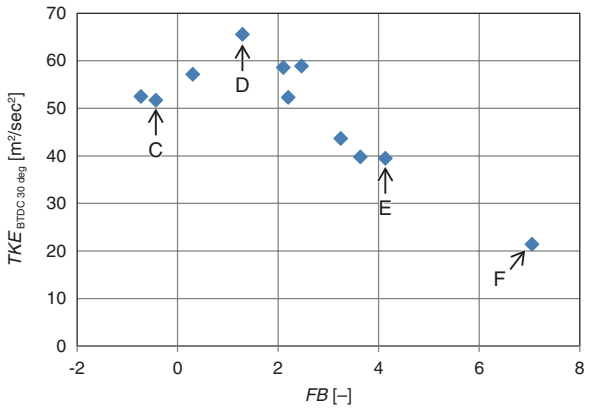


Fig. 8 Relationship between $TKE_{BTDC\ 30\ deg}$ and *FB*

speed areas (yellow surfaces expressing 3 m/sec flows and green iso-velocity surfaces expressing 5 m/sec flows).

Results were compared for Specification D, for which *TKE* was the highest, and Specification C, in which *FB* approaches 0 and it is considered that the flow passing the valve is almost straight. Figure 9 shows iso-velocity surfaces for both specifications. The vortex center line becomes straight more rapidly for Specification D than Specification C, and there is minimal deformation or migration of the vortex following this. In other words, a straight flow of intake air from the intake port in the direction of the exhaust port forms a curved tumble vortex. Directing the flow of intake air slightly towards the outside reduces the bending and distortion of this tumble vortex in the combustion chamber.

Figure 10 shows iso-velocity surfaces, flow velocity vectors at the bore center, and the up-down flow velocity distribution at a position 60 mm below the cylinder head as the position of the center of the tumble vortex at ATDC 150 deg. The results of steady-state flow calculations for Specification C (Fig. 7) showed an area of high-velocity flow at the center of the sleeve on the exhaust port side. In an actual engine, the pistons are beyond this high-velocity area, and the downward flow is transformed into an upward flow. The tumble vortex is formed between these downward and upward flows. As a result, the tumble vortex is formed in a distorted shape, surrounding the area of high-velocity flow.

The direction of the flow passing the valve outwards reduces the flow velocity at the center of the crankshaft direction, and the flow velocity at the sides increases. As a result, the area in which the up-down flow velocity is low becomes a straight line, and the tumble vortex approaches a straight line (Specification D).

Figure 11 shows a conceptual diagram of this flow from the intake valve. Of the flows passing the valve, the flow

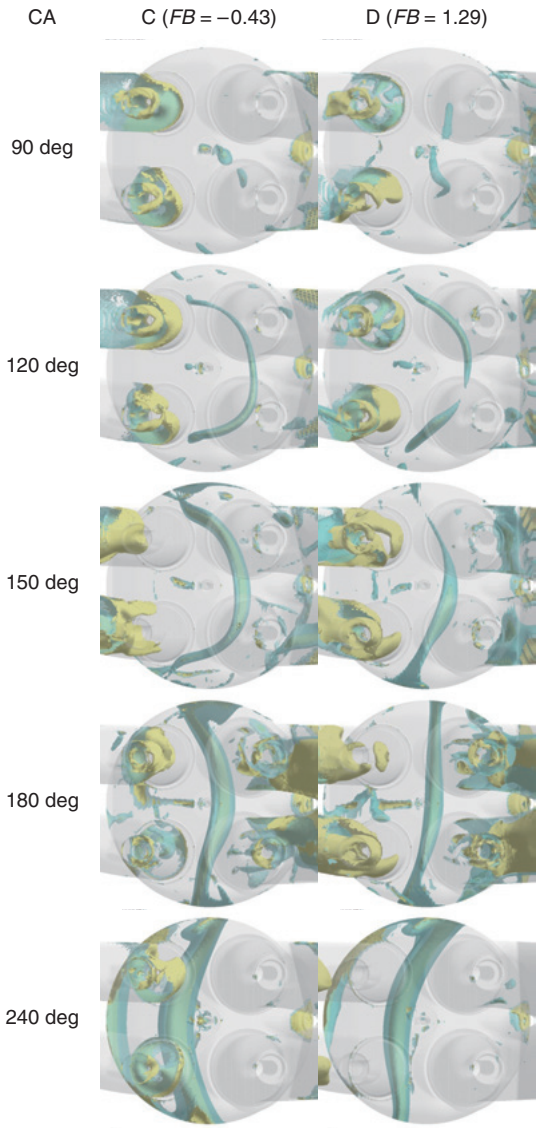


Fig. 9 Generation of curved tumble vortex center line and progression over time

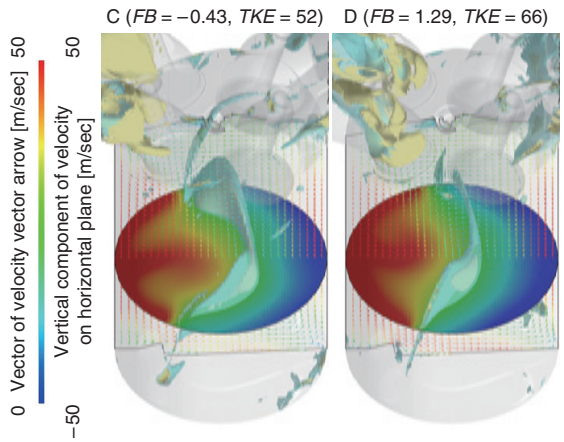


Fig. 10 Spatial relationship between curve of tumble vortex center and downward and upward flows

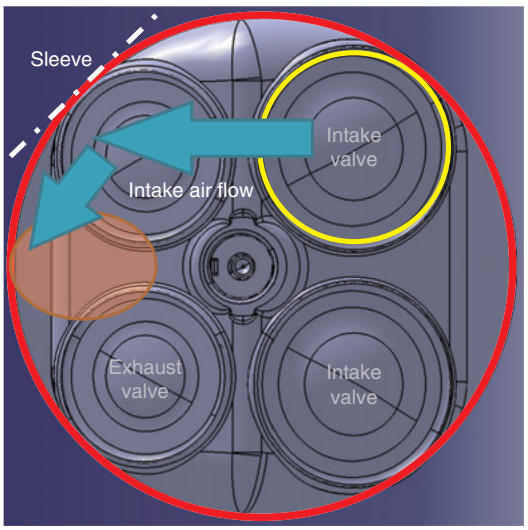


Fig. 11 Conceptual diagram of intake air flow

that runs straight from the intake valve to the exhaust valve is directed inwards when it strikes the bore sleeve because the sleeve is cylindrical, and as in the case of Specification C, the flow concentrates at the center of the exhaust port side of the sleeve. Because of this, the flow being directed outwards to a certain extent is essential to the formation of a linear tumble vortex.

The distortion of the vortex center locally increases the flow velocity, and the velocity gradient steepens. It is normal procedure to treat the air-fuel mixture as a Newtonian fluid; that is, the shear stress acting on the fluid is treated as being proportional to the velocity gradient, and it was considered that a steeper gradient would result in a greater dispersion of kinetic energy.

5.4. Considerations regarding the Relationship between Flow Direction and Stability

Curved tumble vortices were considered next. Figure 12 shows the tumble vortex and flow speed vectors in a cross-section of the bore for Specification C at ATDC 150 deg. The front view shows a normal tumble, but the plan view shows that the tumble vortex is curved. The side view indicates symmetrical vortex motion on the left and right. This phenomenon, known as ω tumble, is focused on when discussing the stability of flow motion from the perspective of variations in cycles[7]. The formation of the distorted tumble vortex axis creates instability for at least the time intervals termed cycle time. In addition, ω tumble

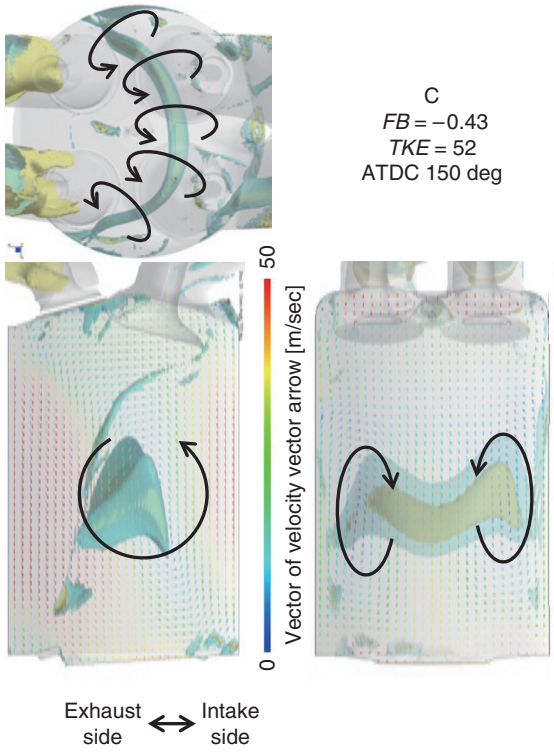


Fig. 12 Curved tumble vortex center line and velocity gradient

is not an independent phenomenon, but occurs as a result of the distortion of the tumble vortex, which is conventionally studied. For this reason, the setting of an appropriate flow balance is an effective means of controlling ω tumble.

When the intake valve is closed and no new gas is being introduced, the curved tumble vortex is unstable from the perspective of symmetry, and is repeatedly distorted even within a single cycle. If it is considered that the distortion of the tumble vortex leads to small motions from the perspective of energy cascades, it is possible that there is a decline in the ability of the tumble vortex to retain kinetic energy.

6. Application to Intake Port Design

6.1. Setting Target *TKE*

Honda's research on the realization of a level of thermal efficiency of 45% in gasoline engines set a main combustion duration within 20 deg at an EGR rate of 30% as targets. However, the main combustion duration of Engine A in Table 1, which employed the intake port of the mass-production base engine, was 35 deg. In addition, it was necessary to advance the position of the combustion center of gravity by 4 deg in order to realize MBT operation. Taking S_C from Eq. (5) into consideration, a 15 deg reduction in the combustion duration would equate to a difference of 8.33 m/sec. If it were possible to advance the position of the combustion center of gravity by 4 deg, Eq. (9) indicates that S_C would be increased by 2 m/sec. Subtracting this from the figure of 6.33 m/sec, it would then be necessary to increase *TKE* by the amount that would realize a 6.33 m/sec increase in S_C. From Eq. (10), this would be an increase of 5.71 m/sec in $\sqrt{TKE}$. Table 3 shows the tumble ratio, *FB*, and *TKE* before and after the study of changes in the shape of the intake port. For the base port shape, *TKE* is 21.6 m^2/sec^2, and $\sqrt{TKE}$ is 4.65 m/sec. This means that a $\sqrt{TKE}$ of 10.4 m/sec and a *TKE* of 107.2 m^2/sec^2 are actually necessary. On the other hand, while the correlation is weak, if the relationship between the tumble ratio and *TKE* is estimated as

$$TKE \propto 22.5\ TR \qquad (12)$$

from Fig. 6, then a tumble ratio of over 4 is necessary. However, CFD results suggested that at a tumble ratio in excess of 4, the intake air would tend to flow back into the intake port. Because of this, it was necessary to realize a *TKE* of 107.2 m^2/sec^2 at a tumble ratio of 4 or below. It was therefore necessary to use the concept of flow balance in order to obtain a greater strength of turbulence from the flow at the same tumble ratio.

6.2. Selection of Intake Ports using CAE and Results of Engine Tests

Intake port shapes were studied with consideration of the limitations inherent in the manufacture of actual

Table 3 Degree of enhancement of intake flow

	TR (–)	*FB* (–)	*TKE* (m^2/sec^2)
Base	2.34	0.04	21.6
Following modification	3.96	0.87	113.3

engine heads in order to determine a shape producing a tumble ratio of around 4. Table 3 shows the tumble ratio and *FB* before and after the study, and Fig. 13 shows the differences in the shapes of the intake ports. Table 3 also shows the results of verification of *TKE*. Because *FB* was at its maximum when the tumble ratio was close to 4, and the target value of 107.2 m^2/sec^2 had been realized for *TKE*, the decision was made to manufacture a prototype engine head at this stage, and tests were conducted in order to determine its effectiveness in reducing the duration of combustion. The results are shown in Fig. 14. The results show that the main combustion duration, which had been 35 deg, had been reduced to 20 deg, indicating that the target for reduction of the duration of combustion had been achieved.

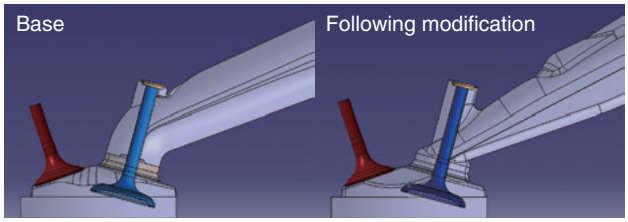


Fig. 13 Intake port shape before and after modification

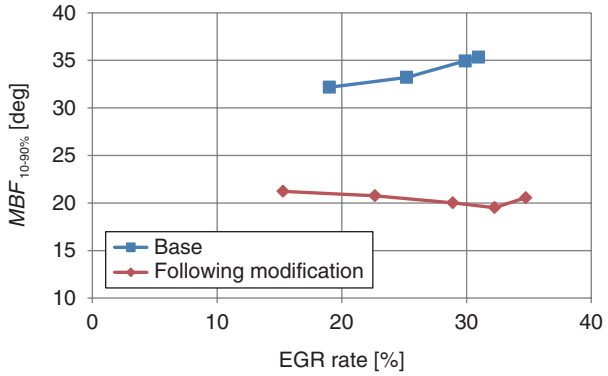


Fig. 14 Reduction of duration of combustion by high *TKE*

7. Conclusion

The research discussed in this paper demonstrated that increasing the *TKE* of the unburned air-fuel mixture is effective in reducing the duration of combustion. The results showed that the *TKE* finally obtained displayed a range of values even for the same tumble ratio, and a study of the *FB* value indicated that greater strength of turbulence could be obtained from flows at the same tumble ratio. These findings were applied in the development of an intake port of engine A in Table 1, making it possible to reduce the main combustion duration by 15 deg at an EGR recirculation rate of 30%, including the amount realized by increasing the tumble ratio, and contributing to the realization of a level of thermal efficiency of 45%.

References

(1) International Energy Agency: Part4 Scenarios and Technology Roadmaps, Chapter13 Transport, Energy Technology Perspectives 2012, p. 443 (2012)
(2) Tagishi, R., Ikeya, K., Takazawa, M., Yamada, T.: Technology for Realization of Gasoline Engine Brake Thermal Efficiency of 45%, Honda R&D Technical Review, Vol. 27, No. 2, p. 1-11
(3) JP, 9-105330 (1997)
(4) JP, 2008-184930 (2008)
(5) U.S., Patent No. 6,385,530 (2002)
(6) Hayakawa, A., Miki, Y., Kubo, T., Nagano, Y., Kitagawa, T.: Variations of Turbulent Burning Velocity and Flame Front Shape of Spherically Propagating Premixed Turbulent Flame with Effective Turbulence Intensity, Journal of the Combustion Sociery of Japan, Vol. 55, No. 172, p. 202-209 (2013)
(7) Adomeit, P., Jakob, M., Pischinger, S., Brunn, A., Ewald, J.: Effect of Intake Port Design on the Flow Field Stability of a Gasoline DI Engine, SAE Technical Paper, 2011-01-1284 (2011)

Author


Taketo YAMADA


Masayoshi TAKAHASHI


Kenichiro IKEYA


Noriyuki TAKEGATA

Study of Spray and Combustion Using Fast Response Common Rail Injector with Micro Orifice Nozzle

Akira KATO* Katsuya MATSUURA* Yasuhiro YOSHIMI*

ABSTRACT

Reduction of the nozzle hole diameter was investigated with the aim of further reducing harmful exhaust emissions from diesel engines. This investigation used a prototype injector with an injection rate gradient at the start of fuel injection that is approximately 80% greater than that of a conventional mass-production injector. Three types of nozzles were prepared that have the same hydraulic flow rate and only different numbers of holes and hole diameters from 0.08 mm to 0.12 mm. Spray measurement results confirmed that as the hole diameter becomes smaller, the spray penetration drops and the droplet Sauter mean diameter also becomes smaller. In addition, the results of engine combustion tests showed that reducing the nozzle hole diameter and increasing the number of holes increased the rich portion of the air-fuel mixture, so this does not contribute to the reduction of harmful exhaust emissions.

1. Introduction

As a recent trend in automobile exhaust emission regulations, various countries are implementing CO_2 emissions regulations as a global warming countermeasure in addition to conventional harmful exhaust emission regulations, and are considering more stringent regulations in the future. Diesel engines generally have higher thermal efficiency than gasoline engines, making them more advantageous in reducing CO_2 emissions. However, an issue with diesel engines is increasing the overall cleanness of emissions. Diesel combustion is basically lean combustion, so NOx cannot be sufficiently reduced using a three-way catalyst in the manner of a gasoline engine. NOx emission after-treatment technology for lean combustion continues to advance[(1)], but the conversion performance cannot yet be considered adequate. In order to reduce NOx it is necessary to introduce EGR gas during engine combustion to lower the combustion temperature. However, the introduction of EGR gas increases the rich portion of the air-fuel mixture, which leads to an increase in particulate matter (PM). In this manner, NOx and PM have a trade-off relationship in diesel combustion, but simultaneous reduction is demanded. New turbocharger technology and fuel injection technology using a common rail system[(2)-(4)] are being introduced to meet these demands. As a result, exhaust emissions are becoming cleaner and are complying with the strict emission regulations of each country. Numerous studies have been reported on premixed charge compression ignition (PCCI) combustion and low-temperature combustion that aims to simultaneously reduce NOx and PM[(5)-(8)] in order to support more stringent exhaust emission regulations in the future. However, these methods have issues such as increased emission of unburned gases such as HC and CO, and limited operating ranges.

The authors focused on the rate of injection of the injector with the aim of increasing fuel diffusion in order to reduce exhaust emissions in conventional diesel combustion without increasing the period of ignition delay in the manner of PCCI combustion. Increasing the injection rate gradient at the start of fuel injection (achieving high-speed injection) was confirmed to effectively reduce exhaust emissions[(9), (10)]. In addition, the influence of high-speed injection on exhaust emissions reduction was clarified by observing the flame behavior and using the two-color method to analyze the flame temperature and soot concentration in a glass piston engine[(11)].

Reduction of the nozzle hole diameter can be given as a method for further reducing exhaust emissions using the prototype injector in this study. Reduction of the nozzle hole diameter is known to promote spray atomization and contribute to the simultaneous reduction of NOx and PM[(12)]. However, when the nozzle hole diameter is reduced but the injection pressure is held constant, the spray penetration decreases, so it is thought that the air-fuel mixture distribution of the spray becomes richer. Therefore, reduction of the nozzle hole diameter is predicted to produce the two contrary phenomena of reduced exhaust

* Automobile R&D Center

emissions due to the promotion of fuel spray atomization and increased exhaust emissions due to a drop in spray penetration.

This study aimed to quantitatively clarify the influence of reducing the nozzle hole diameter from the perspectives of spray and combustion. Nozzles with different hole diameters were prepared, and spray tests were performed to investigate the influence of reducing the hole diameter on the spray shape and droplet size distribution. In addition, the influence of reducing the hole diameter on combustion characteristics was investigated by combustion tests using a diesel engine.

2. Tested Injectors

2.1. Structure and Flow Characteristics

Table 1 shows the specifications of the injectors used in the tests, and Fig. 1 shows a cross-section drawing of the prototype injector structure. To obtain high-speed injection performance unavailable with the conventional method, the prototype injector uses a piezo element to control the common rail hydraulic pressure by means of a valve, and directly opens and closes the nozzle needle using that controlled high fuel hydraulic pressure. In addition, to further increase the rate of injection at the start of injection, the seat angle of the nozzle needle was broadened in comparison to that of the mass-production injector in order to expand the aperture area at low needle lift as shown in Fig. 2. Figure 3 shows the flow rate characteristics test results when nozzles with the specifications given in Table 2 are mounted. Figure 3 confirms that the broadened seat angle increases the fuel flow rate at low needle lift as intended.

2.2. Rate of Injection and Spray Characteristics

Figure 4 shows the results of injection rate measurement when a fuel injection quantity of 18 mm^3/st. is injected at an injection pressure of 100 MPa, which were the injection conditions during the spray characteristics and engine combustion tests described hereafter. The injection rate gradient of the prototype injector at the start of fuel injection was 78% greater than that of the mass-production injector, which confirmed that the method used in this study increased the rate of injection at the start of injection.

Figure 5 shows photographs of the spray 0.5 ms after the start of injection with a fuel injection quantity of 18 mm^3/st. as used to measure the rate of injection. In addition, Fig. 6 shows time series numerical representations of the spray penetration and the spray angle obtained from the recorded high-speed video images. The experimental apparatus is described in the following section.

The spray angle was obtained by measuring the angle at the position 30 mm downstream from the nozzle outlet in the axial direction of the spray. Figure 6 confirms that the different injection rate characteristics of the two injectors produce large differences in the spray, and that the spray

Table 1 Specifications of common rail injection system

Injector	Mass production	Prototype
Max. pressure (MPa)	200	200
Max. injection events	5	5
Actuator	Piezo	Piezo
Needle actuation	Back pressure control	Fuel pressure direct control

Table 2 Specifications of injector nozzles

	Mass production	Prototype
Hole diameter (mm)	0.12	0.12
Number of holes	8	8
Spray hole angle (deg)	160	160
Flow rate (cm^3/min)	740	740
Sac volume (mm^3)	0.17	0.40
Seat angle (deg)	30	60

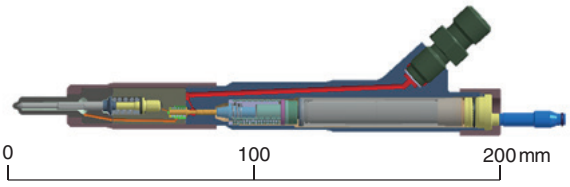


Fig. 1 Cross-section of prototype injector

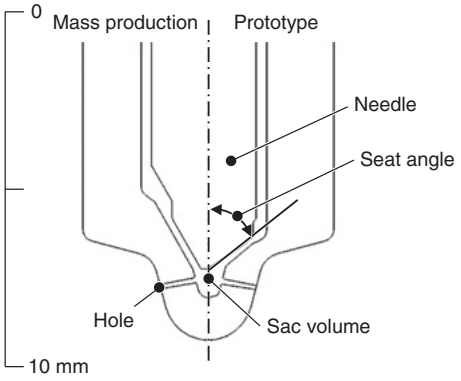


Fig. 2 Comparison of cross-section of special nozzle for fast common rail injector

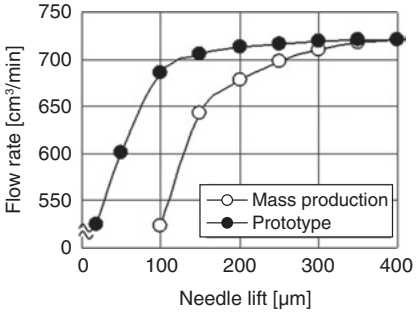


Fig. 3 Nozzle flow rate of two types of injector

penetration of the prototype injector 0.5 ms after the start of injection increased by 23% compared to that of the mass-production injector. However, in the reverse of the above-noted spray penetration increase, the spray angle

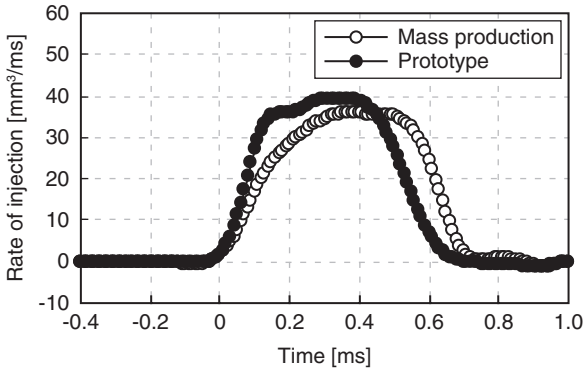


Fig. 4 Comparison of fuel injection rate profiles (1/4 engine load condition)

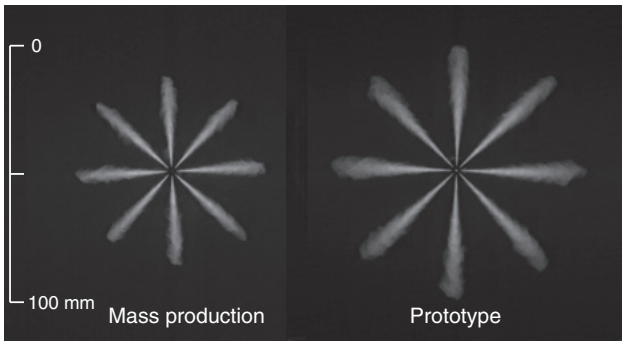


Fig. 5 Photographs of spray using high pressure vessel (0.5 ms after start of injection)

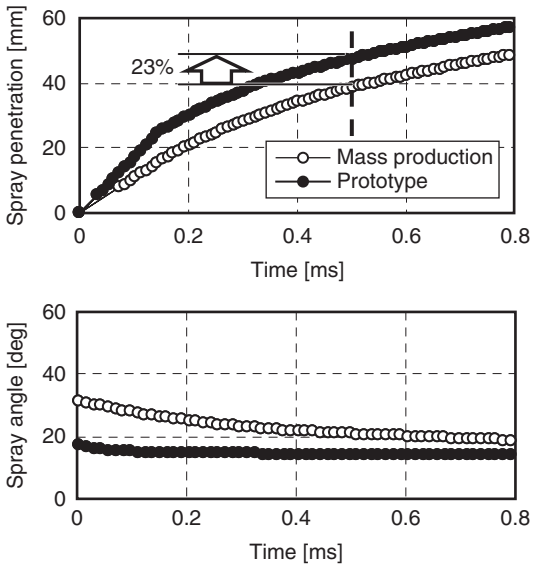


Fig. 6 Comparison of spray characteristics of two types of injector at 1/4 engine load

was confirmed to become narrower. This indicates that increasing the fuel injection rate has a large influence on the spray shape, and the injected fuel takes on a narrower spray shape with longer penetration.

In single-cylinder engine combustion tests using the prototype injector that was confirmed to have high-speed injection characteristics, the trade-off relationship between NOx and soot was enhanced. Soot reduction effects of 35.2% at 1/4 engine load equivalent and 48.4% at 1/2 engine load equivalent were confirmed at the NOx emission point that coincides with the setting point of the base four-cylinder engine. This is thought to indicate that increasing the fuel injection rate increased the spray penetration, which lowered the fuel concentration (lowered the richness) of the air-fuel mixture in the spray at the ignition timing.

3. Spray and Combustion Experiments

3.1. Injector Nozzles

Table 3 shows the specifications of the three nozzle types used in this study. The nozzle hole length was 1.05 mm for all three types. Only the nozzle hole diameter and number of holes differ, and all other parameters such as the hydraulic flow rate are the same. The nozzle sac shape including the needle was changed from the nozzle used in the previous chapter in order to machine 19 holes. This was done to secure sufficient distance between holes due to manufacturing technology constraints, and the sac volume increased by approximately three times compared to the prototype model used in the previous study. This is a factor increasing HC compared to a prototype nozzle, which is an issue. Note that the 0.08 mm nozzle hole machining is nearly the limit when using a normal electric discharge machine.

3.2. Tested Fuel

Table 4 shows the specifications of the fuel used for measurement. Diesel fuel with a cetane index of 43.2 was used in consideration of the U.S. and other countries where fuel with a relatively low cetane index is distributed in the market.

3.3. Spray Measurement Test

The spray characteristics test used a constant volume vessel and a high-speed video camera (FASTCAM-APX RS) made by Photron Limited. Figure 7 shows an overview of the measurement apparatus. A manual focus lens (Nikkor F f/1.2) with a focal length of 50 mm made by Nikon Corporation was mounted on the video camera, and recording was performed under conditions of a recording speed of 10,000 fps, image resolution of 512 × 512 pixels, and exposure time of 2 μs as shown in Table 5. The test was performed in the condition with N_2 gas charged to 1.4 MPa inside the constant volume vessel to achieve the same ambient density as that at the timing when fuel is injected during the engine performance test. The test

Table 3 Specifications of injector nozzles

	Nozzle A	Nozzle B	Nozzle C
Hole diameter (mm)	0.12	0.10	0.08
Number of holes	8	12	19
Spray hole angle (deg)	160	160	160
Flow rate (cm^3/min)	740	740	740
Sac volume (mm^3)	1.23	1.23	1.23
Seat angle (deg)	60	60	60

Table 4 Measured properties of diesel fuel

Item	Test method	
Cetane index	ASTM D-976	43.2
Density (g/cm^3)	ASTM D-4052	0.852
Viscosity (mm^2/s)	ASTM D-445	2.2
T90 (°C)	ASTM D-86	306
Aromatic (vol/%)	ASTM D-1319	28.4
LHV (kJ/kg)	ASTM D-3338	42838

Table 5 Conditions of spray measurement experiment

Recording speed (fps)	10000
Shutter speed (μs)	2
Resolution (pixel)	512 × 512
Ambient gas	N_2
Ambient pressure (MPa)	1.4
Ambient temperature (K)	298

consisted of injecting fuel to the inside of the constant volume vessel under conditions of a fuel injection quantity of 18 mm^3/st. and injection pressure of 100 MPa, recording the spray with the high-speed video camera, and obtaining the spray penetration and spray angle from the resulting images.

3.4. Droplet Size Measurement Test

The droplet size of each nozzle was measured using a Phase Doppler Anemometry (PDA) system made by Dantec Dynamics A/S in order to compare the fuel spray atomization characteristics for different hole diameters. Figure 8 shows an overview of this test apparatus. The density, temperature and other ambient conditions inside

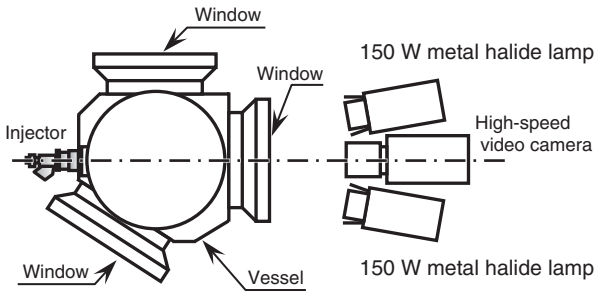


Fig. 7 Schematic diagram of spray measurement

Table 6 Specifications of single-cylinder engine

Engine type	4-st. single cylinder
Displacement volume (cm^3)	550
Bore × Stroke (mm)	85.0 × 97.1
Compression ratio	17.2
Fuel injection system	Piezo common rail
EGR rate	Continuously variable

the constant volume vessel were the same as those when measuring the spray, and measurement was performed at the position 60 mm downstream from the nozzle hole position.

3.5. Combustion Test Using a Single-cylinder Engine

Table 6 shows the specifications of the single-cylinder engine. This single-cylinder engine was manufactured based on a four-cylinder diesel engine that complies with the European emission regulation EURO 5[13]. Figure 9 shows the overall configuration of this single-cylinder engine, and Fig. 10 shows the shape of the engine combustion chamber. The intake is supercharged using a supercharger and the intake temperature is controlled to the designated temperature using a heater and intercooler

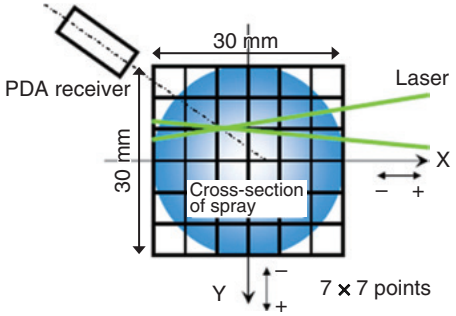


Fig. 8 Outline of droplet size measurement using PDA

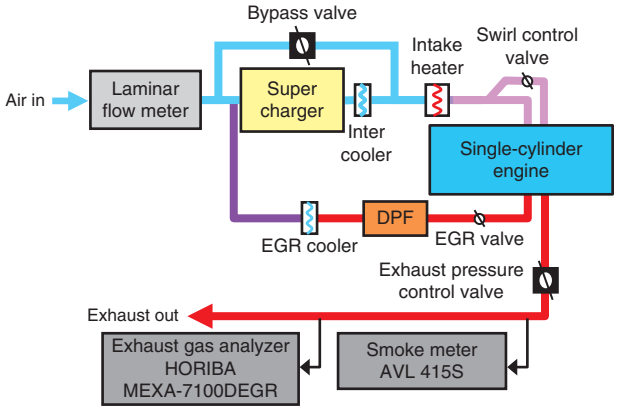


Fig. 9 Schematic diagram of single-cylinder engine system

Table 7 Conditions of engine combustion experiment

Nozzle hole diameter (mm)	0.12		0.10		0.08	
Engine speed (rpm)	1500		1500		1500	
Load	1/4	1/2	1/4	1/2	1/4	1/2
Injection pressure (MPa)	100	110	100	110	100	110
Intake air temperature (K)	343	333	343	333	343	333
Cooling water temperature (K)	353	353	353	353	353	353
Total injection quantity (mm^3/st.)	18	32	18	32	18	32
Pilot injection timing (deg ATDC)	-8.0	-16.6	-8.5	-16.5	-8.7	-17.6
Main injection timing (deg ATDC)	5.8	4.0	6.0	4.1	6.5	4.0

as shown in Fig. 9. In addition, the exhaust is controlled to the set exhaust pressure using a pressure control valve. This configuration enables the single-cylinder engine system to reproduce the actual operating conditions in a four-cylinder engine. An exhaust gas analyzer (MEXA-7100DEGR) made by Horiba, Ltd. and a smoke meter (415S) made by AVL LIST GmbH were installed downstream from the above-noted exhaust pressure control valve to analyze the various exhaust gas components.

The combustion test was performed under conditions corresponding to an engine speed of 1,500 rpm and 1/4 and 1/2 engine loads, which have a high frequency of use in car mode tests. Table 7 shows the engine operating conditions used for this test. The injection pattern used the two-stage pilot and main injection that is the standard injection method in conventional diesel combustion. The pilot injection quantity and timing were adjusted to achieve the same heat release value so that the dP/dθmax used as the index of diesel engine combustion noise would be the same. In addition, the main injection quantity and timing were adjusted to align the main ignition timings. Note that increasing the fuel injection pressure increases the combustion noise and mechanical loss, so this variable was excluded from this study, and the tests using the three nozzles were performed with the same fuel injection pressure.

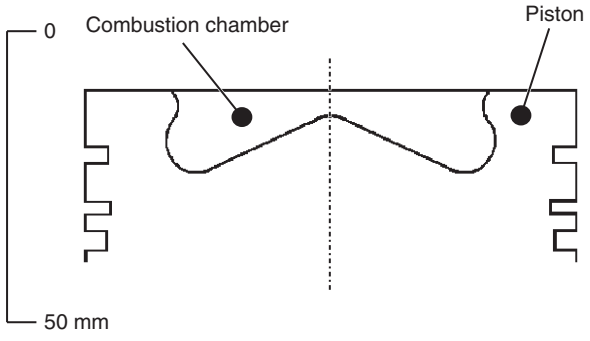


Fig. 10 Combustion chamber shape

4. Results and Discussion

4.1. Spray Measurement Test Results

Figure 11 shows photographs of the spray taken with a high-speed camera, and Fig. 12 shows time series numerical representations of the spray penetration and

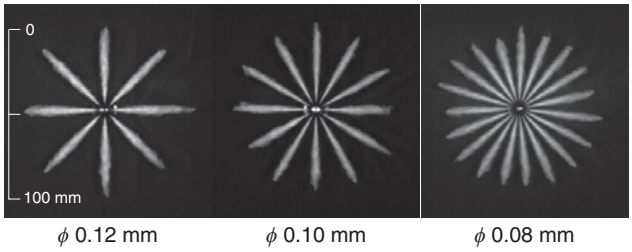


Fig. 11 Photographs of spray with three types of nozzles (0.5 ms after start of injection)

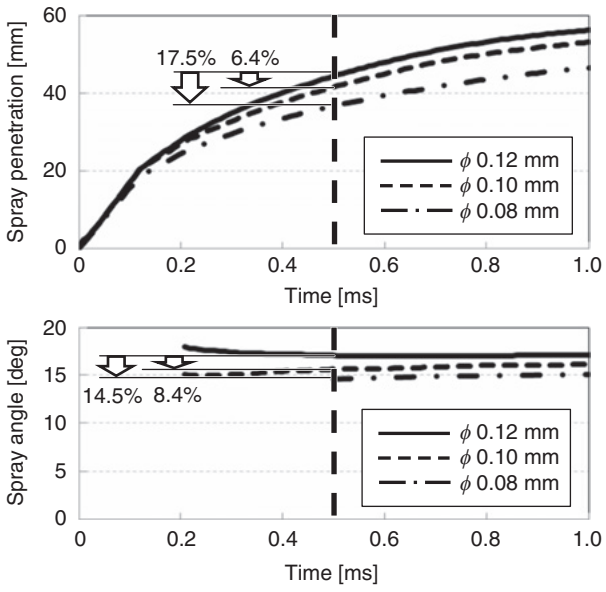


Fig. 12 Numerical comparison of spray penetration and spray angle

the spray angle. This measurement test was performed 10 times, and the spray data of all holes was averaged. The spray angle was measured at the position 30 mm downstream from the nozzle outlet in the axial direction of the spray.

Figure 12 shows that the spray penetration decreases and the spray angle becomes narrower as the nozzle hole diameter becomes smaller. The 0.08 mm nozzle, which has the smallest hole diameter, exhibited 17.5% less spray penetration and a 14.5% narrower spray angle compared to the 0.12 mm nozzle at the point 0.5 ms after the start of injection. Note that measurement of the spray angle at the start of injection has large variance, so the data up to approximately 0.2 ms after the start of injection was excluded.

4.2. Droplet Size Measurement Test Results

Figure 13 shows the droplet size distribution measurement results and Fig. 14 shows the droplet Sauter mean diameter (d32) for the three nozzle types. The droplet surface area is an important factor influencing droplet vaporization and volatilization, so the droplet Sauter mean diameter, which takes into account the surface area, was used as the average droplet size. Figure 13 shows that the droplet size distribution shifts toward the smaller droplet size side as the nozzle hole diameter becomes smaller. The droplet Sauter mean diameter was confirmed to decrease as the nozzle hole diameter becomes smaller. The droplet Sauter mean diameter decreased by 2.6% when the hole diameter was reduced from 0.12 mm to 0.10 mm, and by 6.7% when the hole diameter was reduced to 0.08 mm. This confirmed that reducing the nozzle hole diameter increased fuel atomization.

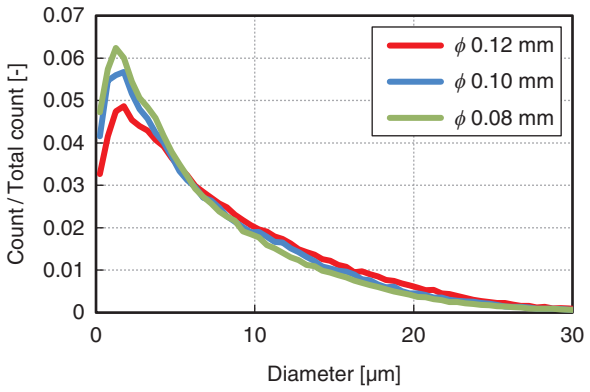


Fig.13 Comparison of droplet size distribution with three types of nozzles

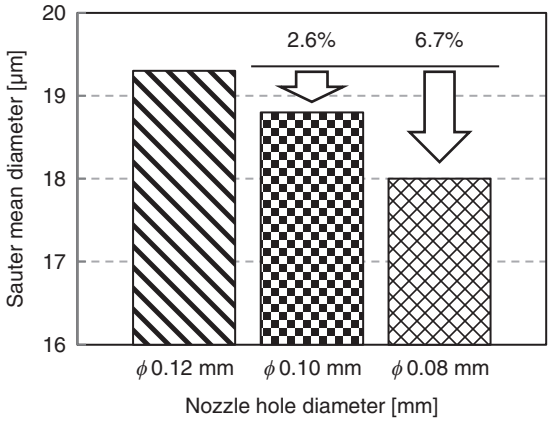


Fig. 14 Comparison of droplet Sauter mean diameter with three types of nozzles

4.3. Engine Combustion Test Results

Figure 15 (1/4 engine load; fuel injection quantity of 18 mm^3/st.) and Fig. 16 (1/2 engine load; fuel injection quantity of 32 mm^3/st.) show the results of combustion tests using the single-cylinder engine. These experiments were performed by gradually opening the EGR valve from the fully closed condition to increase the EGR rate. The figures show NOx on the horizontal axis, and each measurement data on the vertical axis. Comparison of each measurement data at the NOx value (the position of the gray lines in Fig. 15 and Fig. 16) that coincides with the matching point of the mass-production engine shows that in the 1/4 engine

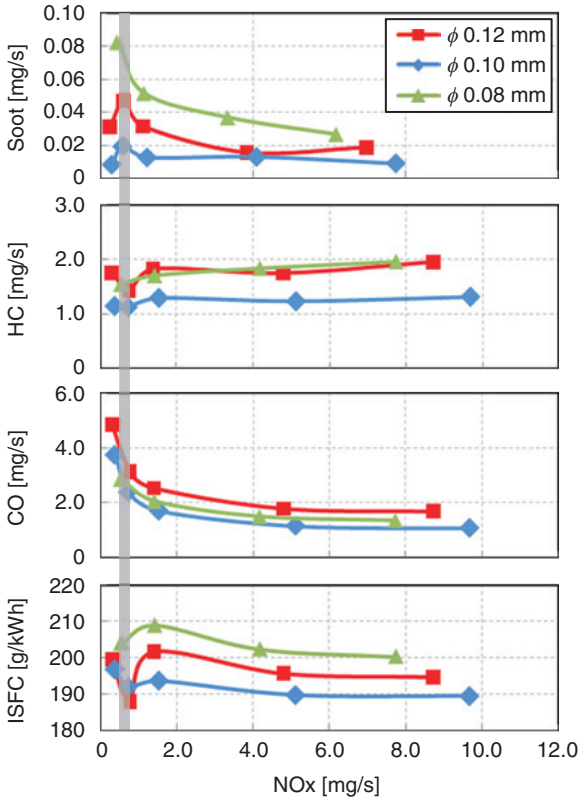


Fig. 15 Exhaust gas emissions at 1500 rpm, 1/4 engine load using three types of micro hole nozzles

load condition, the 0.10 mm nozzle exhibited the lowest soot emission quantity, and soot emission increases for the 0.08 mm nozzle, which has an even smaller nozzle hole diameter. However, in the 1/2 engine load condition, the 0.12 mm nozzle exhibited the lowest soot emission, and the 0.08 mm nozzle exhibited the highest soot emission, approximately four times that of the 0.12 mm nozzle, and also exhibited increased HC, CO and Indicated specific fuel consumption (ISFC).

Figure 17 shows the rate of heat release (ROHR) at the NOx value (the position of the gray line in Fig. 15) that coincides with the matching point of the mass-production engine under conditions of 1/4 engine load and a fuel injection quantity of 18 mm^3/st. According to this ROHR, the heat release peak of the main combustion, which is the dominant factor influencing exhaust emission performance, is largest for the 0.10 mm nozzle and smallest for the 0.08 mm nozzle, which has the smallest hole diameter. In addition, the delayed combustion was confirmed for the 0.08 mm nozzle, with combustion continuing in the latter part of the combustion period from an ATDC of 30° onward.

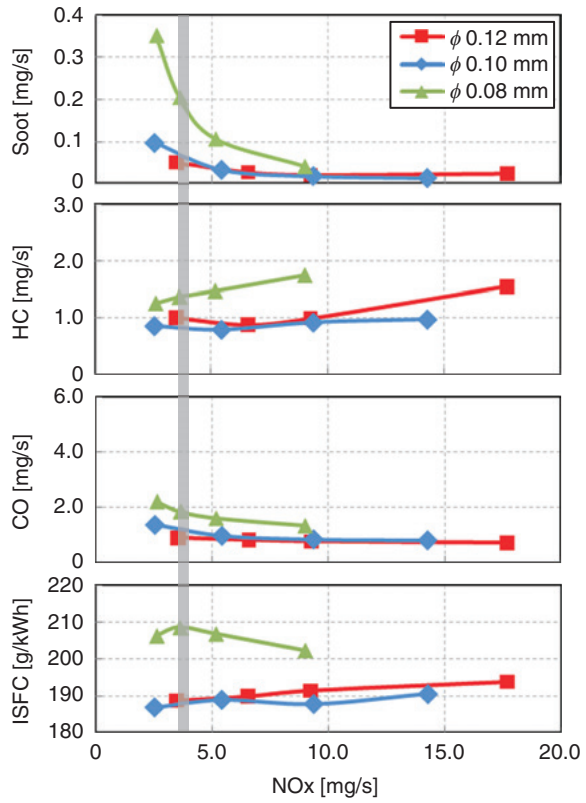


Fig. 16 Exhaust gas emissions at 1500 rpm, 1/2 engine load using three types of micro hole nozzles

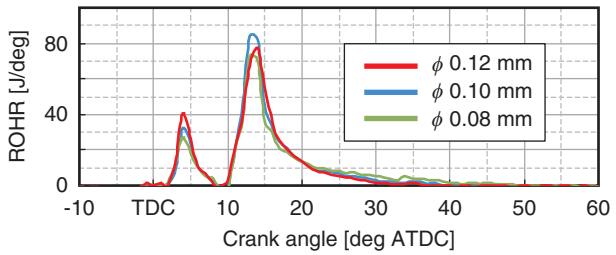


Fig. 17 Comparison of heat release at 1500 rpm, 1/4 engine load using three types of micro orifice nozzles

4.4. Discussion

The spray measurement tests confirmed that reducing the nozzle hole diameter reduces the fuel spray penetration, narrows the spray angle, and reduces the injected fuel droplet size, that is to say, promotes fuel atomization.

The engine combustion test results showed that the soot emission quantity at both 1/4 and 1/2 engine loads was largest during combustion using the 0.08 mm nozzle that was confirmed to increase fuel atomization performance. Based on these results, the smaller hole diameter is presumed to have increased the richness of the air-fuel mixture distribution within the fuel spray. The reason for this is thought to be that the smaller hole diameter resulted in a spray shape with reduced spray penetration and a narrow spray angle. A smaller nozzle hole diameter promotes fuel atomization within the spray, but also reduces spray penetration, reduces the mixture of fuel and air in the fuel spray at the start of injection, and reduces the ratio of air-fuel mixing that is thought to occur due to collision between the spray and the combustion chamber wall. This means that the injected fuel is present in a narrow range inside the combustion chamber, and combustion of this rich spray is thought to produce an increase in soot and HC. The delayed combustion of the 0.08 mm nozzle confirmed by heat release analysis also confirms an increase in the richness of the air-fuel mixture distribution within the fuel spray.

The 0.10 mm nozzle exhibited the smallest soot emission quantity at 1/4 engine load, but the fuel injection quantity was less than that at 1/2 engine load, so both the injection time and the spray penetration were shorter than those at 1/2 engine load. Therefore, the reason why the 0.10 mm nozzle exhibited the smallest soot emission quantity is thought to be that the air-fuel mixing promotion effect of increased atomization due to reducing the hole diameter had a larger influence on combustion than the air inclusion effect of increased spray penetration. In addition, the peak ROHR of the main combustion, which is the dominant factor influencing exhaust emission performance, was also highest for the 0.10 mm nozzle, which confirmed that early combustion is promoted by the atomization effect.

Based on the above, although reducing the nozzle hole diameter under conditions of the same injection pressure promotes fuel atomization, the spray penetration drops

and the richness of the air-fuel mixture within the spray increases, including the influence of wall collision, so there is thought to be an appropriate balance for reducing exhaust emissions. In addition, this balance is thought to change according to the injected fuel quantity and injection pressure, so it is necessary to determine the engine operating conditions to be given importance and set the nozzle hole diameter in consideration of this balance.

Regarding the influence of spray interference between the fuel injected into the engine combustion chamber due to increasing the number of nozzle holes to 19, interference between the spray from each hole of the 0.08 mm nozzle could not be confirmed in tests inside the constant volume vessel shown in Fig. 11, so the likelihood of spray interference is low.

5. Conclusion

Various experiments were performed using a prototype injector with high-speed injection performance that was confirmed to have exhaust emission reduction effects. These experiments used three types of nozzles with the same hydraulic flow rate but different nozzle hole diameters from 0.12 mm to 0.08 mm with the aim of further reducing exhaust emissions, and yielded the following findings.

(1) Reduction of the nozzle hole diameter resulted in a narrow injected fuel spray shape with low penetration.
(2) Reduction of the hole diameter reduced the fuel spray droplet size. The droplet Sauter mean diameter of the 0.08 mm nozzle was 6.7% smaller than that of the 0.12 mm nozzle.
(3) The results of combustion experiments using a single-cylinder engine at medium and low engine loads confirmed an increase in exhaust emissions such as soot during combustion using the 0.08 mm nozzle as compared to the 0.12 mm and 0.10 mm nozzles. The increased soot emission of the 0.08 mm nozzle occurred because the smaller nozzle hole diameter resulted in lower spray penetration, which reduced mixture of the fuel with the air and increased the richness of the air-fuel mixture distribution within the fuel spray.
(4) In combustion under low engine load conditions, the fuel atomization effect of a smaller nozzle hole diameter influences combustion, and the soot emission quantity of the 0.10 mm nozzle is smaller compared to the combustion results for the 0.12 mm and 0.08 mm nozzles. When the engine load is reduced, the injection time becomes shorter, so the spray penetration becomes shorter as well. However, the influence on combustion of atomization due to a reduced hole diameter exceeds the influence of reduced spray penetration, so the 0.10 mm nozzle exhibited the smallest soot emission quantity.

Acknowledgements

The authors wish to express their deepest thanks and dedicate this paper to the late Mr. Takahiro Katano, a collaborator on this study who was in charge of the key item of nozzle design.

References

(1) Morita, T., Suzuki, N., Satoh, N., Wada, K., Ohno, H.: Study on Low NOx Emission Control Using Newly Developed Lean NOx Catalyst for Diesel Engines, SAE Technical Paper, 2007-01-0239, p. 1-7, (2007)
(2) Miyaki, M., Fujisawa, H., Masuda, A., Yamamoto, Y.: Development of New Electronically Controlled Fuel Injection System ECD-U2 for Diesel Engines, SAE Technical Paper, 910252, p. 1-17, (1991)
(3) Nagata, K., Tanaka, Y., Yano, K.: Technologies of DENSO Common Rail for Diesel Engine and Consumer Values, SAE Technical Paper, 2004-21-0075, p. 1-7, (2004)
(4) Akiyama, H., Yuasa, H., Kato, A., Saiki, T., Sanada, K., Kado, N.: Precise Fuel Control of Diesel Common-Rail System by Using OFEM, SAE Technical Paper, 2010-01-0876, p. 1-10, (2010)
(5) Shimazaki, N., Akagawa, H., Tsujimura, K.: An Experimental Study of Premixed Lean Diesel Combustion, SAE Technical Paper, 1999-01-0181, p. 1-10, (1999)
(6) Kimura, S., Aoki, O., Kitahara, Y., Aiyoshizawa, E.: Ultra-Clean Combustion Technology Combining a Low-Temperature and Premixed Combustion Concept for Meeting Future Emission Standards, SAE Technical Paper, 2001-01-0200, p. 1-10, (2001)
(7) Hasegawa, R., Yanagihara, H.: HCCI Combustion in DI Diesel Engine, SAE Technical Paper, 2003-01-0745, p. 1-8, (2003)
(8) Kanda, T., Hakozaki, T., Sono, H., Uchimoto, T., Hatano, J., Kitayama, N.: PCCI Operation with Early Injection of Conventional Diesel Fuel, SAE Technical Paper, 2005-01-0378, p. 1-12, (2005)
(9) Kato, A., Matsuura, K., Hakozaki, T., Suzuki, O., Haraguchi, S., Yoshimi, Y., Hashimoto, T., Katano, T.: Influence of a Fast Injection Rate Common Rail Injector for the Spray and Combustion Characteristics of Diesel Engine, SAE Technical Paper, 2011-01-0687, p. 1-11, (2011)
(10) Haraguchi, S., Nishimura, Y., Yoshimi, Y., Katano, T., Suzuki, O., Matsuura, K., Hakozaki, T., Kato, A.: Effects of Spray Characteristics and Combustion Chamber Geometry on Emission Performance in Diesel Diffusion Combustion Using a Fast-Injection-Rate Injector and the Latest Common Rail Light-Duty DI Diesel Engine, Proceedings of Conference on Thermo- and Fluid Dynamic Processes in Diesel Engines, THIESEL 2010, p. 253-276, (2010)

(11) Matsuura, K., Suzuki, O., Kato, A.: In-cylinder Optical Investigation of Combustion Behavior on a Fast Injection Rate Diesel Common Rail Injector, Transactions of SAE International, Journal of Fuels and Lubricants, January 2012, Vol. 5, Num. 1, p. 88-97, (2012)
(12) Pickett, L. M., Siebers, D. L.: Non-Sooting, Low Flame Temperature Mixing-Controlled DI Diesel Combustion, SAE Technical Paper 2004-01-1399, p. 1-19, (2004)
(13) Matsui, R., Shimoyama, K., Nonaka, S., Chiba, I., Hidaka, S.: Development of High-performance Diesel Engine Compliant with Euro-V, SAE Technical Paper, 2008-01-1198, p. 1-8, (2008)

■ Author ■


Akira KATO


Katsuya MATSUURA


Yasuhiro YOSHIMI

Estimation Technology Establishment for Temperature Distributions of Engine Based on Thermal Balance under Vehicle Running Conditions

Tomokazu NOMURA* Koichiro MATSUSHITA*
Yoshihiko FUJII* Hirofumi FIJIWARA*

ABSTRACT

The estimation of the temperature distributions of an engine requires consideration on the process of releasing heat generated through combustions to the atmosphere. In this study, the heat inflow/outflow balance was calculated using one-dimensional thermal simulation tool. Using those results as boundary conditions, three-dimensional simulation on the structures of an engine was conducted to establish a method to estimate the heat distributions of an engine. An air-cooled engine, whose cooling conditions are highly susceptible to its configuration and shape, was selected as the target engine for investigation.

The 1D simulation for calculating the heat balance was structured with four specific methodologies. The first one was an engine cycle simulation method that calculates the heat transfer from the combustion gas to the engine structures. The second one was a heat transfer simulation method in which engine components were replaced with simple shaped objects. The third one was a CFD coupled with an empirical formula to calculate the heat transfer to oils situated in various regions in an engine. The last method was a CFD simulation applied to the running conditions of a complete vehicle to calculate the heat transfer to the atmosphere.

Utilizing the results yielded through this one-dimensional thermal simulation as the boundary conditions, the three-dimensional temperature distributions were estimated. As the result, it was confirmed that the temperature distributions of an engine could be estimated with a high accuracy under running conditions of a complete vehicle. Moreover, it was verified that the temperature distributions can be estimated accurately for a variety of vehicles with engines of different specifications and mounting conditions.

1. Introduction

The growing demands for fuel economy in recent years call for development of light and compact engines having a high thermal efficiency. While the thermal efficiency of engines is improving due to various innovations, approximately 30% of the fuel's energy is released to the atmosphere, which is referred to as "cooling loss".

The heat in an engine is released to the atmosphere via the engine components, coolant and engine oil. When the cooling is inadequate, the engine temperature rises excessively. As a result, lowering of the volumetric efficiency, knocking and lowering of material strength may occur, which causes loss of engine performance and/or durability. For air-cooled engines in particular, lightness/compactness and the retention of heat dissipation capacity are two contradicting demands. It is therefore necessary to pay attention to the balance between the heat entering the engine and that leaving the engine in order to design an engine while ensuring performance, durability and compactness. Furthermore, in motorcycles equipped with air-cooled engines, the cooling conditions vary significantly depending on the external shapes of the engines and the airflow around them. It is therefore necessary to analyze the engine temperatures of a complete motorcycle under running conditions.

In the meantime, the so-called "digital development", in which no prototype engine is produced in the early stages of development, is becoming the mainstream of recent engine development in an effort to reduce the development period.

* Motorcycle R&D Center

It is necessary to accurately estimate the temperature distribution in the engine in the early stages of development in order to accurately simulate the intake air temperature, which affects volumetric efficiency and knocking, as well as the durability of engine parts.

There are many examples of past research on engine cooling and temperature estimation[(1)-(5)]. The conventional ways include the following.

(1) A method that assesses heat dissipation from the engine outer surface to the atmosphere and from the water jacket to the coolant by the heat transfer coefficient using the 3 Dimensional Computational Fluid Dynamics (3D-CFD)
(2) A method that estimates temperature distribution using a thermal conductivity simulation with measured temperatures and heat fluxes of a part of the engine as the boundary conditions
(3) A method that estimates coolant temperature when operating in test mode using a 1D thermal fluid simulation

As such a method is unable to directly estimate the temperature or requires measured temperatures and/or heat flux data from various parts of the engine, it cannot be used to get an accurate temperature estimate in the design stage. Although the heat balance of coolant is taken into account, the estimate cannot be extended to the temperature distribution in the various parts of the engine.

Accordingly in this project we developed a method for estimating, in an early stage of design, engine temperature distribution in an air-cooled engine under the running conditions of a complete motorcycle. In the first place on this article, estimation methods are explained for the total heat balance and for the temperature distributions of an engine. Subsequently, the results of validations on the accuracies of the temperature estimations are described for the cylinder and the cylinder head whose temperatures are high in operation.

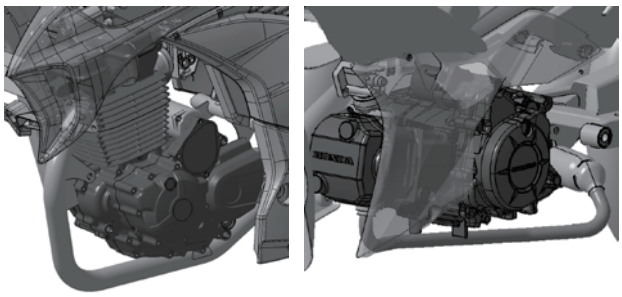
2. Test Motorcycles

The specifications of the two test engines used in this study are shown in Table 1, and the overview of the engine in Fig. 1. An air-cooled, 300 cm^3 engine with its single cylinder canted forward 15 degrees was used for the development and validation of the temperature estimation method (Vehicle A in Table 1). The test motorcycle is equipped with an oil cooler. The air guide plates, or "shroud," direct air flow to the spark plug for cooling.

A motorcycle equipped with an air-cooled, 110 cm^3 engine with its single cylinder canted forward 80 degrees was used for the additional validation of the temperature estimation method in this project (Vehicle B in Table 1). This motorcycle is not equipped with an oil cooler. This motorcycle was selected as having significant differences in engine displacement, power output, engine configuration and airflow around the engine compared to Vehicle A.

Table 1 Engine specifications of test motorcycles

	Vehicle A	Vehicle B
Engine type	4 stroke engine	4 stroke engine
Number of cylinders	1	1
Cooling system	Air-cooled	Air-cooled
Bore [mm]	79	50
Stroke [mm]	59.5	55.6
Displacement [cm^3]	291.6	109.1
Compression ratio [-]	9	9
Maximum brake power [kW]	17.9 (7,500 r/min)	6.2 (7,500 r/min)
Maximum brake torque [Nm]	25.2 (6,000 r/min)	8.6 (5,500 r/min)
Maximum vehicle speed [km/h]	128	89



(a) Vehicle A (b) Vehicle B

Fig. 1 Engine shapes of test motorcycles

3. Overview of Temperature Estimation Method

Figure 2 shows an overview of the temperature estimation method developed in this project. To calculate the heat balance in an air-cooled engine, it is necessary to take into account all the routes from the heat source up to the heat dissipation such as the heat input from the combustion to the engine, the heat transfer within the engine, the heat transfer from engine inner surface to the engine oil, the heat dissipation from the oil cooler to the atmosphere, and the heat dissipation from the cooling fins to the atmosphere. A 1D thermal simulation model is used for the comprehensive calculation with all the above factors coupled. The formulas coupled in the model are as per the following.

- The 1D engine cycle simulation is used to calculate the processes through which the combustion heat is transferred to the structural engine components via the combustion chamber walls.
- The three-dimensional shapes of the cylinder head and the cylinder are converted to the 1D thermal simulation model and incorporated into the simulation for calculation of heat transfer within the engine.

- The 1 Dimensional Computational Fluid Dynamics (1D-CFD) for oil flow rate is used to calculate the heat transfer from the internal walls of the engine to the engine oil. It should be noted that a combination of the 3D-CFD for oil behavior and the empirical equation of the heat transfer coefficient is applied for calculation of the heat transfer in the part where the engine oil flows along the wall such as in the camshaft chamber in the cylinderhead as well as for the heat transfer by the oil from the piston-cooling jet.
- Another 3D-CFD for airflow is used to calculate the heat transfer processes, in which the heat is dissipated to the atmosphere when the complete motorcycle is running.

The heat balance in the engine is determined by coupling the above formulas. Using the accordingly determined temperatures and heat transfer coefficients of the working gas and the engine oil as the boundary conditions, the temperature distribution in the various parts of engine is determined by the 3D thermal conductivity simulation.

4. Details of Temperature Estimation Method

4.1. Calculation of Heat Transfer to Engine

One of the key techniques in temperature estimation is the calculation of heat input from the combustion gas to the structural engine components. 1D engine cycle simulation is a technique commonly applied to engine development[6]-[8], and recently allows a very accurate calculation of power outputs and in-cylinder pressures.

Accordingly, detailed explanations should be sought from other information source. In an engine cycle simulation, the temperature of the wall that contacts the working fluid such as in the combustion chamber and port has to be set as a boundary condition. In the temperature estimation in this study, the wall temperature is obtainable as a calculation result rather than a boundary condition by incorporating the engine cycle simulation into the 1D thermal simulation that calculates heat balance in the engine.

4.2. Calculation of Heat Transfer in Engine Components

The heat in the engine components (e.g., cylinder head, cylinder) is transferred via three-dimensional routes. To convert such a route to the 1D thermal simulation model, we tried discretization to a number of zones as Fig. 3 shows. The thermal conductivity of each component, such as the cylinder head, cylinder, and valves, are also defined in the model. In our study, the specific heats of individual materials are not counted because the estimation is to be conducted for the temperature that has already been saturated state of the heat transfers with a constant vehicle speed condition.

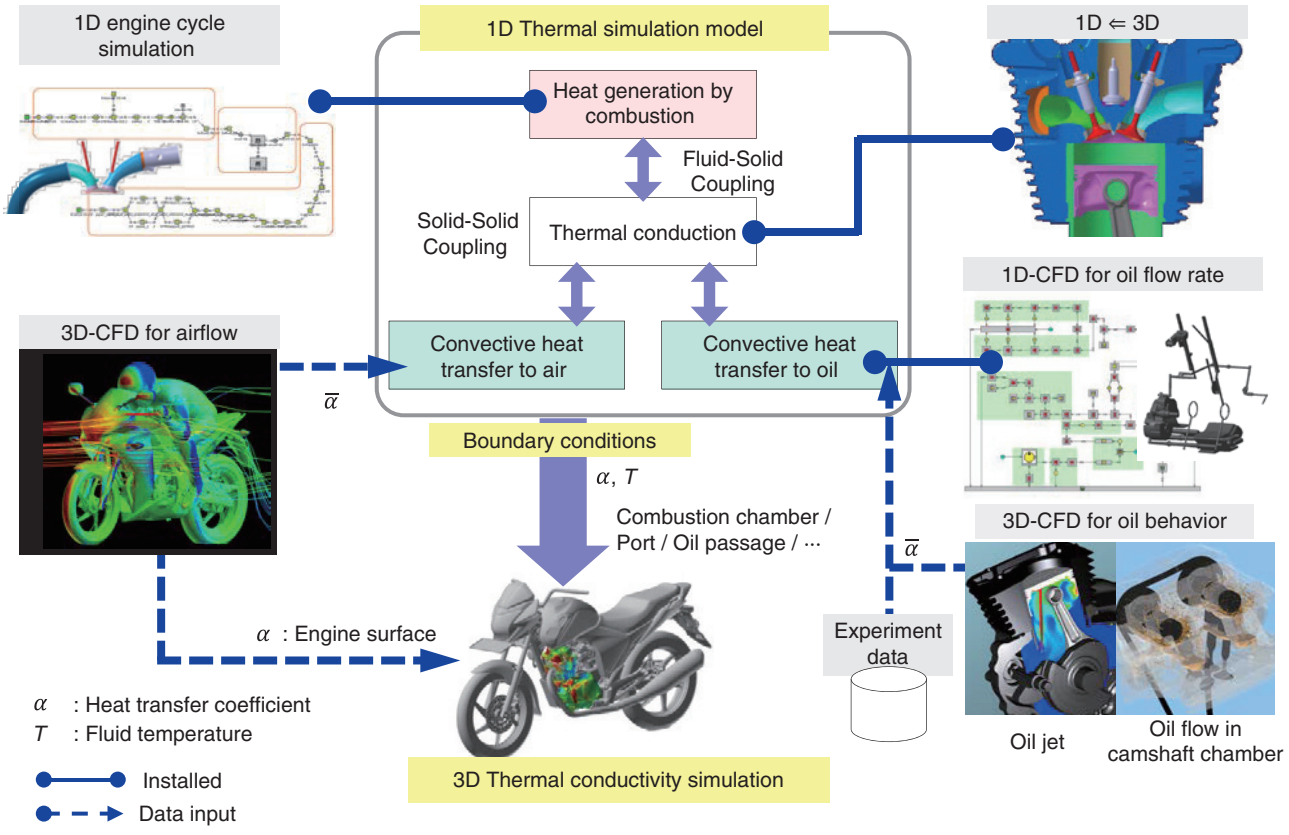


Fig. 2 Overview of temperature estimation method for air-cooled engine

Moreover, the heat transfer coefficients are defined on each boundary surface where the different materials are in contact. In places where a part such as the valve guide and valve seat is press-fit, an infinitely large heat transfer coefficient (i.e., a thermal contact resistance of 0) is set.

As an example other than in the press-fit part, explanations on the heat transfer coefficient between the cylinder and the sleeve are explained in the following section.

4.2.1. Heat transfer coefficient between cylinder body and sleeve

The predominant cylinder construction in small displacement, air-cooled engines is a cast-iron sleeve molded in the aluminum body. It is known that in this type of cylinder, a small clearance occurs between the cylinder body and the sleeve when the engine is operating under high temperature conditions due to the difference in the thermal linear expansion coefficients of aluminum and cast iron. The decrease of contact surface between the two parts due to the clearance interferes with the heat transfer from inside the cylinder to the cooling fins. To incorporate the said conditions into the 1D thermal simulation model, we created test equipment to measure the heat transfer coefficient between the cylinder body and the sleeve. As the test equipment in Figure 4 shows, a temperature gradient was created in the cylinder by heating the cylinder bore surface uniformly with high-temperature fluid (oil) and cooling the outside with low-temperature fluid (water). All the cooling fins were removed from the cylinder body for uniform cooling of the external wall of cylinder. In these tests, a uniform temperature in the axial direction of the cylinder was created by increasing the flow rates of the high-temperature and the low-temperature fluids as much as possible.

Under these conditions, the temperature gradient exists only in the radial direction of the cylinder as Eq. (1) shows.

$$\frac{\partial^2 T}{\partial r^2} + \frac{1}{r}\frac{\partial T}{\partial r} = 0 \tag{1}$$

Where T is the temperature in the cylinder, and r is the distance in the radial direction of cylinder. Under the above assumption, the temperature distribution in the radial direction of the cylinder can be represented by the Eq. (2).

$$T(r) = C_1 \ln r + C_2 \tag{2}$$

where C_1 and C_2 are constants.

Also, the heat flux, q, in the radial direction can be represented by Eq. (3).

$$q(r) = -k \cdot \frac{\partial T}{\partial r} = -\frac{C_1 \cdot k}{r} \tag{3}$$

Where k is the thermal conductivity of cylinder.

The heat transfer coefficient between the cylinder body and the sleeve can be determined by dividing the heat flux on the boundary surface by the temperature difference. However, as the cylinder body and the sleeve of an actual engine are thin, it is difficult to measure the temperature distribution. We therefore decided to calculate

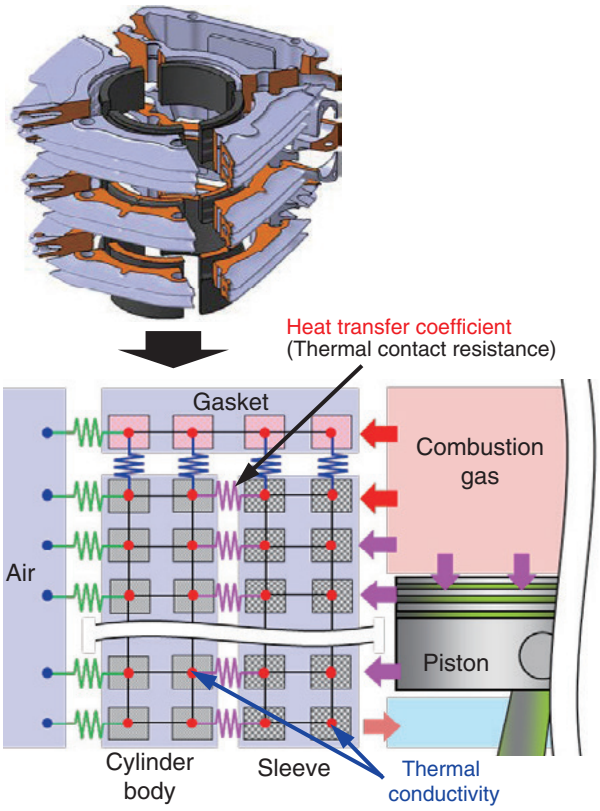


Fig. 3 Outline of heat transfer model in 1D thermal simulation

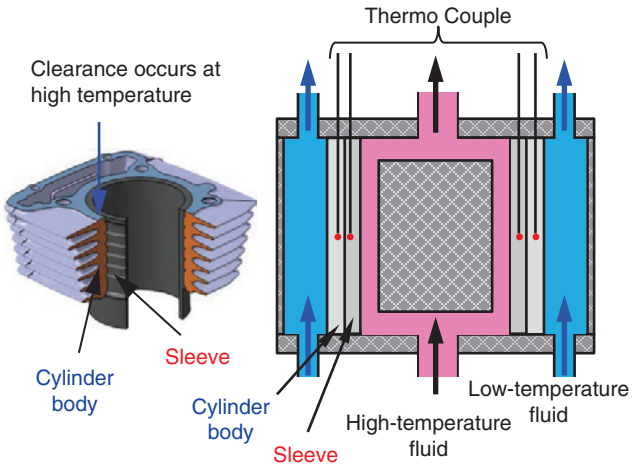


Fig. 4 Test equipment for measurement of heat transfer coefficient between cylinder body and sleeve

the temperature distribution in the cylinder body and sleeve using the heat transfer coefficient between the high-temperature fluid and the sleeve, and between the low-temperature fluid and the cylinder body. Accordingly, these heat transfer coefficients were acquired through a separate experiment using a dummy cylinder. Here, we presumed that the heat transfer coefficient between the fluid and the solid does not depend on the solid material.

Under the above-mentioned conditions, the heat transfer coefficient between the cylinder body and the sleeve is determined by the following steps.

(1) As Fig. 5(a) shows, using the dummy cylinder made of a single material having a known thermal conductivity, the temperature distribution in the radial direction in the dummy cylinder, and the fluid temperatures on the heating side and the cooling side were measured.

(2) Using the outcomes from Step 1, the temperature and the heat flux of the dummy cylinder were determined from Equations (2) and (3).

(3) Using the outcomes from Step 2, the heat transfer coefficients α_{Hot} and α_{Cool} between the high-temperature fluid and the wall, and between the low-temperature fluid and the wall, respectively, were calculated using Equations (4) and (5).

$$\alpha_{Hot} = \frac{q(r_{Hot})}{T_{Oil} - T(r_{Hot})} \tag{4}$$

$$\alpha_{Cool} = \frac{q(r_{Cool})}{T(r_{Cool}) - T_{Water}} \tag{5}$$

(4) As Fig. 5(b) shows, using the actual cylinder body and the sleeve, the temperatures of the sleeve, cylinder body, the high-temperature fluid, and the low-temperature fluid were measured.

(5) Using the temperature measured in Step 4 and the heat transfer coefficients determined in Step 3, the radial distributions of the temperature and the heat flux in the cylinder body and the sleeve were determined, and lastly the heat transfer coefficient between the cylinder body and the sleeve was calculated.

$$\alpha_1 = \frac{q}{T(r_{Sleeve}) - T(r_{Cylinder})} \tag{6}$$

Also, taking into account the deviation of heat transfer coefficient in the circumferential direction of the cylinder, each heat transfer coefficient was determined at some positions along the circumference of the cylinder, and the averaged value of these results was used as the representative value. Also, the heat transfer coefficient determined by this measurement method is a value for a certain surface area that is determined by the radius r without considering the surface area that depends on the shape of sleeve surface.

Figure 6 shows the outer shapes of the two types of sleeves commonly used in motorcycles. The heat transfer coefficient between the cylinder body and each type of sleeve was determined to cope with either type in the engine design stage. The determined heat transfer coefficients are shown in Fig. 7. It can be seen that the heat transfer coefficient of the Type A sleeve is three times larger than that of the Type B sleeve. It can be supposed that the Type A sleeve has a high heat transfer coefficient because it has many small protrusions on the contact surface. These heat transfer coefficients were applied to the 1D thermal simulation model.

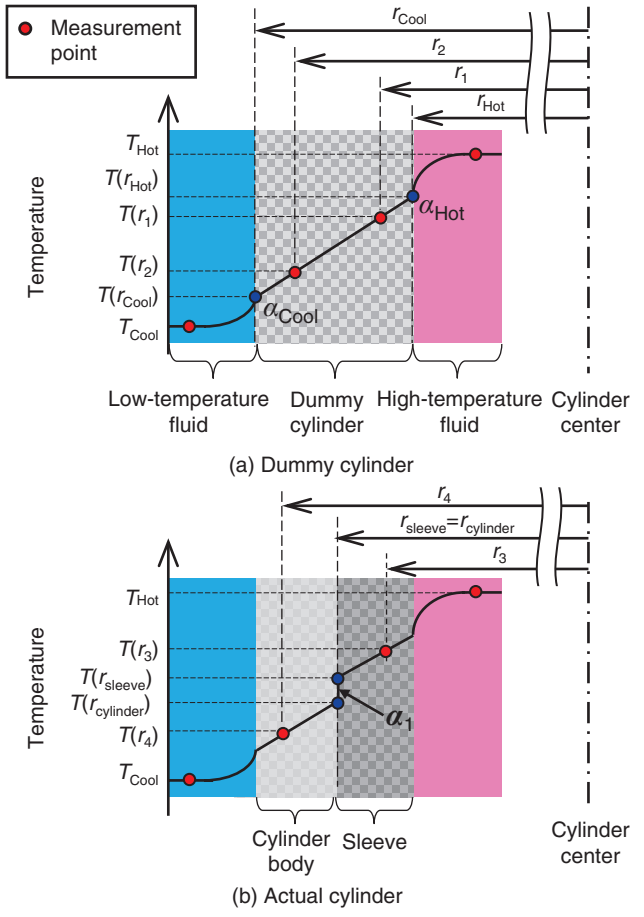


Fig. 5 Calculation technique of heat transfer coefficient between cylinder body and sleeve

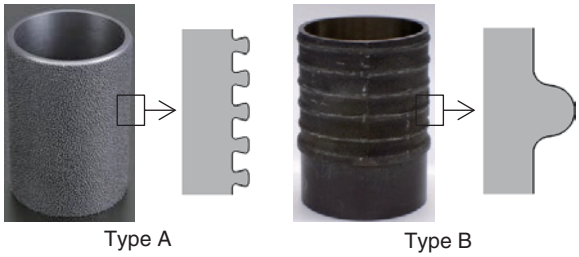


Fig. 6 Outer shapes of sleeves

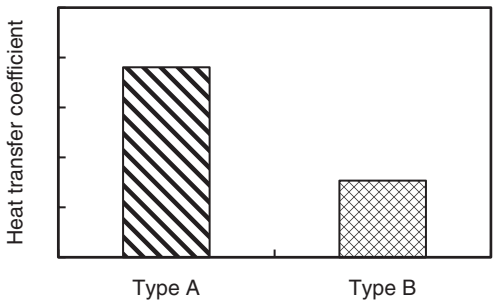


Fig. 7 Measurement results of heat transfer coefficient between cylinder body and sleeve

4.3. Calculation of Heat Transfer to Engine Oil

The heat transfer to the engine oil can be classified into the following three cases.

(1) Heat transfer on the wall in a passage filled with oil such as the channel that feeds oil to various parts of engine
(2) Heat transfer when the oil flows on the wall such as in the camshaft chamber, cam chain chamber
(3) Heat transfer when the oil impinges on the wall such the oil from the piston-cooling jet

Regarding Case (1), the heat transfer at the walls of the oil supply passages can be calculated without difficulty and this calculation can be incorporated relatively easily into the 1D thermal simulation model. For Case (2) and Case (3), however, as the flow of oil in the camshaft chamber and the behavior of oil from the piston-cooling jet impinging on the back surface of the piston crown are complex, it is necessary to make specific considerations to incorporate the heat transfer calculation into the 1D thermal simulation model. Accordingly, it was decided to determine the size of the area where the oil flows in the camshaft chamber, and the area on which the oil from the piston-cooling jet impinges using 3D CFD, and chose to calculate the heat transfer coefficient between the oil and the wall by basic experiments. Using both calculation results, the heat transfer to the oil was calculated in the 1D thermal simulation.

4.3.1. Calculation of oil flow rate in oil supply passages and calculation of heat transfer

For accurate calculation of cooling by oil, the flow rates of the oil supplied to various parts of the engine should be accurately known. In this calculation of oil flow rate, the 1D-CFD[8), (9)] in which the oil passage and the orifice are converted to a model by the diameter or the length of each was used. Also, regarding the oil pump, relief valve, oil cooler, etc., the P-Q characteristics of each were incorporated into the 1D-CFD model. As the 1D-CFD is also a technique commonly used in the product development, detailed explanations therefore are omitted here.

As shown in Fig. 2, the 1D-CFD calculation of the oil flow rate is incorporated into the 1D thermal simulation, and is also used for the calculation of heat transfers in the engines occurring via the oil.

4.3.2. Calculation of heat transfer in camshaft chamber

In the camshaft chamber, the oil flowing out of the small holes in the rotating camshaft runs to the bottom surface of the chamber and returns to the crankcase. In this process, a heat transfer takes place between the oil and the cylinder head.

This oil behavior is analyzed by the particle method using Moving Particle Semi-implicit (MPS) method[(10)], which is an algorithm for calculation of flow of incompressible fluid. The particle method is a numerical simulation method for a continuum using particles, and unlike the widely-applied finite difference method or finite volume method, it does not require meshing. Therefore, the particle method is a technique that has been recently applied to a flow field having a free surface such as the behavior of oil in an engine[(11)], the sloshing of fuel in a fuel tank, and so on.

Here, the processes through which the oil flowing from the camshaft returns to the crankcase via the cam chain chamber were calculated. Figure 8 shows the calculated behavior of the oil in the camshaft chamber. The calculation is for an engine speed of 8000 r/min, at which the camshaft rotates at 4000 r/min. The oil flow rate, which was calculated using the previously-mentioned 1D-CFD, was applied as a calculation condition. Also, for simplification, the motions of the valves and the cam chain were excluded from the calculation. Obtaining a time average of the calculation results, the zone where more than the prescribed numbers of particles exist is used as the area on which the oil flows.

In the analysis using the particle method, the heat transfer coefficient between the oil and the wall depends on factors such as the particle diameter and its influence radius in the calculation. It is therefore difficult to maintain a certain degree of calculation accuracy when applications to a large number of engines are considered. The heat

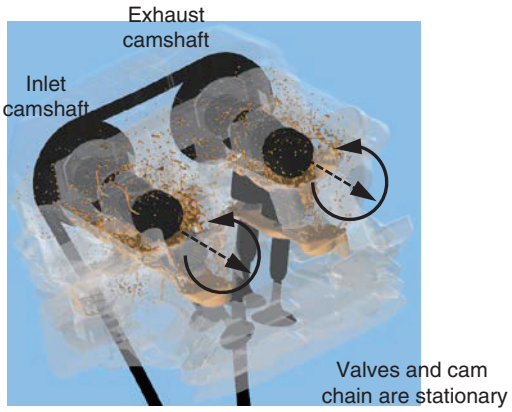


Fig. 8 Calculation result of oil flow in camshaft chamber

transfer coefficients between flowing oil and a flat plate were also acquired experimentally, and these values were used to calculate the heat transfer in the camshaft chamber. Figure 9 shows an overview of the test equipment. It allows a supply of oil on the evenly heated flat plate, in which the flow rate and the temperature are controlled. The flat plate is made of an aluminum alloy for which the thermal conductivity is already known. Also, to prevent heat dissipation from the heated flat plate to the ambient air, the outside of the flat plate is covered with an insulating material.

Using the test equipment, the temperatures of the oil and the inside of flat plate were measured, and the heat flux was calculated using the temperature gradient in the flat plate. By dividing the heat flux by the difference between the surface temperature of the flat plate and the oil temperature, the heat transfer coefficient between the flowing oil and the flat plate was determined. Note that the surface temperature of the flat plate was extrapolated from the temperature gradient in the flat plate.

$$\alpha_2 = \frac{q}{T_{\mathrm{Oil}} - T_{\mathrm{Wall}}} \tag{7}$$

$$q = -k \cdot \frac{\partial T}{\partial x} \tag{8}$$

where,

α_2 : Heat transfer coefficient between flowing oil and flat plate

T_{Oil} : Oil temperature,

T_{Wall} : Flat plate surface temperature,

q : Heat flux in flat plate,

k : Thermal conductivity of flat plate

The calculation of the heat transfer coefficient between the flowing oil and the flat plate was conducted using the oil flow rate, oil temperature, and the flat plate temperature as parameters.

Figure 10 shows the measured heat transfer coefficient between the flowing oil and the flat plate. As Fig. 10(a) shows, the heat transfer coefficient is virtually constant irrespective of the oil temperature or the flat plate temperature within the range where the measurements were conducted. In the meantime, as Fig. 10(b) shows, such a tendency is seen that along with an increase of oil flow rate, i.e., an increase of oil flow speed, the heat transfer coefficient increases.

Accordingly, as seen in Eq. (9), the heat transfer coefficient between the flowing oil and the plate can be expressed as a function of the oil flow rate only, and is applied thus to the 1D thermal simulation model.

$$\alpha_2(Q) = A_1 \cdot Q^{A_2} \tag{9}$$

where,

Q : Oil flow rate

A_1, A_2 : Empirical constants

4.3.3. Calculation of heat transfer from back surface of piston crown

The region where the oil impinges and the heat transfer coefficient are required for calculation of heat transfer between the oil from the piston-cooling jet and the piston in the same manner as in the camshaft chamber.

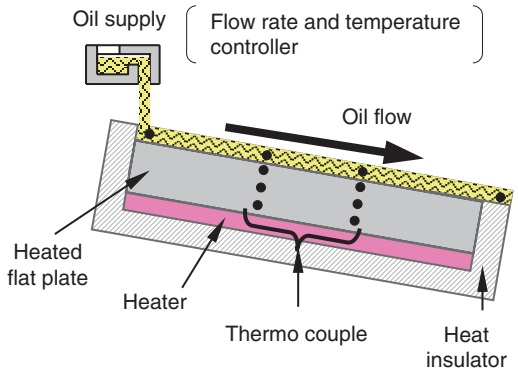
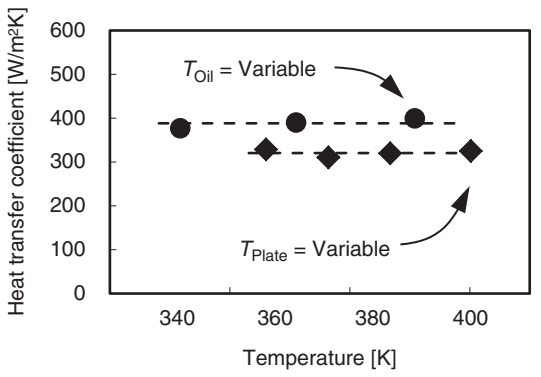
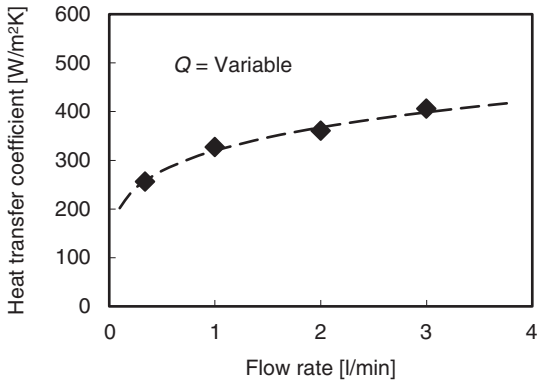


Fig. 9 Test equipment for measurement of heat transfer coefficient between flowing oil and flat plate



(a) Influence of oil and flat plate temperature



(b) Influence of oil flow rate

Fig. 10 Measurement results of heat transfer coefficient between flowing oil and flat plate

Table 2 Calculation conditions of CFD for oil jet

Solution type	Unsteady state
Working fluid	Oil and Air
Compressibility	Incompressible
Pressure velocity coupling	SIMPLE (Semi Implicit Method for Pressure Linked Equation)
Mesh type	Hexahedron
Mesh size [mm]	0.15 - 2.4
Engine speed [r/min]	2,000
Flow rate of oil jet [l/min]	1.0

Firstly, how to calculate behavior of oil from the piston-cooling jet and where on the back surface of piston crown the oil impinges is explained hereafter. As the parts such as pistons and connecting rods are in motion during actual engine operation, the impingement position and the velocity of the oil jet change from moment to moment. Keeping that in mind, using the 3D-CFD taking into account the mutual influence of the airflow and the oil in the crankcase, we attempted to calculate the area where the oil impinges on the back surface of reciprocating piston. The 3D-CFD mentioned here means a gas-fluid multiphase flow calculation of the air and oil. The Euler-Euler approach was adopted and both the gas phase and the fluid phase were treated as continua[12), (13)]. In this calculation, the motions of the piston, the crankshaft and the connecting rod were also taken into account using the moving boundary. Figure 11 shows the outlines and mesh diagram of this calculation. Table 2 shows the calculation conditions. For the region in the proximity of the piston-cooling jet nozzle and in the direction of oil jet, the numerical diffusion of oil is restricted by laying fine meshes.

The oil impingement area was measured to verify the calculation results through recorded images of oil impingement taken with a high-speed camera through a transparent window made from acrylic resin located at the piston crown. The measurements were conducted at 2000 r/min with the engine driven by an electric motor.

Figure 12 shows a comparison of the measured and calculated oil impingement. The measured profile of the area where the oil impinges is shown by green lines, and the calculated profile of the area where the oil impinges is shown by red lines. In the calculation results, the zone on the piston surface where the oil volume ratio exceeds a certain level is deemed as the impingement zone, and the measured profile of the area where the oil impinges is also shown for comparison. The calculated result corresponded to the measurement result at each crank angle.

Accordingly, it was decided that the average value of

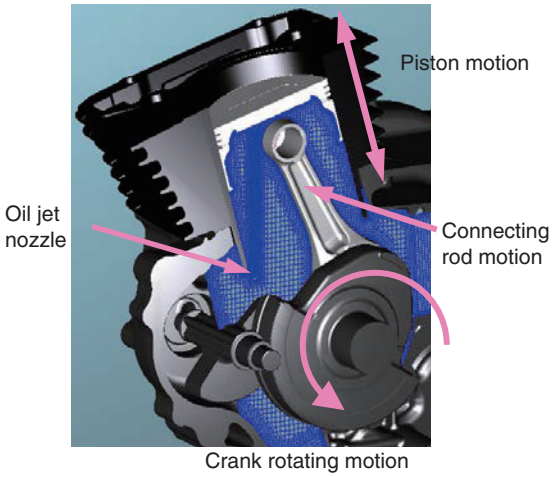


Fig. 11 Outline of CFD model for oil jet and mesh diagram

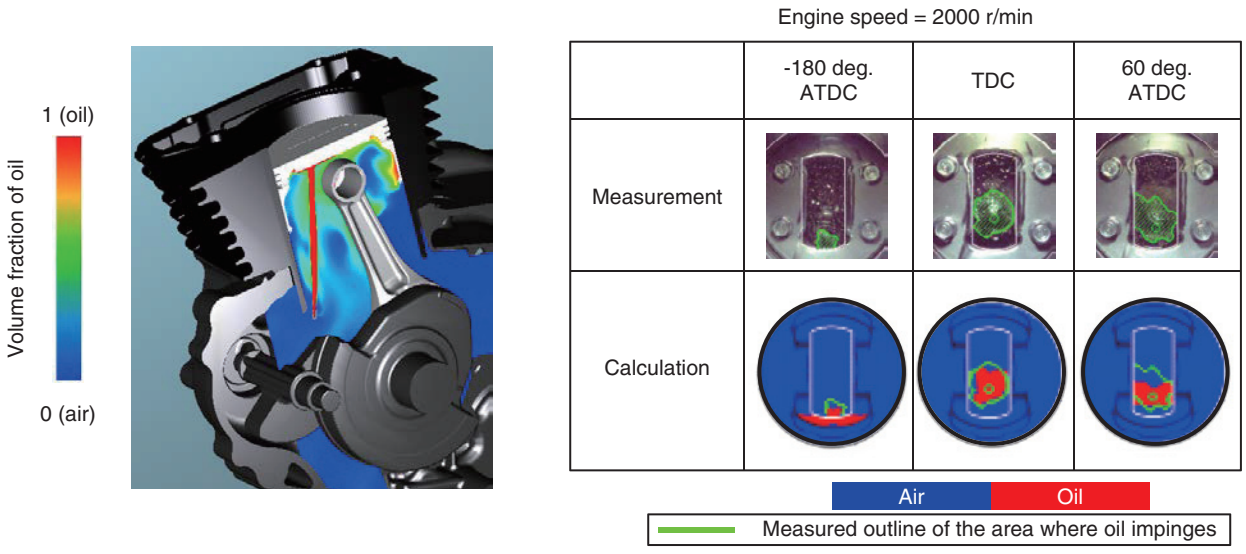


Fig. 12 Comparisons of oil impingement area on back of piston

those calculated results for a single engine cycle was used for the 1D thermal simulation.

As the heat transfer coefficient between the oil and the piston is mesh-dependent also in this CFD, it is decided to use the heat transfer coefficient calculated based on the parameters yielded from measurements.

To obtain an empirical equation for the heat transfer to the oil jet which cools the piston, the heat transfer coefficient was determined using the test equipment shown in Fig. 13. The basic principle of the test equipment is the same as that for the equipment used for determination of heat transfer coefficient of the oil flowing on the flat plate. The heat transfer coefficient was determined by having the oil jet impinge on the heated flat plate and measuring the temperature in the flat plate and the oil temperature at the outlet of nozzle. The heat transfer coefficient between the impinged oil and the flat plate was determined while changing the oil flow rate, piston-cooling jet nozzle diameter and the distance between the nozzle and the flat plate.

Figure 14 shows the measured heat transfer coefficient between the impinged oil and the flat plate. As Fig. 14(a) shows, while a slight variation is seen in the heat transfer coefficient depending on the piston-cooling jet nozzle diameter, the heat transfer coefficient is almost proportional to the flow rate. It is generally known that the heat transfer coefficient in the area where jet flow impinges depends significantly on the flow velocity, and has a radial distribution from the center of impingement[14]. However, in this project, we omitted the measurement of the radial distribution of the heat transfer coefficient as our purpose was to get a typical value representing the heat transfer coefficients in the area where oil is impinged. It is assumed, because of this measurement setting, that the heat transfer coefficient is influenced more by the oil flow rate than the nozzle diameter (i.e. flow velocity, effectively).

Figure 14(b) shows that the heat transfer coefficient increases as the distance between the nozzle and the flat plate is reduced. This tendency is maintained despite differences in oil flow rates. From these findings, the heat transfer coefficient between the impinged oil and the piston is expressed in Eq. (10) as a function of the oil flow rate and the distance from the nozzle to the piston.

$$\alpha_3(Q, L) = B_1 \cdot Q \cdot L + B_2 \cdot Q + B_3 \cdot L + B_4 \qquad (10)$$

where,

L : Distance between nozzle and piston

B_1–B_4 : Empirical constants

The oil impingement areas determined by this calculation and the average heat transfer coefficient on the back surface of piston crown in a cycle of the engine determined empirically from Eq. (10) were applied to the 1D thermal simulation model. Thus, the heat transfer processes in the cylinder head and the cylinder were taken into account in the temperature estimation method of this project.

4.4. Calculation of Heat Dissipation to the Atmosphere

As the flow of air around the engine in a running motorcycle must be taken into account in order to calculate the heat dissipation from the engine surfaces to the atmosphere, an airflow simulation was conducted using the 3D model of a complete motorcycle. On the basis of the findings from the 3D-CFD for the airflow, the engine surfaces were split into a number of zones, and the surface area and the average heat transfer coefficient in the zone

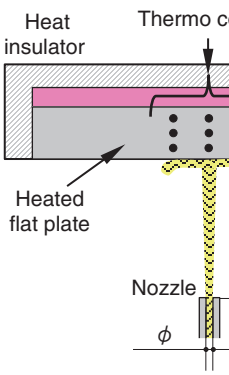
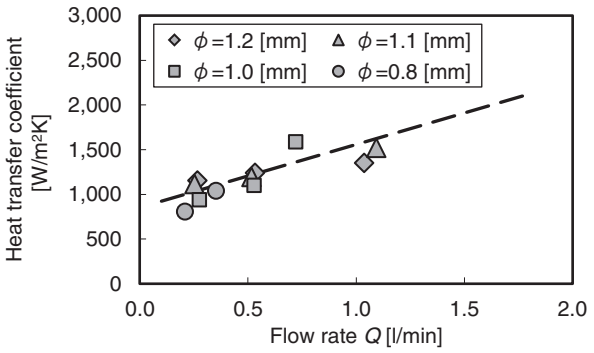
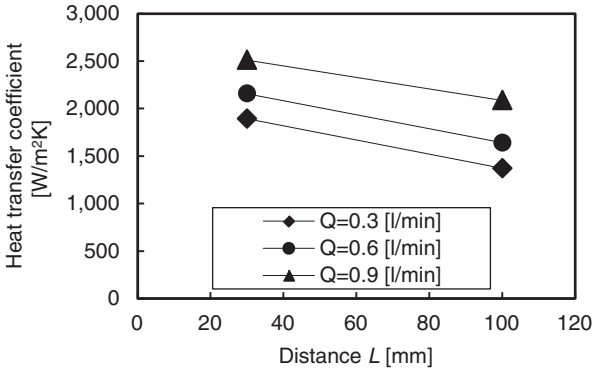


Fig. 13 Test equipment for measurement of heat transfer coefficient between impinged oil and flat plate



(a) Influence of oil flow rate and nozzle diameter



(b) Influence of distance from nozzle to flat plate

Fig. 14 Measurement results of heat transfer coefficient between impinged oil and flat plate

were calculated and used as the boundary conditions of the 1D thermal simulation model. The distribution of heat transfer coefficients was also used as a boundary condition of the detailed temperature distribution estimation.

As an example, a list of CFD calculation conditions in the vehicle A is indicated in Table 3, and the mesh diagram in the proximity of the engine is shown in Fig. 15. The mesh size near the engine surface is 1 mm, and the mesh size is set to a coarse size in accordance with the increase of the distance from the engine. The total number of meshes is approximately 25 million. Recently, unsteady calculation using an LES (Large Eddy Simulation) is widely applied to the estimation of aerodynamic effects and/or noises from turbulence[15]. However, it can be considered that the time scale of temperature changes on the engine surface is significantly larger than the time scale of the vortices occurring on the engine surface. Accordingly, we judged that the 3D-CFD for air flow under the steady conditions is adequate in this project.

4.5. Estimation of Detailed Temperature Distribution in Engine

For estimation of detailed temperature distribution in the engine, the heat balance in the engine shown in Fig. 16 is determined by the calculation in the 1D thermal simulation in which a combination of the technical options explained so far is applied. The diagram is the amount of heat transfer from various walls inside and outside of the engine, indicating one-cycle average of the engine. It indicates that the amount of heat transfer into the engine is very large from the combustion chamber [(1)-(3) in Fig. 16] and from the exhaust port, which is constantly exposed to hot gas. Conversely, the amount of heat dissipation from the engine is largest to the atmosphere [(9), (10)], followed by the heat transfer to the oil from the piston and camshaft chamber. It can also be understood from the aforementioned that in an air cooled engine, the heat transfer to the atmosphere and to the oil is very essential and cannot be ignored.

Next, using the findings from the 1D thermal simulation as the boundary condition, the 3D conductivity simulation

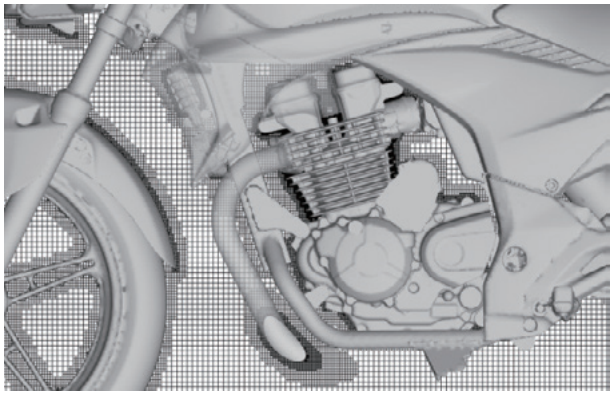
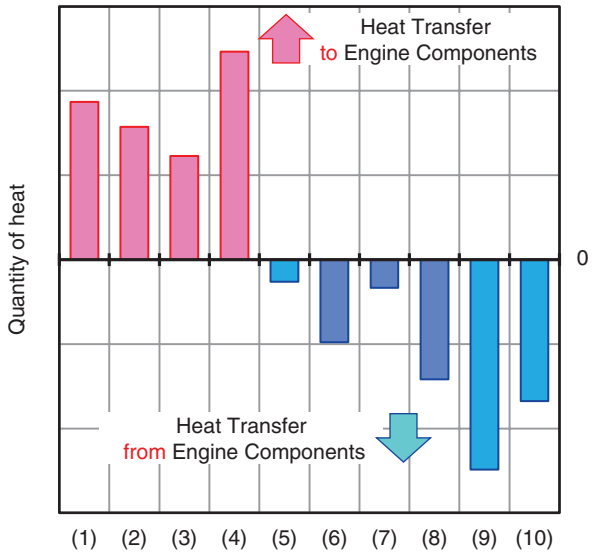


Fig. 15 CFD calculation mesh diagram for airflow around engine

Table 3 Calculation conditions of CFD for airflow

Solution type	Steady state
Working fluid	Air
Compressibility	Incompressible
Turbulence model	Realizable k-ε
Mesh types	Hexahedron Tetrahedron Pyramid
Mesh size around the engine [mm]	1 - 8
Total number of meshes	25,000,000
Vehicle speed [km/h]	128

was conducted in the actual engine configuration. The overview of the calculation model of vehicle A is shown in Fig. 17, and the calculation conditions in Table 4. Regarding the thermal conductivity of engine components and the heat transfer coefficient at an interface between varying materials, the same value as in the 1D thermal simulation model was used. The total number of meshes in the calculation is approximately 15 million, requiring approximately 40 boundary conditions for the entire walls. In this method, as a substitute for the omission of piston shape, the boundary condition taking into account the piston travel obtained from the 1D thermal simulation was incorporated in the cylinder bore wall. The temperature and the heat transfer coefficient applied as the boundary condition are shown in Fig. 18. As shown in the picture,



(1) Combustion chamber (Cylinder head)
(2) Combustion chamber (Cylinder)
(3) Piston
(4) Exhaust port
(5) Inlet port
(6) Oil (Cylinder head)
(7) Oil (Cylinder)
(8) Oil (Piston)
(9) Cooling fin (Cylinder head)
(10) Cooling fin (Cylinder)

Fig. 16 Heat balance in engine of vehicle A

Table 4 Calculation conditions of 3D thermal conductivity simulation

Solution type		Steady state
Mesh type		Tetrahedron
Mesh size [mm]		0.7 – 1.4
Total number of meshes		15,000,000
Number of boundary conditions		40
Boundary conditions	Internal surface of engine	T and α (1D thermal simulation)
	Outer surface of engine	Atmosphere temperature, α distribution (3D-CFD for airflow)

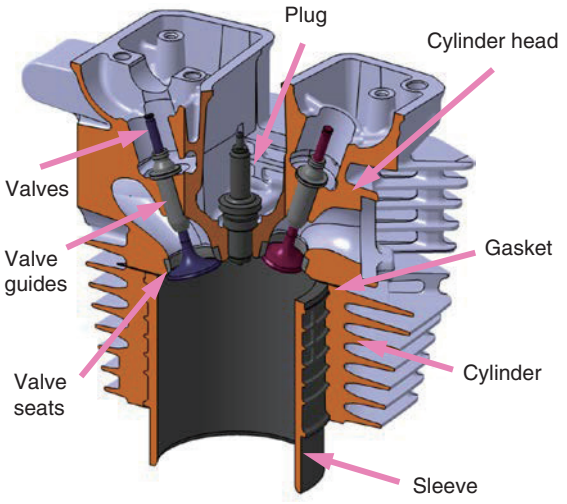


Fig. 17 Outline of 3D thermal conductivity simulation model

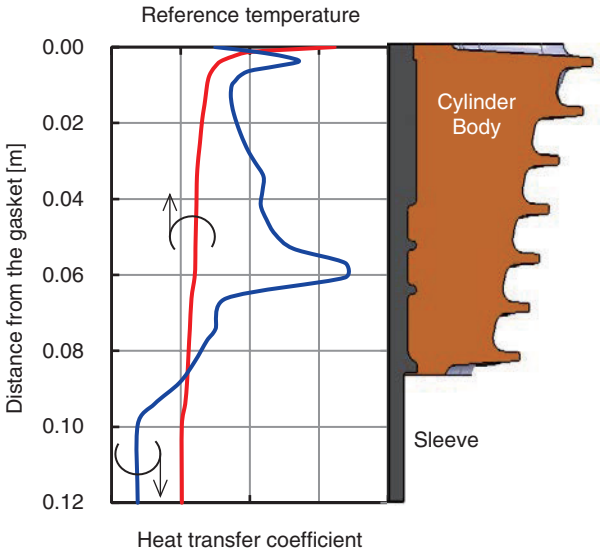


Fig. 18 Boundary conditions on cylinder wall

the reference temperature is high in the region close to the gasket surface that is significantly affected by the combustion gas. Also, the heat transfer coefficient is distributed in such a manner that it is high in the proximity of the TDC (Top Dead Center) and BDC (Bottom Dead Center) of piston.

Moreover, the distribution of heat transfer coefficient calculated by the 3D-CFD under running conditions is mapped on the engine surfaces.

5. Validation of Engine Temperature Estimation Accuracy in Running Motorcycle

5.1. Validation of Temperature Distribution Estimation Accuracy in Vehicle A

To validate developed method, we measured the temperatures of various parts of the engine mounted on vehicle A placed in a wind tunnel equipped with a dynamometer. The measurements were conducted at the maximum speed of the test motorcycle, 128 km/h, and an engine speed of 8150 r/min.

Figure 19 shows the estimated temperature distribution on the engine surfaces. Figure 23 shows a comparison of the temperature distribution in various parts of the cylinder head. The estimated temperatures and the measurements are in good agreement at the four spots in the proximity of the combustion chamber and on the spark plug seating surface. Good agreements between the estimates and the

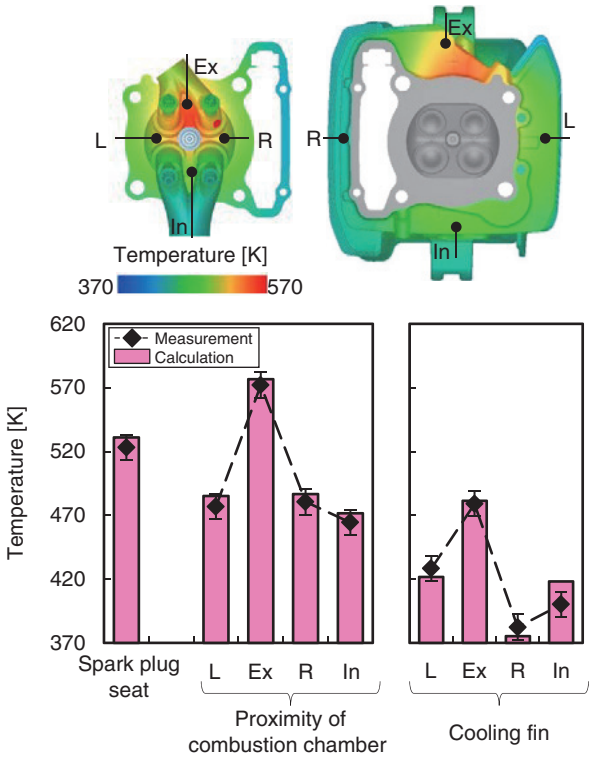


Fig. 19 Comparisons of temperature distribution in cylinder head

measurements are also seen in the cooling fins. In most points, the estimations are within 10 K of the measurements.

Figure 20 shows a comparison of the cylinder temperature distributions at a position 5.5 mm away from the cylinder head mating surface and 2 mm from the bore surface. The estimated and the measured temperature distributions around the cylinder are in very good agreement with a variance less than ±10 K. The measured temperature is higher on the exhaust port side than on the intake port side. The temperature on the right side of engine is higher than on the left side. While the high temperature on the exhaust port side is due to the exhaust gas, the reason why the right side becomes higher in temperature can be considered due to poor heat dissipation to the atmosphere because the cam chain chamber is on the right side and that side of the cylinder is far from the cooling fins. The estimation of this trend is also in a good agreement with the measurement. The variance from the measurement is within ±10 K at any measurement point.

Figure 21 shows a comparison of the temperature distribution in the direction of cylinder axis. The same trend is seen in the estimates and the measurements at any spot around the cylinder. In the conventional method of estimating the temperature distribution using just a 3D thermal conductivity simulation, the temperature gradient along the cylinder axis direction cannot be estimated accurately. In the newly developed method, however, the temperature distribution is accurately estimated by using the 1D thermal simulation model and taking into account the amount of heat transfer from the combustion gas to the cylinder wall in the direction of the cylinder axis.

5.2. Influence of Exterior Specifications

Tests were then conducted with and without a shroud for cooling the area near the spark plug. As Fig. 22(a) shows, the airflow around the spark plug and the heat transfer coefficient vary significantly with and without the shroud. Also, as Fig. 22(b) shows, it has been confirmed that the estimation can adequately represent the changes of temperature in the spark plug seating surface.

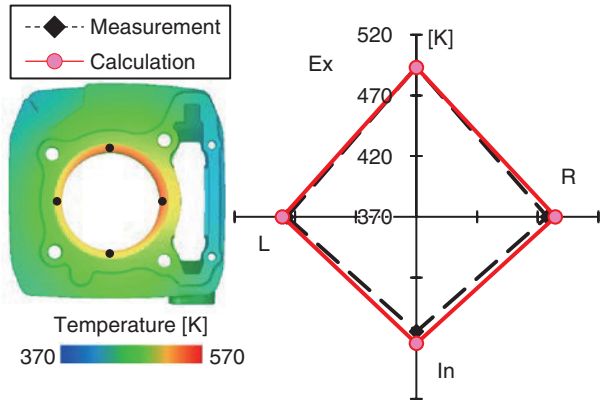


Fig. 20 Comparisons of temperature distribution in cylinder

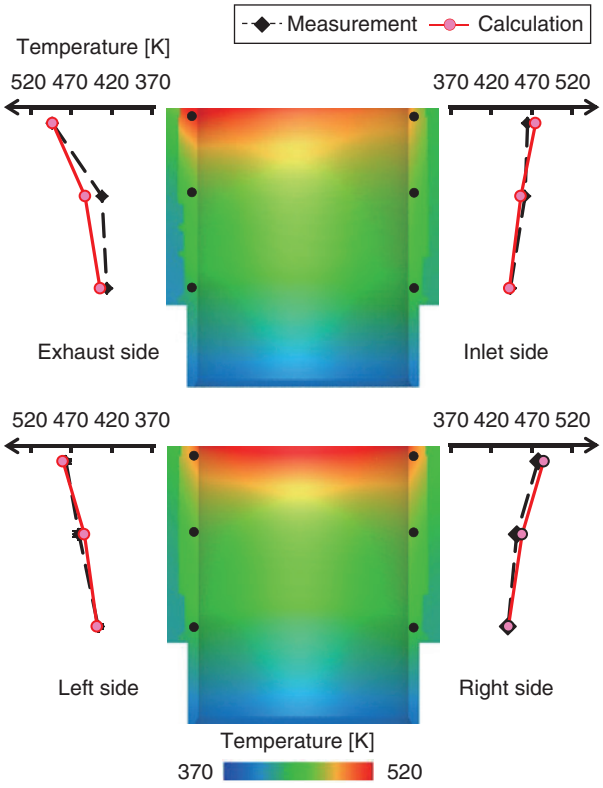
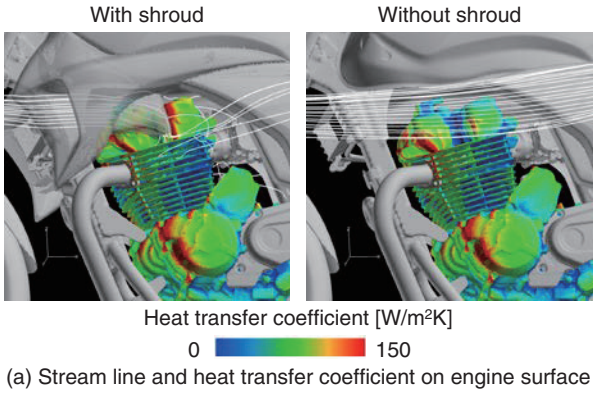
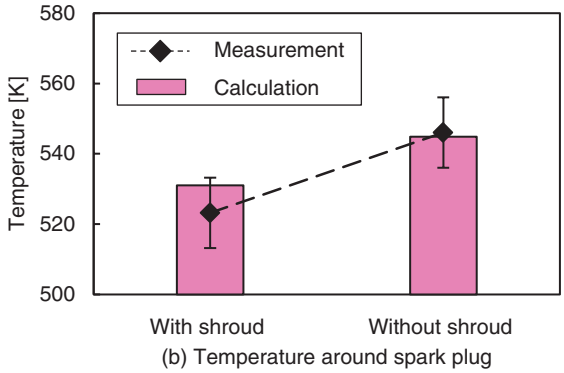


Fig. 21 Comparisons of temperature distribution in the direction of cylinder axis



(a) Stream line and heat transfer coefficient on engine surface



(b) Temperature around spark plug

Fig. 22 Comparisons of heat transfer coefficient and temperature around spark plug

5.3. Validation of Temperature Estimation Accuracy in Vehicle B

This method was validated using a second motorcycle. The specifications of the engine in the test motorcycle are as per vehicle B shown in Table 1. The temperature estimation validation was run at the maximum speed of the test motorcycle, 89 km/h, and an engine speed of 8300 r/min. Figure 23 shows a comparison of engine temperature distributions from the motorcycle. Measurements were taken from the cylinder at a position 23.8 mm away from the cylinder head mating surface and 2 mm from the bore surface. The temperature distribution estimation by this method is in good agreement with the measurement both at the spark plug seat and near the cylinder. In the temperature distribution of this motorcycle, the differences between the estimates and the measurements are less than 10 K.

This proves the high accuracy of this temperature estimation method, since the two motorcycles have significantly different engine displacements, power output, engine configurations, airflow, and so on.

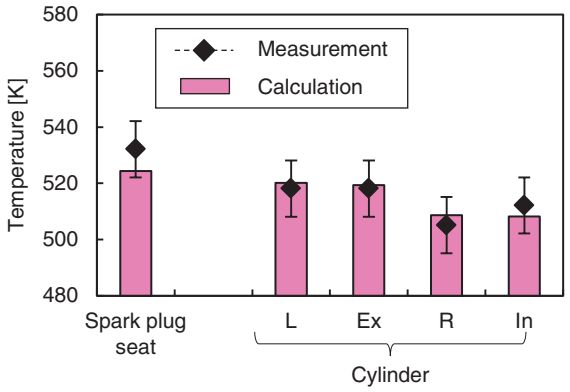


Fig. 23 Comparisons of engine temperature of vehicle B

6. Conclusions

We have developed a new method for estimating the temperature distribution in an air-cooled engine in a running motorcycle at an early stage of product development. The features of this method are outlined in the following.

(1) To determine the heat balance of engine, we created a 1D thermal simulation model in which the heat input from the combustion, the heat transfer in the engine, and the heat dissipation to the atmosphere are coupled.

(2) The heat transfer coefficient between the cylinder body and the sleeve, which has not been taking into account in the past, was empirically-determined and applied to the 1D thermal simulation model

(3) A detailed process of heat transfer to the oil is applied to the 1D thermal simulation model by combining the empirically determined heat transfer coefficient between the oil and the wall with the 3D-CFD for oil behavior.

(4) The proportion was clarified by using 1D thermal simulation between the transferred heat to the various portions of the engine and the heat dissipated to the oil and the atmosphere. Based on the result, the temperatures and the heat transfer coefficients of inside and outside of the engine were obtained. Eventually, those data were implemented to the detailed temperature distribution estimation.

Thus, our method makes it possible to accurately estimate the engine temperature distribution, with a deviation less than ±10 K, in an engine on a running motorcycle without using data measured from the engine. We also confirmed a high correlation even when the flow of air to the engine changes significantly. Moreover, it has been proven that the method provides an accurate estimation of temperature even when the cooling air flow to the engine is significantly altered or in another motorcycle equipped with a different engine. The new method has been thus developed for estimation of temperature distribution in an air-cooled engine in the design stage.

References

(1) Takahashi, Y., Gokan, Y.: CFD Analysis of Air Flow of Air-Cooled Motorcycle Engines, SAE Technical Paper, 2006-32-0005 (2006)

(2) Baird, A., Thornhill, D., Cunningham, G., Troxler, P., Price, B.: CFD Simulations of Heat Transfer from Air Cooled Engines, SAE Technical Paper, 2006-32-0004 (2006)

(3) Gokhale, A., Karthikeyan, N.: Optimization of Engine Cooling Through Conjugate Heat Transfer Simulation and Analysis of Fins, SAE Technical Paper, 2012-32-0054 (2012)

(4) Mahmoud, K., Loibner, E., Krammer, J.: Integrated 1-D Tools for Modeling Vehicle Thermal Management, SAE Technical Paper, 2004-01-3406 (2004)

(5) Moffat, J.: Coupling of 1-D and 3-D CFD Models to Predict Transient Hydraulics in an Engine Cooling Circuit, SAE Technical Paper, 2002-01-1285 (2002)

(6) Horikawa, H., Kido, H., Iijima, S., Murakami, Y.: Prediction Technology of Engine Power and Intake/Exhaust Noise Using 1D-Simulation for Small-Displacement Motorcycles, SAE Int. J. Engines 3(2), p.428-437 (2010)

(7) Onorati, A., Ferrari, G., Cerri, T., Cacciatore, D., Ceccarani, M.: 1D Thermo-Fluid Dynamic Simulation of a High Performance Lamborghini V12 S.I. Engine, SAE Technical Paper, 2005-01-0692 (2005)

(8) Nomura, T., Matsushita, K., Fujii, Y., Fujiwara, H.: Development of Temperature Estimation Method of Whole Engine Considering Heat Balance under Vehicle Running Conditions, SAE Int. J. Engines 8(1), p.120-134 (2015)

(9) Klingebiel, F., Kahlstorf, U.: Simulating Engine Lubricaton Systems with 1-D Fluid Flow Models, SAE

Technical Paper, 2000-01-0284 (2000)
(10) Koshizuka, S., Oka, Y.: Moving-Particle Semi-implicit Method for Fragmentation of Incompressible Fluid, Nuclear. Science and Engineering, Vol. 123, p.421-434 (1996)
(11) Muto, K., Sakai, I., Ozaki, N.: Prediction of the Fluid Resistance in Stirred Fluid Using The Particle Method, Transactions of Society of Automotive Engineers of Japan, Vol. 41, No. 1, p.147-151, (2010) (in Japanese)
(12) Ishii, M.: Thermo-Fluid Dynamics Theory of Two-Phase Flow, Eyrolles, Paris (1975)
(13) Basara, B., Alajbegovic, A., Beader, D.: Simulation of Single- and Two-Phase Flows on Sliding Unstructured Meshes Using Finite Volume Method, International. Journal for Numerical Methods in Fluid, Volume 45, Issue 10, p.1137-1159 (2004)
(14) Martin, H.: Heat and Mass Transfer between Impinging Gas Jets and Solid Surface, Advances in Heat Transfer, Volume 13, p.1-60 (1977)
(15) Tsubokura, M., Nakashima, T., Nouzawa, T., Nakamura, T., Kitoh, K., Zhang, H., Hori, K., Oshima, N. and Kobayashi, T.: Numerical Prediction of Unsteady Aerodynamic Forces on Road Vehicles Using High Performance LES, FISITA World Automotive Congress (2008)

Author


Tomokazu NOMURA


Koichiro MATSUSHITA


Yoshihiko FUJII


Hirofumi FIJIWARA

Technology for Prediction of Housing Wear due to Outer Ring Creep under Bearing Load

Yayoi NAGASOE* Shigeharu WAKUI* Yuta MAEYOSHI*

ABSTRACT

A method for the prediction of the amount of wear occurring to the housings of automotive transmissions due to the rotation of the outer rings of the bearings has been newly developed. The method employs a 3D dynamic analysis in order to simulate the creep behavior of the outer rings of the bearings. The amount of wear to the housing is calculated based on the contact pressure and creep distance of the outer rings of the bearings determined by analysis and the specific wear rate measured in a unit wear test. Because the direction of wear differs for each shift stage, the amount of wear is totalized with consideration of the direction of load. Predictions of the amount of wear to housings display a high level of correlation with the results of durability tests. The high-accuracy prediction of the amount of housing wear makes it possible to study specifications for the control of housing wear from an early stage of the design.

1. Introduction

Growing demand for technologies that will increase fuel efficiency have seen the layouts of automotive transmissions tending to become more complex, with the use of multi-stage and multi-shaft configurations that seek to realize further electrification and wider operating ranges. In addition, demands for reduced weight and greater compactness are tending to reduce the space between neighboring shafts in order to make it possible to fit parts more closely in restricted spaces.

The rolling bearings used for each shaft are fitted in a cast aluminum case housing (Fig. 1). When the rolling bearings are reduced in size or the stiffness of the housing is reduced in order to reduce weight and increase compactness, the outer rings of the bearings rotate in relation to the housing, and the section of the housing in which the bearings are fitted can be subject to wear. This wear is termed housing wear. Because it causes deviation of the positioning of the shaft supports, this type of wear may produce misalignment of the gears, resulting in noise and durability issues.

Responses using indicators including the contact pressure of the outer rings have been investigated in attempts to control housing wear. However, even when factors such as the diameter of the bearings or the housing layout are modified, the process can become one of trial and error, and this has represented an issue in relation to short development periods.

The need to respond to increasingly complex configurations and boost accuracy in relation to predictive indicators for housing wear was therefore increasing.

The phenomenon of rotation of the outer rings of the bearings, which produces housing wear, is termed outer ring creep. A great deal of research has been conducted on the mechanism of outer ring creep and analysis of its effects[(1)-(3)], but there do not appear to be any reports concerning the prediction of the amount of wear occurring to the housing.

This paper will discuss the development of a method of prediction of the amount of housing wear from the design review stage that is sufficiently accurate for practical use.

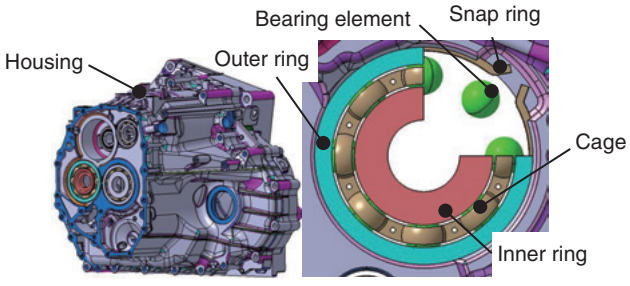


Fig. 1 Bearings

* Automobile R&D Center

2. Housing Wear Resulting from Bearing Outer Ring Creep

At room temperature, the outer rings of the bearings that support the shafts are pressed into the section of the housing in which they are fitted, and are therefore constrained. However, when the unit is in use its temperature increases, and gaps appear due to the difference in thermal expansion between aluminum and iron. As a result, the outer rings become unconstrained in the circumferential direction. Outer ring creep, which results in wear, is a phenomenon in which the outer rings rotate slowly in the same direction as the inner rings in contrast with the fixed housing.

According to Zhan et al.[1], this phenomenon originates in elastic deformation of the surfaces of the outer rings as a result of the fact that the bearing elements forcefully press the outer rings as they rotate. Teramoto et al.[3] reproduced creep in a CAE model and an actual transmission unit, and reported on the degree of contribution to creep of factors related to the bearings.

Housing wear occurs when the bearing outer rings are pressed against the inner wall of the housing in the load direction and slide against the housing due to creep. As Fig. 2 shows, housing wear progresses in the direction of the load on the bearings, and the amount of wear is manifested as the degree of change in the diameter of the housing. Because the outer rings of the bearings are manufactured from steel and ground to a high level of accuracy, they display good surface roughness, and there is no change in their dimensions or the state of their surfaces even after the completion of durability tests. The housing is cast from aluminum, and wear therefore occurs on the housing side only. Housing wear proceeds at the slow pace of around several hundred μ m per 1,000 hr. Because of this, the wear face remains smooth, and does not adhere. The abrasion powder produced floats in the oil without settling, and is so fine that it cannot be identified with the naked eye.

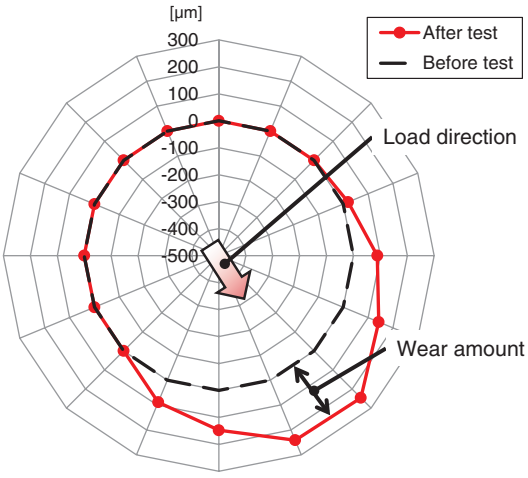


Fig. 2 Housing wear profiles

During durability tests, the amount of wear increases in proportion to the duration of the test, as shown in Fig. 3. Given this, it was hypothesized that the amount of housing wear would display a high correlation with the degree of accumulation of wear-related factors during the durability test. Based on this consideration, the method discussed in this paper attempted to approximately calculate the amount of wear by appropriately cumulating wear-related factors.

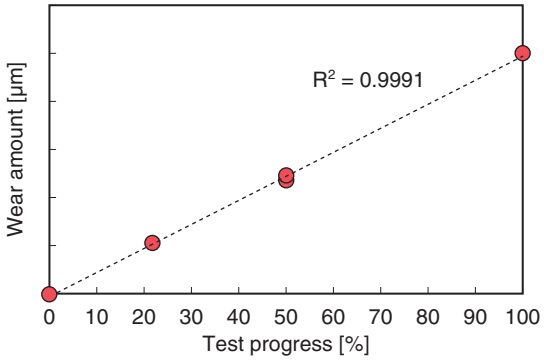


Fig. 3 Progression of housing wear in durability test

3. Development Goals

The amount of wear is generally expressed using the following Eq. (1), with the contact pressure and slip distance of the wear faces as the wear-related factors[4].

$$W = k \cdot P \cdot V \cdot t \quad (1)$$

W: Estimated amount of wear
k: Specific wear rate[5]
P: Bearing load contact pressure
V: Creep speed
t: Creep time

The following substitutions are made in this paper:

$$W = k \cdot P \cdot L = k \cdot P \cdot l \cdot n \quad (2)$$

L: Total creep distance
l: Creep distance for each passage of bearing elements
n: Total number of passages of bearing elements

Because the direction of wear differs for each shift stage, it is necessary to calculate wear separately and total it. First, the contact pressure and creep distance for each shift stage are calculated from the test time chart items and multiplied by the specific wear rate in order to convert them to the amount of wear. Because the form of housing wear is affected by the amount of

wear for all shift stages, the figures are totaled with consideration of the direction of load in each shift stage. The method of totaling the amount of wear for shift stages A and B (Fig. 4) will be considered as an example. The calculated amount of wear indicates the distance that the center of the bearings travels in the direction of bearing load. In this case, the form of wear is crescent-shaped, representing the distance between the initial housing holes and the bearing diameter following the movement of the center of the bearings. The amount of crescent-shaped wear is calculated for each angle on the circumference of the circle. The amount of crescent-shaped wear for each angle on the circumference of the circle is totaled for each shift stage, making it possible to calculate the form of wear produced by the two shift stages, A and B. As indicated above, relational equation (2) was hypothesized based on the fact that housing wear increases in a proportional relationship with the progress of the durability test. This made it possible to establish calculation methods for the following two items:

(1) A simulation technology for the behavior of outer ring creep
(2) A prediction technology for the amount of housing wear

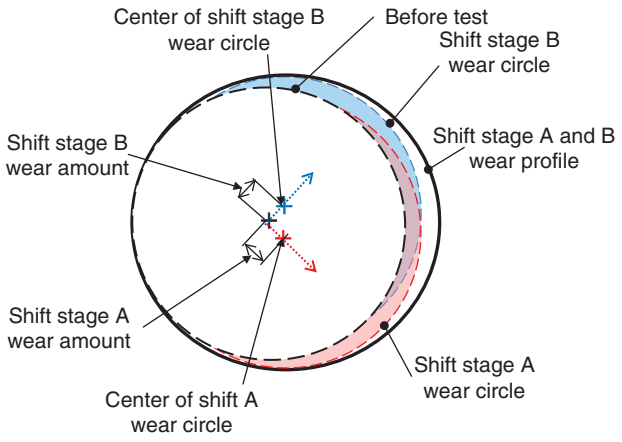


Fig. 4 Totaling housing wear profiles

4. Simulation Technology for Behavior of Outer Ring Creep

An analysis was conducted using general-purpose nonlinear dynamic analysis software in order to reproduce the macro behavior of the bearings and the micro-deformation of the outer rings. Part of the housing, the outer rings, the inner rings, the bearing elements, the cage and the snap rings were modeled in order to reproduce brake behavior as affected by the housing stiffness and the snap rings. Figure 5 shows the 3D analysis model.

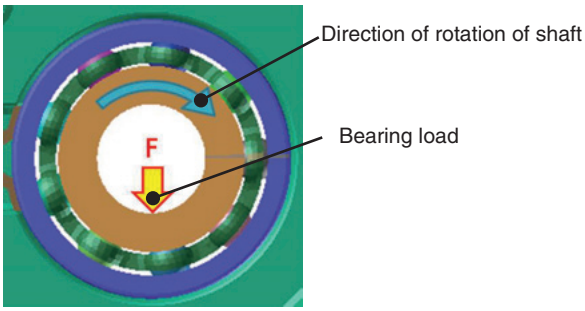
Each part was defined as an elastic body other than the bearing elements, which were defined as rigid bodies in order to reproduce the smooth forms of the elements.

In order to reproduce states in an actual transmission unit, as boundary conditions for the analysis, the outer circumference of the housing was completely constrained, while the bearing load for each shift stage was applied to the inner rings and the inner rings were subjected to forced rotation at a constant speed. A coefficient of friction of 0.15 was used between the outer rings and the housing and for the snap rings, and a coefficient of 0.05 was used for the interiors of the bearings.

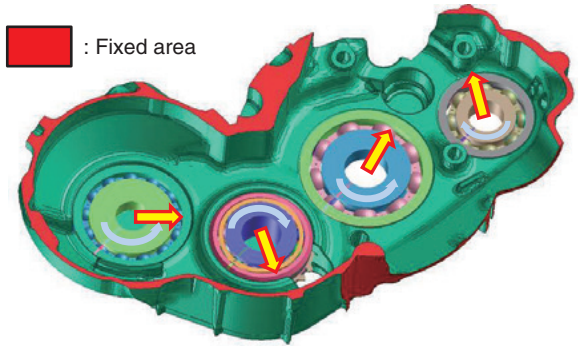
4.1. Study of Distribution of Contact Pressure

Measurements were conducted of contact pressure between the outer rings and the housing in an actual transmission unit in order to verify the accuracy of outer ring contact pressure in the simulation. The measurements were conducted by positioning a thin-film pressure sensor (thickness: 0.1 mm; 56 × 56 mm) between the housing and the outer rings of the bearings. The hole diameter of the housing was increased with consideration of the thickness of the sensor. The sensor was positioned in the direction of load; dummy sheets of equivalent thickness to the sensor were used in the remaining sections (Fig. 6).

Figure 7 shows the results of measurements conducted using the thin-film pressure sensor and the



(a) Concentrated nodal load and speed of rotation



(b) Displacement boundary conditions

Fig. 5 3D-analysis model

results of calculations of contact pressure in the dynamic analysis. Normally when the housing stiffness is uniform, the direction of maximum contact pressure on the bearing elements and the direction of bearing load correspond, but in this case the housing stiffness was low in the direction of load, and the directions did not match in the measurements. It was possible to reproduce the deviation in direction and absolute value of maximum contact pressure by means of faithfully 3D modeling the shape of the surrounding housing and dynamically rotating the bearing elements.

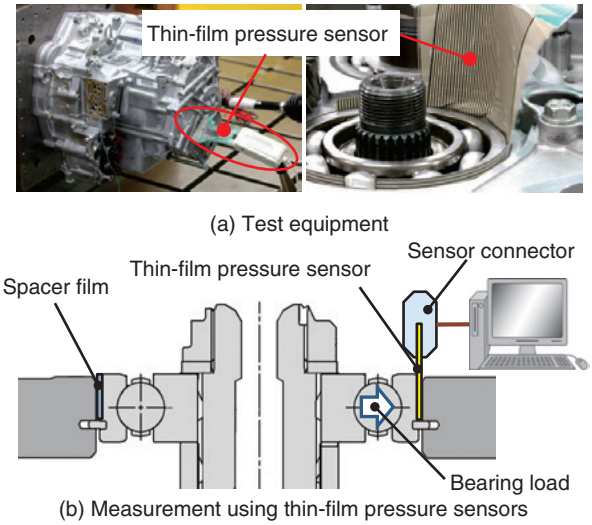


Fig. 6 Schematic of test equipment

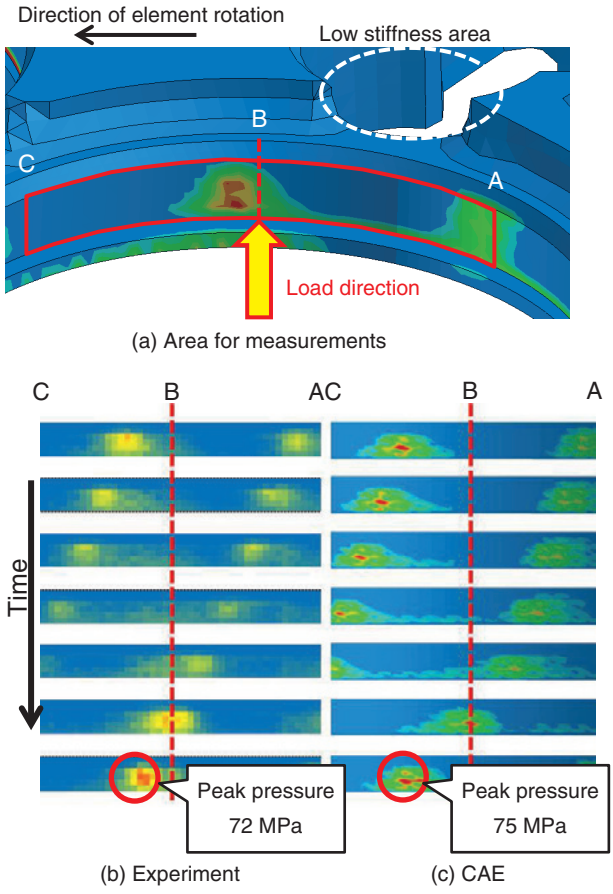


Fig. 7 Comparison of contact pressure

4.2. Calculation of Outer Ring Creep Distance

Figure 8 indicates the results of calculation of displacement of the outer circumferences of the outer rings in the direction of load using the 3D dynamic analysis discussed above. The outer rings move in the direction of progress of the bearing elements, but temporarily move in the opposite direction. Figure 9 explains this behavior.

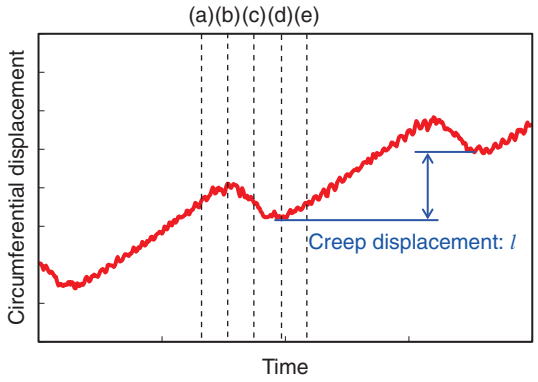


Fig. 8 Circumferential displacement at evaluation point

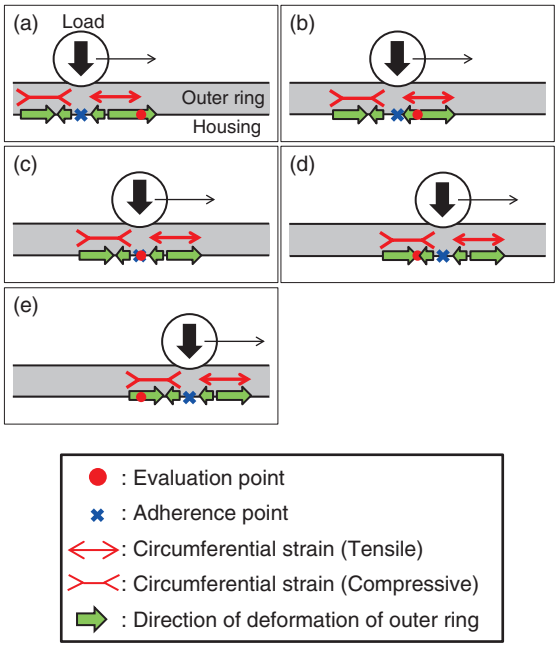


Fig. 9 Behavior of outer ring and ball

(a) Before the passage of the bearing elements, circumferential strain on the surfaces of the outer rings increases in the vanguard of the direction of progress of the bearing elements. Because of this, the evaluation point for maximum contact pressure moves in the direction of progress of the bearing elements.
(b) As the bearing elements approach the evaluation point, the evaluation point moves in the opposite direction due to the effect of the adherence point.
(c) When the bearing elements are directly above the evaluation point, the evaluation point adheres to the housing, and moves in the opposite direction to the bearing elements[2].
(d) When the bearing elements separate, the evaluation point moves in the same direction as the bearing elements due to the effect of the adherence point.
(e) After the passage of the bearing elements, because strain in the circumferential direction on the surfaces of the outer rings declines in the rear of the direction of progress of the bearing elements, the evaluation point moves in the same direction as the bearing elements. Following this, the process returns to (a).

In the calculations conducted in this research, the creep distance produced by one passage of the bearing elements was termed l. It was therefore possible to calculate the total outer ring creep distance, L, by multiplying this figure by the total number of passages of the bearing elements, n.

The total number of passages of the bearing elements was calculated based on parameters including shaft speed, engine torque, and shift stage from test time history data.

4.3. Study of Speed of Outer Ring Creep

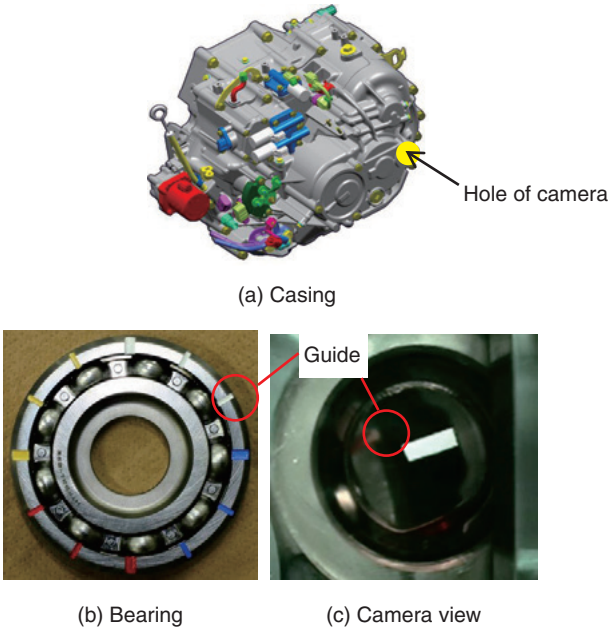
Because the direct measurement of micro-displacement is challenging, the accuracy of the simulation was verified by means of measurements of outer ring creep speed.

Figure 10 shows the set-up for measurement of outer ring creep speed in an actual transmission unit. A hole was drilled into the housing in order to render a section of the bearings visible, and a mark was machined on an outer ring to help enable measurement of the speed of outer ring creep.

Figure 11 shows results for actual measurements and simulation calculations of the speed of outer ring creep when the shift stage was fixed and the inner rings were rotated at 5,500 rpm.

Simulation predictions of outer ring creep speed basically matched the measurements taken in an actual transmission unit.

This demonstrated that the developed simulation technology for the behavior of outer ring creep provides a method of predicting contact pressure and creep distance in actual operation.



(a) Casing

(b) Bearing (c) Camera view

Fig. 10 Measurement of creep speed in bearing outer ring

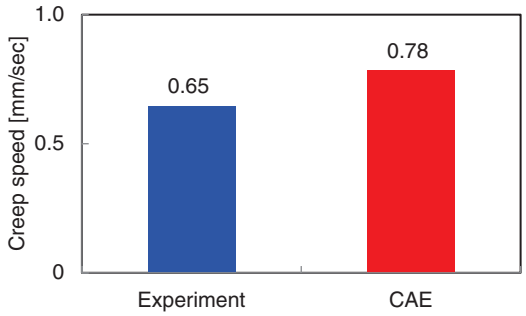


Fig. 11 Comparison of creep speed

5. Technology for Prediction of Housing Wear

5.1. Measurement of Specific Wear Rate

Pin-on-disc unit wear tests simulating the environment in an actual transmission unit were conducted in order to determine the specific wear rate for housing wear. Using a friction and wear tester (FPR-2300; RHESCA CO., LTD), a pin test piece was pressed against the upper edge of a disc-shaped test piece of 80 mm in diameter revolving horizontally, and sliding tests were conducted. The tip of the pin test piece had a cylindrical shape of 1.1 mm in diameter. In order to reproduce conditions corresponding to those in an actual transmission unit, the test was conducted using a pure Honda Automatic Transmission Fluid (ATF) lubricant at 80°C, under contact conditions of friction speeds of

0.4, 1.0, and 1.5 mm/sec and a contact pressure of 51.6 MPa (with a load of 5,000 g). The pin test piece was manufactured from the aluminum material employed in transmission housings. The disc was manufactured from the high carbon chrome steel (SUJ2) used for bearings. To help ensure that the disc displayed identical surface properties to bearings, a surface roughness (Rz) of 0.5 μm was used.

During the tests, the amount of wear of the pin was measured over time, and the relationship between the amount of wear and the friction distance was plotted on a graph. In the range within which the amount of wear increased linearly with increase in friction distance, the amount of wear per unit friction distance and contact pressure was calculated as the specific wear rate (mm^2/N). Tests were conducted three times for each friction speed and the average value of the calculated specific wear rate in each case was taken as the representative figure for that friction speed.

Figure 12 shows the relationship between specific wear rate and friction speed. The specific wear rate increases as the friction speed declines. This is considered to be due to an increase in the contact areas between the disc-shaped test piece and pin test piece as the friction speed declines. Wear is a phenomenon that occurs in the contact areas, and the amount of wear therefore increases with a greater amount of areas in contact. In addition, when the test pieces are sliding together under lubrication, lubricant films are decreasingly formed the lower the sliding speed, increasing the amount of the contact area[5].

Actual outer ring creep proceeds at a pace of 1.0 mm/sec or less, and the range in which the friction speed is 1.0 mm/sec in Fig. 12 corresponds to the speed range under an actual use state. The value on the horizontal axis that the line connecting the maximum values of the specific wear rate for each speed intersected with was taken as the maximum value of the specific wear rate in the speed range corresponding to that of an actual transmission unit (the value indicated by the arrow in Fig. 12; 1.3×10^{-8} mm^2/N), and was used to predict the amount of wear.

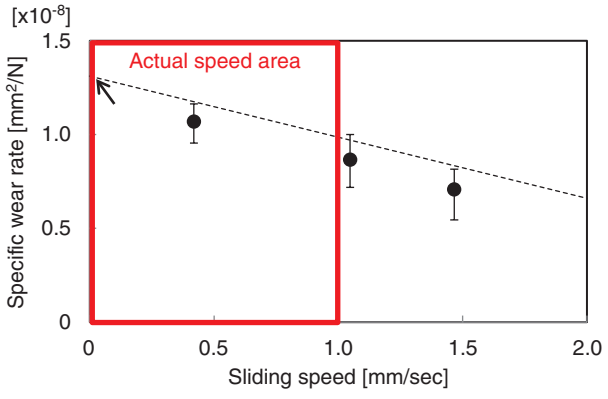


Fig. 12 Specific wear rate in relation to sliding speed

Table 1 Specifications of transmissions

Type	Bearing type
A	Ball
B	Ball
C	Double row angular contact ball
D	Ball
E	Ball
F	Ball
G	Four-point contact ball

5.2. Accuracy of Prediction of Housing Wear

CAE predictions of the amount of housing wear occurring during durability tests were compared with actual measurements in order to verify the general applicability of the developed prediction technology. Results were compared for transmissions using different forms of shift. Table 1 shows the bearings used in each of the transmissions for which comparisons were conducted.

Figure 13 shows results for the bearings in the

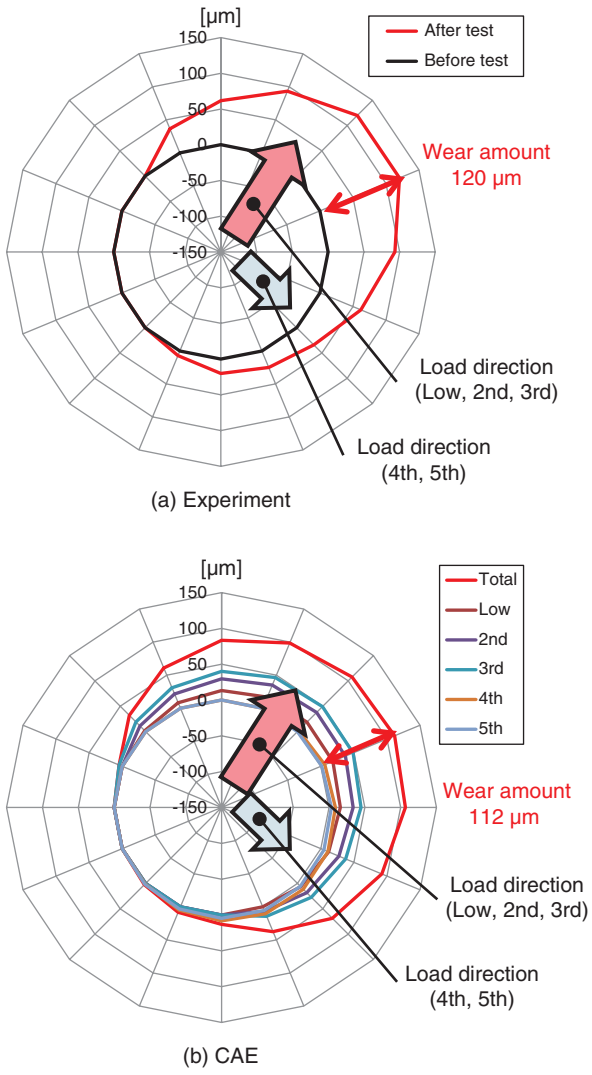


Fig. 13 Housing wear profiles

Type-B transmission. Even when the direction of the load on the bearings differed for each shift stage, this method produced results for maximum amount of wear, direction of ware and form of wear corresponding to measurements.

Figure 14 shows a plot of measured values and CAE predictions for Type-A to -G transmissions. Irrespective of the type of transmission or bearings, there is a high level of correlation between measurement results and CAE predictions.

This demonstrates that it is possible to predict the amount of wear that will occur in a transmission housing using the contact pressure on the outer rings and the creep distance that accumulates in the outer rings.

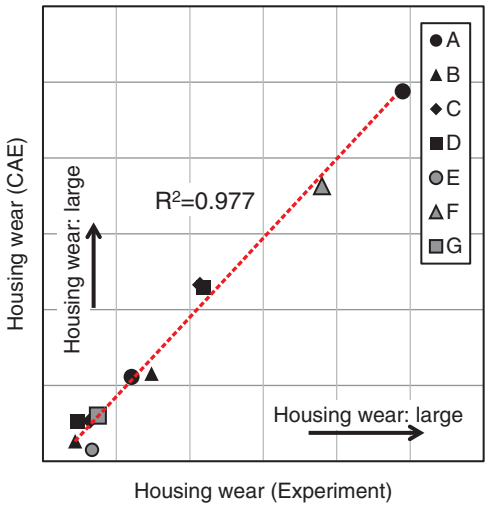
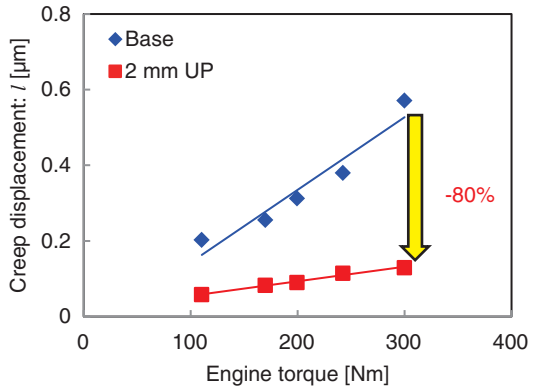


Fig. 14 Comparison of correlation between CAE predictions and measurements of housing wear

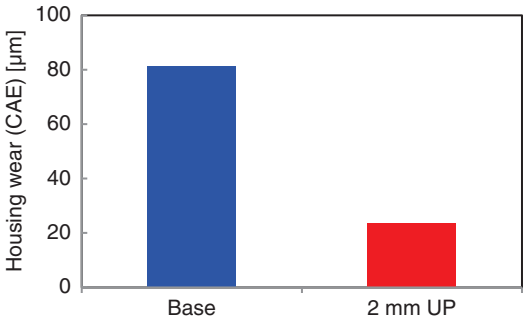
6. Application in Model Development

This chapter will discuss an example in which the developed method was employed to predict the amount of wear occurring in a transmission housing during a development, resulting in changes to the bearing specifications.

In the prediction result using the developed method, shown as Fig. 15, housing wear became a concern. It was predicted that increasing the thickness of the outer rings of the bearings by 2 mm would reduce outer ring creep distance by 80%, and it was possible to review the specifications by means of a theoretical 3D dynamic analysis.



(a) Reduction in creep displacement



(b) Reduction in housing wear

Fig. 15 Results of study of proposed measure

7. Conclusion

A method of prediction of the amount of wear occurring in the housing of an automotive transmission due to the rotation of the outer rings of the bearings has been developed.

(1) A 3D dynamic analysis was conducted in order to reproduce the macro behavior of the bearings and the micro-deformation of the outer rings. This made it possible to reproduce outer ring creep behavior.

(2) A technology for the prediction of the amount of wear to the housing based on the contact pressure and creep distance of the outer rings of the bearings and the specific wear rate was developed.

Application of the method to a variety of bearings of transmissions demonstrated that it was able to predict the maximum amount of wear, the direction of wear, and the form of wear with a high level of correlation with results obtained from actual transmission units.

This method will make it possible to review designs for the control of housing wear, helping to verify specifications at an early stage of development.

References

(1) Zhan, J., Sakajiri, Y., Takemura, H., Yukawa, K.: Outer

Ring Creep of a Bearing, NSK Technical Journal, No. 680, p. 13-18 (2006)
(2) Niwa, T.: A Creep Mechanism of Rolling Bearings, Japanese Society of Tribologists, Manuscript Preparation for JAST Tribology Conference, p. 253-254 (2012)(in Japanese)
(3) Teramoto, T., Sato, Y.: Prediction method of outer ring creep phenomenon of ball bearing under bearing load, 2014 JSAE Annual Congress Proceedings, No.142-14, p.15-20 (2014) (in Japanese)
(4) Sasada, T.: Mamoushiki to Mamouseni, Mamou, Yokendo, p. 32 (2008) (in Japanese)
(5) Muraki, M.: Kyoukaijunkatsu, Zukai, Toraiborojii, Masatsu no Kagaku to Junkatsugijutsu, Nikkan Kogyo Shinbun, p. 63-80 (2007) (in Japanese)

■ Author ■


Yayoi NAGASOE


Shigeharu WAKUI


Yuta MAEYOSHI

Simulation of Adhesively Bonded Parts for Multi-Material Bonding Structure

Tomohiro SHIMAMIYA* Chiaki SATO** Eiichiro YOKOI*
Toru FURUSAWA* Keiichi SATO*

ABSTRACT

In order to perform completed vehicle crash simulations involving the destruction of adhesively bonded parts, a damage mechanics model called a cohesive zone model was applied to the adhesively bonded parts. A dynamic tension-torsion testing method that supports a wide range of strain rates was constructed to take into account the strain rate dependency.

Simulations using cohesive zone model of adhesively bonded parts were performed at levels ranging from the small-scale coupon level to completed vehicle crash simulations. These results were compared with the results of full structure destruction behavior tests and exhibited a good correlation.

1. Introduction

CO_2 emission standards for automobiles are becoming more stringent year by year. Reduction of vehicle body traveling energy by reducing the body weight is an effective method of reducing CO_2 emissions. One measure for achieving this is the replacement of conventionally used steel with other materials, and further body weight reduction is anticipated as bodies become increasingly multi-material through the use in appropriate locations of materials such as nonferrous metals and glass fiber-reinforced plastic that have good specific rigidity, and carbon fiber-reinforced plastic that also has good specific strength.

The issue in these cases is the method used to bond the different materials in place of steel joining methods such as spot welding, and the most promising of these methods is currently adhesive bonding.

Adhesive bonding has been used thus far for applications such as attaching the windshield. When limited to the range lower than the adhesive strength, the degree of contribution of adhesively bonded parts in body design can be predicted by static simulation using a continuum mechanics model. However, when performing simulations that involve the destruction of adhesively bonded parts, it is necessary to first determine the crack initiation position using a continuum mechanics model, and then apply a fracture mechanics model to express the crack propagation from that point[1]. For this reason, the calculation costs increase due to the calculations needed to couple both models. In addition, the resin materials that are the main components of the adhesive generally have a high strain rate dependency, so the strain rate produced on adhesively bonded parts also needs to be taken into account in order to perform crash simulations that include adhesively bonded parts.

One model that deals with crack propagation is the virtual crack closure technique (VCCT)[2], but this method has two major issues. One is that special elements need to be located beforehand in the crack initiation positions; that is to say it is necessary to use some method such as stress analysis to determine the positions where cracks may occur in advance. The other issue is that the analysis time increases due to the need to recreate the analysis mesh in order to determine the path in accordance with crack propagation[3].

Increasing the accuracy of completed vehicle crash simulations helps to avoid reworking due to failure to achieve requirements during actual crash tests, and is essential for efficient vehicle development. This study used a damage mechanics model to express the progression from crack initiation to breaking within the continuum mechanics framework. Specifically, a cohesive zone model (CZM) was used as the damage mechanics model applied to the adhesively bonded parts. In addition, a testing method for acquiring material properties was constructed that also supports strain rates that cannot be covered by conventional testing standards, and verification was performed by

* Automobile R&D Center
** Tokyo Institute of Technology

comparing simulations ranging from the small-scale coupon level to completed vehicle crash simulations with the results of destruction behavior tests to confirm the usefulness of the developed method.

2. CZM and Material Parameters

A CZM is a damage mechanics model that has energy as an input parameter and uses damage to express the drop in rigidity. This enables handling of the entire progression from crack initiation to propagation and breaking as a single process within the continuum mechanics framework[4]. Figure 1 shows an example of typical definitions of CZM material parameters.

This study used definitions of CZM material parameters that express the relationship between deformation and stress with a triangle. The initial gradient K in the figure represents the modulus of elasticity of the adhesive divided by the adhesive thickness, the peak height σ represents the crack initiation stress, and the triangle area Gc represents the energy absorbed per unit area until the crack breaks. This is called the energy release rate. These definitions enable expression of the series of phenomena until adhesively bonded parts break. That is to say, elastic behavior is exhibited until the stress applied to the adhesively bonded parts exceeds σ, crack initiation occurs when the stress reaches σ, and then the stress decreases in a linear manner due to a drop in rigidity as cracking propagates, and breaking ultimately occurs at the point when the stress reaches zero.

Figure 2 shows the types of crack propagation mode handled by CZM.

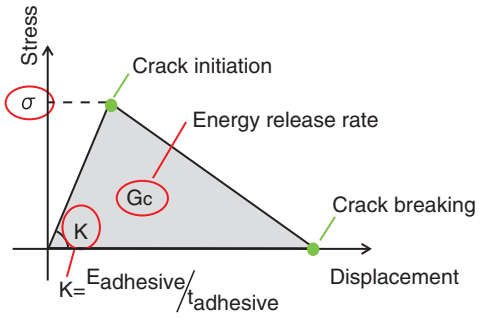


Fig. 1 Example of CZM parameter definition

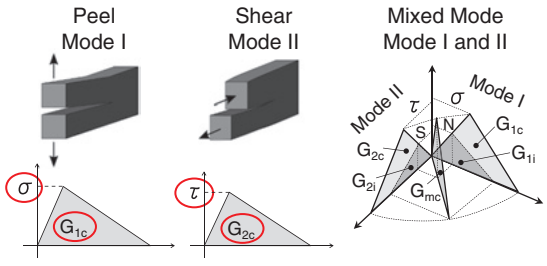


Fig. 2 Types of crack mode

The CZM material parameters are defined separately for Mode I: Peel and Mode II: Shear. In addition, in the case of a peel phenomenon where Modes I and II are mixed and apply in a compound manner (Mixed Mode), the crack initiation stress is defined using Eq. (1), and the energy release rate is defined using Eq. (2)[5].

$$\left(\frac{N}{\sigma}\right)^2 + \left(\frac{S}{\tau}\right)^2 = 1 \tag{1}$$

$$G_{1C} + (G_{2C} - G_{1C}) * \left(\frac{G_{2i}}{G_{1i} + G_{2i}}\right)^{\eta} = G_{mc} \tag{2}$$

The advantage of using CZM to model adhesively bonded parts is that the crack initiation and propagation calculations do not require a detailed stress distribution in the adhesive layer thickness direction, so detailed element division and calculations in the thickness direction are unnecessary, which helps to suppress expansion of the analysis model scale. In addition, the time step determined from the minimum element length in the explicit analysis code does not need to be reduced, enabling reduction of crash simulation costs.

3. Material Property Tests

3.1. Quasi-static Material Property Tests

Table 1 shows the test standards for the three modes described in section 2[6]-[10]. The subject of all the standards is quasi-static tests, and the adhesive bonding standard is only for Mode I: Peel, however interlaminar standards for composite material laminated plates were also referenced.

In all of the above test standards, a force-stroke diagram can be obtained as a result of applying a load to a test piece consisting of two plates joined by adhesive as shown in Fig. 3. A description of the test, the test setup and the obtained force-stroke diagram for each mode are given below.

Figure 4 and Fig. 5 show the Double Cantilever Beam (DCB) test that corresponds to Mode I. The DCB test applies a tensile load to the adhesively bonded parts by applying a vertical load to the test piece via a universal joint.

Figure 6 and Fig. 7 show the End-Notched Flexure (ENF) test that corresponds to Mode II. The ENF test applies a shear load to the adhesively bonded parts by applying 3-point bending directly to the test piece.

Figure 8 and Fig. 9 show the Mixed Mode Bending (MMB) test. The MMB test is able to simultaneously apply both Mode I: Peel and Mode II: Shear to the adhesively bonded parts, and the ratio of peel and shear can be arbitrarily changed by adjusting the arm length c.

3.2. Dynamic Material Property Tests

A dynamic testing method for acquiring material properties was constructed to understand the strain rate dependency. Figure 10 shows an outline of the test method.

Table 1 Test standards for CZM parameters

Standard \ Mode		Mode I Peel	Mode II Shear	Mode I and II Mixed Mode
Adhesive	ASTM	D3433-99(2012)	-	-
FRP Interlaminar	ASTM	D5528-13	D7905M-14	D6671M-13e1
	JIS	K 7086	K 7086	-

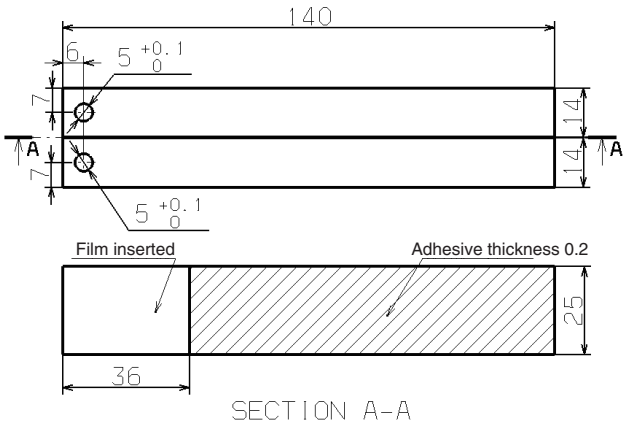


Fig. 3 Test piece drawing

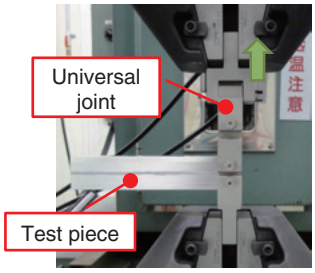


Fig. 4 DCB test setup

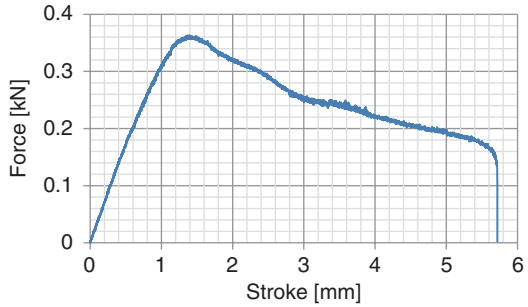


Fig. 5 Force-stroke diagram of DCB test

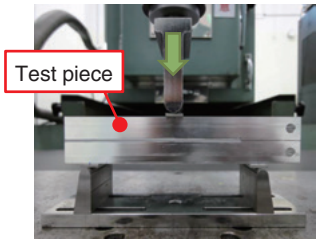


Fig. 6 ENF test setup

This method enables performance of tests for Mode I only and Mode II only as well as the intermediate Mixed Mode with a single apparatus by applying tensile and torsional loads in the arbitrary ratios to a cylindrical test piece joined by adhesive, and also supports high strain rates by increasing the loading rate.

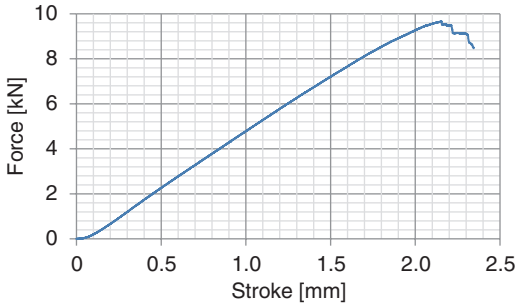


Fig. 7 Force-stroke diagram of ENF test

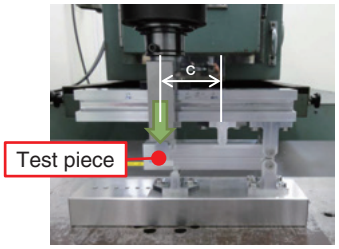


Fig. 8 MMB test setup

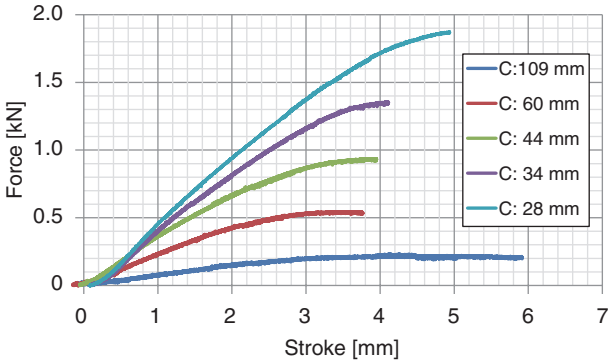


Fig. 9 Force-stroke diagrams of MMB test

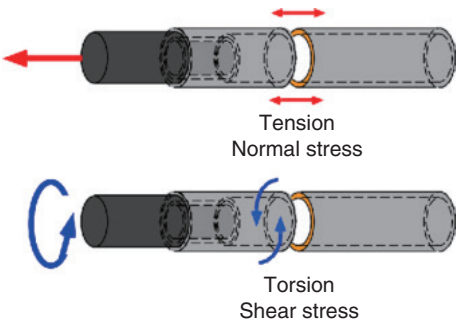


Fig. 10 Concept of loading

Figure 11 shows the overall testing machine. The start timing of the tensile and torsional loads applied to the test piece can be aligned by applying hydraulic pressure supplied from a pump to the drive pistons via two systems of servo valves[11].

Gap sensors that obtain the displacement in the axial and circumferential directions are installed around the test piece set inside the chamber at the top of the testing machine as shown in Fig. 12, and the stress-displacement diagram for each mode can be obtained by combining the load cell value. Figure 13 shows an example of the obtained stress-displacement diagrams, and Fig. 14 shows the relationship between the tensile stress and torsional stress in Mixed Mode.

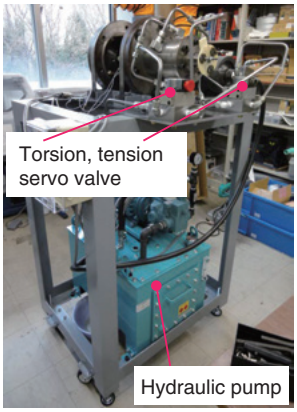


Fig. 11 Dynamic tension-torsion testing machine

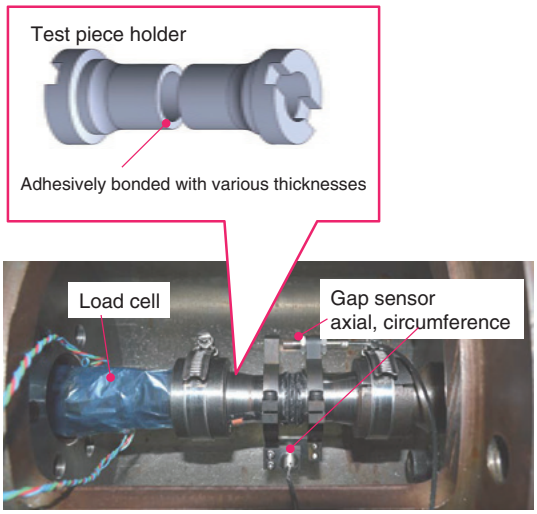


Fig. 12 Setup of test piece

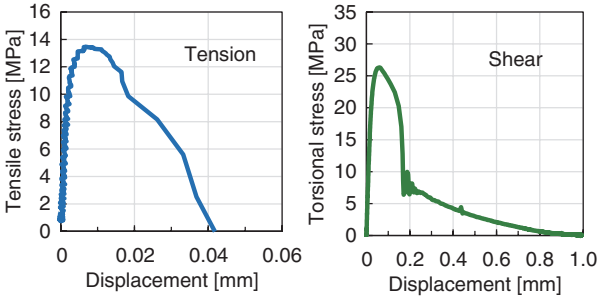


Fig. 13 Stress-displacement diagrams

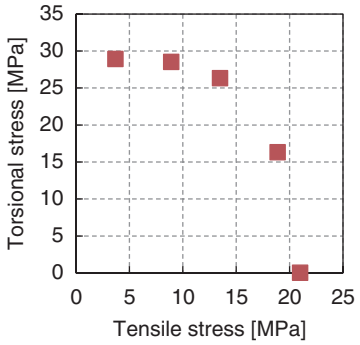


Fig. 14 Tensile-torsional stress diagram

4. Identification of CZM Material Parameters

The test standards noted in Table 1 include methods for directly calculating the energy release rate from the force-stroke diagram obtained by the tests. However, this study adopted the following method for identifying the parameters. First, an analysis model was created with the same test pieces, constraints and loading conditions as those in the material property tests, and then the CZM material parameters were repeatedly adjusted until the force-stroke diagrams obtained by analysis and the tests match.

4.1. Identification of Quasi-static CZM Material Parameters

Regarding the quasi-static CZM material parameters, the Mode I CZM material parameters are identified from the DCB test results, the Mode II CZM material parameters are identified from the ENF test results, and η in Eq. (2) is identified from the MMB test results. Figure 15 shows an example of the CZM material parameters identified for two adhesives.

The adhesives shown here are both acrylic adhesives, but when expressed by the CZM material parameters, the size and balance of the respective triangles differ greatly.

4.2. Identification of Dynamic CZM Material Parameters

Regarding the dynamic CZM material parameters, an

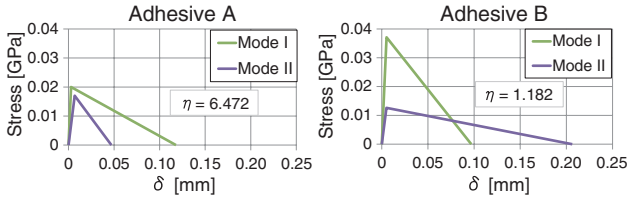


Fig. 15 Two examples of identified quasi-static CZM parameters

analysis model equivalent to the dynamic tension-torsion test was created, and the Mode I and Mode II CZM material parameters and η were all three identified simultaneously from the analysis results. Figure 16 shows the identified CZM material parameters of adhesive A.

This shows that the dynamic CZM material parameters for Mode II in particular differ greatly from the previously identified quasi-static CZM parameters.

The energy release rate is influenced by the element size, so if the element length in the in-plane direction of the adhesive bonding surface differs, the analysis results will differ even when using the same CZM material parameters. Therefore, the element length was standardized within the same analysis model or between different analysis models when modeling adhesively bonded parts.

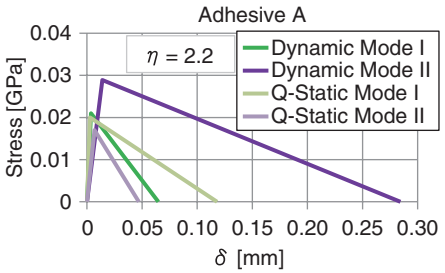


Fig. 16 Example of identified dynamic CZM parameters

5. Confirmation of Usefulness

The usefulness of the adhesive bonding part simulation method using CZM was confirmed by comparative verification with tests at five different levels. The items used to confirm usefulness at each level are as follows.

- Coupon level: quasi-static CZM material parameters
- Element level: dynamic CZM material parameters
- Subcomponent level: dynamic destruction behavior of bonded parts
- Component level: overall behavior of medium-scale structure
- Completed vehicle level: overall behavior of full vehicle

The comparison results at each level are described below.

5.1. Coupon Level: Single Lap Shear Test

The single lap shear test is a quasi-static test that obtains the typical tensile shear strength; that is to say the value obtained by dividing the fracture load of the adhesively bonded parts by the bonded area. Figure 17 shows an outline of the single lap shear test piece.

Single lap shear tests[12] were performed using adhesives A and B with the three different lap lengths of 12.5 mm, 25 mm and 50 mm to confirm the usefulness of the quasi-static CZM material parameters identified in section 4.1. Figure 18 compares the test and analysis results.

Comparison of the tensile shear strength test results (the blue plots in the figure) for lap lengths of 12.5 mm and 50 mm shows that while the tensile shear strength of adhesive A changed by only a small amount from 8.6 MPa to 8.0 MPa, the tensile shear strength of adhesive B dropped from 10.5 MPa to 6.0 MPa.

In addition, analysis that uses CZM (the red plots in the figure) expresses the degree of change in the tensile shear strength relative to the lap length, and the analysis results matched closely with the test results in all cases.

The above results confirmed that CZM material parameters are useful at the coupon test level for predicting the strength of adhesively bonded parts with various lap lengths.

5.2. Element Level: HAT 3-point Bending Test

A dynamic HAT 3-point bending test using a falling weight testing machine was performed to confirm the usefulness of the dynamic CZM material parameters identified in section 4.2. Figure 19 shows an outline of the test. The test piece consisted of a HAT section component and a flat plate molded out of carbon fiber-reinforced thermoplastic (CFRTP) resin and adhesively bonded in the flange parts. Bonding used adhesive A and analysis used the dynamic CZM material parameters identified in section 4.2.

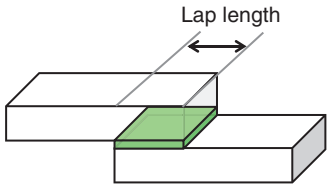


Fig. 17 Test piece for single lap shear test

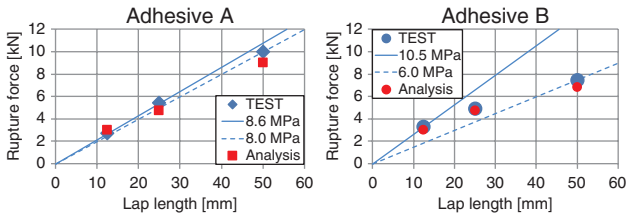


Fig. 18 Rupture force vs. lap length

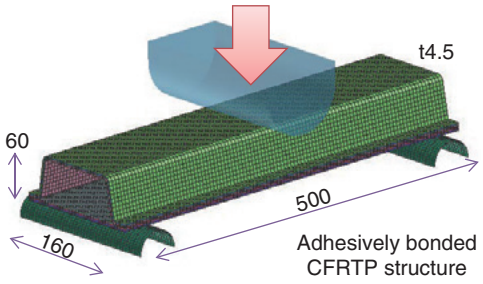


Fig. 19 HAT 3-point bending

Figure 20 compares the test piece destruction formats in the test and the analysis, and Fig. 21 compares the obtained force-stroke diagrams.

The comparison in Fig. 20 shows that the analysis is also able to express the destruction sequence whereby the adhesive in the flange parts peels as the load is applied, with the result that the HAT component and the flat plate are separated, the HAT component fractures, and the flat plate experiences elastic deformation. In addition, the comparison of force-stroke diagrams in Fig. 21 shows that the analysis error at the initial peak force is approximately 10%, and the analysis also closely reproduces the change in force in accordance with the destruction sequence.

The above results confirmed that dynamic CZM material parameters are useful for analysis at the element level that includes the destruction of simple adhesively bonded parts.

5.3. Subcomponent Level: T-Joint Test

A dynamic T-Joint test using a falling weight testing machine was performed to confirm usefulness at the subcomponent level. Figure 22 shows an outline of the test piece. Aluminum HAT components and flat plates adhesively bonded in the flange parts were further assembled into a "T" shape, and the intersecting parts were adhesively bonded using L clips. This means that the adhesively bonded surfaces are located in various directions relative to the loading direction. Bonding used adhesive A and analysis used the dynamic CZM material parameters identified in section 4.2. Figure 23 compares the test piece destruction aspects, and Fig. 24 compares the obtained force-stroke diagrams.

The comparison in Fig. 23 shows that the analysis is also able to express the dynamic destruction sequence, whereby destruction of the adhesively bonded parts started from the tip and propagates toward the base of the test piece. In addition, the comparison of force-stroke diagrams in Fig. 24 shows that the analysis error at the initial peak force is within 10%, and the analysis also closely reproduces the change in force in accordance with the destruction sequence.

The above results confirmed that CZM material parameters are also useful for analysis at the subcomponent level that includes the destruction of complex adhesively bonded parts.

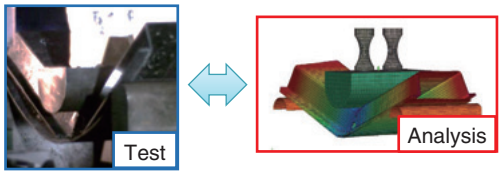


Fig. 20 Comparison of test piece destruction

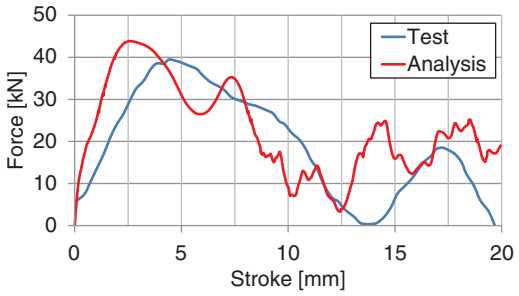


Fig. 21 Comparison of force-stroke diagrams

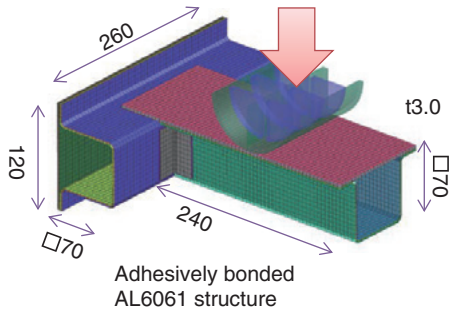


Fig. 22 T-joint test piece

5.4. Component Level: Floor Side Sill Test

A floor side sill test was performed to confirm usefulness at the component level. The floor side sill component used as the test piece consisted of multiple parts joined by adhesive bonding. This test was a quasi-static load test that simulates collision with a pole, and the results were compared with those of a corresponding analysis model. Figure 25 compares the destruction aspects, and Fig. 26 compares the obtained force-stroke diagrams.

The test results in Fig. 25 show that buckling occurred in the floor plate due to adhesive layer peeling of the floor part, and the resulting drop in the floor part yield strength led to increased bending in the side sill parts and destruction

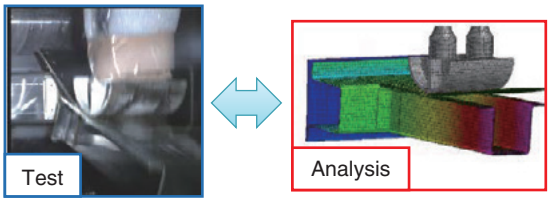


Fig. 23 Comparison of test piece destruction

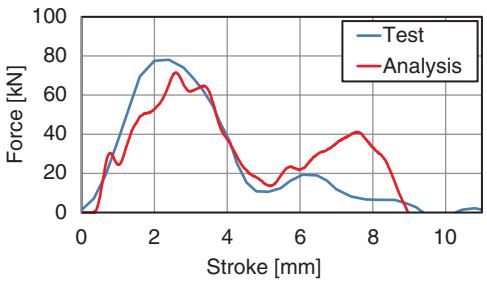


Fig. 24 Comparison of force-stroke diagrams

directly below the indenter. The analysis results accurately reproduced this destruction sequence, and the deformation accompanying the destruction also closely matched the test results. In addition, the force-stroke diagram in Fig. 26 shows that during the test, the force dropped sharply when the floor part yield strength dropped due to adhesive layer peeling, and residual strength was maintained thereafter due to side sill bending. In contrast, in the analysis results when rigid body coupling is applied and adhesively bonded part destruction does not occur (Analysis_RIGID), the floor part adhesive layer does not peel, so there is no drop in the floor part yield strength and the force continues to increase, behavior that completely differs from the test results. On the other hand, the analysis results when CZM are applied to adhesively bonded parts (Analysis_CZM) reproduce the drop in force due to the drop in floor part yield strength, and the residual strength thereafter also closely matches that of the test results. This indicates that the new analysis method accurately modeled the parts that experienced actual destruction, and that expressing this destruction at the appropriate timing accurately reproduces the behavior of the full structure.

The above results confirmed that CZM material parameters are also useful for component level analysis in which the destructive behavior of the full structure may change greatly depending on whether destruction of adhesively bonded parts occurs.

5.5. Completed Vehicle Level: SINCAP Test

A Side Impact New Car Assessment Program (SINCAP) test was performed using a body that includes adhesively bonded parts to confirm usefulness at the completed vehicle level. While the details of the body used and the test contents are omitted here, Fig. 27 compares the obtained force diagrams.

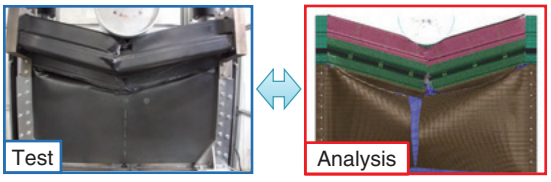


Fig. 25 Comparison of test piece destruction

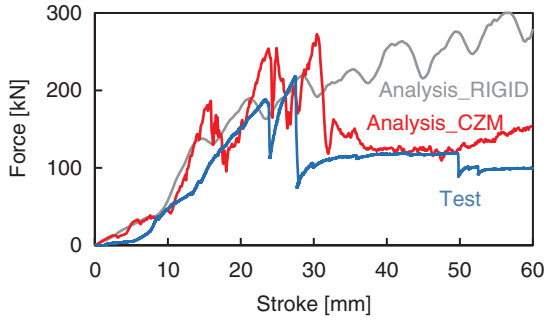


Fig. 26 Comparison of force-stroke diagrams

Compared to the analysis results when rigid body coupling is applied and adhesively bonded part destruction does not occur (Analysis_RIGID), the analysis results when CZM are applied to adhesively bonded parts (Analysis_CZM) accurately reproduced the behavior of the full vehicle including the destruction sequence, which increased the accuracy of the force diagram.

The above results confirmed that CZM material parameters are also useful for large-scale vehicle crash simulations in which destruction of adhesively bonded parts and other destruction phenomena are complexly intertwined.

The results introduced in this paper confirmed the usefulness of this simulation method using CZM from the small-scale coupon level to large-scale vehicle crash simulations.

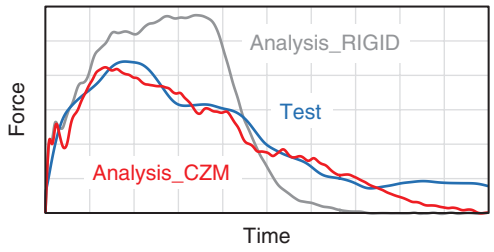


Fig. 27 Comparison of force diagrams

6. Conclusion

Crash simulations using CZM for adhesively bonded parts were performed based on the approach of using a damage mechanics model in the continuum mechanics calculation method. A method was created for acquiring dynamic material properties using a tension-torsion testing machine, and a process was constructed for identifying CZM material parameters from the property test results and executing analysis.

The usefulness of this method was confirmed from the small-scale element level to large-scale vehicle crash simulations. The use of CZM that simulate the entire progression from crack initiation to propagation and breaking as a single process enhanced the reproducibility of full structure behavior that involves the destruction of adhesively bonded parts and obtained good analysis results at all levels.

These results showed that this method is useful for crash simulations at all levels that include adhesive bonding, and particularly for large-scale analyses such as vehicle crash simulations.

References

(1) Banea M. D., da Silva, L. F. M.: Adhesively Bonded Joints in Composite Materials: an overview,

Proceedings of the Institution of Mechanical Engineers, Vol. 223, (2009)
(2) Rybicki, E. F., Kanninen, M. F.: A Finite Element Calculation of Stress Intensity Factors by a Modified Crack Closure Integral, Engineering Fracture Mechanics, Vol. 9, p. 931-938, (1977)
(3) Raju, I. S., Crews, J. H., Aminpour, M. A.: Convergence of Strain Energy Release Rate Components for Edge-Delaminated Composite Laminates, NASA TM-89135, (1987)
(4) Camanho, P. P., Davila, C. G., Ambur, D. R.: Numerical Simulation of Delamination Growth in Composite Materials, NASA TP-2001-211041, (2001)
(5) Camanho, P. P., Davila, C. G.: Mixed-Mode Decohesion Finite Elements for the Simulation of Delamination in Composite Materials, NASA TM-2002-211737, (2002)
(6) ASTM D3433-99(2012): Standard Test Method for Fracture Strength in Cleavage of Adhesives in Bonded Metal Joints, (2012)
(7) ASTM D5528-13: Standard Test Method for Mode I Interlaminar Fracture Toughness of Unidirectional Fiber-Reinforced Polymer Matrix Composites, ASTM International, (2013)
(8) JIS K 7086: Testing methods for interlaminar fracture toughness of carbon fibre reinforced plastics, (1993)
(9) ASTM D7905M-14: Standard Test Method for Determination of the Mode II Interlaminar Fracture Toughness of Unidirectional Fiber-Reinforced Polymer Matrix Composites, ASTM International, (2014)
(10) ASTM D6671M-13e1: Standard Test Method for Mixed Mode I – Mode II Interlaminar Fracture Toughness of Unidirectional Fiber Reinforced Polymer Matrix Composites, ASTM International, (2013)
(11) Furusawa, T., Shimamiya, T., Yokoi, E., Sato, K., Hattori, H., Murakami, S., Sato, C.: Evaluation of Critical Fracture Energy of Adhesively Bonded Joints for Carbon Composites under Combined-Mode High-Strain Rate Loadings, ECCM16 Conference Proceeding, (2014)
(12) ASTM D1002-10: Standard Test Method for Apparent Shear Strength of Single-Lap-Joint Adhesively Bonded Metal Specimens by Tension Loading (Metal-to-Metal), ASTM International, (2010)

Author


Tomohiro SHIMAMIYA


Chiaki SATO


Eiichiro YOKOI


Toru FURUSAWA


Keiichi SATO

Development of Paint and Painting Method for Magnetically Formed Decorative Painting with Enhanced Three Dimensionality

Akiko TANAKA* Ikue SATO*

ABSTRACT

This development was aimed at the creation of the method of magnetically formed decorative painting applied to the outer parts of motorcycles to realize a larger degree of three-dimensional appearance. First, the conditions required for the orientations of the metallic flakes contained in the paint were investigated. Following to that, the method to realize those orientations was examined. Based on the results, the paint and the painting method were developed to enhance the controllability of the flakes' movements while painting. To make the flakes movable more easily, a high magnetic permeability material was adopted as the flake material. In addition, to make the flakes promptly stop after required amount of movements, a high molecular weight resin was added. Moreover, application of the optimized setting of the thinner further enhanced the controllability of the flake movements. By combining these methods, the decorative patterns with the larger degree of three-dimensional appearance were successfully realized under the conditions of mass production lines.

1. Background and Objectives

The markets of motorcycles are predominantly deploying in Southeast Again countries and are continuously growing in these days. A large number of models are released in these markets from each manufacture of motorcycles. Figure 1 illustrates some of the vehicles released in the markets. Many of the motorcycles sold in these regions are getting more areas on their plastic outer coverings, which are concealing the vehicle body, in association with the demands of the vehicle exterior design variations. The decorating method of plastic coverings is becoming one of the technical factors of greater importance than ever to enhance the attractiveness of the products.



Fig. 1 Examples of small motorcycle models

The commonly applied decorative methods are painting and graphic marks, which are drawn with artistic patterns and affixed on the painted surface (Fig. 2). There are various kinds of painting methods. Some of them have brilliant colors and some other kinds have appearances with high illuminance. There are various kinds of graphic marks as well. However, either of those methods has been used for quite a long time of the history and too much familiarized by the customers.

With this background, there is a strong demand for a method of decorating plastic coverings that can provide a novel appearance never experienced before. On the other hand, graphic marks tend to be considered as decorations created by a simple way without any sophistication because there is no significant difference in appearance from the decorations by generally available stickers. Consequently, it has been highly expected to develop a different method from conventional ones that can offer the appearances with

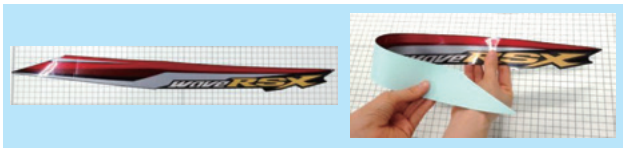


Fig. 2 Example of graphic mark

* Motorcycle R&D Center

a perception of high quality. In our development, a method was investigated to enhance the attractiveness of vehicle appearances by applying a magnetically formed decorative painting on plastic outer coverings[(1), (2)].

Magnetically formed decorative painting is a method of painting that uses a paint containing small metallic leaves (i.e. flakes) having a magnetic permeability and is conducted while attaching behind the painting object a sheet of a material, such as a magnetic sheet, that generates lines of magnetic force. Magnetically formed decorative painting itself is one of the existing painting methods. However, there used be various obstacles for its application to mass produced products. One of such obstacles is that, during the painting procedure, it needs to have magnet sheets engaged to the parts of plastic coverings. Therefore, it was not practically implemented as a painting method applied to motorcycle parts. Nonetheless, we devised a method to overcome the issues involved in this magnet sheet engagement and accomplished the mass production of the motorcycles applying with this painting method in Thailand in 2008 (Fig. 3).

By applying magnetically formed decorative painting, the figurative patterns with the appearance like the representations made by manual drawing with an airbrush can be created. Moreover, the created patterns represent the appearance having a depth despite its small thickness of the paint layer placed on a flat surface without any dents or protrusions.

The key that enabled the application to the mass production in 2008 was to use a flexible magnetic sheet as the magnetic field generating material to be attached to the part while painting. By applying this painting method, the perceptions of a novel and high quality decoration with three-dimensional decorative patterns were successfully achieved.

Based on this success in application, the request from the marked evolved to request for providing even higher degree of three-dimensional appearances that attracts people while the vehicle is in motion as well. Accordingly, the goal of this particular development was set to establish a method of magnetically formed decorative painting that provides higher three-dimensional appearances than former methods through the enhancements of paint formula and painting process.

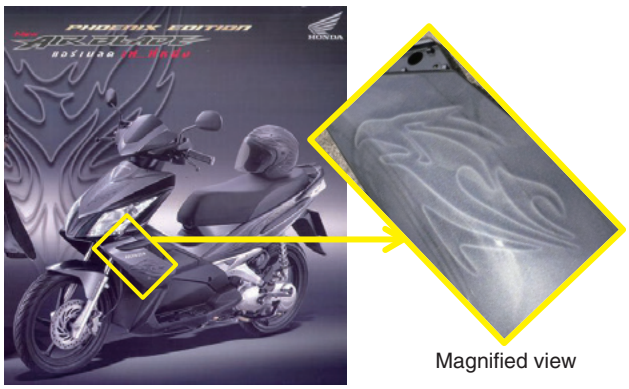


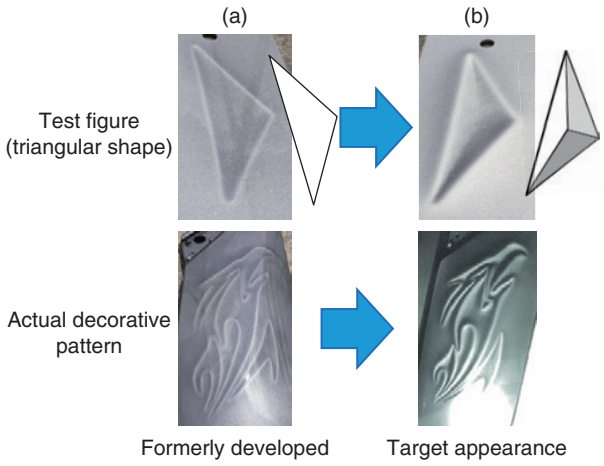
Fig. 3 Mass production model (2008, Thailand)

2. Defining Requirements

2.1. Definition of Three-dimensionality

On the surface that is painted with a magnetically formed decorative painting, a kind of optical illusion brings about the effect that presents appearances having virtual depths that makes observers perceive three-dimensional objects without actual substances. In this paper, this "illusive effect that presents three-dimensional appearance" is called "Plasticity" (a term used in pictorial arts). It is considered that the decorative pattern stands out significantly if this illusive effect can be designed to appear more strongly.

The target "plasticity" in this development was expected to have a characteristic of generating the optical illusion over the whole area surrounded by the perimeter of the figurative pattern. Figure 4 (a) shows the appearance of the pattern equivalent to that of the formerly developed product. On the other hand, (b) shows the appearance of the pattern with the plasticity level of the development goal aimed this time. When the appearances of the patterns created using a triangular magnetic sheet are compared, in the case of (a), only the surrounding perimeter of the triangular pattern shows three-dimensional appearance and the inner part of the triangular pattern presents a flat appearance. On the other hand, (b) looks like its inner area of the triangular pattern is presenting an appearance of a trigonal pyramid with three-dimensionality. The pattern as shown in (b) was



(a): It is representing insufficient perception of depth as the area of high luminosity is limited only around the area just adjacent the perimeter.

(b): It is representing the perception of depth with gradual changes of the brightness ranging over the area within the perimeters of the triangle.

Fig. 4 Plasticity defined as development target

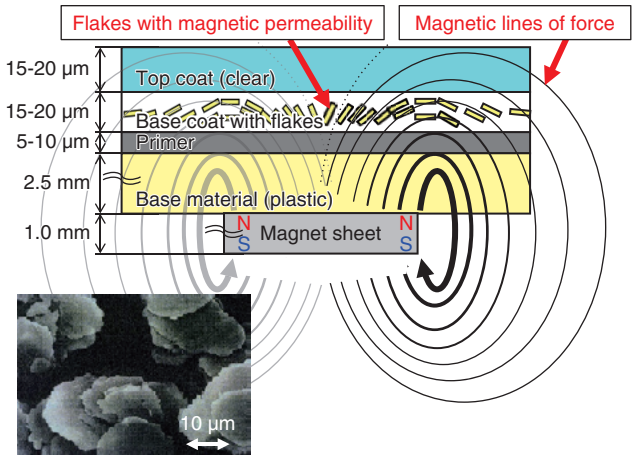
defined as the pattern with a higher plasticity. The reason why the pattern is perceived like a three-dimensional trigonal pyramid is that the light intensity of the inner area, which is under the influences from the applied magnetic fields, varies depending on the observing angles inducing the effect of manifestation of the depth in the appearance. From the comparison between (a) and (b), it is considered that an observer perceives the depth of the pattern when it has a larger area of varying intensities of reflected light within the area surrounded by the triangle.

2.2. Mechanism of Presenting Three-dimensional Appearances

2.2.1. Hypothesis for phenomenon of manifestation

An attempt was made to clarify the structural configurations that constitute a paint layer providing three-dimensional appearances through the investigations on various paint layers produced under different conditions by implementing pre-established methodology. In general, when a paint using flakes is applied, the flakes are usually contained in the base coat, which is applied after painting a primer. Following to that, after the application of the base coat, a method is usually used in which a clear top coat is applied to provide a glossy appearance to the paint surface. In the same way, the paint layers of a magnetically formed decorative painting are structured with three coatings of primer, base coat and top coat as shown in Fig. 5.

In the base coat layer of magnetically formed decorative painting, the flakes are situated with predetermined angles being parallel with the directions of the lines of magnetic force generated from the magnetic sheet attached behind the part. It is understood that the three-dimensional patterns are generated by this structure. Moreover, the intensity of the reflected light from the flakes, which have a distribution of orientation angles, changes depending on the viewing angle of an observer of the decorative pattern. In association with those changes in viewing angles, the brightness of each part in the pattern varies. Accordingly, it was assumed that change of brightness makes it look three-dimensional (Fig. 6). To substantiate this assumption, two kinds of experiments were conducted as described below.



The magnetic lines of forces (magnetic fields) originate at the N-pole and reach the S-pole by traveling along circular lines. The magnetically permeable flakes are aligned along those lines.

Tesla is used as the unit for describing the density of magnetic field (the index for strength of a magnet), where one tesla is ten thousand gausses.

Fig. 5 Assumed principle of flake pattern generation in magnetically formed decorative painting

2.2.2. Measurement of light intensity variations

At the beginning, variations in the distribution of reflected light to the changes of the observation angles were examined. For the measurement, a variable-angular photometer that measures light intensities while varying the detection angle was used. The detailed explanations on descriptions used in this paper, such as light intensity, luminosity or luminous intensity, are presented in Appendix 1. A magnetically formed decorative paint was applied while attaching a magnetic sheet in isosceles triangular shape with the base length of 100 mm and the base angles of 30 degrees. Measurements were conducted to the patterns appeared after the paint application (Fig. 7). This triangular shape was used as the common base figure

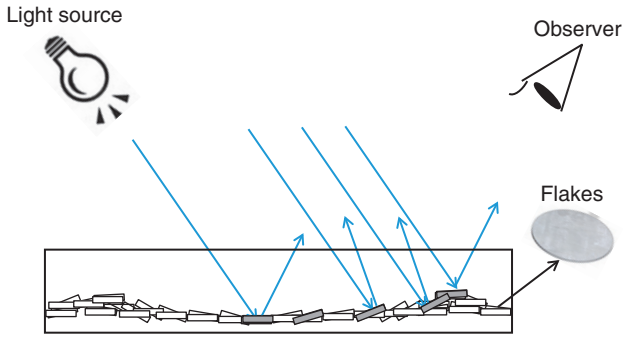
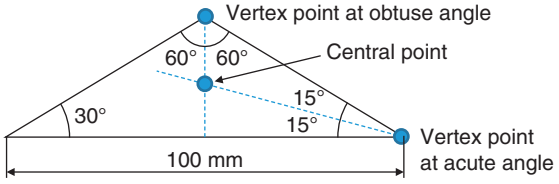


Fig. 6 Presumption of the reason why magnetically formed decorative painting appears three-dimensional



Measurement point	Intensity of magnetic field (mT)*
Central point	4.0 – 8.0
Vertex point at acute angle	9.0 – 15.0
Vertex point at obtuse angle	7.0 – 12.0

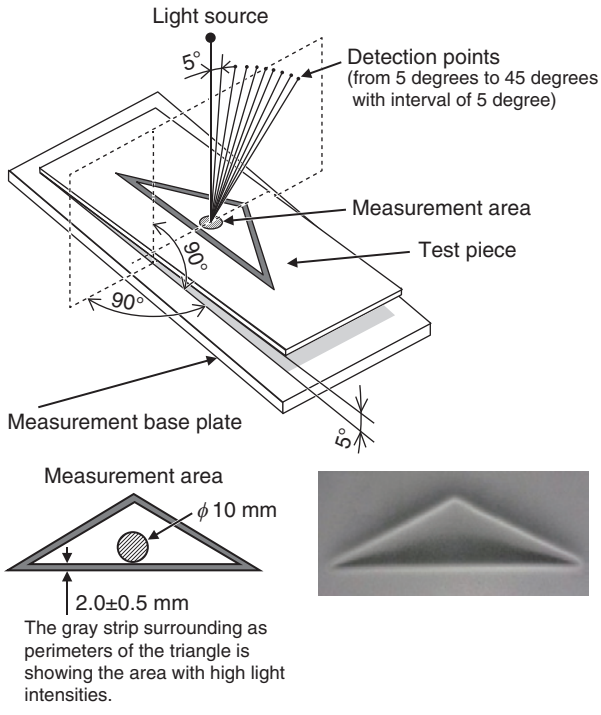
* Measurement equipment: Tesla Meter (TM-601, KANETEC Co., Ltd.)

Fig. 7 Standardized specifications of magnetic sheet for testing

for the following measurements.

Figure 8 illustrates the measurement method. The light intensity from the paint surface painted with magnetic sheet of the aforementioned shape attached on the back side of an ABS resin plate of 3 mm thickness was measured. The distribution of the light intensity reflected from the hatched circular area of 10 mm diameter, shown in Fig. 8, was measured. This part is the area where the variations of the light intensities of the pattern are largely demonstrated. For this measurement, the area adjacent to around the perimeter of the triangle was excluded from the target area of the measurement, because variations of light intensity are small because of an unchanging high intensity of the light in this area. In addition, the measurement for a general metallic painting was also conducted to make a comparison.

The light source was located vertically above the base plate of the measurement equipment. The test piece was placed so that it was slanted to the plane of measurement base with an angel of 5 degrees as shown in Fig. 8 to avoid the direct reflection of the light. The results of the angular distributions of the reflected light measured by this method are shown in Fig. 9. In the case of conventional metallic painting, the light intensity becomes significantly large at around the angle close to that of the direct reflection (at the angle of 5 degrees) but it abruptly goes down when the detection angle is shifted from that angle. In the case of the magnetically formed decorative painting, it was confirmed that the light intensity was not suddenly decreasing but was gradually changing when the detection angel was varied. As it had been expected, it was understood that the angles of flakes in the layer of magnetically formed decorative paint had a broadly spread distribution. Observing angles for the decorative pattern correspond to the angles for the detection of the measurement. Consequently, based on the results from the experiment, it was confirmed that the appearance exhibited by the variations of the reflected light when the decorative pattern was observed corresponded to the representations of the light intensity distribution.



Measurement with variable-angular photometer and measured area (GP200, Murakami Color Research Laboratory)

Fig. 8 Methodological configuration of measurement using variable-angular photometer

2.2.3. Flake angles and brightness changes derived from magnetic field

In the next step, the relationship between flake angles and the reflected light intensities was investigated. Test pieces to be examined were prepared using a magnetic field generator shown in Fig. 10. The preparation procedures are described as follows. An apparatus structured to provide lines of magnetic force with the same direction was arranged. In that apparatus, spacing was provided so that a plastic plate of 10 by 40 mm in size could be placed in that gap. A plastic plate painted with a paint containing magnetic flakes was set in this spacing before drying.

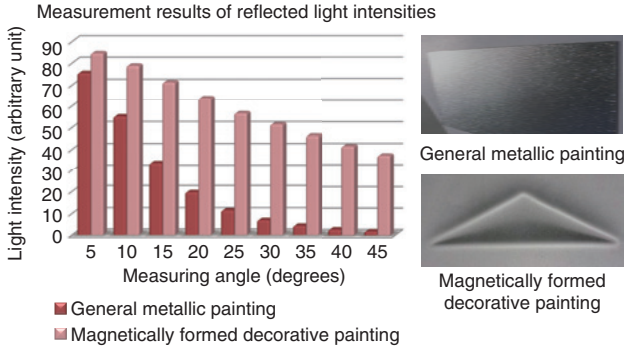


Fig. 9 Measurement results of angular distributions of reflected light intensities detected by variable-angular photometer

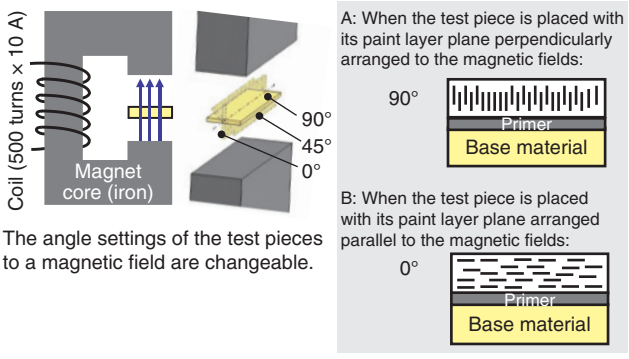


Fig. 10 Apparatus to examine directional relationship between magnetic lines of force and flakes

The directions of the lines of magnetic force are equally oriented to a single direction for any place within this spacing. Therefore, if the flakes change the slanting angles aligning to the line of magnetic force, it was assumed that almost all the flakes located within this space were equally oriented to the same direction (as shown in the figures on the right in Fig. 10). Without changing the direction of the lines of magnetic force on the apparatus, plastic plates were placed in it so that each orientation of those plates was directed to the five kinds of angular settings of 0 degrees (parallel), 30 degrees, 45 degrees, 60 degrees or 90 degrees (perpendicular). Using these plastic plates, the test pieces were prepared to examine the variations of reflected light intensities from the paint layer that had been exposed with magnetic fields of different directions.

The largest intensity was observed, as shown in Fig. 11, for the plate that had been placed in parallel to the direction of the lines of magnetic force (at 0 degrees). On the contrary, when the plate had been placed vertically to the direction of magnetic field (at 90 degrees), almost all the flakes represented the state of being standing perpendicularly to the paint surface plain. In this case, the coating applied underneath (which is the primer layer with black color) could not be concealed by the flakes representing the lowest intensity of the reflected light as a result. Accordingly, it was revealed that a large difference occurs in the magnitude of reflected light intensities from the test pieces between the one having set in parallel and the one having set vertically. In addition, on the pieces with the set angles in between, the brightness varied depending on the angles at which the plate had been set against the direction of the magnetic field and gradational changes of the light intensity were observed. The gradational changes of light intensities presented in the test were in the same manner manifested by those in the pattern created by application of the magnetically formed decorative painting. Based on those results, it is considered that the variation of the light intensities at the part of the decorative pattern is caused by the arrangement of the flakes with slant angles varying in association with the directional changes of the lines of magnetic force.

Moreover, when the cross sections of the paint layers of those test pieces were actually observed with a microscope, the flakes are situated having the same direction with a particular angle of the imposed magnetic field as shown in Fig. 12. Consequently, it was confirmed that the gradational appearances observed at the decorative pattern were generated by the variations of flake angles.

2.2.4. Mechanism that presents three-dimensional appearances

Through the measurement results of these two experiments, it was verified that the flakes contained in the paint layer were aligned in parallel to the direction of the lines of magnetic force and the intensity of the reflected light varies depending on the observation angles. The mechanism described above is considered to be the reason why the patterns created by the magnetically formed decorative painting represent three-dimensional appearances.

2.3. Defining Target Plasticity

In this chapter, numerical levels for evaluating the plasticity are defined and the target level is clarified. The samples were fabricated with consideration of the relationship between the flake arrangement, which influences the degree of plasticity, and the light intensity described before. These samples were investigated to define the indices of plasticity. The target plasticity level was decided by exterior designers by observing the appearances.

2.3.1. Preparation of samples for evaluation of appearance define target plasticity level

As it was mentioned in the paragraph 2.2.2, when compared to a conventional metallic painting, a noticeable characteristic of a magnetically formed decorative painting is that the intensity of the reflected light does not decrease suddenly but changes gradually when the detecting angle

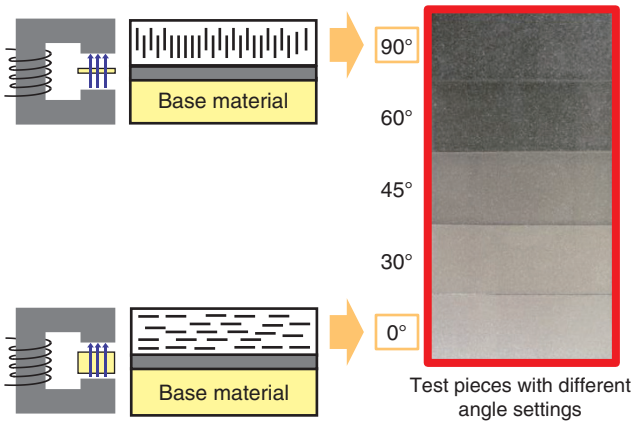


Fig. 11 Light intensity differences among test pieces when varying angle settings to magnetic field

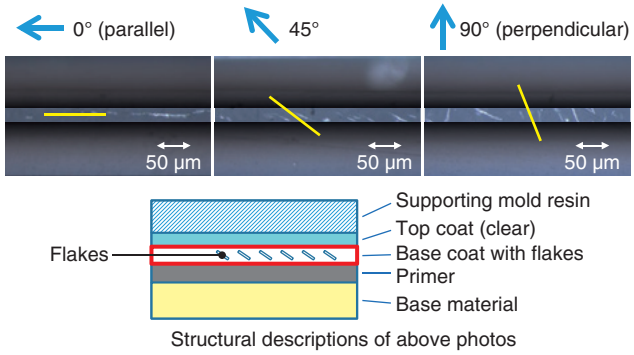


Fig. 12 Cross sectional views of painted layers of test pieces

is shifted. The plasticity represented by the pattern is more enhanced if the area within the pattern where the light intensity changes depending on the variation of observation angles is larger. In order to get a larger area for this light intensity varying region, the area in which the flakes move to align with the directions of the lines of magnetic force must range over a broader area. To fulfill that requirement, the painting method is necessary that satisfies the condition in which the flakes are easy to move in a large area. For preparation of the samples, this must be taken into account.

As one of the methods that realize the abovementioned condition, there is a method that elongates the duration of the flake movements. To implement this method, a thinner that has a slower evaporation speed was used. Thinners with stepwise different evaporation speeds had been prepared and five different test pieces were produced. (The production method and detailed conditions are described in Appendix 2.) The conditions of thinner evaporation speed applied for the test piece fabrication were those only for making test pieces used for visual evaluations to identify the degree of target plasticity, and those conditions were determined without considering the process actually applied to the manufacturing process of the painting. In other words, the samples for the tests were made giving priority to yielding the desired plasticity but without consideration on the time needed for drying.

2.3.2. Defining numerical levels of plasticity and setting target level

As it was mentioned before, the plasticity level differs depending on the magnitudes of the light intensities measured at individual detecting angles. Accordingly, for the test pieces made as described in the paragraph of 2.3.1, the variations in light intensities at individual detection angles were examined. The measurement method was the same as that shown in the paragraph 2.2.2. Regarding the target measurement area, it was also set the same as in the paragraph 2.2.2, which was the area away from the perimeter by some distance. Thus, the intensities of the light were measured varying the detection angle.

The absolute values yielded through the measurements on individual test pieces cannot be directly compared because they may be varied depending on the test piece fabrication conditions. The parameter that plays an important role for evaluation of the plasticity is not the absolute value of the observed brightness but is the relative variation ratio. Therefore, the comparisons between relative values are the effectual way of the investigation. Consequently, in this evaluation process, the individual data lines are parallel shifted properly in the direction of the vertical axis of the graph so that the beginning points of the measurement (at the detecting angle of 5 degrees) meet to each other as shown in Fig. 13. In this manner, the variations of the light intensities (L) in different test conditions are effectively compared relatively based on the predetermined fix point of measurement at 5 degrees.

Table 1 Coefficients of inclination calculated by linear approximation for individual test pieces

	Inclination of approximation line
Test piece 1	-0.46
Test piece 2	-0.82
Test piece 3	-1.06
Test piece 4	-1.22
Test piece 5	-1.60

Table 2 Plasticity classification defined by coefficients of inclination calculated by linear approximation

Plasticity level	Inclination of approximation line (/degree)
4	-0.49- 0.00
3	-0.99- -0.50
2	-1.49- -1.00
1	-1.50 or lower

The purpose of this evaluation is to investigate the differences among the test pieces comparing variations in brightness at the inner area of the triangular shape of the decorative patterns. The condition that provides high plasticity, as mentioned in the paragraph 2.2.2, can be translated as the degree of "How much gradually the intensity of the light varies." Linear approximate equations were calculated based on the plotted points yielded through these measurements. The degrees of variations in the light intensities were indicated by the degrees of slope inclinations of those approximation lines. The values of slope inclinations of the approximation lines for the prepared five kinds of test pieces are shown in Table 1.

By sorting out those approximation lines by grouping with increments of 0.5 of inclination value, four ranges were defined (Table 2). These four ranges were defined as the plasticity levels and they were understood as such the larger

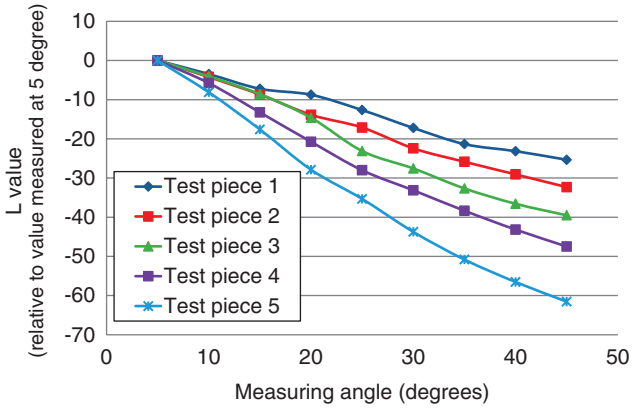


Fig. 13 Comparison of five test pieces with different plasticity levels evaluated by intensity distributions in the areas inside the triangular shape

the value is the higher the plasticity is. Visual evaluations of plasticity were conducted by exterior designers on the five kinds of test pieces. Based on the evaluations, positively rated results were referred to the four ranges defined above. Through the results, it was concluded that the plasticity to be defined as the target index for the development dealt with in this research is classified in "level 3" or above of the defined plasticity scales. Eventually, this level was set as the target requirement for the development.

3. Selection of Materials to Achieve Objectives

3.1. Presumption of Flake Arrangement that Fulfill Objectives

Investigations were conducted to identify the way in which the flakes should be actually arranged to achieve the plasticity goal of level three which was determined as described in the previous section.

Firstly, it was investigated how the flake angles and the brightness of the paint layer relate to each other. As shown in Fig. 14, triangular pattern (a) of the upper left in the figure that is presenting a lower degree of plasticity and triangular pattern (b) of the upper right in the figure that is presenting a higher degree of plasticity are compared. As described before, (b) looks like a flat plane in its inner area while (a) looks a concaved trigonal pyramid. Accordingly, it looks like as if the flakes are arranged in the manner shown in the figure at the second low in Fig. 14. (In this paper, this cross sectional plane of the imaginary object is called virtual cross section.) Based on the results shown in the paragraph 2.2.2 and the results on the relationship between a flake angle and the reflected light intensity shown in the paragraph 2.2.3, the shapes of the flakes that were supposed to appear on the cross section of the paint layer were assumed. The actual paint layer has only a thin thickness of 20 μm. Consequently, it is assumed that the flakes are arranged with respective angles as shown in the cross sectional shapes illustrated in the third row of Fig. 14. It is understood that these flakes are slanted to hold the same angles as the angels appeared at corresponding positions in the virtual cross section and are distributed in the paint layer. Thus, the plasticity is considered to be observed because of the reflected light intensities from the flakes that are distributed varying their angles, i.e., because of the differences in the reflected light intensities that vary depending on the positions in the paint layer. Moreover, unlike an ordinary painting, the distribution of the light intensities changes according to the observed angle. As a result, the appearance that is close to the real object is manifested. Subsequently, the difference in flake angle arrangements relative to the lines of the applied magnetic force is shown in the figure at the lowest row of Fig. 14. As shown in the figure, it can be assumed that the flakes are mostly arranged parallel to the line of magnetic force for a high plasticity pattern while only a part of the flakes are arranged parallel to the line of magnetic force for a low plasticity pattern. This can be translated that it is because the flakes could not fully move to change their angles. The detailed explanation of this matter will be described later.

Based on these investigations above, to realize a high plasticity through magnetically formed decorative painting, a paint and a painting method are required that enable the flakes in larger area in a decorative pattern to fully change their orientations along the lines of magnetic force.

3.2. Methodology to Make Flakes Easy to Move and Associated Issues

3.2.1. Investigating methodology

As mentioned in the previous section, if the necessary conditions are prepared to make the flakes in the paint layer to move easily to align towards the directions of the lines of magnetic force, the angular arrangement of the flakes becomes ideal situation and the decorative pattern with a higher plasticity can be created. There are three measures for helping the flakes to change their orientations, that is to say, for facilitating the movements of the flakes.

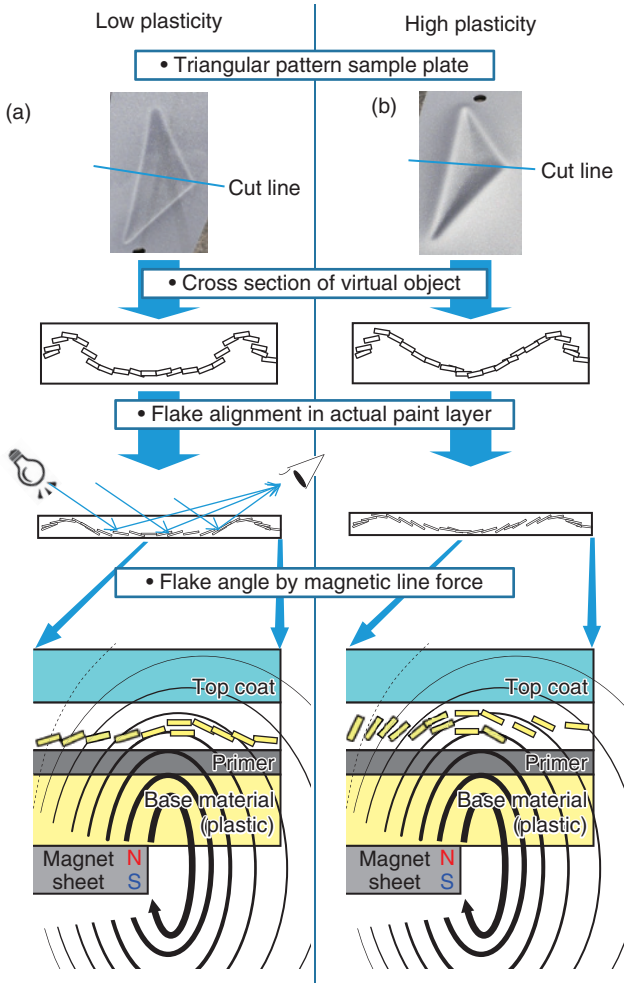


Fig. 14 Relationship of plasticity with flake angle and light intensities

Measure 1: To extend the time for flakes to move by using a thinner with low evaporation speed. (The same method used for preparing the test pieces for defining the level of target plasticity.)
Measure 2: To enhance the force to drive the flakes' mobility by using a magnetic sheet with a stronger magnetic force.
Measure 3: To enhance the flakes' sensitivity to the magnetic force by using a flake material with a higher magnetic permeability.

In the following, the detailed explanation and the associated issues are described for each of these measures.

Measure 1: Using a thinner with low evaporation speed.

The plasticity of the decorative pattern becomes good when the evaporation speed of the thinner is slow. However, at the same time, an ample time is given to the flakes in the area without a pattern as well to change their orientations. That results in potentially high risk of generating a disorder of flake orientation arrangement reflecting any subtle unevenness of the property on the target part surface. In addition, with the this slow thinner condition, it is highly possible, because of the limited tact time for production process, that the painting part is transferred to the next step process (i.e., the top coat painting process) before the base coat is fully dried in the actual production line. In that case, the top coat paint permeates through the base coat to deteriorate the necessary glossiness as a result. In addition, the resulting elongation of the period for flake to move may cause a gloss loss (loss of glossiness) to become another issue of the appearance. Regarding gloss loss, the detail will be described later.

Measure 2: Using a magnetic sheet with a stronger magnetic force.

Currently, magnet sheets are widely used for various applications. Generally speaking, magnet sheets used for stationery, and so on, are magnetized so as to have S poles and N poles in turn on the same side of the sheet. However, the magnet sheet used for the painting of this development is magnetized to have S pole on the whole area of its one side and N pole on all of the other side. For the magnet sheet magnetized in this manner, a special method has to be devised to enhance the magnetic force. This results in increase of the const. Meanwhile, there is another way to enhance the magnetic force without changing magnetizing method but by increasing the sheet thickness. However, many of the plastic covering parts used in motorcycles have complex shapes with protrusions and dents. Therefore, if the sheet thickness is increased, it becomes difficult to affix it closely to the rear side of these plastic coverings. Under those constraints from cost and production process, it is required to use the magnetic sheet with thickness of 1 mm that has been used from before. In addition, the enhanced magnetic force contributes to make the flakes erect in the central area of a decorative pattern. This potentially leads to the generation of a gloss loss resulting in failure to meet the requirements for appearance.

Table 3 Applicable options of measures to create good plasticity

#	Measures	Issues on production process	Issues on product quality
1	Slow volatilization thinner	Excessively long tact time	Gloss loss at central area
2	Strong magnetic sheet	Unacceptably costly or too thick to fit on parts	Gloss loss at central area
3	High permeability flakes	None	Gloss loss at central area

Measure 3: Using a flake material with a higher magnetic permeability.

There is no issue arisen regarding production process when this measure is applied. However, it has the issue of the gloss loss generation leading to deterioration of appearance quality, which is the same as the cases of applying measures 1 or 2. The application of high magnetic permeability flakes makes the flakes further susceptible to the lines of magnetic force and more affected by them. As a consequence, the flakes have a higher tendency to stick together to form a chain status. Mostly in the central area of the decorative pattern, the flakes stand towards the surface plane of the painted layer. At the same time, the flakes form chain connection status to stick out from the interface of coatings generating a gloss loss. The same method had been investigated in the production in 2008 as well but any effective countermeasure had not been found to fulfill the requirements both for a good plasticity and a quality of appearance.

Table 3 summarizes the descriptions on individual measures and the respective issues involved. In the development conducted this time, it was hardly possible to apply Measure 1 or Measure 2 that has issues in relation to the production process and/or the cost. Accordingly, the possible option to apply is only Measure 3 in which high magnetic permeability flakes are used. Eventually, it was decided to apply this measure to develop a method that would overcome the generation of a gloss loss and successfully achieve the development objectives.

3.2.2. Selection of high permeability flake material

The applicable metallic materials to the flakes in the paint are aluminum, nickel, iron-based material and stainless steel. Stainless steel was used for the mass production in 2008. The magnetic permeability, which shows the sensitivity to magnetic force, was measured for the flakes made from individual materials (refer to Appendix 3). The results are shown in Fig. 15. The magnetic permeability is the highest in iron-based material and it becomes smaller in nickel followed by stainless steel. Meanwhile, aluminum is non-magnetic material.

In addition, the color of flakes is desirable when it is brighter and closer to an achromatic color. Accordingly, the hues of flakes are also measured. The measurement of hue was conducted based on CIE L*a*b* color space defined by Commission Internationale de l'Éclairage (CIE)[3]. As

shown in Fig. 16, it is brighter when L* is large and it is closer to achromatic color when the absolute values of a* and b* are small. Accordingly, in the selection, a larger value of L* and small values of a* and b* are sought. The measurement results are shown in Fig. 15. The superiority order in relation to hue was like aluminum, iron-based material, stainless steel followed by nickel. Based on the measurement results on magnetic permeability and hue, the flake made from iron-based material was selected for our development.

Flakes type	Magnetic permeability values (μ)	Color tones		
		L*	a*	b*
Aluminum (general metallic)	1.000	81.80	-0.40	1.00
Nickel	1.780	69.14	0.53	4.44
Stainless steel (conventional flakes)	1.213	50.37	0.16	2.22
Ferrous-material	2.263	53.12	-0.08	-0.50

■ Sample preparation:
The flakes are ultrasonically cleaned in acetone bath. After that, they are dried and bottled in a container 6 mm. In diameter and 2.5 mm in height. The measurement is conducted to the container.

■ Magnetic permeability measurement
(1) Instrument:
(1) Vibrating Sample Magnetometer
(2) BHV-50
(3) Riken Denshi Co., Ltd.

(2) Measurement condition:
Applied magnetic field: 10000 oersteds

■ Color measurement
(1) Instrument:
(1) Name (generic): Spectrophotometer
(2) Model: CM - 700 d
(3) Make: KONIKA MINOLTA

(2) Measurement condition
(1) Light source: D65 10
(2) Detection mode: SCI

The color tones are measured using the base coat layer of paint resin with only flakes but without color pigments.

Fig. 15 Flakes with magnetic permeability and their color tones

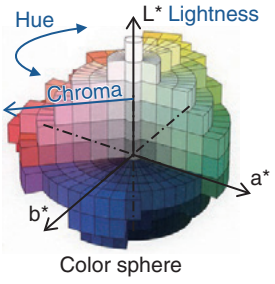


Fig. 16 L* a* b* color sphere

3.2.3. Understanding gloss loss generation mechanism and conception of measure to prevent it

As mentioned before, the ideal flake arrangement can be realized if the angles of the flakes can be fully changed to align with the lines of magnetic force before the paint is dried. However, if this is actually realized by applying some measure, a gloss loss occurs as a serious side effect in the central area of the decorative pattern. Gloss loss is a phenomenon with which the smoothness of the paint surface is lost and its glossiness is seriously deteriorated.

In Fig. 17, pictures that show appearances of gloss loss are presented as actual examples. A black and white striped pattern is irradiated with a light and the reflected light pattern is exposed onto the plate painted with a magnetically formed decorative paint. The picture shows the appearance of the plate in that condition. (a) shows the painted plate with gloss loss and (b) shows the one without it. The representations of the edges of the striped pattern in (a) are vague compared with (b). As shown in this example, gloss loss is a phenomenon with which the glossiness of a paint surface is seriously deteriorated. This gloss loss cannot be allowed in terms of the quality of paint appearance and it is inevitable to consider the measures to avoid that.

In the following, the reason why the gloss loss like this is caused is described. The magnetic sheet used for this painting has N pole on whole area of its one side and S pole on the other side. As illustrated in Fig. 18, the lines of magnetic force are radiated to spread around from the whole area of the surface. In the central area, the radiated lines of magnetic force are almost perpendicular to the sheet surface. Thus, the flakes in this area are eventually arranged almost perpendicular to the paint surface if they full move to change their orientations to align with the lines of magnetic force. (The simulation method that is provided the result shown in Fig. 18 is explained in Appendix 4.)

Consequently, the flakes stand perpendicular to the paint plane and get close to each other to form a chain connection to stick out of the interface of the paint layers. This generates the degradation of the paint smoothness resulting in a gloss loss (Fig. 19). Accordingly, for the central area of the decorative pattern, some strategic measure is necessary

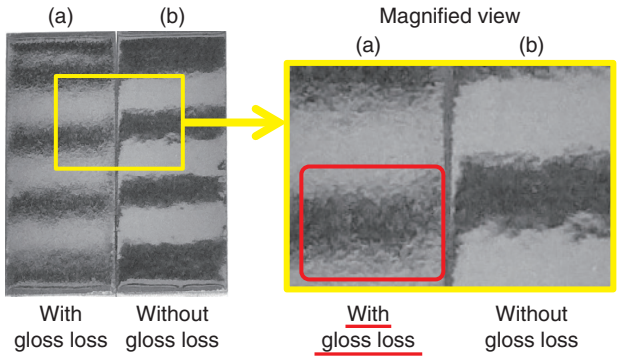


Fig. 17 Appearance of “gloss loss”

to prevent the angles of the flakes from getting angles close to perpendicular and make them stay within the range of the smaller angles.

3.2.4. Investigations to create method to overcome the obstacle

The movements of the flakes should be restrained so that their orientation angles stay within an angular range that is small enough to prevent a gloss loss. On the other hand, the flakes should be movable enough to yield a good plasticity. Accordingly, the allowable range of flake angles was tried to identify. To do so, the surfaces of the painted samples prepared in the process described in 2.2.3., which were made by changing the setup angles to a predetermined paralleled magnetic field, were observed to confirm the occurrences of a gloss loss.

In the upper row of Fig. 20, the photos of painted samples for individual angles that were taken in the same manner as taken for Fig. 17. From these photos, it can be noticed that a significant gloss loss was generated in the sample that was made with the angle of 90 degrees to the paint layer. Moreover, a slight gloss loss is observed for the sample of 60 degrees. However, the sample of 45 degrees has no gloss loss. Consequently, it was confirmed that, if the flake slant angles are restrained within 45 degrees, the flakes would not stick out of the interface of the paint layers and the gloss loss can be prevented.

In the next step, a method to make the orientations of the flakes, which move to align with the lines of magnetic force, stay within 45 degrees to the paint surface was investigated. In the procedure of determining a paint formulation and a painting method to realize the desired flake angle arrangement, the investigation focus was set on the strength of magnetic force in the area where a gloss loss occurs. The graph in the lower row of Fig. 21 shows the results of the measurement on the strength of the magnetic field. The strength of the magnetic field, which is radiated as shown in the illustration in the upper row of the figure, was

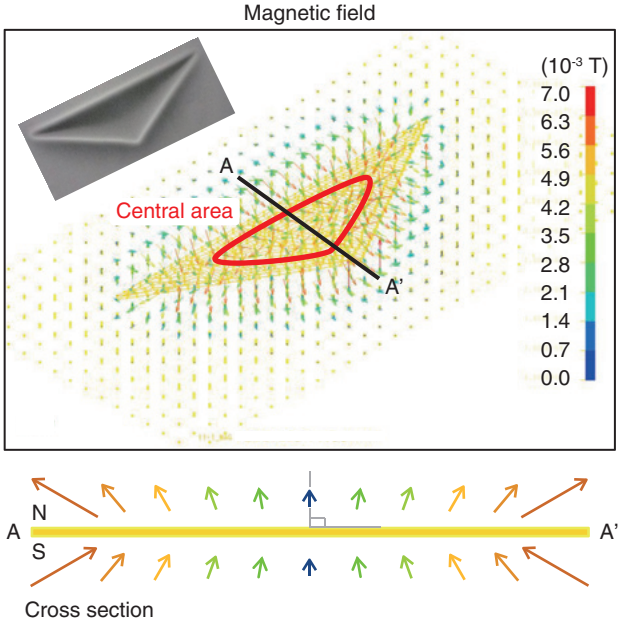


Fig. 18 Directions and strengths of magnetic fields from magnetic sheet

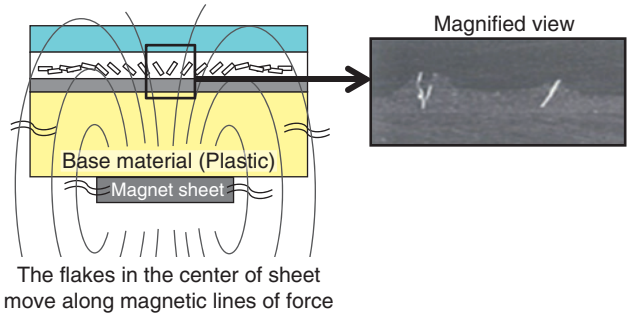


Fig. 19 Flake directions in area with gloss loss

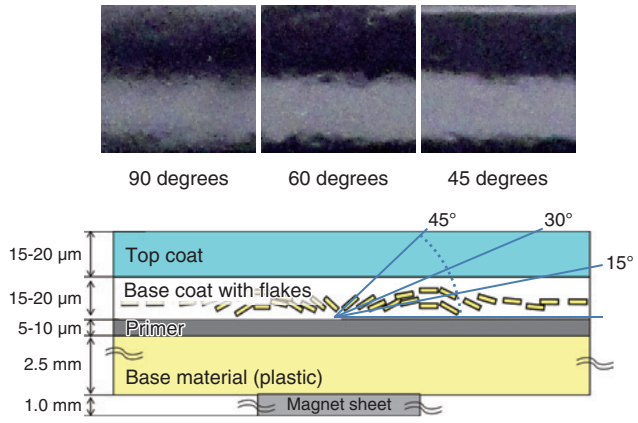


Fig. 20 Maximum flake angle to avoid gloss loss

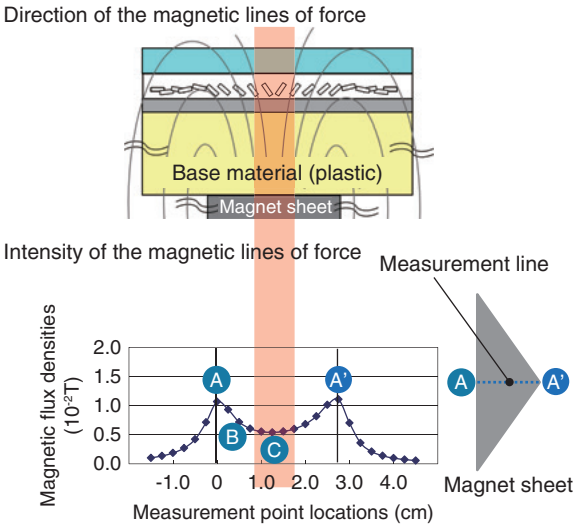


Fig. 21 Intensity of magnetic lines of force

measured at each position. The measurement was carried out through the line that is connecting point A and point A' on the magnet sheet. This data of the strength of magnetic force shown in the graph indicates that it is weak in the central area of the decorative pattern when it is compared to the area close to the perimeter. Based on this fact, it can be expected that it takes longer time for the flakes in the central area to move along the lines of magnetic force than for the flakes around the perimeter. A gloss loss occurs in the central area of the decorative pattern. That is to say, it occurs in the central area of the magnet sheet. Meanwhile, as the magnetic force is weak in the central area, it is assumed that it takes relatively long time for the flakes in this area to move to align their orientations to the angles close to 90 degrees. This delay was utilized to control the flake movements.

The measured regions and the respective final reaching angles are shown in Fig. 22. Three regions of A, B and C are picked up as representing portions. In each of the portions, there is a different flake angle distribution from the other portions in the magnetically formed decorative painting. The characteristics of each of them are described in the following. As shown in the upper right photo in Fig. 22, A is for the peripheral area, C is for the central area and B is for the area in between. As illustrated in the lower right drawing, the lines of magnetic force are emitted radially. Accordingly, the angles of the lines of magnetic force are getting larger along with the changes of positions from the peripheral area to the central area. Therefore, if the flakes moved to be completely aligned with the lines of magnetic force, the angle for the flakes in region A becomes 0 to 5 degrees, that of B is 45 degree and 90 degrees for region C. The angle that the flakes in a certain region are fully aligned with the line of magnetic force was defined as final reaching angle, or final angle (The table in Fig. 22).

A gloss loss occurs in region C that is the central area of the decorative pattern. As mentioned before, the angles for flake movements in region C should be restricted because it generates a gloss loss if they fully move to change the angles. On the contrary, the flakes in other regions,

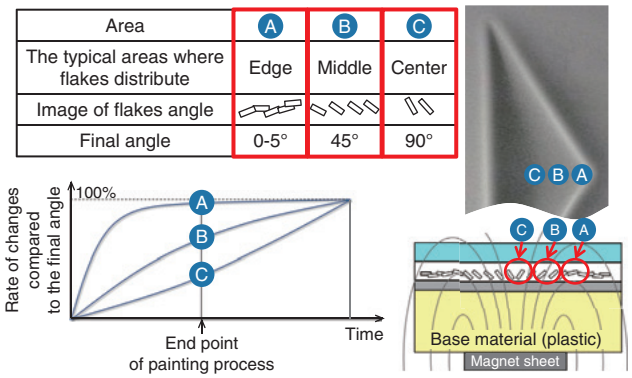


Fig. 22 Measurement points and final angles of flakes

especially those in region B, which are largely contributing to the manifestation of plasticity, should move fully to completely align with the lines of magnetic force to yield a high plasticity. As examined in the paragraph 3.2.4, in the central area, the strength of the magnetic force is weaker than that of the peripheral area and the flakes take more time to move. Therefore, the method was examined that makes the flakes in the peripheral region A and intermediate region B move in the full amounts while restricting the movable time for the flakes in central region C.

The relationship between the elapsed time after painting and the flake orientation angle is shown in the lower left graph in Fig. 22. The horizontal axis is for the time elapsed after the paint reaches the surface of the target part surface. The vertical axis is for the percentage of the flake angle to the final angle. Accordingly, reaching 100% of the final angle means that the angles of the flakes in a specific region, region A, B or C, fully reach the final angle of its individual region (e.g., 45 degrees for region B).

The vertical line shown in the middle of the graph in Fig. 22 indicates the completion timing of the painting process of the magnetically formed decorative painting. At this point, for the peripheral region A, the angle is almost reaching the final angle (0 degrees to 5 degrees). However, for region B and C, the angles have not reached the final angles when the painting process is finished. In other words, the painting has finished with a low plasticity. If the painting process time is extended so that the flake angles in region B, which has a significant influence on plasticity, reach the final angle (45 degrees), the flake angles in region C also reach almost their final angle (90 degrees) causing a gloss loss as a consequence. The paint formula dealt with in this graph is an equivalent condition as what we applied in the mass production in 2008. In reality, we prioritized the paint appearance free from a gloss loss and a high plasticity could not be achieved as a result. To achieve the target level of plasticity, the flakes in region B should be moved to reach their final angle before the paint process ends and, at the same time, the flake movements in region C should be terminated before they reach their final angle (at a smaller angle than 45 degrees). In short, regarding the flake movements, the manner shown in the graph (a) should be changed to the manner shown in the graph (b) in Fig. 23. To realize that, a paint formula design was investigated to move flakes fast and stop immediately.

To move the flakes fast, as it was mentioned earlier, application of a high magnetic permeability material to the flakes is one of the measures. On the other hand, the flake movement is largely influenced by the viscosity of the paint layer as well. Therefore, the control method of paint viscosity was also investigated as a measure to move flakes fast and stop immediately. Flake movements are under the control of paint viscosity. That is to say, flakes are movable only when the viscosity of the paint layer is smaller than some certain value. While the base coat was in wet condition, the behavior of the flakes moved

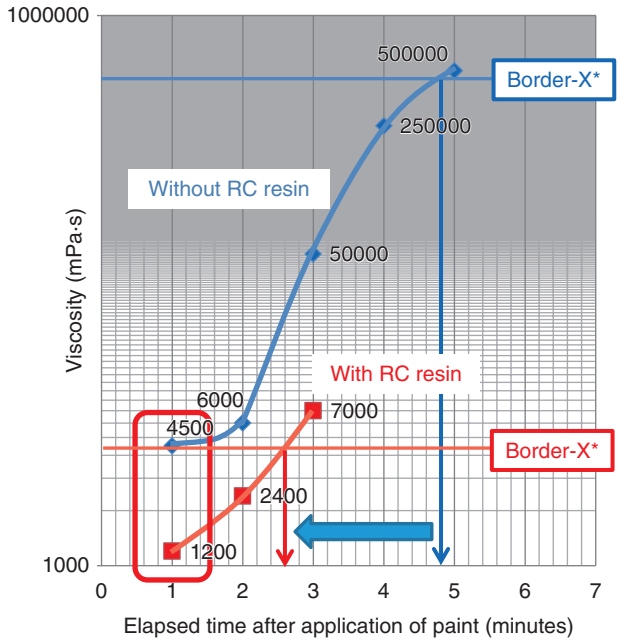
by an applied magnetic force was observed. Through this observation, a threshold value of the viscosity in the paint layer that distinguishes whether or not the flakes can move to align under the influences of lines of magnetic force was identified. This threshold viscosity value was defined as "Border-X viscosity." The strategy was set to design the viscosity changes of the paint in the manner as described below. The viscosity stays still lower than the Border-X viscosity at the moment when the paint, which has been ejected from a spray gun, just lands on the surface of the painting object. Following to that, the viscosity increases immediately and reaches the Border-X viscosity or beyond. To realize this steep increase of the viscosity, a high molecular weight resin (rheology control resin or RC resin), the molecular weight of which is more than a hundred thousand was used. When a RC resin is added, the viscosity of paint before spraying is also increased and it generally causes a difficulty in maintaining the smoothness of the paint surface after painting. To cope with this difficulty, the dilution rate of the thinner was also increased. This made the paint viscosity decreased just after the spraying contributing to realize quick movements of the flakes as a consequence (Table 4).

The graph in Fig. 24 shows the viscosity variations of the paint comparing the paint added with a high molecular weight resin and the one without it. The horizontal axis is for elapsed time and the vertical is for viscosity in logarithmic scale. The red line in the graph show the data for the paint developed this time, in comparison with the one without adding the high molecular weight resin (shown by the blue line) that is in almost equivalent condition as the paint developed for the mass production in 2008. It can be understood that the viscosity value of Border-X, which is the viscosity to make the flakes unmovable, goes down significantly by adding the high molecular weight resin. Moreover, by increasing the dilution rate, the initial viscosity of the developed paint was also decreased to be smaller than before. Through these results, the flakes were allowed to move quickly but the time until the flake movements were halted was shortened after the paint application. By implementing those methods, a paint

Table 4 Purposes and measures of viscosity adjustment

Required effects on flake	Viscosity requirements	Method
Move fast	The initial viscosity should be low.	Increasing the **dilution ratio** of the paint
Stop immediately	The viscosity should quickly reach to the level where the flakes stop moving.	Adding the **high-molecular-weight resin***

* High-molecular-weight resin (RC resin): Material used for rheology control that stops movements of flakes in paints



* Border X: The viscosity at which flake movements stop

Fig. 24 Viscosity increases of paint with and without RC resin

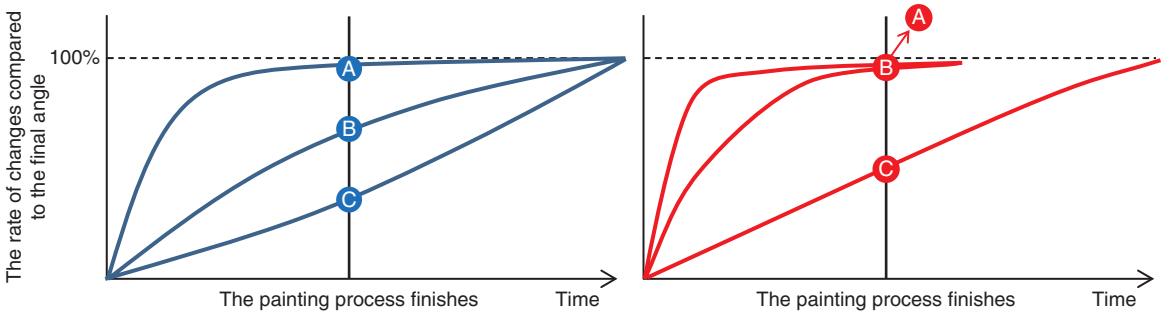


Fig. 23 Flake movements of fast move and immediate stop

formula that satisfied the target viscosity characteristics was successfully designed. The measurement method is explained in Appendix 5.

Based on this paint formula, test paintings were conducted with different constituent ratios of the high molecular weight resin and those of the thinner to compare the performances of the paint layer and the workability of them. With those results, the paint specification to be applied to the mass production was decided.

4. Results

4.1. Conditions for Deciding Paint Formula

For investigating the paint specification, four kinds of paints were prepared with different constituent ratios of the high molecular weight resin that help the flakes to stop their movement promptly. The variations of the constituent ratio were 20%, 30%, 40% and 50%. The paint that contains no high molecular weight resin was also prepared for a comparative evaluation purpose. This formula without high molecular resin is almost the same formula applied for the mass production in 2008. However, in this particular evaluation test, the high magnetic permeability flakes were used for this paint as well, like the other paints to be evaluated, to conduct the comparative evaluation effectively. These prepared paints were painted while the magnet sheet of the triangular shape, which was defined as the base decorative pattern, was attached to the rear side. Following to these paint samples' preparations, comparative evaluations on basic paint coating performances, paint appearance and paint workability were conducted to finalize the specification selection. The workability in this particular evaluation means whether or not the necessary paint layer thickness can be obtained through the production process supposed to be deployed. The evaporation speed of the thinner was decided based on the settings of temperature and humidity for the painting booth used in the factory in Vietnam where the actual mass production was planned. Moreover, the non-volatizing material ratio after dilution by thinner (NV%) was also decided based on the evaluation results yielded using those formulae. For example, when the dilution ratio is increased, the NV% is decreased. For the paint that contain 0% of the high molecular weight resin (RC resin), the NV% was set at High. For 20% of that, it was set at Middle, and they were set at Low for other percentages.

4.2. Detailed Descriptions on Results

The test results are shown in Fig. 25. The photos show the individual appearances of the painted samples of the evaluation formulae 0 to 4. It is observed that there is a correlation between the constituent ratio of the high molecular weight resin and the plasticity. When the constituent ratio of the high molecular weight resin is high, the plasticity is high presenting a favorable appearance. The plasticity was rated based on the evaluation method described in the paragraph 2.3.2. The levels of plasticity were rated as equal or above plasticity level 3 for all the evaluated paints containing the high molecular weight resin (specifications from 1 to 4). In any paints of evaluated specifications, there was no gloss loss occurred in either of the decorative pattern area or the area without it.

Furthermore, performances for the general requirements for a paint layer, e.g. adhesion performance, were also confirmed. The results were obtained that indicated no defect and satisfied all the paint requirements for all of the specifications. The details on evaluation methods for individual tests are presented in Appendix 6.

Lastly, touching on the workability, the results showed that it gets harder to obtain the necessary paint layer thickness through the painting line in the mass production process when a larger amount of the high molecular weight resin is added. Consequently, it was finally judged that the specification that contain approximately 30% of the high molecular weight resin, which was defined as specification number 2, was the allowable limit within the permissible performance range (refer to the lower most row in Fig. 25). Based on those results, to determine the final specification for mass production, the appearance and the paint workability in the actual mass production line were further investigated to conclude the judgment.

4.3. Deciding Specification for Mass Production

The judgment process of the mass production specification, taking the requirements for the appearance and the workability into account, is described below. As mentioned in the paragraph 3.2.4., as the viscosity is increased by the addition of the high molecular weight resin, the paint viscosity should be set low by increasing the dilution ratio of the thinner to maintain the smoothness of the paint surface. When the dilution ratio of the thinner is increased, the ratio of the non-volatizing material (NV%) that constitutes the paint layer finally formed goes down. Thus, the required concealing thickness of the paint layer (15 to 17 μm) cannot be obtained by one paint spraying process.

Moreover, under the mass production process condition, the amount of the paint to be sprayed at a time has a limit. The number of times for repetitive painting is generally restrained within two or three in a mass production process. Accordingly, in light of the paint process requirement, it is required to form the necessary concealing thickness of the paint layer within these numbers of times of spraying.

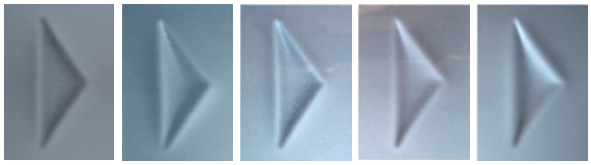
The number of times of painting conditioned in the manufacturing line was three in Vietnam factory, which was planned for the mass production factory for the vehicle. Accordingly, it was required to determine the dilution rate so that the necessary paint layer thickness could be obtained (which was 15 to 20% when defined by NV%) within the number of repetitive paint sprayings. By adding larger amount of the high molecular weight resin, the plasticity can be more enhanced. However, the limitation of the setting for the dilution rate of the thinner, which arises from the restrictions in the mass production process mentioned

above, should be taken into account as well. Consequently, the constituent ratio of the high molecular weight resin was determined so as to meet the requirement for the thickness of the formed paint layer.

Following these considerations, the constituent ratio of the high molecular weight resin to the amount of base resin was determined as 20 to 25% for the finalized paint design to be used in mass production. Finally, the specification number 1, which is one of the options meeting the overall evaluation criteria shown in Fig. 25, was selected as the specification for mass production.

The practical test painting was conducted at the production line in Vietnam factory using the developed paint applying the conditions described above. As a result, it was confirmed that a good plasticity was achieved without any issues on its workability as well. By applying the same test painting process, painting was conducted using the triangular magnet sheet that was defined as the base shape for plasticity measurement mentioned before. It was followed by the measurement of the variation of the light intensity to the detecting angle, and it was verified that the target plasticity of level 3 had been achieved. The developed paint was applied in the mass production in Vietnam (Fig. 26).

	Specification No.		0	1	2	3	4
	Addition of RC resin		None	Applied	Applied	Applied	Applied
Paint specifications	Contained ratio of RC resin*1		0.0%	20.0%	32.0%	40.0%	50.0%
	Contained flake ratio (PHR)*1		15 PHR	15 PHR	15 PHR	15 PHR	15 PHR
	Non-volatizing material ratio after diluted by thinner (NV%)*2		HIGH	MIDDLE	LOW	LOW	LOW
Results Appearance	Plasticity level (Inclination of approximation line)		2 (-1.22)	3 (-0.73)	3 (-0.71)	4 (-0.38)	4 (-0.28)
	Initial gloss value*3	The area of design pattern	95	95	96	94	94
		The area without pattern	95	97	98	97	96
Results Performance	Initial adhesion performance*4		Good	Good	Good	Good	Good
	Water resistance*4		Good	Good	Good	Good	Good
	Durability against accelerated weather stress*5	Non-discoloring*6	Good	Good	Good	Good	Good
		Gloss*7	Good	Good	Good	Good	Good
		Adhesion performance*4	Good	Good	Good	Good	Good
		Disorders of paint layers*8	None	None	None	None	None
Results Paintability	Thickness of paint layers*7,*9		Good	Good	Fair	Poor	Very poor



*1 Ratio to the base resin

*2 The thinner is added until the viscosity reaches 13 second at 26 degrees in Celsius using Iwata-cup.

*3 Measurement is carried out using gloss meter and the detecting angle is set at 60 degrees.
(Equipment: Gloss meter, Micro tri gloss, BYK Additives & Instruments)

*4 “Good” denotes that none of the tiles are peeled off.

*5 Results are evaluated for the areas both with and without design patterns and the evaluation results shown in the table are the total performances.

*6 Color difference ⊿E is measured using Spectrophotometer.
“Good” denotes ⊿E = 2 or less.
(Equipment: Spectrophotometer, CR-300, MINOLTA)

*7 “Good” denotes satisfying the requirement,
“Fair” denotes barely satisfying the requirement and
“Poor” denotes unsatisfying the requirement.

*8 Disorders include checkings, cracks and blister. Those are visually observed.

*9 Whether or not the total thickness of sprayed base coat paint reaches the required thickness for hiding the primer layer under the paint process in actual manufacturing.

Fig. 25 Test results



Fig. 26 Final product with plastic coverings painted by magnetically formed decorative painting

5. Conclusions

Paint was developed to enhance the attractiveness of the outer look of plastic coverings in motorcycles. For that purpose, a magnetically formed decorative painting was employed and the developments of the paint and the painting method were conducted aiming at an enhancement of the plasticity (three-dimensionality) represented by a decorative pattern compared to the existing painting method. Through the process of identifying the obstacles and solving the issues experienced in this development, the knowledge described in the following was acquired.

(1) The target plasticity level was numerically defined based on the numerical scale created to describe the degree of light intensity variation that significantly involves in the degree of plasticity.
(2) The mechanism through which plasticity is generated was investigated and the flake orientation arrangement in the paint layer was clarified to practically realize the target plasticity.

In the process of the concrete development of the paint and the painting method, the effectiveness was verified for the methods described below.

1. Paint

(1) As for the flake material, iron-based material is the best fitted because of its high magnetic permeability (the magnetic permeability of 2.2), high brightness (L* value of 50 or above) and closeness to an achromatic color.
(2) The characteristic of the paint viscosity is designed so that the flake movements stop within a short period by using the high molecular weight resin (RC resin, with the molecular weight of a hundred thousand or above) to fully increase the viscosity in a short time after the paint application.

2. Painting method

(1) The target scheme of the viscosity changes, which is designed to move the flakes promptly and stop them within a short period, was determined. Based on that scheme, the addition amount of the high molecular-weight resin was determined. The constituent ratio was decided from 20% to 25% or around. These were fixed with consideration of the restrictions that arise from the existing painting procedures in a factory.
(2) Non-volatizing material ratio (NV%) is set at from 15% to 20% or around by adjusting the dilution rate of the thinner.

By combining the methods described above, a magnetically formed decorative painting method was successfully realizing the target plasticity that is higher than the one by existing method.

Through the development of this technology, motorcycles with enhanced attractiveness in the vehicle exterior design were able to be offered to the customers.

Acknowledgments

We would like to show our special thanks to the people listed below for their efforts to contribute to our study.

Akinori Kotera, Thai Kansai Paint Co., Ltd
Hideaki Katsuta, Kansai Paint Co., Ltd

References

(1) JP, 2857276 (1999)
(2) JP, 2868948 (1999)
(3) http://www.konicaminolta.jp/instruments/knowledge/color/part1/07.html

Appendix 1

<Light intensity>

There are many units to indicate some value of light depending on how the value is defined. The measurement target in our study is a surface of painted object, and is not generating a light by itself. We considered the most appropriate physical expression to be used is luminosity (= luminous intensity) under a condition of exposure with an external light.

However, some of the apparatuses we used in our experiments were not employing SI units. The non-standardized units are still viable for particular purposes of measurement. The precise calibrations are needed if they are to be converted into SI units. Those calibrations are not practical in many cases and we would get no further information about the concerned matter even though we conducted the calibration.

Under the study goal we set, most of the measurements were conducted to know the degree of plasticity. Therefore, basically, the absolute value of an intensity of a light is not a matter of concern. The purposes of measurements are to

know the variations of intensity of a light depending on the positions of measurement points and/or the changes of the measurement angle.

Based on this background, when the measurement values were yielded in the unit of "luminosity", we applied that unit. If the measured data are expressed in other units, just like the measured values by a variable-angular photometer, we used "light intensity" instead of using some standardized expression. In the descriptions appeared in our paper, we used "luminosity" when it was clearly measured or defined so, and we used "light intensity" when we were referring to a strength of light in general.

As mentioned before, when it is considered with the intension of this paper, in which relative value is the subject to be investigated, using luminosity and light intensity are practically the same.

Appendix 2

<Test piece fabrication method>

(1) Three kinds of thinners were prepared beforehand.
  (a) Thinner with a composition mainly using solvents with boiling points of 100 to 130 degrees Celsius
  (b) Thinner with a composition mainly using solvents with boiling points of 140 to 180 degrees Celsius
  (c) Thinner with a composition using a solvent with a boiling point over 180 degrees Celsius
(2) The thinners were mixed to have five different constituent ratios to realize five different volatilization performances.
(3) A base paint resin and a hardener were mixed in a predetermined constituent ratio and combined with different thinners described above.
(4) Thus prepared five different paints were applied to ABS resin plates with the standardized magnet sheets attached to them.

Appendix 3

<Magnetic permeability>

Magnetic permeability is the degree of magnetization that a material obtains in response to an applied magnetic field. It also shows the ability of a material to support the formation of a magnetic field within itself.

In our study context, the larger the permeability is the easier the flakes are oriented to the direction of the magnetic field.

Magnetic permeability is usually defined as a property inherent to individual material itself. However, in our applications, the shapes of the metal are processed into flakes and the effective permeability value may be different from that of the un-processed original material.

The permeability values shown in Fig. 15 are the values in flake forms.

Appendix 4

<Simulation method>

Directions and strengths of the magnetic field are simulated by software application (ELF MAGIC ver. 3.40, Elf Co., Ltd.) providing the inherent residual magnetic flux density of the sheet material (228.0 mT) and its shape with the dimensions. The comparison between the simulation results and measured values is shown in Table 5 and the representations by graphs are shown in Fig. 27.

The simulation results were verified at some points with actual measurement data as shown below.

Table 5 Comparison of measurement value and simulation result

A-A' (mm)	Actual measurement (10^{-3}T)	Simulation (10^{-3}T)	Measurement value divided by simulation result
0.0	1.55	1.66	93.37%
2.5	3.89	3.99	97.49%
5.0	5.09	4.84	105.17%
7.5	5.25	4.91	106.92%
10.0	5.16	4.83	106.83%
12.5	5.13	4.81	106.65%
15.0	5.22	4.88	106.97%
17.5	5.41	5.03	107.55%
20.0	5.65	5.20	108.65%
22.5	5.67	5.17	109.67%
25.0	4.92	4.41	111.56%
27.5	2.65	2.34	113.25%
30.0	0.00	-0.01	0.00%

Simulation software : ELF MAGIC ver.3.40, ELF Co., Ltd.
Measurement equipment: Magnetic flux density meter (Tesla Meter, TM-601, KANETEC Co., Ltd.)
- Measurement points and conditions
  (1) The positions located on the A-A' line at Fig. 21 and the height is 5.0 millimeters.
  (2) The magnetic flux densities in vertical direction were measured.
  (3) On the side of North Pole of the magnet sheet polarity.

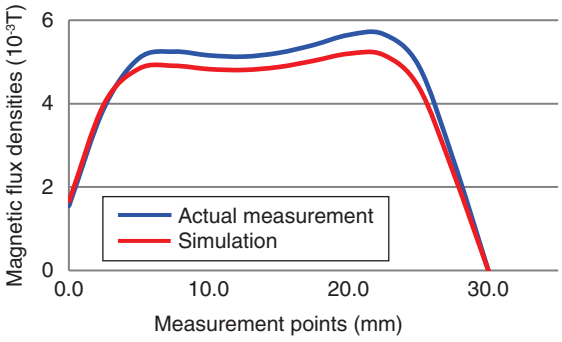


Fig. 27 Comparison of measurement value and simulation result

Appendix 5

<Measurement method of viscosity>

Step 1: Making the reference graph between non-volatilizing substance constituent ratio and viscosity

(1) Base resin, hardener and thinner are mixed together in a standard constituent ratio.
(2) The mixed paint material is put on a platter and the solvent is volatilized while stirring at room temperature.
(3) Pick up samples several times after the increase of the viscosity is visually observed.
(4) Non-volatilizing substance constituent ratios and viscosities are measured.
(5) Based on these measured values, the graph showing the relationship between a non-volatilizing substance constituent ratio of the paint and its corresponding viscosity is created.
(6) This reference graph is used in the actual viscosity measurement, which is described below, converting plotted data of non-volatilizing substance constituent ratios into viscosities.

(Measurement equipment and conditions)

(a) Viscosity
- Viscometer: LVDV-1+, Brookfield Engineering Laboratories
- Spindle/rotational speed: #4/60 rpm
- Temperature: 26 degrees Celsius

(b) Non-volatizing substance constituent ratio
- Two grams of a sample is put on a tin plate.
- The sample is heated at 110 degrees Celsius for 3 hours.
- The weight after heating is measured and used for the calculation.

Step 2: Measuring a non-volatilizing substance constituent ratio and converting into the viscosity value

(1) A couple of sheets of aluminum foil cut to a predetermined size are attached to the target part, and a prepared paint is sprayed onto the part.
(2) Peel off a sheet of aluminum foil and fold it immediately to seal it up after the predetermined time; one, two and three minutes, after the spraying.
(3) Measure the weight of the sheet of foil while keeping folded.
(4) Unfold the sheet of foil and leave it for a predetermined time and measure the weight again.
(5) The weight difference between before and after drying is used to calculate the non-volatilized substance constituent ratio in percent.
(6) Using the conversion graph we have got in Step 1, the yielded value is converted into the corresponding viscosity value.

Appendix 6

<Descriptions of individual evaluation tests>

1. Plasticity

The plasticity of magnetically formed design patterns was evaluated for the sample plates painted in different conditions. A variable-angular photometer was used for the measurement and the results were compared to the plasticity scale we defined.

2. Adhesion performance, water resistance and durability against weather stress.

We conducted the evaluation of initial adhesion performance, water resistance and durability against weather stress on each painted sample plate by applying the test methods described below.

(1) Initial adhesion performance:

We applied scratched lines with a box cutter so as for the grooves to reach the base material of the paint target part under the paint layers for both the area of the design pattern and the area without pattern on the sample plate of the individual paint condition. Thus we formed 100 tiles on the paint surface with square shapes of 1 mm by 1 mm.

After that, adhesive cellophane tape ("Sellotape" under British Trade Mark) was firmly applied to the paint surface with pressure and the numbers of the remaining tiles were counted for the area of design pattern and the non-patterned area after applying abrupt peeling of the tape off the surface at the temperature of 20 degrees in Celsius.

(2) Water resistance

Each painted sample plate was immersed in a water bath at 40 degree Celsius and kept for 10 days. After that, the sample plates were pulled out and dried. The adhesive performance test procedures were applied in the same manner as mentioned earlier for the initial adhesion test.

(3) Durability against accelerated weather stress

Each painted sample plate was exposed to light, water and heat in a sunshine weather meter for 85 hours and immersed in a water bath at 40 degrees Celsius. After that, it was pulled out from the bath and dried. The same test procedures as the initial adhesion performance test was applied to conduct evaluations by counting the remaining tiles for the area with design patterns and without them following the same manner as described before.

This series of procedures was defined as one test cycle and we kept doing the evaluation until it reaches to 10 cycles.

■ Author ■



Akiko TANAKA



Ikue SATO

Honda R&D Co., Ltd.
Honda R&D Technical Review Editorial Committee

Motorcycle R&D Center
Automobile R&D Center
Power Products R&D Center
Aircraft Engine R&D Center
Fundamental Technology Research Center

Editorial Afterword

Formerly, Japan's manufacturing industry expanded through the development of technologies and the creation of products in Japan and the manufacture of those products, also in Japan, for export to the rest of the world.

Eventually, however, Japan's manufacturing industry sought regions in which manufacturing costs were low, and made the transition overseas. Today, it is standard procedure to manufacture overseas in countries where costs are low. As a result, a significant portion of the share of manufacturing operations previously performed by Japanese industry has been lost to the manufacturing industries of emerging nations.

In order to win out over these low-cost manufacturing industries in future, Japan needs to create higher-quality technologies.

Technology is a marvelous thing, and sometimes has the power to change the world.

Technical papers have an extremely significant role to play as essential tools for the communication of technologies to the world. Technical papers are woven from the theoretical concepts of their authors. If those theoretical concepts are not solid, then a coherent paper cannot be written, rendering authors unable to communicate the details of the technology concerned.

The Honda R&D Technical Review is written and edited as vindication of unmatched ingenuity.

We will be delighted if readers use the Honda R&D Technical Review as an engine to drive the future creation of new technologies.

Chiba

©2015 Honda Motor Co., Ltd. (All rights reserved)

ISSN 1881-6223

Published by:
Honda Motor Co., Ltd.
2-1-1, Minami-Aoyama, Minato-ku,
Tokyo 107-8556, Japan

Edited by:
Honda R&D Co., Ltd.
Honda R&D Technical Review Editorial Committee

Printed:
Sep. 1, 2015

